New Negative Ion Time Projection Chamber Technology for Directional Detection of Dark Matter, Neutrinos and Fast Neutrons

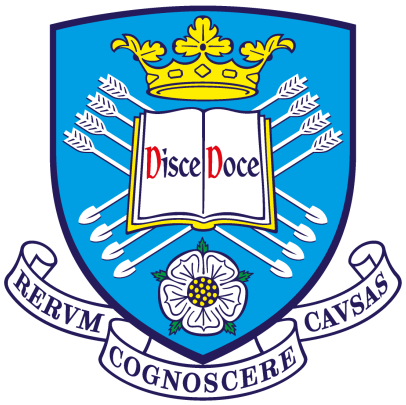

The University Of Sheffield.

Callum Eldridge

A thesis submitted in partial fulfillment for the degree of
Doctor of Philosophy

The University of Sheffield
Department of Physics and Astronomy
March 15, 2021

The candidate confirms that the work submitted is his own and that appropriate credit has been given where reference has been made to the work of others.

Abstract

Low energy nuclear recoils are one of the few signatures of the passage of WIMPs, fast neutrons and neutrinos though matter. The directional information encoded in the nuclear recoils provides valuable data which is otherwise inaccessible to a particle detector. Gas TPCs are one of the few technologies capable of reconstructing a low energy nuclear recoil track well enough to extract directional information. Scaling TPCs to large volumes while maintaining a low energy threshold and good position resolution is vital for these applications where the rarity of the interactions with matter can only be offset with larger target mass.

This work focuses on amplification, charge collection and readout technologies which are able to achieve a low energy threshold on the order of keV in negative ion gases and which have the potential to scale to large areas. Initially the gain and energy resolution of the ThGEM device is determined in low pressure SF_6. Results for the first operation of the novel MM-ThGEM amplification device in a negative ion drift gas are presented, showing that the device overcomes a number of problems encountered with the ThGEM while maintaining good gain in SF_6. A resistive layer micromegas is used to achieve three dimensional reconstruction of events in combination with the MM-THGEM which is shown to be necessary to obtain overall gas gains sufficient to achieve a low energy threshold. The MMThGEM-micromegas is shown to work well in combination with the scalable Kobe NI-DAQ electronics and to be sensitive to alpha particles, x-rays, neutrons and gamma rays. The results indicate that the novel technology is a promising avenue of development towards a large directional nuclear recoil detector. A study of the feasibility of a gas TPC experiment aiming to observe the CEνNS scattering of reactor neutrinos is also presented for the first time.

Acknowledgments

This work was made possible by funding from AWE and Sheffield University and I'd like to thank both organisations for providing me the opportunity to undertake this work. The guidance and direction of my supervisor, Neil Spooner, was invaluable and enabled this work to take the form it did. I'd also like to extend my thanks to my supervisory team at AWE, Jon Burns and Tom Crane who were generous in their support and assistance. A large amount of support was also provided by various current and former members of the DRIFT group at Sheffield, particularly by Anthony Ezeribe, Warren Lynch, Andrew Scarff and Rob Gregorio who were all a pleasure to work with.

The deep pool of expertise and experience provided by members of the CYGNUS gas working group was also of great help for this work, including advice from James Battat, Sven Vahsen, Dinesh Loomba and Elisabetta Baracchini. I'd also like to acknowledge our collaborators at Kobe University, specifically Kentaro Miuchi, Hirohisa Ishiura and Takuma Nakamura for their incredible hospitality and for helping to make the work undertaken in Japan so fruitful.

Author's Contributions

Chapter 3 The experimental design for the ThGEM experiments was based on previous work by Andrew Scarff and the Labview DAQ code was written by Anthony Ezeribe. The author assembled the ThGEM rig, took all of the presented data and wrote all of the analysis code for the ThGEM signal waveforms.

Chapter 4 The author implemented the simulation of electron and Fluorine recoils in SF_6 in the existing DEGRAD, SRIM and Geant4 simulation codes. The presented range, quenching and performance analyses were the author's own work as was the directional and energy analysis of the recoils generated by ^{55}Fe and ^{252}Cf in Geant4. The author was responsible for the generation of the DEGRAD electron recoils for the CYGNUS paper, further analysis to obtain the electron rejection factor and the projected limits was undertaken by other authors of the paper.

Chapter 5 The author wrote the readout modelling code and the code for the analysis of the modeled signal. All of the contributing simulations were implemented in their respective codes and executed by the author. All of the analysis of the modeled recoils was performed by the author.

Chapter 6 The author participated in and contributed to the initial design meeting at CERN with Neil Spooner, Rui De Oliveria, Jon Burns and Tom Crane when the MM-THGEM design was selected. The author was responsible for the experimental design, setup, execution and subsequent data analysis of the MM-ThGEM experiments. The author also wrote the charge transport simulations in the Garfield++ simulation code and analysed the results.

Chapter 7 The micromegas design was selected in consultation with CERN and James Battat. The multichannel amplification and digitisation chains were broadly kept the same as from previous experiments into ThGEM multi-wire designs by Anthony Ezeribe and Warren Lynch. The author designed and performed the micromegas and micromegas-MMThGEM experiments as well as the data analysis using analysis code also written by the author. The presented analytic model of charge dissipation in the resistive layer of the micromegas was adapted by the author from derivations reported by W. Riegler.

Chapter 8 The micromegas-MMThGEM runs in Kobe Japan with the NI-DAQ readout were undertaken by the author in collaboration with Hirohisa Ishiura, Kentaro Miuchi and Takuma Nakamura. The author was responsible for the micromegas-MMThGEM and cathode setup and operation and the selection of the gas pressure, radioactive sources and operating voltages. Hirohisa Ishiura and Takuma Nakamura operated the DAQ and provided assistance with detector setup and operations. The datafile parsing code was adapted from the work of Ikeda Tomonori and the rest

of the analysis code was written by the author. The presented data analysis was undertaken by the author with some input by Hirohisa Ishiura.

Chapter 9 The author wrote the code to import micromegas events into MATLAB and perform the MATLAB implementation of the RL-deconvolution on each event. The PSF was constructed by the author and all of the presented analysis was also the work of the author.

Chapter 10 The author undertook all of the calculations and analysis of the neutrino fluxes and associated recoil rates in a hypothetical gas detector at the Hartlepool reactor. A tour of the Hartlepool power station, site suggestions and a discussion of the issues associated with detector operations at a reactor were kindly provided by Andrew Petts of EDF energy.

Other Contributions The author participated in shift and maintenance work on the DRIFT-IId detector from 2017 to 2019.

Contents

List of Figures

List of Tables

Chapter 1

Dark matter, neutrons and neutrinos

This chapter will provide an overview of WIMPs, neutrons and neutrinos; particles which rarely interact with matter but can produce nuclear recoils. The commonality between the interactions of these particles means that detection solutions for one of the particles might be applied to the observation of all three particles.

When a particle travels through matter it will often leave distinctive signatures of it's passage. This is particularly true when a particle carries an electric charge; the long range (on the atomic scale) of the electromagnetic force and the many charged particles that constitute ordinary matter make electromagnetic interactions fairly common. However, when a particle carries no charge its interactions become much more infrequent and as a consequence the detection of such particles becomes more challenging. Neutrons and neutrinos are two known uncharged particles with small interaction cross-sections which pose unique detection challenges, another uncharged particle is the theoretical WIMP which (if it exists) might interact less than even the neutrino. Although these particles are very distinct and their detection serves different applications, they are united by the nuclear recoils that can be generated by their interaction with matter and consequently by the technology that might be applied to their detection.

The topic of this thesis is the development of negative ion gas TPC technology for the directional detection of nuclear recoils generated by WIMPs, neutrinos and neutrons. This chapter will describe each of the particles in turn, their main interactions with matter and describe the motivation for their detection with a focus on the benefits accrued by obtaining directional information. Section 1.1 gives an overview of the motivation for dark matter and more specifically WIMPs and their properties. Section 1.2 describes how neutrons are produced and gives an overview of their interactions with matter. Finally in Section 1.3 the main sources and interactions of neutrinos are discussed.

1.1 Dark matter

The Sloan Digital Sky Survey has catalogued some 930,000 galaxies in the night sky [1], which is only a tiny fraction of the total number of galaxies in the observable universe. The sum total of all visible matter in the universe is incredibly large and yet still is thought to be only a fraction of the total matter content of the space it occupies. The matter that has not been observed, dark matter, accounts for more than five times [2] the mass of the visible matter and yet we still know very little about it. The further development of technology to probe this unknown material is one of the main motivations for this work.

1.1.1 Evidence for dark matter

One of the earliest pieces of evidence suggesting the presence dark matter was the apparently anomalous mass measurement of the coma cluster obtained by Fritz Zwicky in 1933 [3]. Using the virial theorem to relate the velocity and dispersion for galaxies in the cluster to determine its gravitational mass Zwicky found that there was far more gravitating matter than accounted for by just the visible stars and gas.

Developments in astronomy in the 60's enabled the rotation of individual galaxies to be accurately measured, the results of which presented further evidence that matter was missing from existing models. A model for a galaxy based on the visible matter would predict the rotational speed of matter outside the luminous disk would drop off as the inverse square of the radius. In 1969, the velocity of a number of regions in the Andromeda galaxy were determined by measuring the doppler shift of the H-α emission line [4]. It was shown that rather than dropping off, the rotational speed was in fact flat out beyond the central bulge and this was soon shown to be a consistent feature of observable galaxies [5]. This showed that not only did dark matter account for far more gravitational mass than the visible matter but also that it was distributed out to larger radii than the luminous matter. These measurements pointed towards a roughly spherical halo of dark matter extending beyond the visible edge of a galaxy.

In recent decades gravitational lensing has provided a more direct measurement of the gravitating matter content of space and therefore provided a powerful means of studying dark matter. Gravitational lensing refers to the bending of light in a gravitational field the magnitude of which is directly related to the gravitational field in the space the light travels through. Weak lensing is a regime of gravitational lensing where the effect on the arriving light is the production of fairly small distortions of the background light source. Measuring these distrotions can produce an estimate of the intervening mass. This technique has been used to probe the dark matter halo of single galaxies; for instance the COSMOS survey obtained density profiles for around 600 galaxies and found profiles consistent with dark matter [6]. Weak-lensing measurements also provide one of the more striking pieces of evidence for dark matter in the observations of the bullet cluster, a cluster of galaxies which collided with another resulting in the separation of most of the baryonic mass from most of the gravitational mass. Figure 1.1 shows an X-ray image of the cluster corresponding to the hot gasses overlayed with the mass distribution reconstructed from weak-lensing.

The mass distribution, indicated by green contours in Figure 1.1, shows the gravitating matter is sorted into two clusters with centres separated by about 600 kpc. The visible mass in the form of x-ray emitting hot gases, indicated by the colour scale, does not match the location of the gravitating matter and is mostly located between the densest regions of space. This distribution is a result of the gases in each cluster mutually interacting and slowing during the collision while the dark matter content of each cluster continues moving without signifcantly slowing. This is fairly firm evidence that the gravitational anomalies attributed to dark matter cannot be explained by an alternate theory of gravity but must instead be a separate and unobserved form of matter.

A dark component is vital in the formation of astrophysical structure in simulations, from dwarf galaxies up to clusters, super clusters and filaments [8, 9]. There are some ways in which astrophysical structure is not reconciled with simulation. For instance the missing satellite problem which refers to the unexpectedly low number of dwarf galaxies observed orbiting the Milky Way. Other problems include the cusp-core problem and the to big to fail problem [10]. It is possible that these signatures might give clues about the

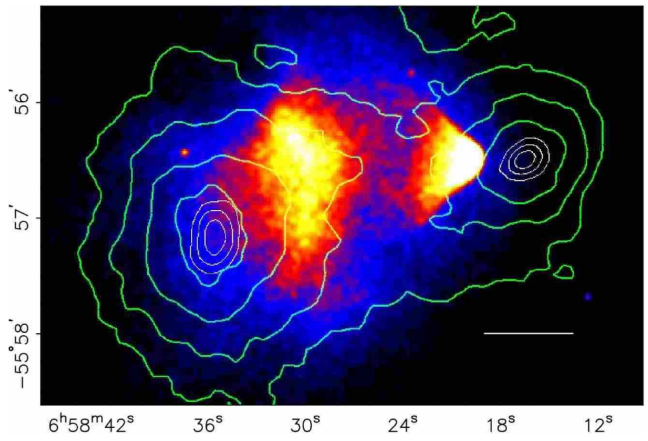

Figure 1.1: X-ray image of the bullet cluster, Green contours show the mass distribution reconstructed from gravitational lensing, white bar indicates 200 kpc. Adopted from [7].

nature of dark matter.

Signs of dark matter are even detectable in the earliest era of the universe that we can probe. The Cosmic Microwave Background (CMB), made up of photons which have been traveling through the universe since it first became transparent to light, contains indications of the structure of the universe at $\sim 400\,000$ yr after the big bang. In the early universe, fluctuations in the density of space were amplified by gravitational instability. Normal matter would feel both the pull of gravity towards these pockets and the repelling effects of radiation pressure pushing away from them, dark matter on the other hand would only be affected by gravity. The net result was a patchwork of different regions space oscillating between high and low density with the structure dictated by the relative densities of baryonic and dark matter. When the universe became cool enough for electrons and protons to recombine the map of these hot and cold spots was encoded in the photons which could now travel freely. Today those photons have been redshifted into the microwave spectrum but they still contain indications of this early structure. Figure 1.2 shows the power spectrum of the CMB temperature from Planck microwave telescope [2].

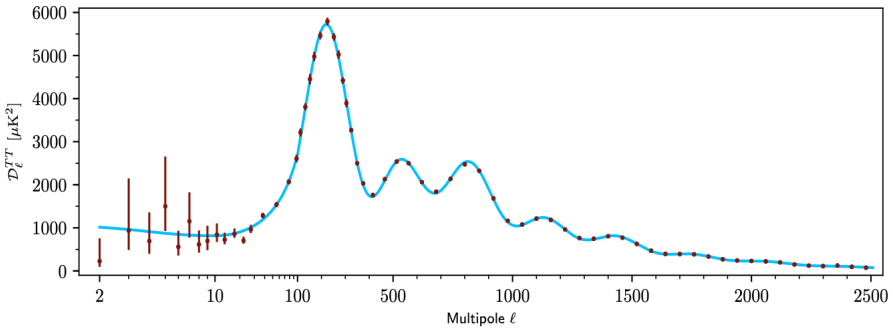

Figure 1.2: Planck CMB angular power spectrum for temperature, the blue line shows the best fit from the ΛCDM model.

The horizontal scale corresponds to the angular size of features in the CMB temperature map and the vertical scale to the contribution of those features to the overall map. The peaks in the spectrum correspond to the peaks and troughs in matter density of the universe prior to recombination. The ΛCDM model provides a 6-parameter fit to this

data with a total matter component $\Omega_m = 0.308$ and a baryonic component $\Omega_b = 0.048$. Put another way the fit to the power spectrum implies that ordinary matter comprised 4.8% of the universe's energy density at recombination while dark matter made up 26.0% of the energy content [11]. (the remaining 69.2% of the universe's energy density would be made up of dark energy, a topic not in the scope of this work). The numbers fairly well match other measuments of the dark matter fraction.

1.1.2 Dark matter candidates

Thus far the only interactions between dark matter and visible matter that have been observed are gravitational. The lack of information beyond this means that there are a number of models which have been put forward to explain dark matter which span a mass range from below an electronvolt through to tens of solar masses. The candidates put forward usually solve another outstanding problem or anomaly in particle physics and have a wide variety of couplings to matter which result in a equally wide range of techniques to identify them. Figure 1.3 shows the mass range of the various dark matter candidate particles, the mass associated with various anomalies related to dark matter and the mass range of DM search techniques.

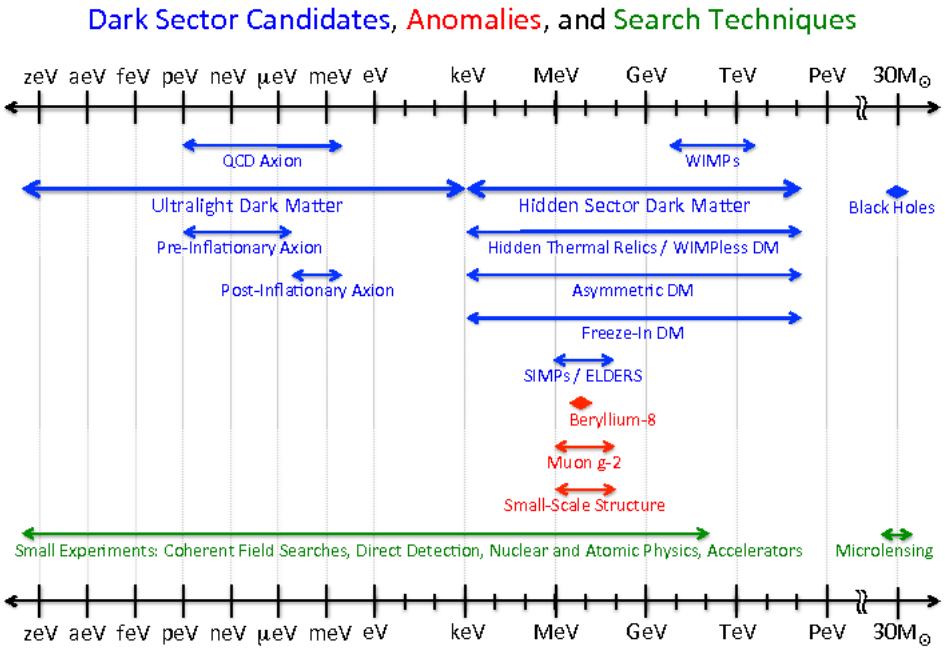

Figure 1.3: Mass constraints of potential dark matter candidates and search methods as outlined in the U.S. Cosmic Visions conference 2017 [12].

At very low masses particles of dark matter would act quantum mechanically on a galactic scale, enabling the particles to collectively form a super-fluid and/or Bose-Einstein condensate depending on the model [13]. The lowest bound on dark matter mass originates from the requirement that the particle must be gravitationally bound to a galaxy against quantum pressure, excluding masses of less than about 10×10^{-22} eV.

The highest mass candidates conversely are black holes which on the order of thirty solar masses with higher masses excluded by the absence of observations of the tidal distribution of astrophysical structure [10]. Between these extremes are various types of particulate dark matter with different properties and couplings to the visible sector. This is not a exhaustive list and the categories of candidates sometimes overlap or might exist concurrently if dark matter consists of multiple components. The most prominent candidates will be discussed in more detail in the following. WIMP are the dark matter candidate which are most relevant to the detector development that is the focus of this thesis and are discussed separately in Section 1.1.3.

Primordial black holes

Without assuming any new physics dark matter might be accounted for by non-luminous baryonic objects. The objects that fall into this class that we have observed such as brown dwarfs and black holes of stellar origin are however excluded due to the requirement that dark matter exist in the early universe as seen in the CMB. Black holes formed in the early universe before the formation of any stars, known as primordial black holes, might range in mass from 10^{-18} to 10^{6} solar masses and are potential dark matter candidates. There are a number of potential formation mechanisms for primordial black holes including the collapse of over dense regions of the primordial universe or the collapse of domain walls.

The observation of the slight bending of light around these massive astronomical objects (micro-lensing) is the primary method by which such black holes might be detected. Constraints from the CMB and astrophysical observations exclude a large part of the parameter space for these objects, although subject to certain mass constraints they still could account for the entirety of dark matter [14] and could otherwise constitute a significant part of it.

Axions

Axions were proposed as a solution to the strong-CP problem which refers to the apparent lack of observable CP-violation in strong interactions despite such violation being permitted by the standard model. To get around the fine tuning problem this poses the Peccei-Quinn (PQ) solution proposes an additional global symmetry which is spontaneously broken [15]. A consequence of this is a new field and accompanying boson, the axion.

There are a number of different types of axion that could satisfy the strong-CP problem, and subject to certain constraints, some of these could also constitute dark matter. Two models that are commonly used as benchmarks for axions are the Kim–Shifman--Vainshtein–Zakharov (KSVZ) and Dine-Fischler-Srednicki-Zhitnitskii (DFSZ) models [16]. The KSVZ and DFSZ models are examples of the two prevailing classes of axion models. KSVZ for "hadronic axions" which involves the introduction of new heavy quarks which carry PQ charges and which mediate couplings with the standard model. The DFSZ model on the other hand is the prototype for a class of models where ordinary quarks and leptons carry PQ charges and can couple directly to axions and which additionally postulates a total of two or more Higgs doublets which also carry PQ charges.

If axions constitute dark matter they would be extremely light, would have no electric charge, and they might be detected through their coupling to electrons or photons. The exclusion limits for axion-photon coupling is shown in Figure 1.4.

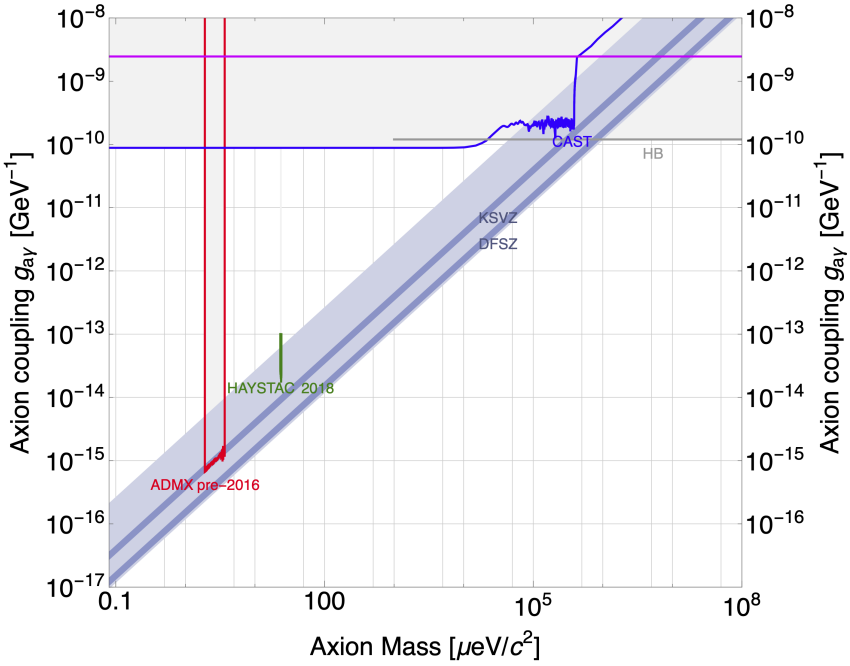

Figure 1.4: Constraints on the dark matter axion coupling to photons [17–20].

The dark blue regions indicate the allowed regions by DFSZ and KSVZ axions and the lighter blue region the generally allowed region. The gray exclusion limits come from astrophysical observations which impose a maximum on the axion-photon coupling. Axion direct detection experiments for the axion-photon coupling can utilise resonantly-enhanced conversion of axions to photons in magnetic fields. The direct dark matter detection experiment ADMX used a resonant microwave cavity to exclude axion masses between 2.6 µeV and 3.4 µeV [20]. HAYSTAC is another experiment using the same method to search higher mass axions, excluding a small region above 20 µeV [17].

Axions might also be produced in significant numbers in the Sun, with sufficient coupling to photons or electrons these solar axions might be observed. CAST is an experiment at CERN to observe the conversion of solar axions to photons in a strong magnetic field, and has set limits on the axion-photon coupling [19].

Limits on axion-electron coupling are mostly set by the exclusion of electron recoils caused by solar axions which have much more energy than DM-axions. Limits on the axion-electron coupling have been set by the X-MASS liquid-Xenon and EDELWEISS-III germanium detectors among others [21, 22]. A recent report of an excess in electronic recoils in the XENON-1t detector might be attributed to solar axions although further investigation is required [23].

Sterile neutrinos

The neutrino mass problem relates to the incompatibility of the standard model and the observation of neutrino flavour oscillations and therefore the presence of a neutrino mass. The addition of right-handed neutrinos to the standard model might resolve this issue. These neutrinos would be significantly more massive than the observed (left-handed) neutrinos. If these right handed neutrinos had masses on the order of kilo-electronvolts they could be produced with sufficient abundance in the early universe to constitute dark matter [24].

There a few potential detection methods for sterile neutrinos. A sterile neutrino could potentially decay into a photon and an active neutrino, resulting in an astrophysical signal which would consist of a spatially diffuse signal of mono-energetic photons in the x-ray band. The XMM-Newton spacecraft reported the detection of an unexplained 3.5 keV emission line from the stacked x-ray spectrum of 73 galaxy clusters which might be consistent with the annihilation of sterile neutrinos [25]. The detection is fairly close to the systematic uncertainties of the instrument however and is in tension with a later result from the more sensitive Hitomi spacecraft [26].

Other limits are imposed by measurements of the active neutrino mass by the KATRIN experiment, which precisely measures the β decay spectrum of Tritium. The lack of a perturbation of the β spectrum observed by KATRIN sets limits on the mass and mixing angle of sterile neutrinos [27].

Hidden dark matter

It is possible that dark matter might not interact at all with the visible sector beyond the already observed gravitational effects. There are a wide variety of models for this type of 'hidden sector' dark matter [28–31]. One of the biggest issues with hidden dark matter models is that they are difficult to impossible to verify experimentally. Many of the hidden sector models explored therefore have some coupling to the visible sector through connector particles or might otherwise produce an annihilation signal which might be observed.

1.1.3 WIMPS

The most relevant of the dark matter candidates for our work are Weakly Interacting Massive Particles (WIMPs) which are a family of proposed dark matter candidate particles which are stable, neutral, have tree level interactions with W and Z gauge bosons and have masses from 10 GeV to 1000 GeV. Such particles are expected to have been created in the early universe in thermal equilibrium with the other particles. As the universe cooled the number of WIMPs would have dropped exponentially. At the same time the universe was also expanding, making the process of annihilation rarer as the WIMPs become more dilute. Eventually annihilation almost completely stops and the WIMPs 'Freeze out' with their number approaching a constant. Using what is known about the temperature and density of the early universe enables one to arrive at the WIMP particle mass that would be required to produce the observed dark matter density, about 10 GeV to 1000 GeV for single component dark matter. Independently there exists an outstanding issue in particle physics known as the gauge hierarchy problem which relates to the very small physical mass of the Higgs boson relative to the natural mass predicted by the standard model [31]. Reconciling the observed Higgs mass with the 30 orders of magnitude larger standard model prediction implies new physics in on the weak scale (10 GeV to 1000 GeV). The confluence of the astrophysical motivation from freeze out for new particles on the weak scale with the new particles implied by solutions to the gauge hierarchy problem is referred to as the 'WIMP miracle'. The WIMP miracle provides a strong motivation for this kind of particle to constitute dark matter.

A good candidate particle for the WIMP can be found in supersymmetry (SUSY). Supersymmetric extensions of the standard model introduce new, supersymmetric partners to each of the SM particles which differ in spin by 1/2. Consequently the partners of SM bosons are SUSY fermions and vice-versa. Of these new particles the neutralino makes a

good WIMP candidate as in many SUSY models it is the lightest supersymmetric particle, making it stable, and it has mass and coupling to the SM on the correct scales. There are other theoretical candidates for WIMPs from different theories such as Kaluza-Klein dark matter from Universal Extra Dimensions (UED) theories, branons in theories with large extra dimensions and a number of others. These theories all produce WIMPs that are equivalent astrophysically.

The main non-gravitational WIMP interaction is a coherent elastic scattering process with matter, specifically with atomic nuclei. In WIMP dark matter the cross-section for this process is exceedingly low and depending on the model might be dependent on the spin of the nucleus or not. The maximum recoil energies that might be produced by these interactions are ∼100 keV meaning detectors need a low energy threshold to be sensitive to WIMPs.

The WIMP flux present on Earth comes primarily from the motion of the Sun around the galactic centre. The Milky Way is embedded in a halo of dark matter which, as it does not interact significantly, is not expected to have significant net rotation. The motion of the Sun around the galactic centre moves it though this halo, if WIMPs constitute dark matter this results in a prevailing "WIMP wind" from the direction of motion (approximately the direction of the Cygnus constellation). Figure 1.5 illustrates the motion of the Sun through the DM halo and the consequent angular flux of WIMPs capable of producing a detectable recoil at Earth assuming a 100 GeV WIMP and a 25 keV threshold for fluorine recoils.

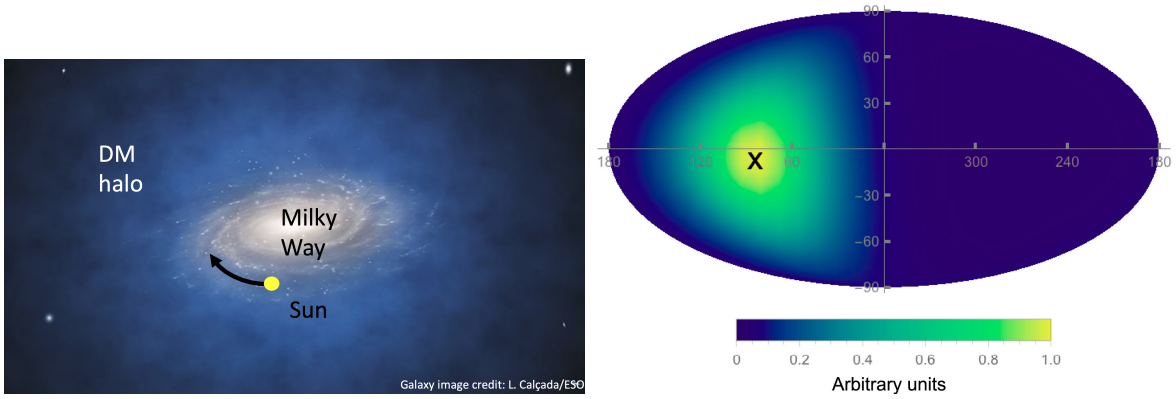

Figure 1.5: Left: Diagram of the motion of the Sun through the dark matter halo of the Milky-way. Right: Flux of WIMPs observable at Earth moving with speeds sufficient to induce to produce 25 keV fluorine recoils assuming 100 GeV WIMP mass (reproduced from [32]). Mollweide equal-area projection in Galactic coordinates.

As shown in the figure, effectively all the WIMP flux observed at Earth originates from a single hemisphere in galactic coordinates orientated toward the direction of motion of the Sun around the galactic centre. These figures are based on the Standard Halo Model (SHM) is a simple model for the expected velocity distribution of dark matter within the galactic halo. It assumes a spherical halo of dark matter with the velocities modelled by a gaussian truncated at the escape velocity of the galaxy.

A recent refinement of the SHM is the SHM++ which was inspired by the recent discovery of the 'Gaia sausage', a flattened, anisotropic region of stars in the galactic halo resulting from the collision of the Milky way with a dwarf galaxy. These stars would have brought a significant amount of dark matter with them which would have introduced a detectable anisotropy into the galactic dark matter halo. The SHM++ updates the SHM

to include this anisotropy [33]. For most experiments adopting the SHM++ over the SHM only results in a slight modification of the excluded WIMP cross-section.

The continuous flux of WIMPs provides an opportunity for detection on Earth by their occasional collisions with atomic nuclei, inducing recoils that might be detected by a sufficiently sensitive detector. Figure 1.6 shows some of the exclusion limits for WIMPs assuming a spin-independent coupling to matter as of the start of 2021.

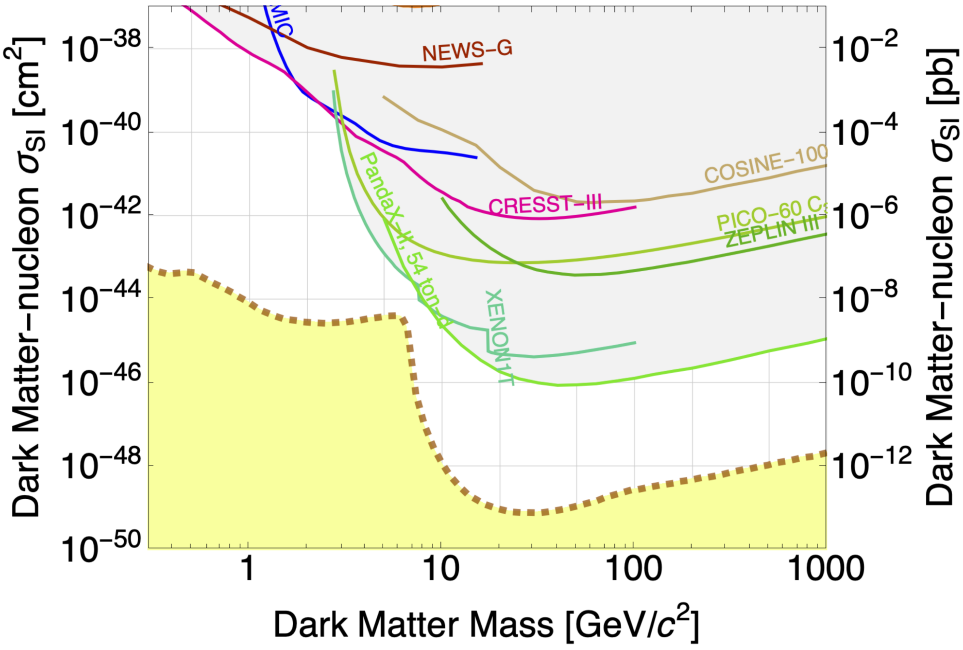

Figure 1.6: Exclusion limits [34–42] for spin independent nuclear Dark Matter interactions assuming a local dark matter density of 0.3 GeV/c^2. Dotted curve indicates the neutrino floor for Xenon.

The exclusion limits, shown by the coloured curves labeled with the name of each experiment, indicate the region of the WIMP mass/cross-section parameter space which the respective experiments were sensitive to and did not report a detection. The currently leading limits over most of the mass range are from the liquid Xenon detectors PandaX-II [43] and Xenon1T [35]. At lower WIMP masses though detectors capable of obtaining lower thresholds such as the crystal based CRESST-III [36] become competitive.

The ultimate irreducible background for most WIMP direct detection experiments is the coherent scattering of neutrinos from the Sun. This background presents a lower limit to the WIMP cross-section that can be probed by most direct detection experiments, a limit known as the 'neutrino floor' [44]. The neutrino floor for a Xenon target is indicated in Figure 1.6 by the dotted line and yellow shaded region. Detectors sensitive enough to reach the neutrino floor would begin to observe the scattering of solar neutrinos off nuclei in the detector. For most detectors the resultant nuclear recoils are indistinguishable from WIMP produced nuclear recoils, and the discovery of a WIMP with a cross-section significantly less than the floor would be impossible.

The only distinguishing feature between nuclear recoils induced by solar neutrinos and by WIMPs are their direction; recoils from neutrinos would be orientated away from the direction of the Sun while recoils from WIMPs would be oriented in the direction of the WIMP wind. Directional detectors therefore present a unique method of completely tran-

scending the neutrino floor and could potentially probe other aspects of the dark matter halo, such as the anisotropy associated with the Gaia sausage, after WIMP discovery.

Because of the rarity of WIMP interactions with matter, WIMP detectors are universally located deep underground. On the surface, backgrounds produced by cosmic ray muons dominate any detector signal and only by shielding the detectors with several kilometers of rock or water can backgrounds be lowered significantly enough for competitive detection. Within a detector the non-trivial background interactions can be broadly divided into high energy electrons, produced mainly by gamma rays, and nuclear recoils produced by neutrons. As the WIMP interactions of interest produce only nuclear recoils, distinguishing electrons and nuclear recoils is an important part of the background rejection for a detector. The nuclear recoils produced by fast neutrons are more difficult as they are functionally the same as nuclear recoils produced WIMP elastic scattering. Neutron backgrounds are controlled by careful selection of radio-pure materials in the detector, shielding and careful analysis.

Detectors sensitive to WIMPs are by construction also sensitive to neutrons and the technology developed for WIMP detection can have applications in the field of neutron detection. A significant part of the motivation for this work is the directional detection of fast neutrons; neutron sources, interactions and the motivations for their detection are discussed in the next section.

1.2 Neutrons

Neutrons, are a neutral subatomic baryon which, along with protons, constitute the components of the atomic nucleus and a large proportion of the matter we con observe [45]. Free neutrons are unstable with a lifetime of 885 s and decay into a proton, an electron and a neutrino. Stable neutrons on Earth are exclusively located in atomic nuclei and are only liberated by nuclear reactions. Neutrons, being neutral, don't interact through the coulomb force in matter, the only interactions occur directly with atomic nuclei and consequently neutrons are very penetrating compared to alpha, beta and gamma radiation.

1.2.1 Neutron production

Neutrons can be ejected from atoms by a variety of transitions including fission, fusion and spallation reactions. Spallation and fission reactions contribute the most significantly to the background neutron flux on Earth.

On Earth's surface, most of the neutron background can be attributed to cosmic rays. Cosmic rays are high energy particles of astrophysical origin which, when they encounter the Earths atmosphere, produce a shower of particles as they are slowed [46]. The most numerous shower particles at sea level are muons originating from the decay of pions and even kaons higher in the atmosphere. Neutron ejected off atmospheric nuclei by high energy muons comprise the majority of neutron flux at sea level. Cosmic ray neutrons are a large part of the background for WIMP direct detection experiments and consequently WIMP detectors are universally located deep underground to escape the majority of this background.

Spallation reactions are also utilised as an artificial neutron source by using a light ion accelerator in conjunction some sort of target. The ISIS neutron and muon source for example uses a proton beam and a tungsten target to generate neutrons for a variety of research applications [47].

Neutrons are also produced by light elements as a byproduct of certain fusion reactions. Deuterium-deuterium, deuterium-tritium and tritium-hydrogen reactions all produce neutrons as a byproduct. These reactions are the basis of most nuclear fusion research and consequently copious amounts of neutrons are produced by research fusion reactors such as Tokamaks. Sufficiently fast alpha particles can also overcome the coulomb barrier to fuse with certain light isotopes such as carbon, beryllium and lithium [48]. The production of neutrons from these reactions as well as deuterium and tritium fusion are often used to generate neutrons for research.

Another common source of neutrons is the nuclear fission of certain isotopes. Some heavy elements with $Z > 232$ can spontaneously fission into a number of fragments which often includes multiple free neutrons [48]. Spontaneous fission of trace heavy isotopes in rock produce the majority of the neutron flux observed underground and form the main background for WIMP experiments.

Interactions between certain heavy elements and neutrons can also induce fission resulting in the production of further neutrons, the resulting feedback loop is the basis of both nuclear power and nuclear fission weapons. The majority of heavy elements capable of spontaneous fission which are long lived enough to be accumulated in significant quantities are either fuel for, or byproducts of, nuclear reactors [49]. The fissile isotopes ^{239}Pu and ^{235}U are necessary for the synthesis of nuclear weapons and controlling the supply of these isotopes is crucial for non-proliferation efforts [50].

1.2.2 Neutron interactions

The probabilities of the different types of neutron interaction is highly dependent on energy, consequently neutron radiation is often divided into subcategories depending on speed. To a first degree neutrons can be divided into two categories: 'slow' and 'fast' neutrons. A common way to divide the two groups is the *cadmium cutoff*, the energy of an abrupt reduction in absorption cross section on ^{113}Cd at about 0.5 eV [51].

Fast neutrons are very unlikely to be captured by atomic nuclei but will be slowed by scattering interactions. Elastic scattering involves the transfer of kinetic energy from the neutron to an atomic nucleus resulting in a nuclear recoil. The momentum transfer between two bodies in an elastic collision is maximised when they are approximately the same mass and as such light nuclei make the most efficient targets for scattering. If sufficiently energetic, the nuclear recoils produced by scattering reactions can subsequently be detected by the produced ionisation, phonon or scintillation signals.

Fast neutrons can also undergo inelastic scattering where a portion of the transferred energy elevates the recoil nucleus into an excited state which will subsequently decay and release a gamma ray. The gamma rays produced by inelastic collisions can form a background in some applications and complicate gamma/neutron discrimination.

Slow neutrons also undergo scattering with nuclei, although the small energy transfers mean such interactions are not detectable. Additionally slow neutrons can be absorbed by a nucleus, absorption reactions include (n,γ), (n,α), (n,β), (n,p) and (n,*fission*). The cross sections of these neutron induced reactions are dependent on the target nucleus and must have a positive Q-value to be energetically possible. As the recoils from slow neutrons are generally too small to be detectable, most detectors observing slow neutrons rely on these neutron induced nuclear reactions. The (n,α), (n,p) and (n,*fission*) reactions are favoured for detection purposes due to the relative ease of detecting the secondary particles. Some of the most significant reactions for neutron detection purposes are listed

in Table 1.1.

Table 1.1: Reactions and reaction cross-sections for thermal neutrons (0.025 eV) for common isotopes used in neutron detection [51–53]

Target	**Reaction**	**Cross-section (barns)**
^{10}B	(n,α)	3840
^{6}Li	(n,α)	940
^{3}He	(n,p)	5330
^{157}Gd	(n,β),(n,γ)	255000
^{233}U,^{235}U,^{239}Pu	(n,*fission*)	524, 586, 748

1.2.3 The applications of neutron detection

Neutrons are generally more challenging to detect than directly ionising radiation but their detection serves a number of purposes.

One reason for accurate neutron measurements is for health physics and dosimetry. Neutrons can contribute significantly to the equivalent radiation dose with a radiation weighting factor of up to 20 [54] (gamma and x-rays score 1). Obtaining an accurate assessment of ambient neutron fields is an important safety consideration in nuclear industry and research.

The accurate measurement of neutron fluxes is also useful for the instrumentation of nuclear fission and fusion reactors. The neutron flux in a nuclear fission reactor is directly related to the fission rate and measurements are important for monitoring core criticality [55, 56]. Fusion reactor similarly produce large numbers of neutrons and accurate determination of the neutron flux and energy spectrum is a probe of the ion temperature, fusion power and fuel ratio [57]. Neutrons make up the most penetrating radiation from a number of types of nuclear waste including spent fuel and activated product, accurate neutron flux information can inform clean-up efforts and storage decisions.

Another reason for neutron detection, and the most relevent for this work, is to detect illicit trafficking in radioactive material [48]. Neutrons are among the most challenging type of radiation to effectively shield on a small scale and are also much less common in the normal flow of commerce than gamma emitting sources [50]. Significant numbers of neutrons are emitted by plutonium in particular which is among the most severe threats from a nuclear proliferation standpoint. Neutron screening of stream of commerce cargo is therefore a useful tool for nuclear security. Obtaining directional information from fast neutrons in particular would be a useful capability as an idea of the neutron source location could speed up the manual inspection which follows a container or truck being flagged.

1.3 Neutrinos

Neutrinos are a particle with only rare interactions with matter, they have interactions with both electrons and nuclei and can produce nuclear recoils in a similar way to the previously discussed WIMPs and fast neutrons. Neutrinos are the charge-less, light partners to the charged leptons: electrons, muons and tauons. The exact mass of neutrinos

is not known, although they are known to be extremely light with a maximum mass on the order of electronvolts [46]. Neutrino interactions with matter proceed entirely via the weak force and gravity; this results in an extremely low interaction cross-section which makes the detection of neutrinos very challenging.

The three flavours of neutrinos are electron neutrinos, ν_e, muon neutrinos, ν_μ, and tauon or tau neutrinos ν_τ. Like their charged counterparts the generations of neutrinos are known to have different masses, although the values of the masses are not known nor is the order of the neutrinos in terms of mass.

1.3.1 Neutrino production

Apart from annihilation and pair production, neutrinos are involved in effectively all interactions where a charged lepton is created or destroyed. Weak interactions will conserve lepton family number so the production of an electron, muon or tauon will be accompanied by the corresponding creation of an electron, muon or tau anti-neutrino. Likewise the decay of a muon or tauon will produce a muon or tauon neutrino in addition to the other products.

One significant process for neutrino production is the conversion of a proton to a neutron, $p \rightarrow n + e^+ + \nu_e$, this process is integral to fusion in the Sun as well as the underlaying process occurring in the nucleus during the β^+ decays of various proton rich isotopes. The positron and neutrino share the energy liberated by the reaction resulting in a continuous spectrum of energies for both particles up to the Q-value of the specific reaction. The corresponding process $n \rightarrow p + e^- + \overline{\nu_e}$ is conversely associated with fission and the β^- decay of neutron rich isotopes

The fusion of hydrogen into helium powers the Sun, and although the fusion proceeds via several pathways the net effect is the conversion of two protons into neutrons and the corresponding emission of two electron neutrinos. Solar neutrinos comprise the majority of the neutrino flux observable at Earth, the energy spectrum of neutrinos observed at earth from the most common solar fusion pathways is shown in Figure 1.7.

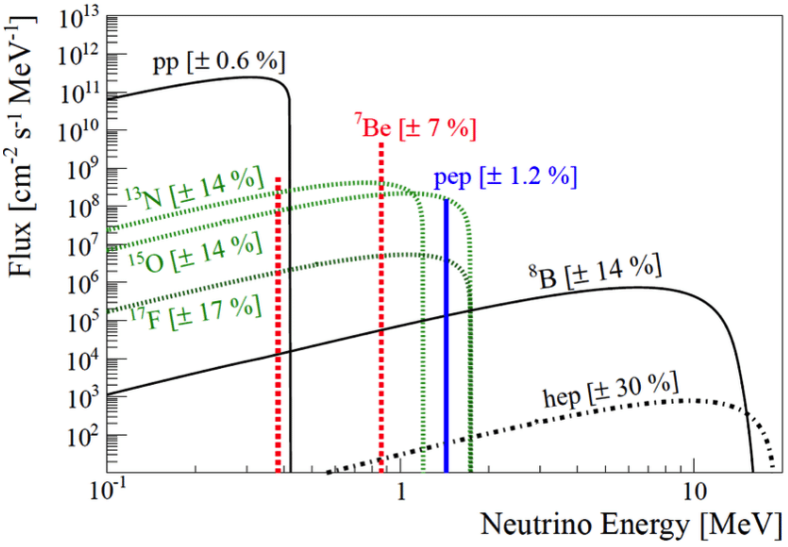

Figure 1.7: Solar Neutrino flux at Earth from a subset of the neutrino producing interactions. The decaying nucleus which produces the neutrinos is indicated in brackets for reactions not initiated between free protons. Reproduced from [58].

The dominant process is pp fusion which consists of the reaction $p + p \rightarrow D + e^+ + \nu_e$ and results in a spectrum of neutrino energies up to 0.42 MeV.. A significant amount of the rest of the neutrinos are from the β^+ decays of the ^{8}B, ^{13}N and ^{15}O in the PP-III chain and CNO cycle and have similarly smooth energy spectra. The mono-energetic neutrinos from the PP-II (^{7}Be) and PEP branches on the other hand are produced instead by electron capture reactions, $p + e^- \rightarrow n + \nu_e$ where the neutrino carries away the entirety of the decay energy. Although exclusively produced as electron neutrinos, flavour oscillation is a significant factor over the distance between the Earth and the Sun and as a result the Solar neutrino flux at Earth is a mix of all three neutrino flavours [58].

The process which powers nuclear reactors is the fission of heavy elements into fragments and the subsequent decay of these fragments toward stability. The fission fragments produced are extremely neutron rich and as a result β^- decays feature heavily in the decay chains of these elements; on average each fission results in six β^- decays in the timescale of a fuel cycle [59]. Consequently a running nuclear reactor will produce about 2×10^{20} electron anti-neutrinos per second for every gigawatt of thermal power. Anti-neutrinos will also be produced by β^- decays of long lived isotopes in the spent fuel, although at a much slower rate. This anti-neutrino flux is of interest for reactor monitoring and potentially for some specific neutrino physics.

Finally there are a number of astrophysical sources of neutrinos including supernovae, active galactic nuclei, and white dwarf and neutron star mergers [60]. The observation of supernova neutrinos is particularly interesting for astrophysics and for probing stellar nucleosynthesis. The cosmic rays created by these high energy processes also contribute to the observable neutrino flux at Earth, producing neutrinos as part of the shower of particles they generate in the atmosphere.

1.3.2 Neutrino interactions

The distinguishing feature of neutrinos is their incredibly low interaction cross-section with matter. Neutrinos interact with matter only through gravity and the weak nuclear force.

The weak interactions of neutrino can be divided in to neutral current (exchange of a Z^0 boson) and charged current ($W^\pm$) interactions [61–63]. Figure 1.8 shows the Feynman diagrams for neutrino charged current and neutral current elastic scattering processes with electrons. Flavour conservation is maintained in these interactions which means that only electron neutrinos elastically scatter with electrons through the charged current process. The neutral current interaction conversely can occur between neutrinos and charged leptons of any flavour.

Charged and neutral current interactions also occur between neutrinos and nucleons [64]. Neutral current interactions between neutrinos and nucleons results in elastic scattering without a change in the nucleon. Charged current interactions between neutrinos and nucleons however result in the conversion of the nucleon; the Inverse Beta Decay (IDB) reaction, $\bar{\nu_e} + p \rightarrow n + e^+$, is particularly important for anti-neutrino detection and will be exploited by SuperK-Gd by using Gadolinium doping to detect neutrons in conjunction with the annihilation signal from the positron [65, 66].

Importantly for this work, neutrinos also have the capacity to scatter coherently off the entirety of an atomic nucleus rather than off individual nucleons. Coherent Elastic Neutrino-Nucleus Scattering (CEνNS) results in an enhancement of the cross section for low momentum transfer neutral current interactions. The scattering of solar neutrinos

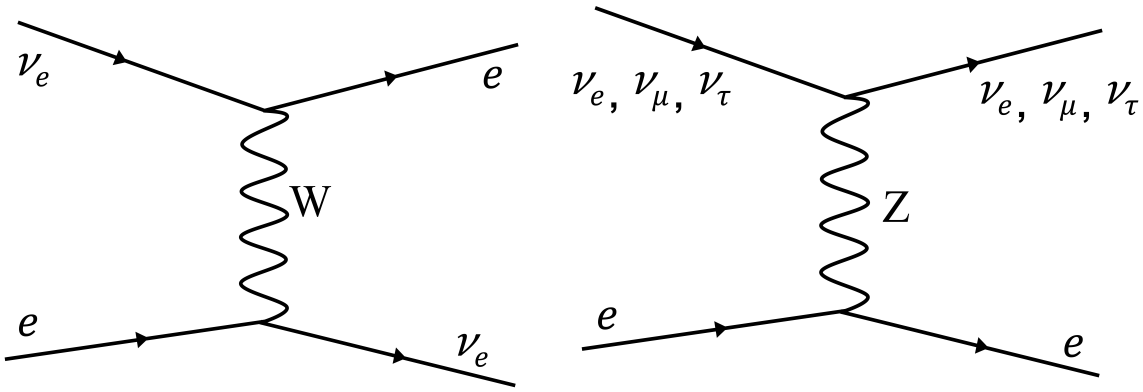

Figure 1.8: Elastic neutrino-electron scattering via charged current (left) and neutral current (right) interactions.

through the CEνNS process produces the 'neutrino floor' for WIMP detection experiments described in Section 1.1.3. The despite the comparatively large cross-section of the CEνNS process, the low energies at which it occurs have presented an challenge for its detection and it has not been comprehensively studied. The first observation of the CEνNS process was reported only in 2017 from a pulsed accelerator neutrino source [67]. The rate of CEνNS recoils from reactor and solar neutrinos in a potential gas-based nuclear recoil detector is explored in Chapter 10.

1.4 Conclusions

From a detection standpoint WIMPs, neutrons and neutrinos are united by the nuclear recoils which can be produced by their elastic scattering processes. Both neutrons and neutrinos present a background to WIMP direct detection experiments but the detection of each particle has applications in its own right.

As discussed, WIMPs are one of the proposed candidate particles which might make up dark matter, the unobserved gravitating matter which out weighs the visible sector by a factor of 5. The observation of nuclear recoils induced by WIMPs would be revolutionary for both particle physics and astrophysics and could resolve some of the most fundamental issues at the heart of physics. Neutrons have the highest interaction cross-section of the discussed particles but are still very penetrating. WIMP detector technology has the potential to produce accurate measurements of the elastic scattering of fast neutrons and serve a number of neutron detection applications.

Nuclear recoils produce by neutrinos through the CEνNS process is an important background for WIMP detection but has only been observed in a single experiment. A more comprehensive exploration of the CEνNS process has the potential to uncover physics beyond the standard model, explore solar fusion processes and would provide a useful benchmark for WIMP detection technology.

The detection of the nuclear recoils produced by each of these particles is an entire topic in itself and there a number of technologies that can be applied to do so. Particularly interesting is extracting directional information from nuclear recoils which can confer a number of benefits for the detection and identification of the discussed particles. The principals of detecting nuclear recoils, directionality and a number of examples of detectors are discussed in the next chapter.

Chapter 2

Detectors and Directionality

The technology for ionising particle detection has evolved considerably over the last century, particularly with the progress in electronics and computer technology. The first ionising radiation detectors consisted of fluorescent screens viewed in a darkened room or photographic plates [68] with analysis proceeding entirely by hand. While the underlaying processes remain the same, modern particle detectors can consists of thousands of elements and can produce vast quantities of data down to the interactions of individual particles. These advances have allowed for increasingly more information to be extracted about the interactions occurring in detectors; one such frontier is the extraction of directional information from individual recoils.

This chapter will describe the basic principals of detector technology with a focus particularly on nuclear recoils, directionality, and gas Time Projection Chambers (TPCs). First some of the broad properties of recoils in matter which are relevant to their detection are discussed in Section 2.1. One specific technology for particle detection, gas TPCs, are described in Section 2.2 which covers the basics of electron amplification, negative ion gases and ER discrimination. Section 2.3 introduces directional detection as it applies to induced nuclear recoils, describing the different degrees of directionality and examples of directional WIMP, neutron and neutrino detectors. Finally the overall conclusions are drawn in Section 2.4.

2.1 Properties of keV recoils in matter

A charged particle with significant energy traveling in a medium will collide with the electrons and nuclei that make up the medium and slow down. For detectors sensitive to electrons and nuclear recoils it is the effects of the passage of the recoiling particle through the medium that are observed.

The dynamics of particle slowing are complicated, consisting of many discrete interactions with electrons and other nuclei and often producing additional secondary recoils which have their own sets of interactions. This is illustrated in Figure 2.1 which shows a single 15 keV recoil in silicon simulated in SRIM [69].

The path taken by the primary Si recoil, indicated in white, bends as it travels due to the effect of many discrete scattering interactions which each deflect the nucleus in a random direction. Light particles generally exhibit more of this bending than heavy particles because a given momentum transfer will result in a significantly larger change in velocity for a lighter particle. The bending as well as variations in the number and energy exchanged in collisions results in a variation in the range of a slowing particle.

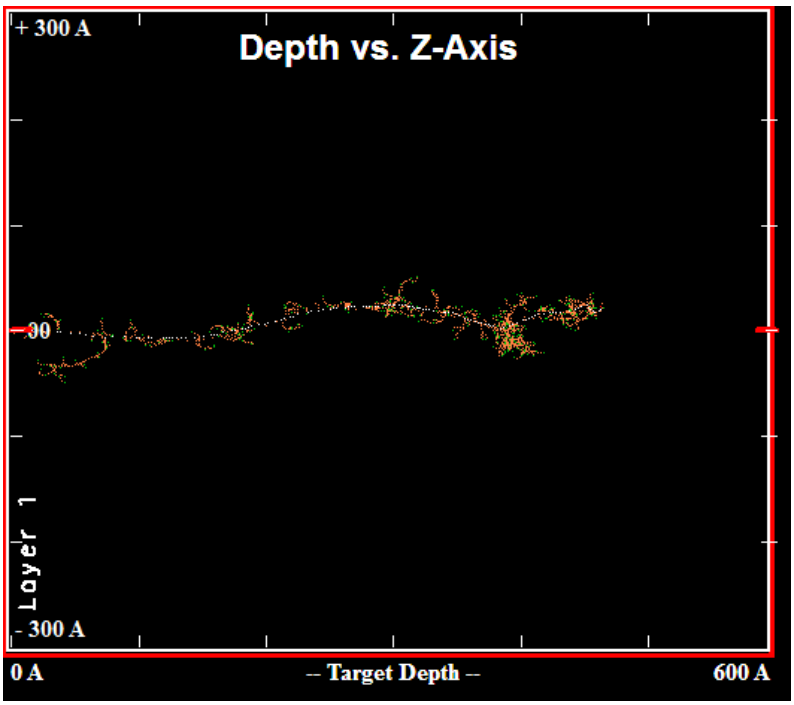

Figure 2.1: SRIM simulated 15 keV recoil in silicon, primary Si recoil indicated in white and secondary recoils are indicated in orange. Green indicates the ion endpoints.

The variation in range is referred to as the range straggling of the particle.

Scattering interactions between a primary recoil and other atoms and electrons can transfer enough energy that the other particle is significantly displaced, becoming a secondary recoil which can itself also produce secondaries. These secondary Si recoils are indicated in orange in Figure 2.1 with the endpoint of each of displaced atom indicated in green.

The primary atom itself eventually thermalises after dissipating all of it's initial energy. The energy of a recoil can be dissipated in a number of forms, including heat, light and ionisation. The recoil signature of interest in this work is the ionisation signal.

An ionisation occurs when enough energy is transferred to a bound electron that it is liberated from its atom creating an electron-ion pair. The average amount of energy needed to ionise a single electron from an atom in a medium is referred to as the medium's w-value. W-values are normally on the order of tens of electronvolts, for the gas CF_4 for example the w-value is 34.4 eV [70]. For electron recoils in a detector the average number of electron-ion pairs created is equal to the initial electron energy divided by the w-value of the medium.

Because the slowing and ionisation of particles is a stochastic process, the number of electron-ion pairs created by an individual recoil will fluctuate from the average [71]. This fluctuation is commonly characterised by the Fano factor, F, which is the ratio between the average fluctuation in ionisation for mono-energetic recoils and the fluctuation that would be expected from pure Poisson statistics [72]. The Poisson fluctuation is uniformly larger than reality as the ionisations are not independent of each other; a value of close to 0.4 is typical for the Fano factor. The Fano factor of a radiation in a material sets a lower bound on the energy resolution of a detector.

For nuclear recoils, a significant amount of the initial recoil energy does not contribute to the ionisation of electrons but is instead dissipated through other channels, mostly

heat. The Ionisation Quenching Factor (IQF) is equal to the fraction of a recoil's energy which contributes to the ionisation of electrons. The Lindhard model is a semi-empirical formula for the IQF of recoils in a material [73]. The Lindhard model can be expressed as a function of the reduced energy of the recoil, ϵ, and a constant, k, which is related to the stopping power of the medium. The IQF in this model is given by

$$IQF = \frac{kg(\epsilon)}{1 + kg(\epsilon)} \tag{2.1}$$

with

$$\epsilon = 11.5 E_R Z^{-\frac{7}{3}}, k = 0.133 Z^{\frac{2}{3}} A^{-\frac{1}{2}}, \tag{2.2}$$

where Z and A are the atomic number and mass number of the recoiling nucleus and medium and E_R is the recoil energy, the function $g(\epsilon)$ is given by

$$g(\epsilon) = 3\epsilon^{0.15} + 0.7\epsilon^{0.6} + \epsilon. \tag{2.3}$$

The Lindhard model neglects the atomic binding energy of electrons which means this model becomes quite crude at low reduced energies, with a lower limit of $\epsilon \sim 10^{-2}$, equivalent to $\sim 0.2\,\text{keV}$ for fluorine [74]. The IQF of a number of gases determined by the Lindhard model is shown in Figure 2.2.

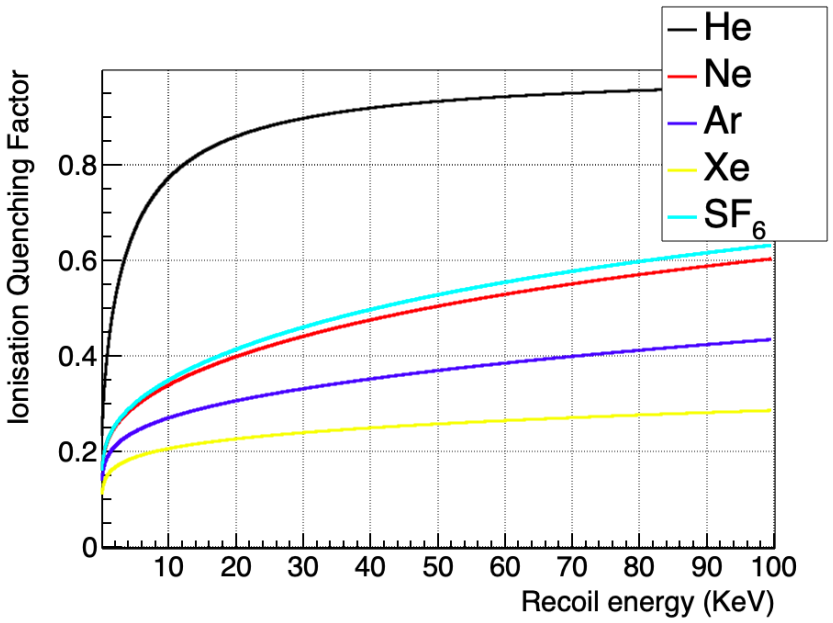

Figure 2.2: The IQF of various gases determined with the Lindhard model.

The fraction of energy which contributes to ionisation decreases with decreasing energy. There is also a dependence on the atoms constituting the recoil and target gas; lighter atoms generally deposit a larger fraction of ionising energy than heavy atoms. The effects of quenching contribute to the relative amounts of ionisation created at the start and end of a recoil and are an important correction for calculations of the recoil energy. Electrons deposit effectively all of their energy as ionising energy so the IQF does not need to be considered for electrons. The units KeV_{ee} or KeVee (KeV-electron-equivalent) are sometimes used to refer to the ionising energy deposit of a particle to distinguish from the total recoil energy. For electrons the units KeVee and KeV are equivalent while for nuclear recoils KeVee is less than the recoil energy in KeV by the quenching factor.

2.2 Gas TPCs

A WIMP, neutron or neutrino can produce a nuclear recoil in matter in any phase: solid, liquid or gas. The phase and density of a material effects the properties of a recoil and has implications for the detection. One of the advantages of gas-based detectors is that the very low density of the target medium significantly extends the tracks of low energy recoils. The longer tracks can enable more of the recoil detail to be extracted which can be beneficial for directionality and particle identification.

A Time Projection Chamber (TPC) is a type of particle detector which uses electric fields to drift the charge ionised by a radiation interaction in the target medium to a readout element [51]. In a constant electric field the arrival time of charge at the readout will be linear with the initial displacement of the ionisation interaction; the resulting projection of the displacement into arrival time gives the detector it's name [75]. The target medium in a TPC can be a gas or liquid noble gas such liquid Argon or Xenon. A diagram of a generalised TPC detector with a planar geometry is shown in Figure 2.3.

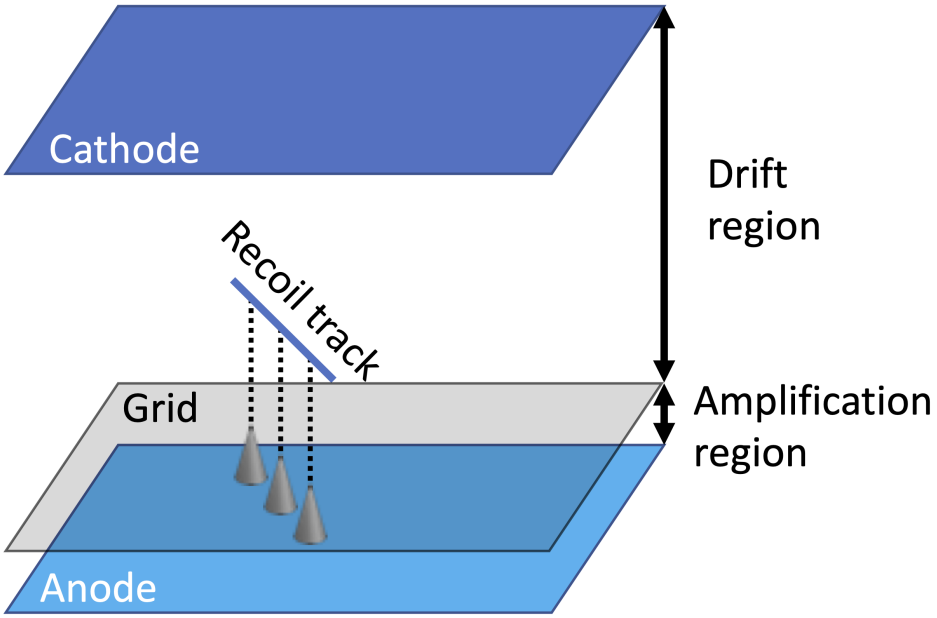

Figure 2.3: Diagram of a generic gas TPC with a planar readout.

The initial interaction in a TPC consists of the deposition of enough energy to ionise electrons from the target medium. Commonly the energy deposition consists of an ionising radiation interaction producing an electron or nuclear recoil. As it travels a recoiling particle will ionise atoms along its track resulting in a cloud of electron-ion pairs. If the cloud is in an electric field the negatively charged electrons and positively charged ions will drift in opposite directions, the ions drifting in the field direction and the electrons drifting against the field.

For some interactions that a TPC might observe the amount of ionised charge will be small, often on the order of hundreds of electrons. For these interactions to be observed, the ionised charge must be amplified significantly. This occurs in the amplification region of the TPC, a region of high electric field around or near the anode which accelerates the arriving electrons such that they have enough energy to ionise further electrons. Each of the resultantly liberated electrons can go on to ionise further electrons resulting in

an 'avalanche' of charge which can amplify the initially arriving charge by a factor of hundreds to hundreds of thousands.

Most detectors utilise the current induced by the motion of the amplified charge toward an anode element to observe signal [76]. There are also designs where the scintillation light produced by the electron multiplication is instead observed or a combination of the anode current and scintillation signal are recorded. Even after gas amplification the anode current is often very small and detectors will implement electronic amplification stages to further enhance the signal before further analysis.

2.2.1 Electron amplification in gasses

An important aspect of gas TPC detectors is the amplification of charge in the gas, there are a variety of different detector geometries and devices for generating the gas electron amplification. They universally utilise a region of high electric field of sufficient length and strength for the development of an electron avalanche. One of the key operating parameters for electron amplification devices is their *gain*, which is simply the ratio between the charge arriving at the amplification device and the charge extracted/collected.

The process of electron amplification in the gas is often parameterised with the Townsend model. For an amplification gap with constant field and assuming no photo-ionisation the first order Townsend's coefficients, A and B, are given by the equation

$$\ln(\text{Gain}) = dPAe^{-\frac{BP}{E}}, \tag{2.4}$$

where d is the gap width, P is the gas pressure and E is the electric field strength. A different parameterisation of this Townsend equation is given by the Rose-Korff gain model [77, 78]:

$$\ln(\text{Gain}) = \frac{d}{\lambda}e^{\left(\frac{-I_e}{\lambda E}\right)}, \tag{2.5}$$

where λ is the electron mean free path in the gas and I_e is the ionisation energy of electrons in the gas. This parameterisation is a bit more intuitive with the factor $\frac{d}{\lambda}$ giving the average number of electron collisions in the gap, and the factor $\frac{\lambda E}{I_e}$ giving the average fraction of the electron ionisation energy obtained between collisions.

There are a number of devices to generate these amplification fields. The original TPC detectors exploited the radial nature of a field in the vicinity of a thin wire to generate the necessary strong electric field. Multi-Wire Proportional Counters (MWPCs) are a type of readout for TPCs which use an array of wires to create the drift and amplification fields. MWPCs can track recoils using the time and magnitude of charge arriving on each of the wires.

MWPCs compete with the newer generation of devices grouped into the category of Micro-Pattern Gas Detector (MPGD) which are characterised by the small separation between individual detector components and have superseded wire based readouts in many instances. There are a number of different types of MPGD used to create strong localised fields for electron amplification, the micromegas and GEM MPGDs are described below.

Gas Electron Multipliers (GEMs) are a type of MPGD which consists of a thin dielectric foil with a regular pattern of holes through it [79]. The electrodes of a GEM consist of layers of metal on the front and back of the dielectric, the amplification field is generated in the holes by the bias applied between the electrodes, a microscope image of a GEM foil is shown in Figure 2.4. For applications where the gain of a single GEM is insufficient two or three GEMs can be arranged sequentially such that charge from the drift region

passes through and is amplified in each stage. GEMs only create the amplification field and are not conventionally used to readout the signal, instead the charge amplified by the GEM is collected by an 'induction plane' behind the GEM which is often patterned with strips, pixels or pads. The Thick-GEM (ThGEM) is a variant on the GEM with the same shape and operating principal but with each of the dimensions scale by a factor of approximately ten.

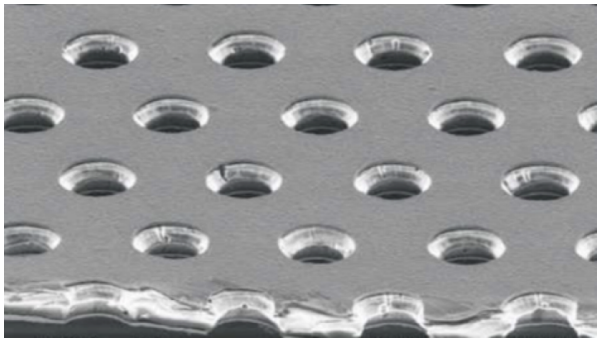

Figure 2.4: Microscope image of a standard GEM foil.

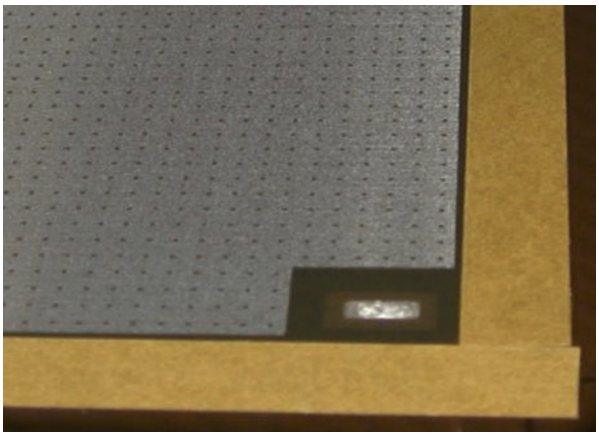

Figure 2.5: Close image of a micromegas detector.

In a micromegas type TPC like the one in Figure 2.3 the drift and amplification regions are delimited by a metal mesh or grid between the anode and cathode. A picture of a micromegas detector is shown in Figure 2.5. By applying an intermediate bias between the anode and cathode voltage to the mesh the relatively weak $\sim 0.5\,\mathrm{kV\,cm^{-1}}$ drift field is divided from a stronger $\sim 10\,\mathrm{kV\,cm^{-1}}$ amplification field. Micromegas mesh is typically supported by an array of pillars above the anode, the pillars are visible in Figure 2.5 as a array of dots in the sensitive region. The anode plane of micromegas devices are often patterned with strips or a pixel array to enable micromegas detectors to be position sensitive.

2.2.2 Negative ion gases

Fundamentally all TPCs rely on the transport of the ionised charge within their sensitive region to an anode. For most gases ionised charge is transported in the form of free electrons, which have a large charge to mass ratio and therefore drift very fast. In negative ion drift gases however, an electro-negative component of the gas attaches to any free electrons at the site of the recoil creating negative ions. The negative ions are then the transported in the drift field rather than electrons, a diagram of the difference between these charge transport processes is shown in Figure 2.6. Drifting negative ions rather than electrons results in a much slower drift speed and, importantly, less diffusion of the charge cloud.

The drift speed, v_{drift} of negative ions at a given gas density is proportional to the electric field strength with a constant of proportionality given by the mobility, μ, of the ion. The mobility is itself inversely proportional to the density of the gas so it is more useful to use the reduced mobility, μ_0, which is the mobility at STP. The relationship between drift speed and electric field in terms of reduced mobility is then given by

$$v_{drift} = \mu_0 E \frac{N_0}{N} = \mu_0 E \frac{P_0 T}{P T_0}, \tag{2.6}$$

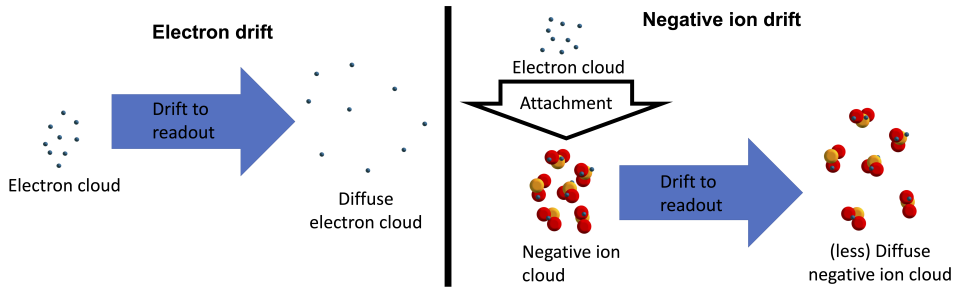

Figure 2.6: Diagram of the transport of electrons and negative ions in a gas TPC.

where N, P, and T are respectively the number density, pressure, and temperature of the gas and the subscript zero denotes the value of that quantity at STP. For the negative ion drift gas SF_6 for example, the reduced mobility of the dominant ion, SF_6^-, is $53\,mm^2/V/s$, which produces drift speeds on the order of $0.1\,mm\,\mu s^{-1}$ at typical detector operating points.

Often free electrons in an electronegative gas will form more than one species of negative ion. These species generally drift at different speeds due mostly to different mass to charge ratios. In a TPC the different drift speeds of the ions in the gas results in correspondingly different arrival times at the anode. The presence of these different carriers can enable the absolute distance of an event from the anode to be determined [80]. This is useful for ensuring that events are fully contained within the active volume of the detector, a process known as fiducialisation. Fiducialisation is useful because recoiling nuclei from radioactive decays in the material of the anode or cathode can contribute significantly to the background of a TPC detector, vetoing events near the edges of the sensitive volume can considerably cut down the background signal.

The main reason for selecting a negative ion drift gas is the fact that the diffusion of the ions is lower than that of electrons drifting over the same distance. Diffusion results in a smearing of the signal and a corresponding degradation in the achievable resolution of the detector which is proportional to the distance drifted by the charge. Diffusion is therefore often the limiting factor in the length of the drift region of a gas TPC.

The diffusion of negative ions at low fields can be close to thermal in many gases [81]. The thermal diffusion constant, D, of can be described by the Nernst-Townsend-Einstein relation [82]:

$$D = \frac{\mu k T}{e}, \tag{2.7}$$

where μ is the mobility at zero field, T is the temperature and e is the charge of the ion. Assuming the diffusion is thermal, the diffusion width, σ_x, in axis x can be determined from the diffusion time, t,

$$\sigma_x^2 = 2Dt. \tag{2.8}$$

The diffusion time is simply the drift length, z, divided by the ion velocity, v_d, and so this equation can be written:

$$\sigma_x^2(z) = 2\frac{\mu k T}{e}\frac{z}{v_d} = \frac{2k_b T z}{eE}, \tag{2.9}$$

where E is the drift field. Significantly the total diffusion is independent of the mobility of the ions as the faster diffusion is canceled out by the faster drift. The diffusion is often expressed in a reduced form normalized relative to the drift length: $\sigma_0 = \frac{\sigma_x}{\sqrt{L}}$.

For a drift length of 1 m and a drift field of 30 kV m^{-1} the thermal diffusion width of ions at room temperature will be about 1.29 mm. Consequently the diffusion exhibited by negative ions enables structure on the order of millimeters to be resolved over drift lengths on the order of a meter. As extending the drift region is the cheapest way to increase the volume of a detector, reducing the diffusion is vital for scaling a detector to large volumes and negative ion drift gases present a useful tool for achieving this [83].

2.2.3 ER discrimination

For physics applications the ability of a detector to identify the type of incident radiation is vital. The characteristic signal used to differentiate different types of radiation is heavily dependent on the application, detector and energy range of the particles. Of particular interest at low energy is differentiating between electron and nuclear recoils, the capability of a detector to do so is referred to as Electron-Recoil (ER) discrimination.

The Compton scattering and photoabsorption of gamma rays produces electron recoils in the gas of a TPC. Electrons are very light and have a high charge to mass ratio, consequently electron tracks tend to exhibit significant bending and ionisation clustering and have a relatively low energy deposition per unit length ($\frac{dE}{dx}$). Neutron and WIMP elastic scattering on the other hand induce the recoils of nuclei in a detector. The heavier, slower nuclear recoils tend to have a much shorter range than equivalently energetic electron recoils and will tend to produce a denser cloud of ionisation with a higher $\frac{dE}{dx}$ as compared to electron recoils. For an example in the differences of the topology of electron and nuclear recoils in gas, Figure 2.7 shows tracks of electrons and nuclear recoils observed in low pressure helium gas in the ORANGE detector exposed to an AmBe neutron source.

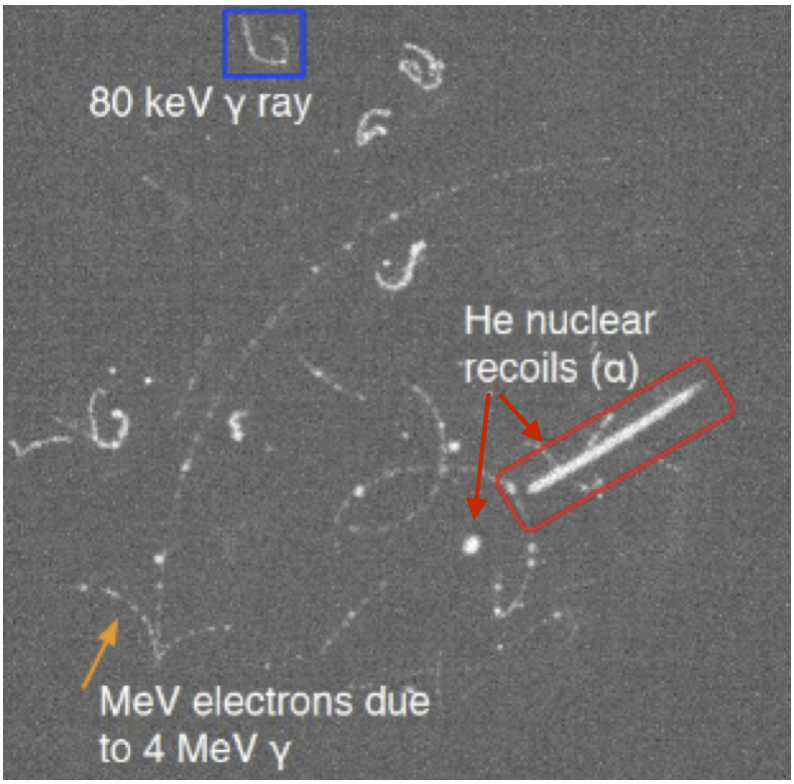

Figure 2.7: Sample image for the ORANGE development detector under exposure to radiation from an AmBe source [84].

The white areas in the Figure corresponds to light collected from the charge amplification of ionisation in the gas. The electron tracks are generally fainter and are more bent in on themselves corresponding to the lower $\frac{dE}{dx}$ and greater scattering angles they exhibit. Nuclear recoils are brighter and straighter, consistent with a higher $\frac{dE}{dx}$ and lower angles .

At lower energy both types of recoil become much shorter and distinguishing between them becomes significantly more difficult. The extension of the recoil track length in low pressure gas can however lower the energy threshold for ER discrimination.

ER discrimination can be quantified by the electron rejection factor; the ratio of electrons at a given energy which are accepted by an electron rejection cut. This can be written as

$$R = \frac{N_{all}}{N_{surv}} \tag{2.10}$$

where R is the electron rejection factor, N_{all} is the total number of observed electrons and N_{surv} is the number of electrons which survive an electron rejection cut. An electron veto cut can have a varying amount of efficiency for accepting nuclear recoils which generally tracks with the efficiency for accepting electrons. Consequently the electron rejection factor is quoted for a given efficiency for nuclear recoils, often 50%.

The electron rejection cuts consist of selecting acceptance regions from the event observables produced by a detector, for example recoil energy, $\frac{dE}{dx}$ or track length. An example of the electron rejection factor based of a single observable for simulated electrons and nuclear recoils in 755:5 Torr He:SF_6 from [83] is shown in Figure 2.8.

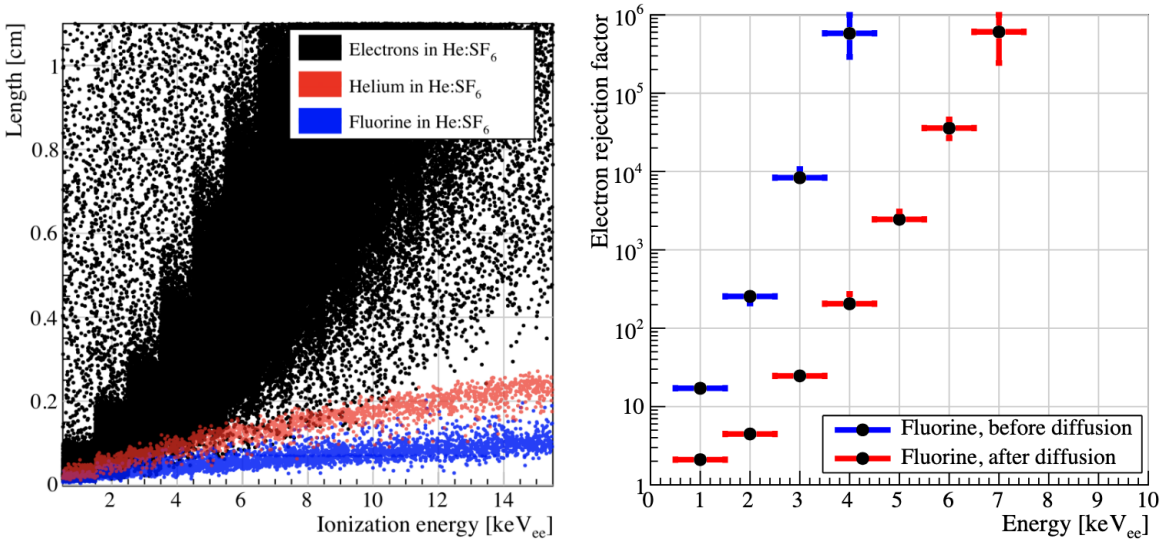

(a) The track length observable versus ionization energy for DEGRAD electron recoils (black) and TRIM fluorine (blue) and helium recoils (red).

(b) Electron rejection factor for a track length cut accepting 50% of fluorine recoils before and after the diffusion from 25 cm of drift.

Figure 2.8: Simulated electron, fluorine and helium recoils in 755:5 Torr He:SF_6 from [83].

Figure 2.8a shows the discriminating observable, track length, for electron, fluorine and helium recoils against deposited ionising energy. The track lengths of the nuclear recoils are generally lower than those of electrons at a given energy so discrimination can be achieved by selecting only tracks shorter than a given value at a given energy. The

electron rejection factor arrived for this observable for a cut on track length cut accepting 50% of fluorine recoils is shown in Figure 2.8b. The rejection factor gets larger (better) for higher energy recoils as the distributions in Figure 2.8a become better separated. The diffusion introduced by 25 cm of drift degrades the discrimination significantly underlining the importance of minimising diffusion effects in a TPC.

More than one observable can contribute to the discrimination and electron rejection cuts can be applied to a number of different observables of a recoil. Cuts on derived parameters are also quite common, including the output from machine learning algorithms like boosted decision trees or neural networks [85, 86]. Techniques like machine learning can significantly boost discrimination and maximise the possible discrimination with the extracted data.

The neutral particles neutrons, neutrinos and WIMPs are not ionising in themselves and their elastic scattering processes can produce nuclear recoils which are close to identical. Distinguishing between individual nuclear recoils produced by these particles is impossible but well controlling and modelling backgrounds can enable positive identification of WIMP or neutrino CEνNS scattering interactions in the detector volume. Directionality can help significantly in this regard due to the different prevailing flux directions of each of the respective particles.

2.3 Directional detection for nuclear recoils

As previously discussed the elastic scattering of a WIMP, neutrino or neutron with an atomic nucleus can produce a detectable recoil. A sketch of the elastic scattering is shown in Figure 2.9.

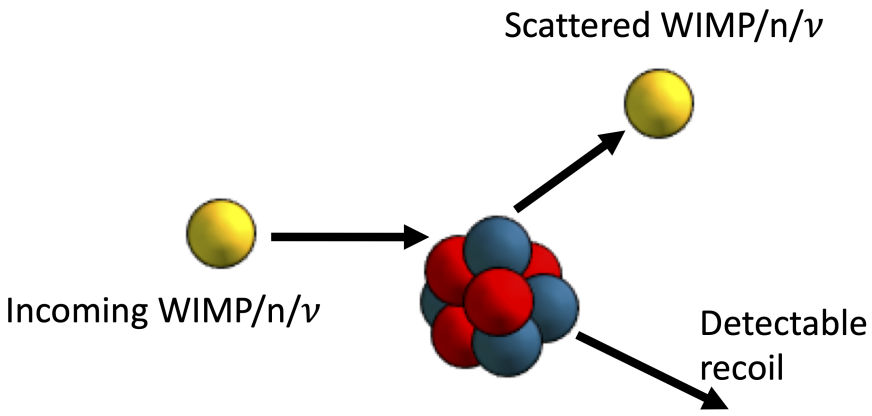

Figure 2.9: Diagram of a nuclear recoil produced by an elastic scattering process.

The nucleus will recoil broadly in the same direction as the incident particle was moving as a consequence of the dynamics of elastic collisions. The information encoded in the motion of a nuclear recoil can therefore give directional information about the incident particle. This information can be incredibly useful, Section 1.1.3 for example discussed how the WIMP wind provides an unambiguous signature for WIMP detection based on the direction of the incoming particles at Earth.

2.3.1 Degrees of directional signal

Directionality does not require the identification of the exact vector of the recoiling particle; there are degrees of directional information that can be extracted with varying levels of statistical significance for the determination of the direction of the prevailing particle flux. Figure 2.10 shows the degrees of directional information which can be determined for a single recoil from least to most powerful pointing ability.

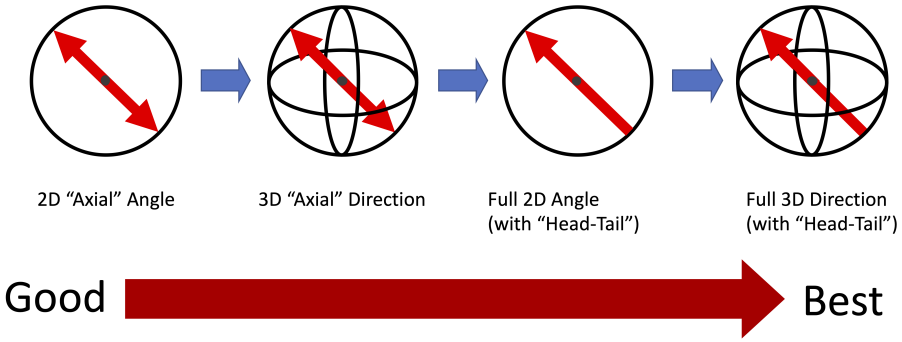

Figure 2.10: The different levels of directional information which can be determined from a single recoil.

The least powerful is the determination of the 2D axial angle, where the only information known is the polar angle between the recoil axis and some detector-defined direction. In this case the direction of the recoil along the recoil axis (the sign of the vector) is not known. A stronger measure of the direction is obtained if the azimuthal angle of the recoil is also determined, giving the orientation of the recoil axis in 3D. More desirable than obtaining a 3D-axial direction though is the determination of the vector direction in the 2D projection. This is because knowledge of only the axial orientation of the recoil presents an irreducible 2-fold degeneracy in the source direction. Determination of the "head" and "tail" of a recoil track, even just in a 2D projection, can determine the direction of a particle wind if there are sufficient statistics and different projection axes (I.E. different detector orientations). Head/tail information is a consequence of the change in rate of slowing and ionisation with ion velocity resulting in a different amount of ionisation at the start and end of a recoil. The strongest possible directional signature is the determination of the full 3D vector direction of a recoil; extracting both the 3D orientation of the track and the correct assignment of head and tail of a recoil track.

The above describes the degrees of directionality which can be extracted for a single recoil; detectors which produce little to no directional information about individual recoils can sometimes determine directional information from the statistics of multiple interactions. Detectors which have an anisotropic response are ones in which the detection efficiency is dependent on the direction of the recoil relative to the detector. An anisotropic detector might only produce signal for recoils close to parallel to a certain axis with recoils in other directions producing no signal. If a significant number of events can be accrued with different orientations of the detector axis then the source direction can be inferred. Anisotropic response is less desirable than extracting directional information from individual recoils when the number of signal events which can be observed is low, such as in the field of dark matter detection.

2.3.2 Directional WIMP detectors

WIMP direct detection experiments seek to observe nuclear recoils in excess of expected backgrounds in detectors deep underground. As described in Section 1.1.3, one of the distinguishing features of the WIMP flux at Earth is the 'WIMP wind', the orientation of the flux in the opposite direction of the motion of the Sun around the galactic centre. The presence of this directional signature provides a method of surpassing the neutrino floor, which is the ultimate irreducible nuclear recoil background for this type of experiment.

The existing directional WIMP detectors are all gas TPCs, these operate by measuring the ionisation created by the recoil of particles in an instrumented gas volume, the low density of gas means that the recoils are long compared to those in solid or liquid detectors which enables directional information to be extracted at lower energies. Section 2.2 describes the operating principals of gas TPCs in more detail. Figure 2.11 shows images of a selection of dark matter gas detectors and development platforms.

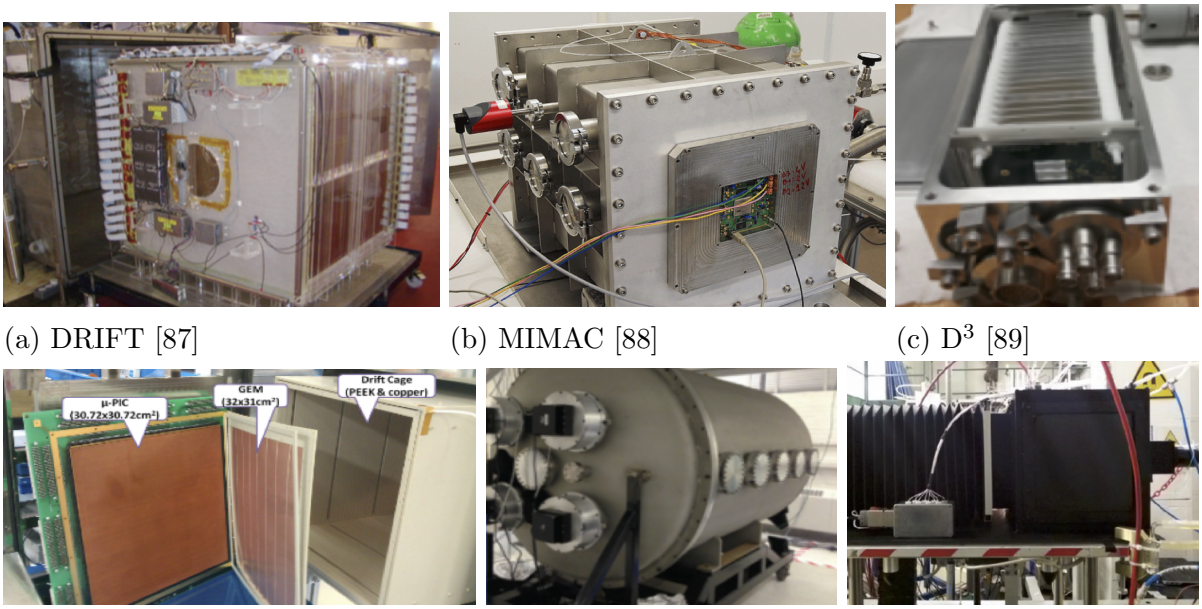

(a) DRIFT [87] (b) MIMAC [88] (c) D^3 [89]

(d) NEWAGE [90] (e) DMTPC [91] (f) LEMON [92]

Figure 2.11: Gas TPC Dark matter detectors and development platforms.

Only the DRIFT [87], NEWAGE [90] and DMTPC [91] detectors have operated underground and set WIMP exclusion limits, MIMAC [88], D^3 [89] and LEMON [92] act as development platforms for technology intended to scale to larger detectors. DRIFT is a cubic meter detector situated at Boulby underground laboratory, it has duel endplates consisting of an array of wires with 2 mm spacing, it has also pioneered the use of negative ion gases and fiducialisation with minority carriers [87]. The NEWAGE detector uses a μ-PIC MPGD which consists of an array of individual pixel amplification elements and has set a 5600 pb limit for 150 GeV WIMPs [90]. The DMTPC detector conversely observes the scintillation light produced by electron amplification in a high field generated between two meshes using an array of CCDs and PMTs. MWPC, MPGD, and CCD based readouts are representative of the different readout approaches for gas based TPCs.

A feature of gas TPCs is that the low density of the target medium means that a future WIMP detector must scale to comparatively large volumes to observe WIMPs at the not yet excluded cross-sections. The CYGNUS detector is a proposed gas detector with total

volume on the order of 1000 m^3 supported by several of the existing small detector groups for this purpose [83].

There are other techniques under development for directional WIMP detection, although none of the technologies have yet been deployed for this purpose. Two technologies which have experimentally demonstrated directionality are anisotropic scintillators and nuclear emulsion.

The scintillator crystal $ZnWO_4$ has an anisotropic response to nuclear recoils [93]. The scintillation induced by recoils along certain axes of the crystal structure is significantly lower than optimally directed recoils. As a result, such a detector should observe a characteristic variation in the count rate due to the rotation of the detector relative to the WIMP wind over the duration of a sidereal day. ADAMO is a proposed detector which would consist of a 200 kg fiducial mass $ZnWO_4$ that could obtain an unambiguous confirmation of a WIMP wind. One of the $ZnWO_4$ crystals used for the development and characterisation of the technology is shown in Figure 2.12. Other proposed anisotropic detectors include using carbon nanotubes, diamond and columnar recombination in liquid noble gasses.

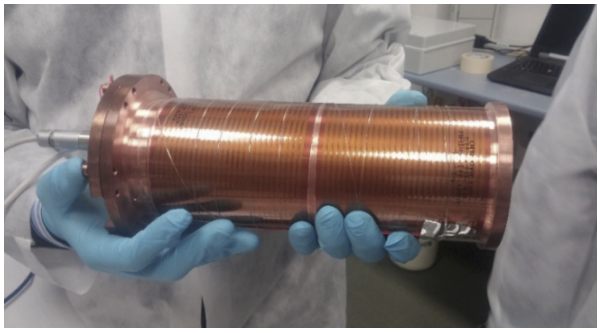

Figure 2.12: Anisotropic $ZnWO_4$ crystal enclosed in a light-guide.

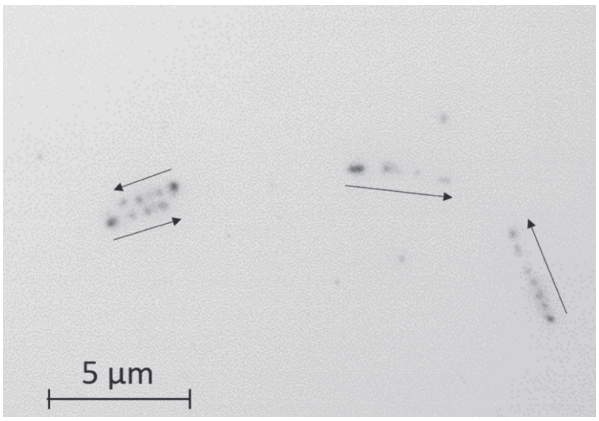

Figure 2.13: Microscope image of nuclear recoil tracks in nuclear emulsion, arrows indicate determined recoil direction (reproduced from [94]).

Nuclear emulsion is a directional recoil detection technology which operates on similar principals to photographic film. Exposure to ionising radiation results in an activation of grains in the (usually silver halide) emulsion following the particle track. The activated grains act as nucleation centres when the emulsion is developed, resulting tracks with detail on the order of microns which can be observed with a microscope; an example of recoil tracks in a developed nuclear emulsion is shown in Figure 2.13. The recoil length of the trackd in the figure is on the order of micrometers, the relatively short tracks however are offset by the extreme resolution obtainable by the technology. Each recoil leaves a track of activated grains behind which are visible in black after development, the start of the recoil is visible as a darker spot due to the larger ionising energy deposited.

The Nuclear Emulsions for WIMP Search – Directional Measurement (NEWSdm) experiment is exploring the use of nuclear emulsions for directional WIMP detection [95]. Such a detector would have a number of unique challenges to overcome including the uniform mass production of the emulsion with sufficiently small grain size, automation of the development and scanning of the emulsion plates and accurate 3D reconstruction of the recoils. Another issue is that the direction of the WIMP flux on Earth varies over the

course of a sidereal day but nuclear emulsion plates might be exposed for several days or weeks and do not give any timing information about the observed recoils. Consequently the NEWSdm experiment proposes mounting the detector on a rotating platform such that the orientation of the detector is constant with respect to galactic coordinates.

2.3.3 Directional neutron detectors

The applications of neutron detection were discussed in Section 1.2.3 and include health physics, reactor instrumentation, nuclear waste disposal and security. Obtaining directional information in addition to rate or energy data can be useful for a number of these applications and a number of technologies have been applied to these problems. A list of some directional detectors designed specifically for neutron detection along with the detector type, level of directionality and application is shown in Table 2.1.

Detector/group	**Method**	**Directionality**	**Application**
DSNDS [96]	Detector Array	Differential rate	Security / Disposal
PNNL [97]	Boron collimator	Anisotropic response	Security
ANL [98]	GaAs layer	Anisotropic response	Security
Sci-Fi [99]	Scintillating Fiber	Anisotropic response	Fusion
JTA [100]	Scintillating Fiber	2d Axial	Fusion
Nagoya [94]	Nuclear emulsion	2d Vector	Neutron imaging
EMCCD [101]	Gas TPC-hybrid	2d Vector	Disposal
D^3 [102]	Gas TPC	3d Vector	Collider

Table 2.1: Selection of directional neutron detectors

The Direction Sensitive Neutron Detection System (DSNDS) was designed for the clean-up of contaminated sites and consists of an array of Boron based detectors embedded in a polyethylene cylinder. Direction is determined using the DSNDS by simply looking at the differential rate in the different detectors [96].

The PNNL and ANL detectors were developed for security applications and have an anisotropic response to neutrons. The PNNL detector uses a honeycomb boron collimator in front of sensitive ^{3}He tubes to eliminate a fraction of thermal neutrons not approaching from directly in front of the detector. The ANL detectors, shown in Figure 2.14, use a layer of GaAs semiconductor to detect neutron induced recoils from a polyethylene sheet with efficient detection relying on the sheet being between the neutron source and GaAs.

Scintillating fiber detectors have been used for direction sensitive detection of fast neutrons from fusion reactors [99, 100]. The Scintillating Fiber (Sci-Fi) detector has an anisotropic energy response whereby recoils traveling along the axis of the fibre can deposit the entirety of their energy in the fiber, while recoils perpendicular can escape the fiber before doing so. The JTA detector, shown in Figure 2.15, also uses scintillating fibers and can track high energy recoils across several fibers providing 2D axial information about those recoils. These detectors have relatively low efficiencies although this is offset by the incredibly high neutron fluxes they observe.

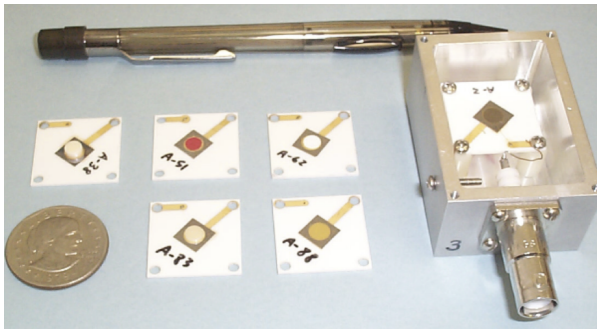

Figure 2.14: ANL GaAs/polyethylene anisotropic neutron detectors [98]

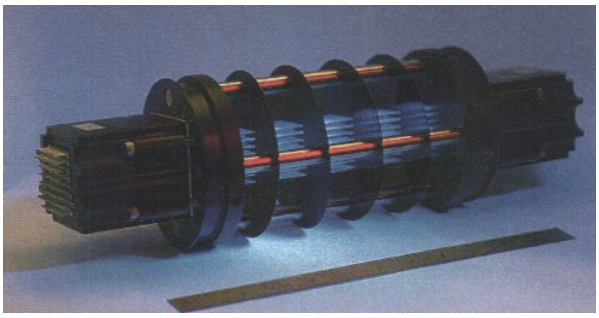

Figure 2.15: The JTA scintillating fiber neutron detector [100]

Nuclear emulsion is also potentially an effective neutron detector which can obtain 2D vector recoil direction. The emulsion developed at Nagoya was designed for minimal sensitivity to gammas for dark matter detection with a spin-off for use in neutron transmission imaging.

The EMCCD man-portable detector is a spin off from the DMTPC dark matter detector, it consists of a gas TPC in a small, portable package. The readout consists of a CCD camera observing the scintillation light generated in the amplification region, providing 2d vector information about the recoils.

The D^3 detector is also a gas TPC with a micro-pixel readout which can extract the 3d vector recoil direction. The detector is part of the neutron instrumentation of the Belle-II detector at the SuperKEK accelerator.

2.3.4 Directional neutrino detectors

While nuclear recoils from the CEνNS neutrino interaction process are very similar to those produced by dark matter and neutrons and might contain directional signatures, no experiment has extracted directional information from CEνNS recoils. The directional detection of CEνNS recoils from the Sun is a secondary mission of the proposed CYGNUS nuclear recoil observatory [83]. Chapter 10 also studies the feasibility of a directional detector for CEνNS recoils from a nuclear reactor.

Neutrino detectors which do observe the neutrino direction instead rely on generally higher energy processes which produce electron or muon recoils. One of the mechanisms by which neutrinos are detected is the emission of Cherenkov radiation from fast electrons or muons created by neutrino interactions. Cherenkov radiation is the detection mechanism used by the Super-Kamiokande [103], Ice-Cube [104] and SNO detectors [105] among others. Cherenkov radiation is emitted when a charge particle is moving through a medium at faster than the speed of light in that medium and consists of photons emitted in a cone in the direction of travel of the particle. The radius, intensity and other shape characteristics of the Cherenkov cone can be used to determine the direction, energy and type of particle generating it. An alternative mechanism which might yield directional information is the inverse beta decay process, the conversion of an electron anti-neutrino and a proton to a neutron and positron. The entirety of the incoming neutrino momentum is invested in the products of the reaction which means that in a detector the offset between the location of the prompt positron annihilation and delayed neutron capture by an absorber like Gadolinium might provide pointing ability with sufficient statistics [106].

2.4 Conclusions

Nuclear recoils produced by particles like WIMPs, neutrons and neutrinos leave a distinct signature of their passage through matter. The objective of a nuclear recoil detector is to detect that signature and extract information like the recoil location, direction, energy, and particle type from it. The recoil direction in particular is challenging to determine but directional information confers a number of advantages in a variety of applications.

Gas TPCs have a number of advantages for high fidelity reconstruction of recoils due to the extension of the recoil length stemming from the comparatively low densities of the gas target. The spatial resolution of gas TPCs can be further enhanced by reducing the electron diffusion though the use of negative ion drift gases. The synthesis of good ER-discrimination, directionality and low energy threshold makes gas TPCs a technology with a large amount of potential for the directional detection of neutrons, WIMPs and neutrinos. This thesis focuses on the development of negative ion gas TPC technology for the directional detection of WIMPs, neutrinos and fast neutrons.

Chapter 3

Operation of a ThGEM detector in SF_6

This chapter seeks to explore the suitability of the ThGEM MGPD as an amplification device for a negative ion drift TPC detector using the gas SF_6 The main goals are to shows that a ThGEM device can obtain sufficient gain in SF_6 to observe the ionisation of keV scale interactions, to quantify the stability of the ThGEM at operating voltages and to determine if ThGEMs are capable of observing directional signal in directed neutron recoils.

The principals of electron amplification devices for gas detectors was discussed in section 2.2.1. There are a number of different designs for devices which generate the necessary amplification fields, one such device is the Thick Gas Electron Multiplier (ThGEM). The ThGEM consists of a lattice of holes in a layer of insulator with metal layers on the front and back, the amplification field is generated in the holes of the device by applying a potential difference between the metal layers [107]. ThGEMs have a number of characteristics which make them an attractive design for a particle detector; they are self supporting, scalable to large areas and can reach high gains in a single stage of amplification in low pressure gas [108, 109].

Section 3.1 describes the operating principals ThGEMs and describes the dimensions of ThGEM device used in the rest of the chapter. The experimental setup including the back-to-back ThGEM setup within the vessel, the bias lines and signal amplification chain are described in Section 3.2. The signal parameters used in the analysis are described in Section 3.3 and Section 3.4 outlines how the electronic gain of the amplification chain is determined. Section 3.5 describes the measurement of the ThGEM gain and energy resolution using the ^{55}Fe x-ray source in CF_4 at different pressures and voltages. A measurement of the ThGEM gain and energy resolution in SF_6 is presented in Section 3.6 along with an exploration of the observed event topology and its effect on the signal parameters. Section 3.7 discusses the response of the ThGEM detector in SF_6 under exposure to a ^{252}Cf neutron source and explores the event populations and directional signals present. The damage sustained over the operating period is explored in Section 3.8 and the overall conclusions are discussed in Section 3.9.

3.1 Description and operating principals of ThGEM detectors

Thick-GEMs are a significantly larger version of the earlier standard GEM detector [110]. Both GEMs and ThGEMs consist of a lattice of holes through a plane consisting of layer of dielectric sandwiched between two layers of conductor. By applying a bias between the top and bottom conductive layers an amplification field is generated in each of the holes. Typical GEMs have a thickness of around 50 µm while ThGEMs are frequently over ten times thicker, on the order of 500 µm [111].

In addition to the thickness, ThGEMs are defined by the diameter of the drilled holes, the separation between the holes (the hole pitch), and the width of the copper 'rim' on the holes. A cross-section of a ThGEM is shown in Figure 3.1a indicating the key design dimensions. Etching an additional rim to the holes into the copper faces of the ThGEM is important for preventing discharges [107] and collected charge on the bare dielectric surface of the rim plays an important role in field shaping [112].

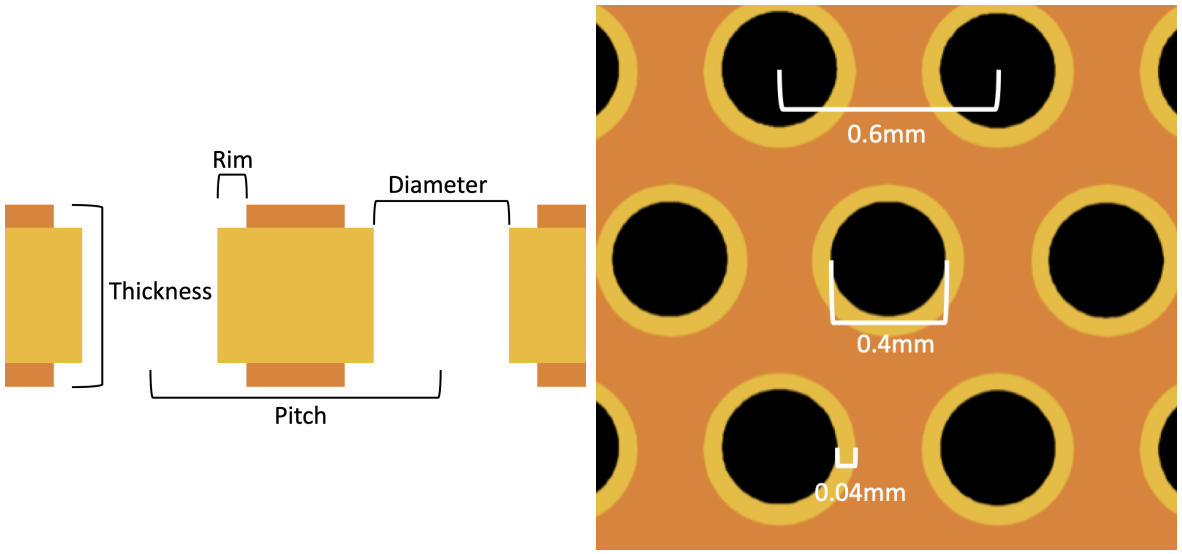

(a) Cross-sectional view of a ThGEM showing the key design dimensions.

(b) Plan view of the holes, showing respectively the hole pitch, diameter and rim size of the ThGEM used in this work.

Figure 3.1: Cross-sectional and plan view diagrams of ThGEM holes, yellow regions indicate dielectric and orange indicate copper.

Two identical ThGEMs produced by CERN are used for this work which are labeled 'A' and 'B' to keep track of them. These ThGEMs have a thickness of 0.4 mm, a hole diameter of 0.4 mm, a hole pitch of 0.6 mm and a rim around each hole of width 0.04 mm. The holes are drilled in a hexagonal lattice to maximise the packing fraction; Figure 3.1b shows a plan of a section of ThGEM with the hole pitch, diameter and rim size indicated. The ThGEMs are circular with the dielectric having radius 6 cm and the copper layers on the front and back having a radius of 5 cm.

3.2 Experimental setup

The ThGEMs are mounted together in a back-to-back configuration (i.e. sharing a common cathode). Figure 3.3 shows the electronic setup of the ThGEMs and cathode.

The front plane (toward cathode) of each of the ThGEMs is grounded while the back plane (away from cathode) is biased and instrumented through a CR-150 evaluation board. The CR-150 board is a PCB which mounts a Cremat charge sensitive preamplifier and contains the supporting circuitry for power and basic noise filtering [113]. Each board implements a low-pass filter to eliminate noise and decouples the preamplifier input from the high voltage through a 0.01 µF capacitor. The circuit diagram of the CR-150 evaluation board is shown in Figure 3.2, also shown is the location of the protection diodes added after the observation of the sparks described in Section 3.5.

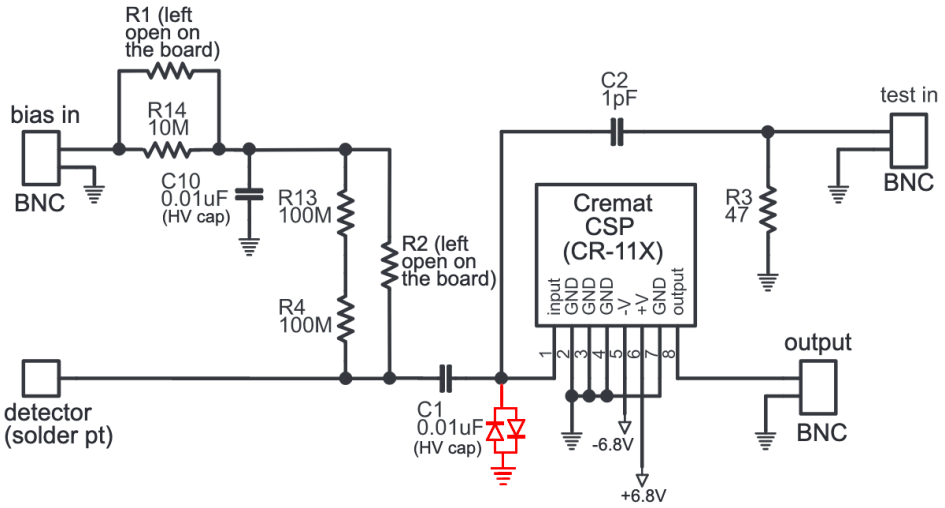

Figure 3.2: Schematic diagram of the CR150 evaluation board [113], the added protection diodes shown in red.

A CR-111 preamplifier mounted on the board is used to amplify the signal induced on the back plane of each ThGEM. CR-111 is a single channel charge sensitive preamplifier with a gain of $0.15\,\mathrm{V\,pC^{-1}}$ [114]. The output of the preamp connects to a CR-200-4 µs shaper, itself on a CR-160 evaluation board [115]. The shaped signal is connected to an appropriate device for analysis; either an oscilloscope, a multi-channel analyser or a digitiser.

The ThGEMs are set up inside a cylindrical vacuum vessel, pictures of the outside and inside of the vessel are shown in Figure 3.4. The preamplifiers are also located inside the vessel to minimise the length of wire traveled by the unamplified signal and therefore reduce noise, the preamplifier box is visible in the bottom of the vessel in the right pane of Figure 3.4. The shapers and other subsequent readout components are located outside the vessel as they are less susceptible to noise. The gas inlet, and the signal and preamp power feedthroughs are located on the arms of the vessel while the high voltage for the cathode and ThGEMs run through the lid of the vessel. The cathode consists of an old ThGEM of the same size as the ThGEMs with the front and back planes connected, the separation between the cathode and ThGEM on each side is 2 cm. In the figure the ThGEMs are mounted horizontally in the vessel (i.e. parallel to the lid) although they are sometimes mounted vertically with the same relative positions and electronic setup.

An ^{55}Fe and an ^{241}Am radioactive source are attached to magnets and enclosed inside

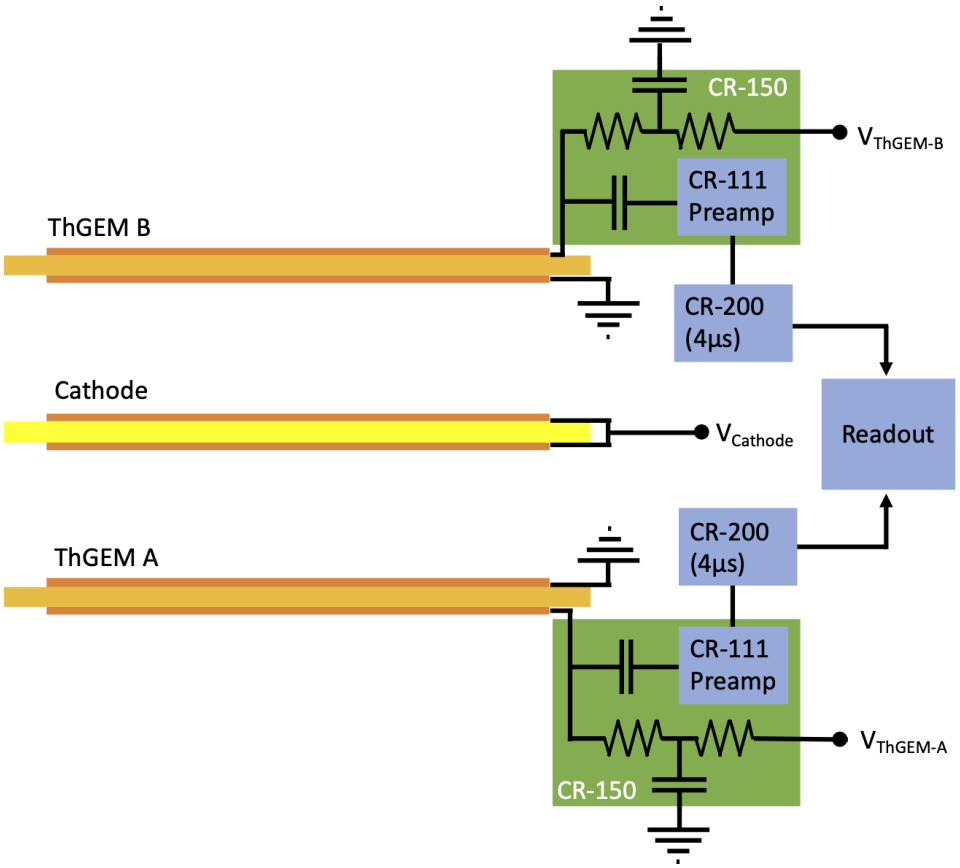

Figure 3.3: Circuit diagram of the ThGEM setup in the vacuum vessel.

the vessel such that they can be manipulated by magnets situated outside the vessel. This enables the sources to be moved into position to expose the drift regions of the ThGEMs to X-rays or alpha particles and moved away to cease exposure.

3.3 Waveform analysis parameters

For some parts of the experiments the ThGEM signal was digitised using a National Instruments NI 5751 digitiser. The digitised signal consisted of the shaper output signal voltage binned at increments of 1 µs. The digitiser was self-triggered by a simple voltage threshold with a digitisation window of 2000 µs to 4000 µs where the trigger was generally located at bin 1000 or 2000 of the waveform.

To analyse the signal in bulk an algorithm was used to extract a number of parameters from the stored digitised signal waveforms. The analysis code was written in C++/ROOT and the extracted parameters for each event were stored in a tree in a root file for subsequent analysis. Figure 3.5 shows a sample waveform with some of the extracted parameters labeled and a short description of the parameters extracted is given below with the units of each parameter indicated in square brackets:

pedestal [V]: The baseline voltage of the signal line. Equal to the average voltage of the first 700 time bins, the `pedestal` value is subtracted from all of the digitised signal bins prior to the calculation of the rest of the parameters.

v_max [V]: The maximum voltage reached by the signal in the digitisation window.

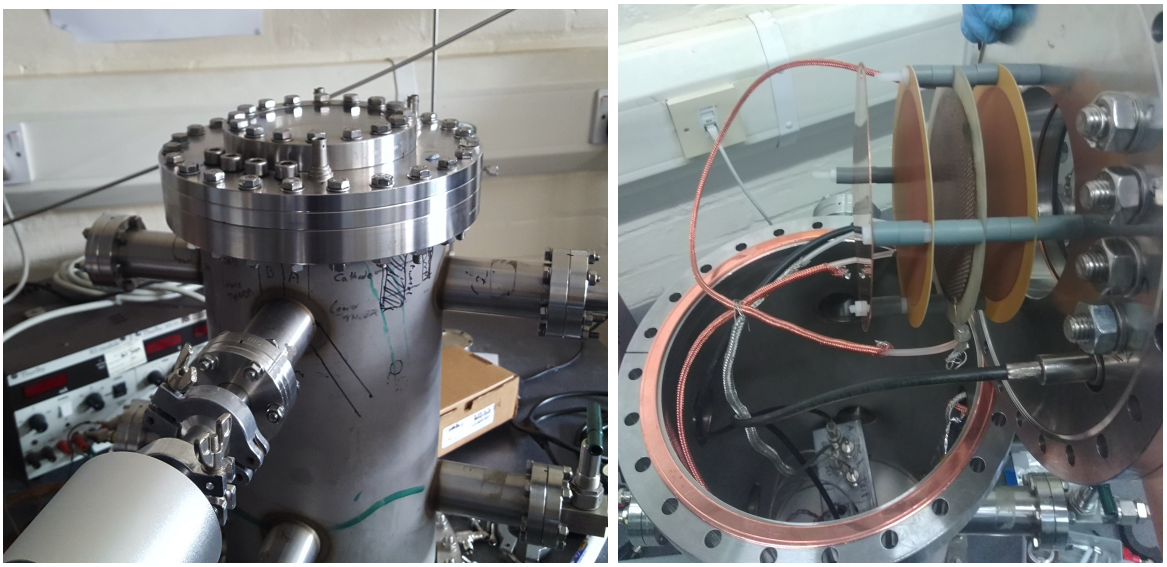

Figure 3.4: Picture of the ThGEM rig closed (left) and open displaying the ThGEMs, cathode and preamplifier box (right).

v_min [V]: The minimum voltage reached by the signal in the digitisation window.

t_peak [µs]: The timebin which contains the highest voltage value in the digitisation window.

threshold [V]: The threshold in volts for the integration and width determination, this is either a constant value above the baseline fluctuation or a fraction of `v_max`. This value is distinct from the trigger threshold of the digitiser which was set separately.

t_width [µs]: The width of the peak measured by counting the number of timebins contiguous with bin `t_peak` which have a voltage in excess of that given by the `threshold` parameter.

q_tot [V·µs]: Integral of the voltage of the entire signal waveform.

q_peak [V·µs]: Integral of the voltage of all the timebins contiguous with bin `t_peak` which have a voltage higher than `threshold`.

roi_1 [V·µs]: Integral of the voltage of the first half of the timebins in the identified peak.

roi_2 [V·µs]: Integral of the voltage of the second half of the timebins in the identified peak.

n_peaks [peaks]: Number of distinct identifiable peaks above the `threshold` voltage. `n_peaks` is calculated by counting the number of voltage maxima in the signal which have a voltage larger than the `threshold` parameter. The peaks are counted even if they are part of the same region of bins over threshold.

After the parameters were extracted and stored, analysis was performed mostly in the ROOT interpreter, enabling cuts for noise and background rejection and other tasks. Other parameters were examined, including measurements of the rise time and secondary peak heights but these were not found to contribute to the analysis.

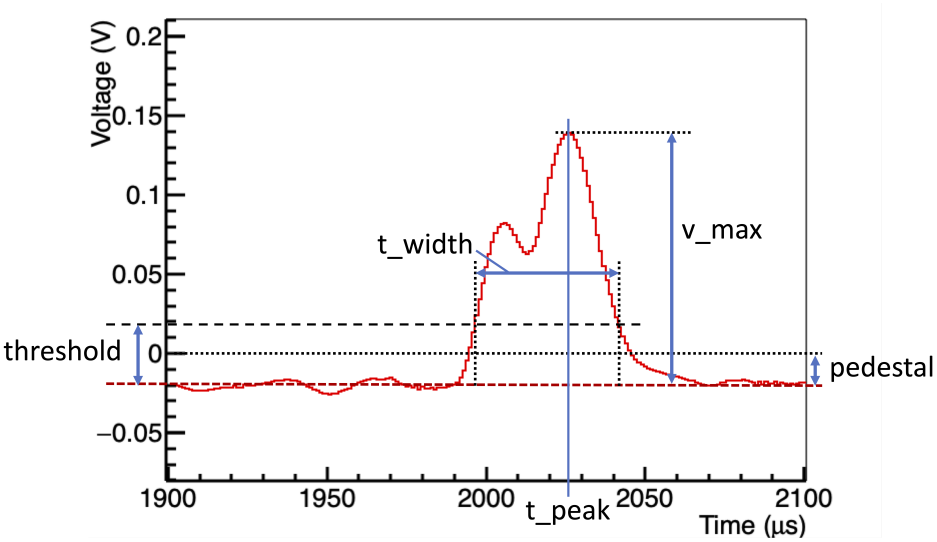

Figure 3.5: An example event waveform some of the important analysis values which are extracted in the digital analysis.

3.4 Electronic calibration

A determination of the electronic gain of the amplification chain is required to determine the charge collected by the ThGEM and therefore the gas gain of the device. The electronic gain is determined by injecting a test pulse of a known voltage onto a 1 pF capacitor connected to the input of the amplification chain. The charge at the preamplifier input can then be trivially determined from $Q = VC$ and the electronic gain of the amplification chain is simply the ratio between the injected charge and output signal. Figure 3.6 shows an example trace of the injected pulse and the resultant amplification chain output signal.

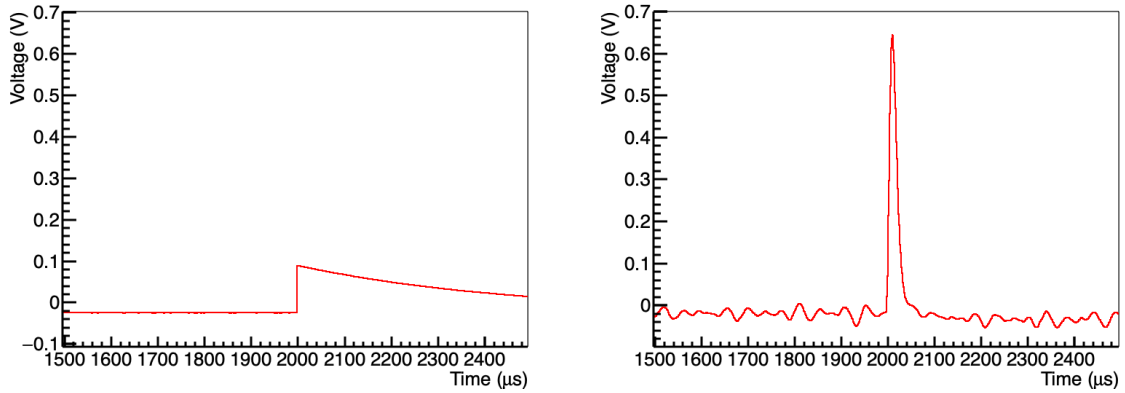

(a) Pulsar output

(b) Amplification chain output

Figure 3.6: The pulsar and amplification chain output used for the calibration of the electronics chain.

The injected pulse consists of a near instantaneous rise in voltage followed by a long exponential decay, while the resultant signal is a short gaussian pulse, consistent with the 4 µs shaping applied after the preamplifier.

Two measurements of the output signal magnitude are used in this work: peak signal voltage and the integrated signal voltage, corresponding to the parameters `v_max` and

`q_peak` discussed earlier. The peak signal voltage is used for runs where charge collection is significantly faster than the 4 µs shaping time of the amplification chain. When the charge collection is slower than this, a significant amount of signal is not included in the shaped peak resulting in an underestimate of the event energy from peak height. This effect is known as ballistic deficit and in order to compensate in these cases an integration of the signal voltage is performed instead.

Figure 3.7 shows the plots of test pulse against the maximum and integrated signal voltage for the calibration performed on 09/08/2018. Both the maximum voltage and integrated voltage are linear with test pulse magnitude as would be expected if the gain were linear. The electronic gain determined from peak voltage in this case is 6.02 V pC^{-1} for amplification chain A and 5.84 V pC^{-1} for amplification chain B. Using integrated peak voltage, the electronic gain is 97.5 V.µs/pC for amplification chain A and 114.6 V.µs/pC for amplification chain B.

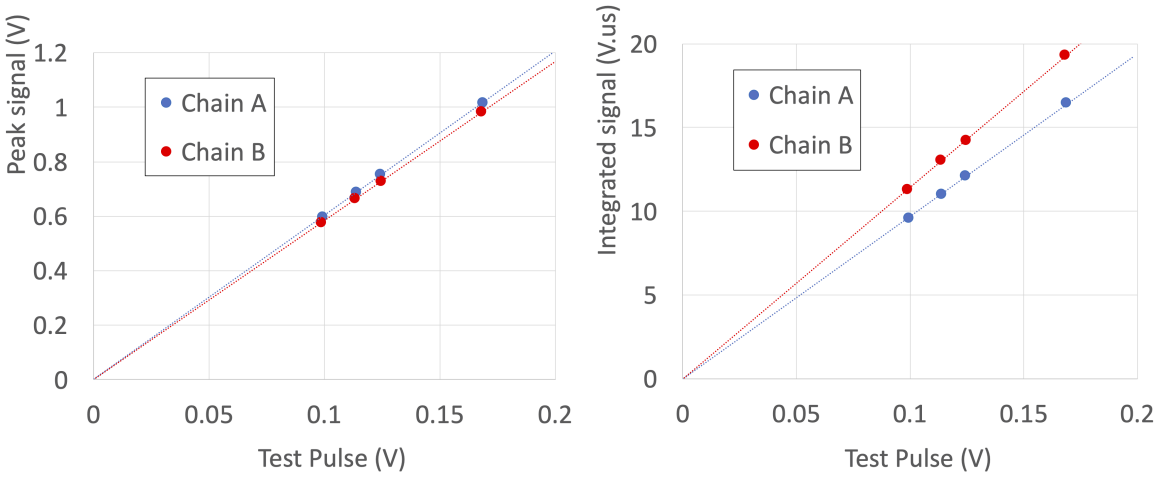

(a) Pulsar input against maximum signal voltage.

(b) Pulsar input against integrated signal voltage

Figure 3.7: Calibration plots taken on 09/08/2018 for amplification chains A and B for a test pulse injected through a 1 pF capacitor.

Over the course of the operation of the ThGEMs several different gain settings are used to optimise factors like noise and signal range. This was achieved by the adjustment of the in-built linear amplifier on the CR-160 evaluation board which has a manually adjustable gain from 0 to 100. Consequently, whenever the output chain was adjusted a new calibration was performed to apply to all subsequent experimental data.

3.5 Determination of ThGEM gain with ^{55}Fe in CF_4

CF_4 is an electron drift gas which is commonly used in particle detectors. As the gas gain achievable in CF_4 is fairly high, it is considered a good test gas to ensure the ThGEMs work as expected before progressing to the more challenging SF_6. As electrons are drifted in CF_4 rather than negative ions, the charge is collected at the anode over a period of tens of nano-seconds. This is significantly faster than the 4 µs shaping time of the shaper, meaning that the pulse height can reliably be used as a measurement of the collected charge. This section reports on the determination of the gain and energy resolution of the ThGEM detectors in low pressure CF_4.

3.5.1 ^{55}Fe

The x-ray source ^{55}Fe is used extensively for the calibration of the detector technologies focusing on keV scale recoils. ^{55}Fe decays via electron capture into ^{55}Mn with a half life of about 2.7 years [116]. The vacancy left in the K shell by the captured electron is filled by an electron from a higher shell with the energy difference accounted for by the release of Auger electrons or x-rays. The main emitted x-rays are the Kα_1 with energy 5.898 keV which is emitted in 16.2 % of decays, Kα_2 with energy 5.888 keV and probability 8.2 % and Kβ with energy 6.490 keV and probability 2.9 % [117]. The remaining decays primarily emit Auger electrons with energy 5.19 keV.

For detector calibrations the electrons generated by interaction of the Kα x-rays in the gas are used. Because of the proximity of the two x-rays in energy and the achievable energy resolution, the two can be treated as a single peak at 5.9 keV.

3.5.2 Gain determination method

The gas gain of a TPC is the ratio between the charge that is created by radiation interactions in the gas and the charge that arrives at the anode. To determine the gas gain, a known quantity of charge must be ionised in the gas and then the charge arriving after amplification must be measured.

The amount of ionising energy required to liberate an electron in a gas is given by it's w-value, which for CF_4 is 34 eV [118]. For the 5.9 keV ^{55}Fe x-rays this means that the ionised charge in the gas will average $Q_{fe55} = 173$ electron-ion pairs. This provides a fairly consistent initial quantity of charge in the gas for the gain determination.

To determine the collected charge, the electronics chain is calibrated with the method presented in Section 3.4. An Ortec 926 ADCAM MCB is connected to the shaper output and used for data acquisition, this provides a histogram of the pulse heights of the ^{55}Fe events. The pre-run calibration determined the charge present at preamp input, Q_{coll}, is linear with MCA channel with the relationship given by the equation

$$\text{MCA channel} = \frac{Q_{\text{coll}}}{1.16\,\text{fC}} - 46.8. \tag{3.1}$$

With the determination of both the collected charge and the ionised charge for ^{55}Fe x-rays the gas gain can be determined from the ratio Q_{coll}/Q_{fe55}.

3.5.3 Gain determination in CF_4

The vessel is pumped to vacuum and filled with low pressure CF_4, the cathode is ramped to produce a drift field of 300 V cm^{-1} to 400 V cm^{-1} and then the anode voltage is increased until ^{55}Fe events are clearly observable. Figure 3.8 shows the MCA spectrum generated in 10 minutes for ThGEM-A in 60.7 Torr CF_4 with $V_{cath} = -650$ V and $V_{ThGEM-A} = 650$ V when no source was present (blue) and when the drift region was exposed to ^{55}Fe (red).

The background (no source) run shows an exponential drop-off in events with energy while the ^{55}Fe has the same distribution with an additional well defined peak centred around MCA channel ∼100. The noise events in the background run originate mostly from background radiation originating from the surrounding environment and gammas from the ^{241}Am source contained in the same vessel. This is consistent with expectation, with the peak in the ^{55}Fe spectrum corresponding to the 5.9 keV x-ray peak of ^{55}Fe.

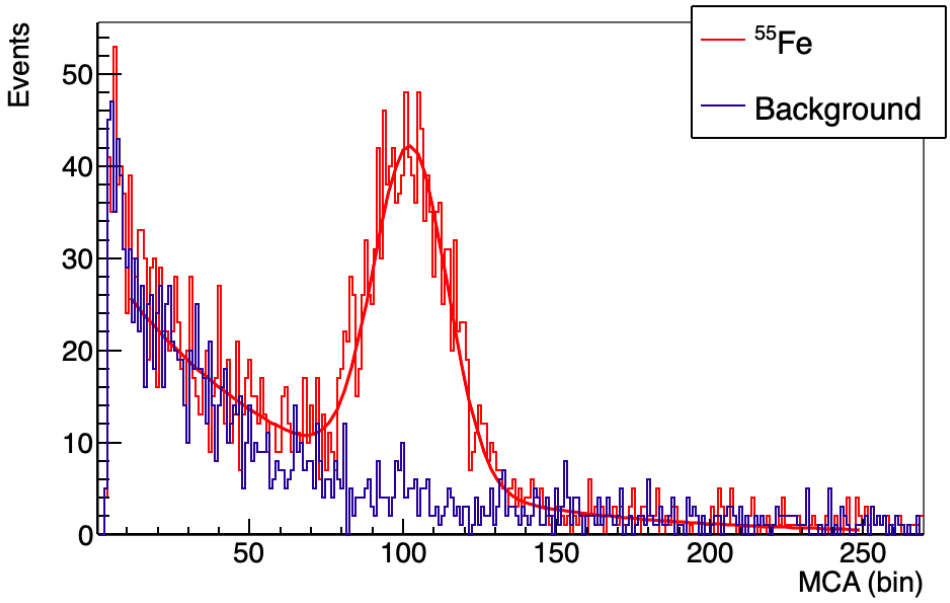

Figure 3.8: MCA spectra 10 minutes of background (blue) and exposure to ^{55}Fe x-rays (red) of ThGEM-A in 60.7 Torr CF_4 with the cathode at −650 V and the anode at 650 V.

The smooth red line in the graph indicates a fit to the ^{55}Fe spectrum. The fit consists of an exponential added to a gaussian to fit the background and 5.9 keV peak respectively, the fit equation is given by

$$y = e^{c_0 + c_1 x} + A e^{-\frac{1}{2}\left(\frac{x-x_0}{\sigma}\right)^2}, \tag{3.2}$$

where c_0 and c_1 are the constants for the exponential fit and A, x_0 and σ are respectively the amplitude, average and standard deviation of the gaussian. The fitted gaussian peak is centred at $x_0 = 102.4 \pm 0.5$ and has a width of $\sigma = 12.1 \pm 0.4$ MCA channels. An important measurement is the energy resolution of the detector which can be expressed as the FWHM of this gaussian divided by its average [51]. For the spectrum in Figure 3.8, the energy resolution is 0.28. This is fairly consistent with the energy resolution observed on similar ThGEMs, for example [119] which found energy resolutions between 0.22 and 0.36 for ThGEMs in Ar:CO_2. Equation 3.1 is used to determine the average Q_{coll} from the gaussian average and subsequently determine the gas gain, which is found to be 6240 ± 100 at this pressure and anode voltage.

The pressure and anode voltage is varied and equation 3.2 is fitted to the ^{55}Fe spectrum for each setting for which the 5.9 keV peak could be resolved. Figure 3.9 shows the resultantly determined gas gains in 40, 60 and 80 Torr CF_4 against ThGEM bias determined for ThGEM-A with a drift field of 325 V cm^{-1}. The gain appears to be exponential with anode voltage and higher voltages are required to obtain a given gain at larger gas pressures. The lowest observable gain is around 2700, below which the peak is not accurately distinguishable from the noise. The highest gas gain obtained is in 40 Torr CF_4 and is 27700 ± 200.

The upper limit of the gain is limited by the onset of sparking, extremely energetic events corresponding to electrical discharges between the front and back plane of the ThGEM. An example of the digitised signal from a sparking event is shown in Figure 3.10. The initial sharp rise in the voltage saturates the ±1 V range of the digitiser and is followed by a baseline undershoot which also exceeds the digitiser range. The signal then oscillates

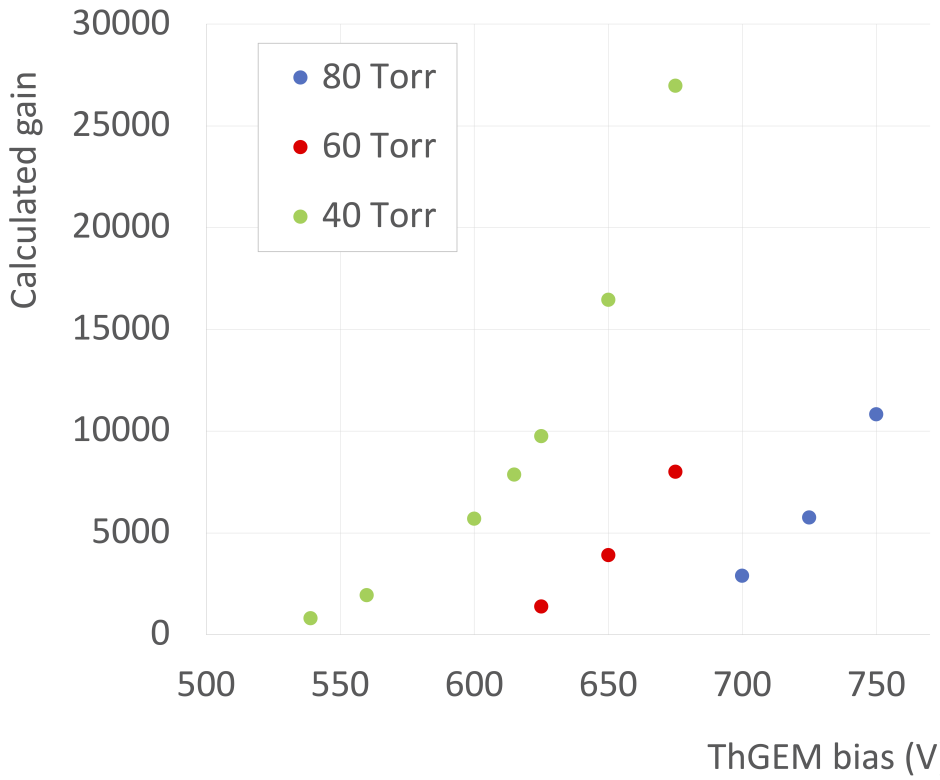

Figure 3.9: Gain curves for ThGEM-A in CF_4 at different pressures with a constant drift field of 325 V cm^{-1}.

between positive and negative saturation before the baseline starts to return to zero, although there is distinct structure visible in the baseline restoration.

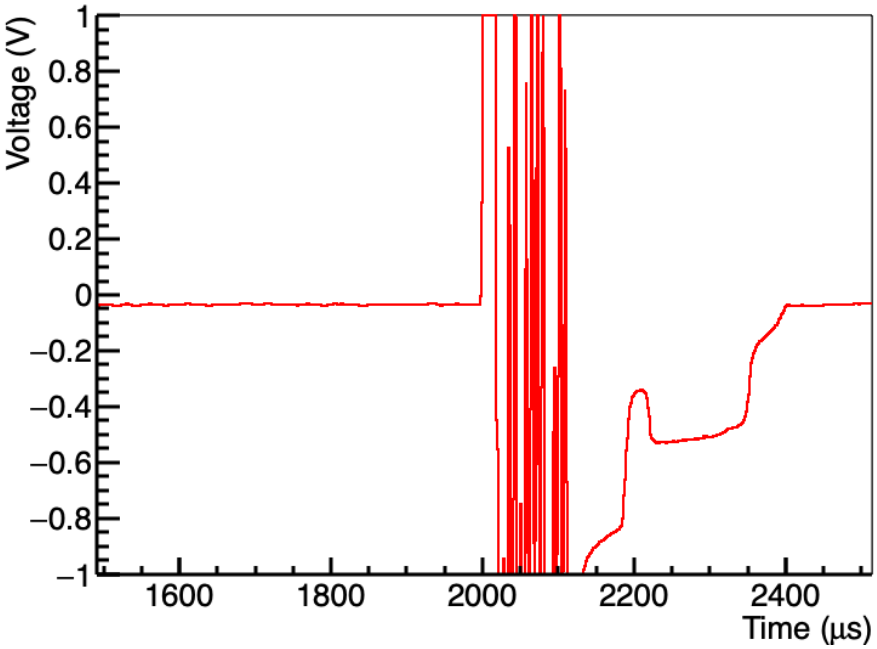

Figure 3.10: Example of a 'sparking' event on a ThGEM

Most of the visible structure is due to the non-linear reaction of the electronics to

the extreme energy of a sparking event; grounding through protection diodes, baseline restoration circuits and ringing effects from RC components of the circuit likely all contribute to the resultant waveform. The signal topology is however useful for distinguishing sparking events from simple high-energy interactions in the detector volume that might induce a saturation of the signal range. Sparks are not good for the detector, they are suspected to contribute to a reduction of the maximum operating voltage of the ThGEM as surface damage caused by a sparking event to the dielectric can start to form a path for subsequent sparks to follow. They can also damage the electronics, particularly the preamplifiers which are directly coupled through a capacitor to the back of the ThGEM. Several preamplifiers were destroyed by sparking events necessitating the addition of protection diodes on the preamp side of the decoupling capacitor to ground high voltages. Section 3.8 will discuss some of the damage and defects observed on the ThGEMs after prolonged use which are related to events like the one shown.

3.5.4 Discussion

The operation in CF_4 provides a good baseline for the gain and energy resolution that might be achieved in SF_6. The fast collection time of the charge made the analysis fairly simple and the observation of the 5.9 keV peak confirms the ThGEMs are producing significant gas gain in the thousands. The gain results obtained here are consistent with the gain determined for a ThGEM of the same dimensions in low pressure CF_4 reported in [120].

It was found that the ThGEMs appear to be able to operate over a wider range of operating voltages at lower pressures. The lower limit of the operating voltage was imposed by the lowest gas gain required to observe the ^{55}Fe peak and the upper limit by the onset of high energy sparking events. Increasing the range of possible operating voltages would require lowering the threshold at which the ^{55}Fe peak can be distinguished from the noise or increasing the voltage that can be achieved before the onset of sparking.

3.6 Determination of ThGEM gain with ^{55}Fe in SF_6

The reason for using SF_6 is to utilise its properties as a negative ion drift gas. The SF_6 molecules have a very high electron affinity and as a consequence rapidly attach to ionised electrons in the gas. The resultant negative ions are much heavier than electrons and therefore diffuse and drift far more slowly. The drift speed, v_{drift} of the negative ions in an electric field, E, can be described by the equation

$$v_{drift} = \mu_0 E \frac{P_0 T}{P T_0} \tag{3.3}$$

where P and T are the pressure and temperature of the gas and P_0 and T_0 are the pressure and temperature at STP. μ_0 is the reduced mobility of the ion in the gas mixture, for SF_6^- in SF_6 the reduced mobility is about $53\,\mathrm{mm^2/V/s}$ [121]. Consequently the drift velocity of most of the signal in 20 Torr SF_6 at room temperature in an electric field of $450\,\mathrm{V\,cm^{-1}}$ is expected to be around $96.6\,\mathrm{m\,s^{-1}}$ or approximately $\sim 0.1\,\mathrm{mm\,\mu s^{-1}}$. This means a significant amount of the structure of a millimeter scale recoil will be visible after the 4 µs shaping time of the shaper.

At a sufficiently high electric field the ionised electrons are detached from the ions in the gas, this is required for electron amplification to occur in the gas. The requirement

that electrons are detached from the very electronegative SF_6 molecules means that the gain obtained at a given electric field in SF_6 is significantly lower than is encountered in the more common electron drift gasses.

3.6.1 Determined gas gain and limits

One of the issues encountered while operating in SF_6 is that the ThGEM bias voltages required to observe ^{55}Fe were significantly higher than those required in CF_4. In 30 and 40 Torr SF_6 it was not possible to reach a voltage where the 5.9 keV peak could be isolated without the onset of significant sparking. At 20 Torr though it was found that the ^{55}Fe peak could be observed without significant sparking at a ThGEM bias of 720 V. Figure 3.11 shows the integrated signal voltage, `q_peak`, of events on ThGEM-B in 20.1 Torr SF_6 with ΔV_{ThGEM}=720 V and a drift field of 460 V cm^{-1} for background and ^{55}Fe exposure of the drift region.

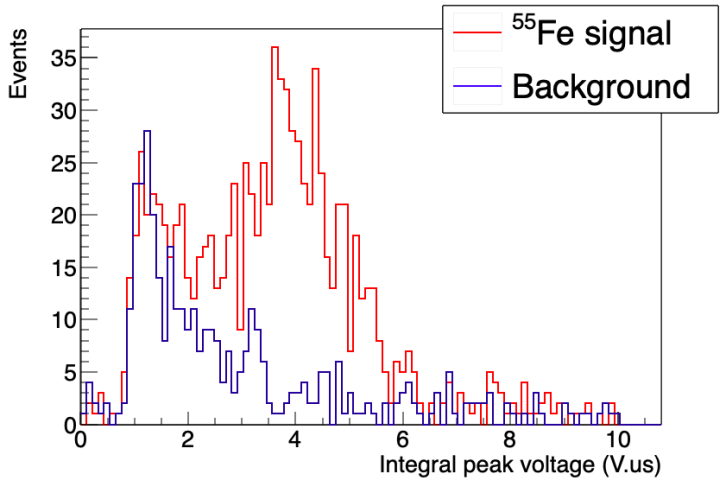

Figure 3.11: The background and ^{55}Fe spectrum for ThGEM-A in 20.1 Torr SF_6 with ΔV_{ThGEM}=720 V and a drift field of 460 V cm^{-1}.

As observed in CF_4, the background rate increases exponentially with decreasing energy while the ^{55}Fe peak forms an approximate gaussian on top of the background. The energy resolution is 0.58 in this case, considerably worse than the 0.28 achieved with the same device in CF_4. As a consequence of the slower drift speed of negative ions it was found that no peak is resolvable if `v_max` is plotted instead.

To accurately compare the ThGEMs they are operated with the same gas fill and bias voltages, the integral signal for each event is measured and converted to collected charge based on the pulsar calibration for the specific electronic chain. Figure 3.12 shows the ^{55}Fe and background event energy spectrum in units of collected charge for ThGEM-A and ThGEM-B with curves fitted to the background and signal, the ThGEM bias is ΔV_{ThGEM}=720 V, the drift field is 450 V cm^{-1}, and the SF_6 pressure is 20.2 Torr. The gain for ThGEM-A is determined to be 910 ± 60 and the energy resolution is 0.42 ± 0.04, for ThGEM-B the gain and energy resolution are 1550 ± 80 and 0.53 ± 0.04 respectively.

Despite the identical manufacturing specifications and bias voltages, there is a significant difference in the charge collected from the 5.9 keV peak for ThGEM-A and ThGEM-B. It is also noted that although the gain is lower, the energy resolution appears to be better for ThGEM-A and it also appears to suffer from less frequent sparking. The fact

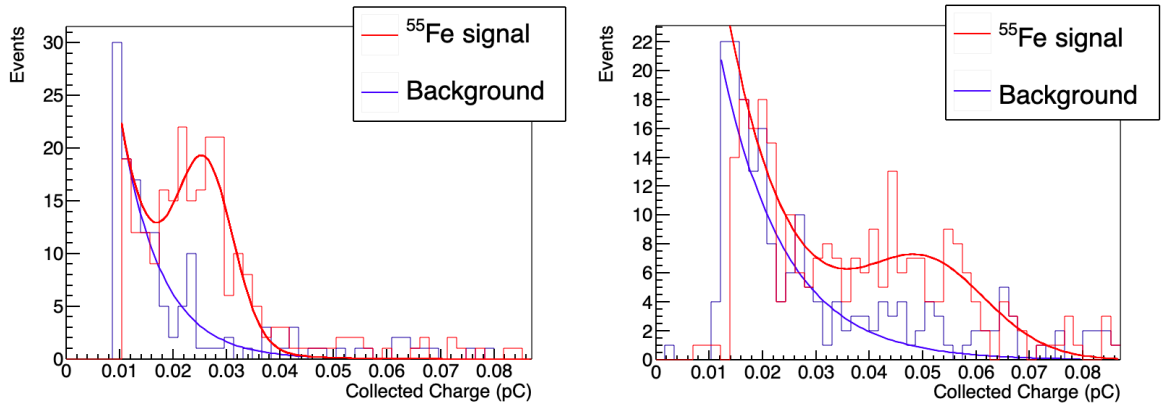

(a) ThGEM-A (b) ThGEM-B

Figure 3.12: Examples of the ^{55}Fe spectrum with fitted functions on the ThGEMs A and B with ΔV_{ThGEM}=720 V and a drift field of 450 V cm^{-1}.

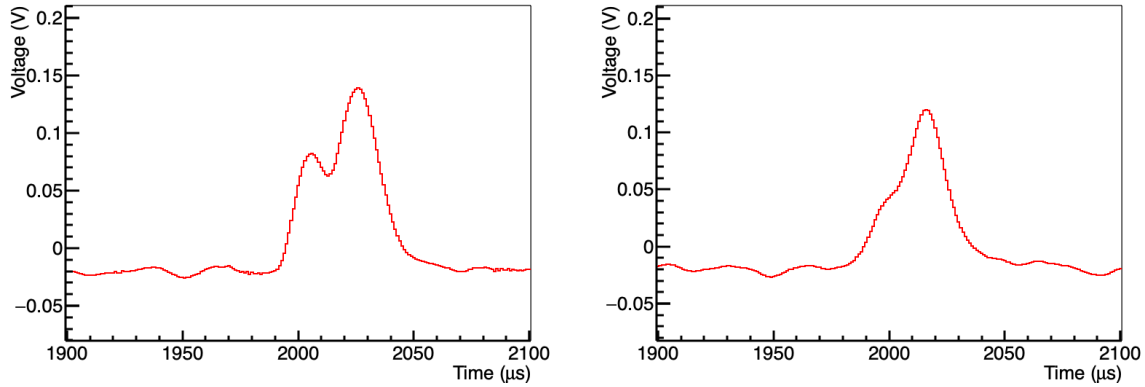

(a) (b)

Figure 3.13: Sample events for ^{55}Fe exposure of the ThGEM-A detector in 20.1 Torr SF_6 with ΔV_{ThGEM}=720 V and a drift field of 460 V cm^{-1}.

that the ^{55}Fe peak can be seen shows that the ThGEM detector is sufficient to observe energy depositions down to at least 5.9 keV. The onset of sparking however demonstrates that in SF_6 this is close to the limit of the reliable gain of these ThGEMs.

3.6.2 ^{55}Fe event topology

The shaped signal for the SF_6 runs does not form a simple gaussian due to the long collection time but instead displays structure in the waveforms with the shape varying from event to event. For ^{55}Fe events, the presence of a number of merged 'peaks' in the shaper output is typical of the observed signal with as many as three distinguishable peaks. Figure 3.13 shows the shaper output for some sample events for an ^{55}Fe exposure of the ThGEM-A detector in 20.1 Torr SF_6 with a ThGEM bias of V_{ThGEM}=720 V and a drift field of 460 V cm^{-1}.

The event in Figure 3.13a consists of two peaks with different heights and a separation between their centres of around 20 µs, the widths of the the peaks is sufficient that they merge into one another. The event rate is not high enough that this could be explained by

multiple coincident recoils, suggesting that the observed structure is from a single recoil.

This effect can be explored in more detail by looking at the extracted parameters for an entire run. The parameter `t_width` is a measurement of the number of contiguous time bins over the threshold value. Figure 3.14 shows the distribution of the `t_width` parameter for each ThGEM for a threshold equal to `v_max/4`. For each ThGEM the distribution shows an exponential tail-off in the rate with increasing `t_width` above a minimum value, below which there are few to no events. It is found that the value of the `t_width` parameter extracted when the same analysis is performed on test pulses well coincides with this minimum value; for amplification chain A the `t_width` for test pulses was 23 µs and for amplification chain B it was 28 µs.

Given the literature mobility of negative ions at this pressure and the drift field, every 10 µs of ion drift is equivalent to $\sim$ 1 mm of travel. This suggests that the collected charge from ^{55}Fe interactions have an extent of up to 7 mm in space.

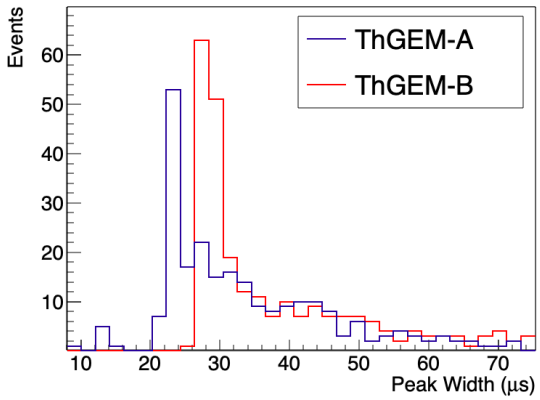

Figure 3.14: The distribution of the `t_width` parameter for the ThGEMs in 20.1 Torr SF_6 with ΔV_{ThGEM}=720 V and a drift field of 450 V cm^{-1}.

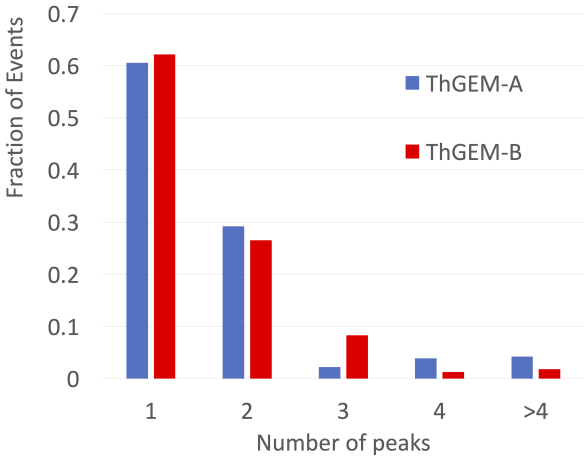

Figure 3.15: The distribution of the `n_peaks` parameter for the ThGEMs in 20.1 Torr SF_6 with ΔV_{ThGEM}=720 V and a drift field of 450 V cm^{-1}.

The parameter `n_peaks` measures the number of signal maxima above the analysis threshold voltage in an event. The distribution of the `n_peaks` parameter for each ThGEM is shown in Figure 3.15. Most events on both ThGEMs have only one identifiable maxima, although almost 40% of events have 2 or more peaks with the fraction of events dropping off with increasing peaks. There are slight differences between the fractions of peaks for each ThGEM, although this might be attributed to slight differences between the amplification chains. Within the subset of events with one identified peak, many events resemble the event in Figure 3.13b where there is only one turning point but an additional shoulder like feature on one side suggests there may be separable clusters of arriving charge.

The presence of multiple peaks in the signal points to the phenomenon of 'charge clustering' where the induced ionisation is produced in discrete clusters. This feature of electron recoils might be a useful signature for the discrimination between electron and nuclear recoils.

3.6.3 Discussion

The operation of ThGEMs in SF_6 was found to be challenging, with a very narrow window of voltages capable of producing sufficient gain for the observation of the 5.9 keV peak

while not resulting in sparking. The SF_6 pressure 20 Torr with ΔV_{ThGEM}=720 V and a drift field of 450 V cm^{-1} was the only operating point which produced a resolved 5.9 keV peak on both ThGEMs. The obtained gain for ThGEM-A was 910 ± 60 and the energy resolution was 0.42 ± 0.04, for ThGEM-B the gain and energy resolution were 1550 ± 80 and 0.53 ± 0.04 respectively.

The difference in the gas gains between the ThGEMs was unexpectedly large considering the identical bias and manufacturing specifications. It is known that the rims around the holes, and more specifically charge embedding in the dielectric of these rims can result in a change in the gain of a given device by a factor of up to 400% [112]. It is speculated that this charge-up effect might be responsible for the gain difference between the devices. It is also possible that the usage history contributes to the maximum attainable voltages and the gains of the device. A study of the stability of the ThGEM gain over a long duration might help to resolve the contribution of the charge-up and damage to these differences.

The slow drift speed of the negative ions meant that a significant amount of (one dimensional) structure could be discerned from the produced recoils. This included the identification of what is thought to be the distinct charge clusters produced by recoiling electrons and a measurement of the projected track length in the form of the width of the signal peak. The presence of clustering might be useful for discriminating between electrons and nuclear recoils where less clustering is expected. Chapters 4 and 5 will explore simulations of the electron recoils produced by ^{55}Fe in low pressure SF_6 and how consistent the observations reported here are with expectation.

3.7 Directed neutron runs in SF_6

As discussed in Chapter 1, the interactions of neutrons or WIMPs can produce nuclear recoils in matter. As a consequence nuclear recoils are of particular interest for dark matter detection and neutron assay applications. The observation of a direction in the produced nuclear recoils can provide a much stronger discovery signal for WIMPs and is useful for certain neutron assay applications. This section will describe the operation of the ThGEM detector in SF_6 under exposure to neutrons from a Californium-252 source utilising the experience gained from the operation with ^{55}Fe.

3.7.1 Directed neutron run setup

^{252}Cf is a radioactive source which decays by both alpha and neutron emission. Its moderate half life makes it a convenient mobile neutron source for exploring the response of the detector to neutrons. Figure 3.16 shows an approximation of the energy spectrum of neutrons emitted from ^{252}Cf [51]. The spectrum peaks at about 1 MeV and quickly tails off with higher energies up to a maximum of 13 MeV. It should be noted that scattering interaction with the environment and detector vessel will result in a significant distortion of the neutron spectrum observed at the detector. Furthermore both the alpha and neutron emitting decays of ^{252}Cf produce gamma-rays which will also be observed in the detector as electron recoils.

The ThGEMs are mounted vertically in the vessel described in Section 3.2. The readout chain is identical to previously described with both channels connected to a National instruments NI 5751 digitiser.

The vessel is pumped to vacuum and allowed to out gas for several days before filling with about 20 Torr of SF_6. The ThGEMs were then biased to the operating voltage and an energy calibration was performed with ^{55}Fe. A ^{252}Cf source was positioned on the 'arms' of the vessel with a constant offset of 23 cm from the centre of the cathode. The three locations that the source was positioned relative to the body of the vessel and the ThGEMs is shown in Figure 3.17. The locations are labeled the 'A-side', 'B-side' and 'Offside' to refer respectively to the locations on the side of ThGEM-A, ThGEM-B and on the plane of the cathode.

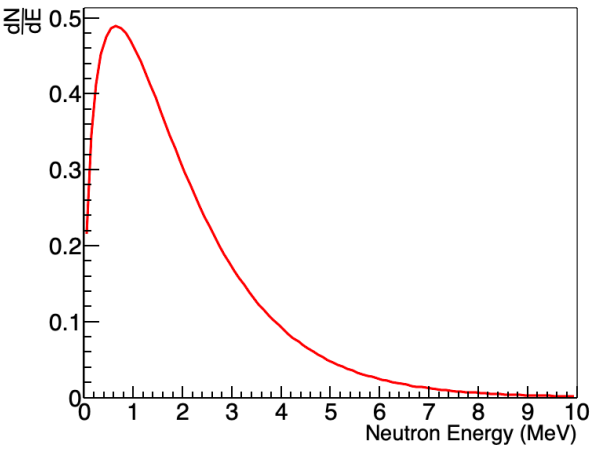

Figure 3.16: The ^{252}Cf neutron spectrum approximated by the equation $\frac{dN}{dE} = \sqrt{E}e^{-\frac{E}{T}}$ with $T = 1.3\,\text{MeV}$ [51].

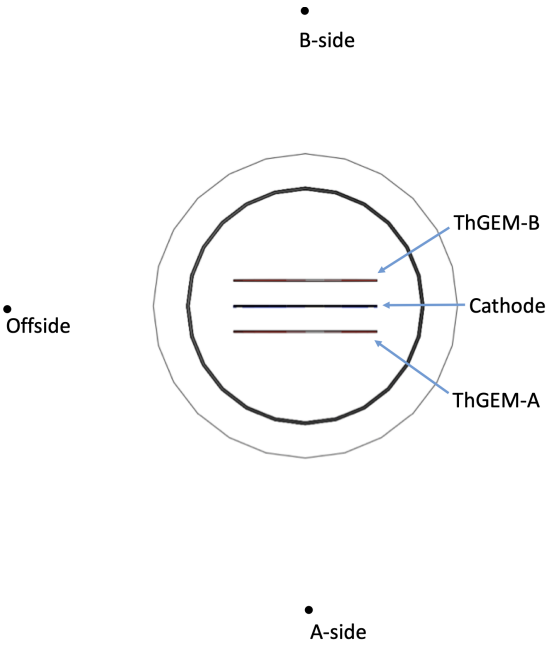

Figure 3.17: overhead view of the ^{252}Cf source locations during directed neutron runs.

For the 'A-side' and 'B-side' runs the back-to-back setup means that the drift fields of each ThGEM are in opposite directions relative to the prevailing neutron flux. This back-to-back configuration is similar to that used in the DRIFT detector and should provide a better control of the systematics for exploring directional signatures [122].

For simplicity, the signal in a given ThGEM is sometimes referred to by the expected direction of an induced neutron recoil relative to the ThGEM. 'up-going' recoils refer to those away from the ThGEM plane and towards the cathode (e.g. Recoils observed on ThGEM A when the source is in the A-side position) and 'down-going' recoils refer to those towards the ThGEM plane (e.g. Recoils observed on ThGEM A for neutron source in B-side position).

3.7.2 Observed ^{252}Cf signal

The initial runs consisted of 1 hour of exposure with the source in the 'A-side' and 'B-side' positions. The SF_6 pressure was 20.1 Torr with a ThGEM voltage of ΔV_{ThGEM}=720 V and a drift field of 450 V cm^{-1}. Some sample events from the B-side exposure run are shown in Figure 3.18.

Observed events had a range of shapes, with some being very compact and close to gaussian as in Figure 3.18a and some consisting of a very wide peak with many individual sub-peaks as in Figure 3.18b. Events with a wide range of energies were observed on both

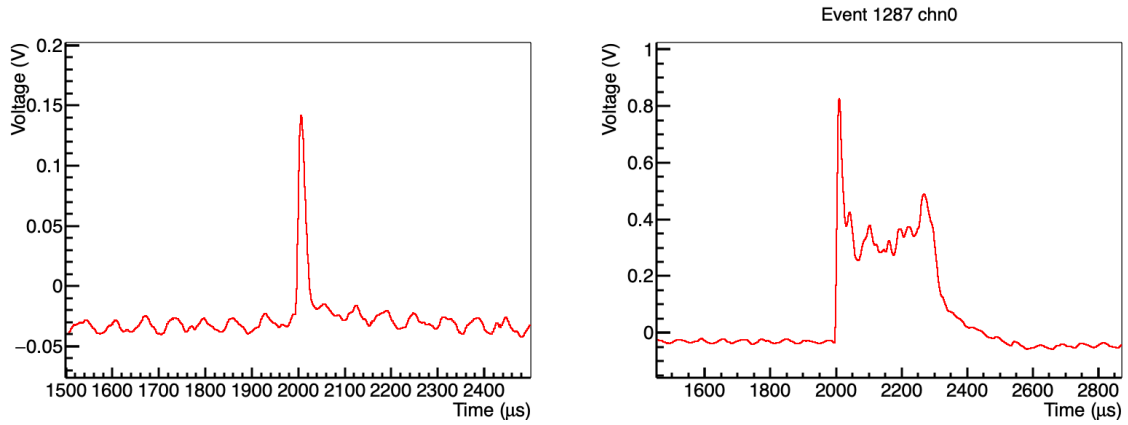

(a) Sample compact event on ThGEM-B (b) Sample wide event on ThGEM-B

Figure 3.18: Sample events during the ^{252}Cf B-side run in 20.1 Torr with a ThGEM voltage of ΔV_{ThGEM}=720 V and a drift field of 450 V cm^{-1}.

ThGEMs, the energy spectrum from the `q_peak` parameter of ^{252}Cf events (determined from prior ^{55}Fe calibration) for each ThGEM is shown in Figure 3.19. In this case the runs are labeled 'up-going' or 'down-going' so that the direction of the neutron source relative to the ThGEM is consistent.

Note that in both cases the energy spectrum is truncated by the rejection of events which saturate the ±1 V range of the digitiser. For ThGEM-A the saturation occurs for gaussian shaped events at around 48 keV and for ThGEM-B this occurs at an energy of about 29 keV. Non-gaussian shaped events can transcend this energy limit but the requirement that the signal not saturate the digitiser severely limits the observable energy range of recoils.

An issue encountered with the long neutron runs was a continuous escalation in the rate of sparking events observed over the duration of the run. Figure 3.20 shows the per-event spark rate observed in the B-side exposure run.

Over the duration of the 1 hour B-side run there are a total of 317 sparking events, with the rate being approximately linear with event number. In the first 1000 events only one spark is observed while there are 14 sparking events in the last 1000 events. The effect this has had on the ThGEMs is explored further in Section 3.8.

As a result of the escalating sparking rate and the limited observable energy range of events, after the A-side and B-side runs the ThGEMs were ramped down to resolve these issues. It was found that any further attempts to reach the previous 720 V operating voltage of the ThGEM resulted in rapid repeated sparking so subsequent neutron runs were undertaken with a lower bias voltage of ΔV_{ThGEM}=650 V. The lower bias voltage meant that the ^{55}Fe peak could not be resolved so an energy calibration was not available. The lower bias voltage did however mean that the higher energy neutron events could be observed without saturation of the digitiser.

The distribution of the `t_width` parameter for each ThGEM with ΔV_{ThGEM}=650 V bias is shown in Figure 3.21. The figure compares the distribution for the 'up going' and offside runs with the cut `q_peak`> 10 V.µs imposed to rejected lower energy events.

As with the ^{55}Fe events the distribution shows an exponential tail-off in rate with energy above a given threshold. The distribution ends at a maximum width of 300 µs where there is a defined peak. The event in Figure 3.18b is part of this population of ∼300 µs wide events and has a typical shape. These events are thought to correspond to

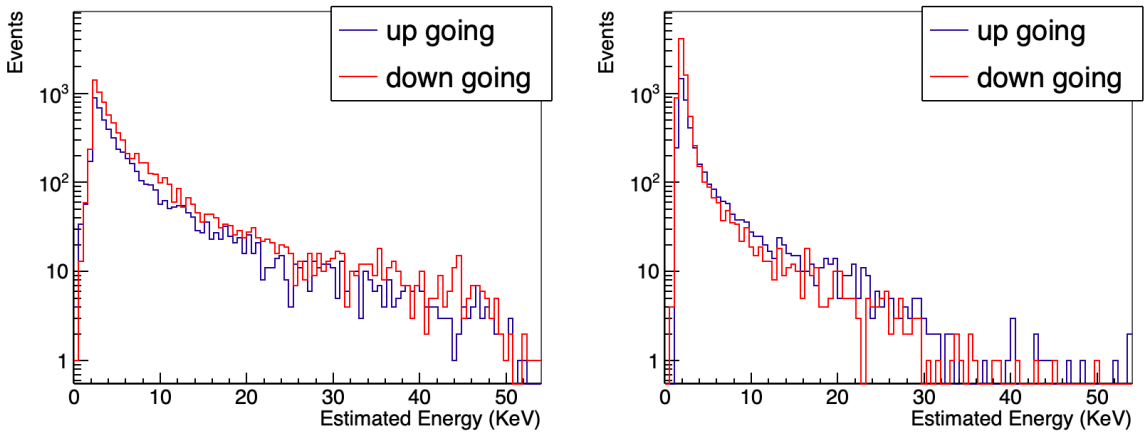

(a) ThGEM-A (b) ThGEM-B

Figure 3.19: Estimated energy spectrum of events during the neutron runs with 20.1 Torr SF_6, a ThGEM voltage of ΔV_{ThGEM}=720 V and a drift field of 450 V cm^{-1}. 'up' going events are those behind the given ThGEM, 'down-going' are on the cathode side of the ThGEM.

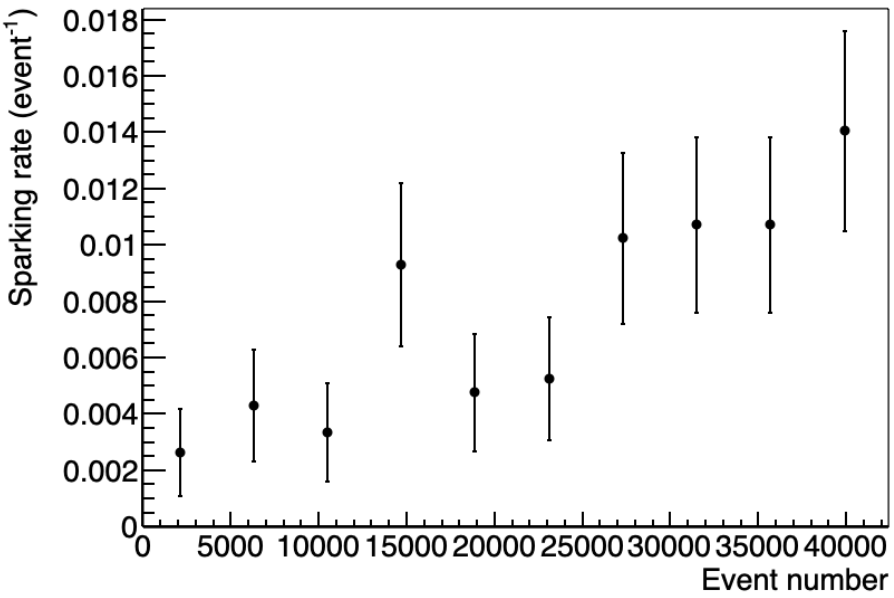

Figure 3.20: Sparking rate over the duration of the b-side exposure 1 hour neutron run.

ionising particles crossing the full width of the drift region. The peak at 300 µs is more pronounced when the neutron exposure direction is parallel to the drift field. Assuming the literature mobility of SF_6^-, drift across the full 2 cm detector width should take only 200 µs. The presence of events with widths in excess of this suggests that the ions in the drift region are not traveling at the speed expected. The distribution is instead more consistent with a mobility of around 35 mm^2/V/s, although the reason for this is unknown.

There are consistent differences between the ThGEMs in the shape of the distribution of the `t_width` parameter for different exposure directions. The offside exposure run shows more of a tendency for events to be have the minimum `t_width`. This is expected as the width is effectively a 1D projection of the track onto the axis perpendicular to the

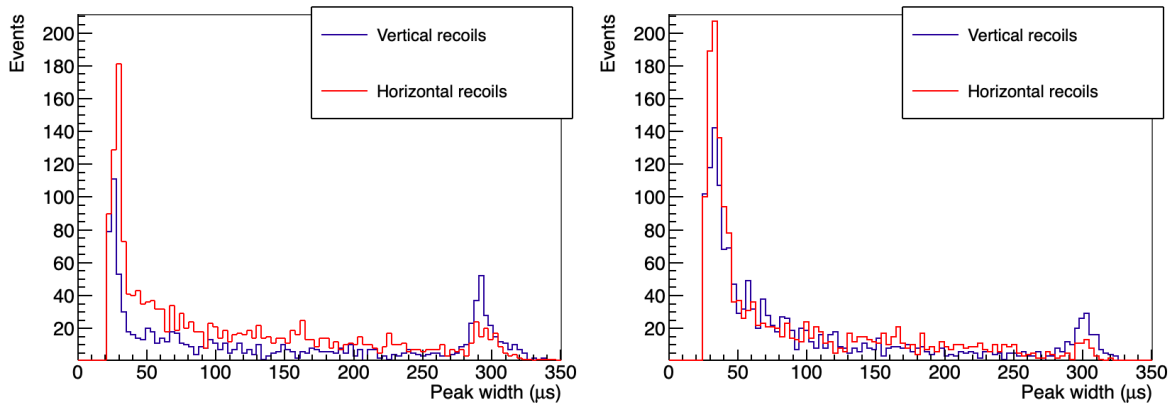

(a) ThGEM-A (b) ThGEM-B

Figure 3.21: Distribution of peak widths for events with integral charge larger than 10 V.μs ^{252}Cf exposure of the detector with 20.4 Torr SF_6 with ΔV_{ThGEM}=650 V and a drift field of 450 V cm^{-1}.

ThGEM. Tracks from the A-side and B-side exposure will be more parallel to this axis than the offside exposure and therefore have a longer projected width.

Figure 3.22 shows the determined number of peaks on each ThGEM for exposure from different directions. The distribution is similar to that observed with ^{55}Fe although the multi-peak events are weighted considerably more toward having more than 4 peaks. This is consistent with the generally higher energy of events in the ^{252}Cf exposure runs which results in longer track and therefore more resolvable clusters. Single peak events were observed more often during the offside exposure run (lateral recoils) than the A-side or B-side runs. This makes sense as charge clusters deposited by a recoil traveling parallel to the ThGEM plane will arrive at the detector at the same time and therefore appear as a single peak.

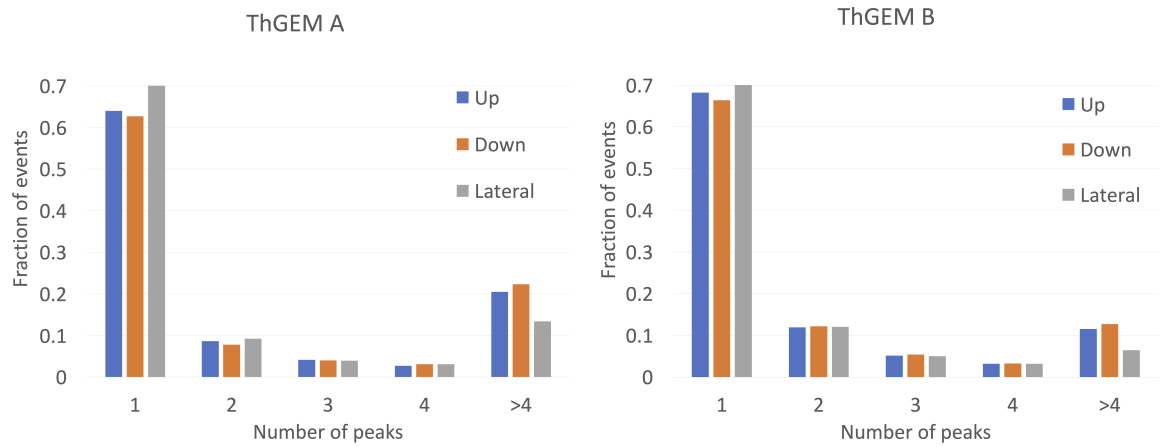

(a) ThGEM-A (b) ThGEM-B

Figure 3.22: Number of peaks identified by the `n_peaks` parameter for different directions of ^{252}Cf exposure of the detector in 20.4 Torr SF_6 with ΔV_{ThGEM}=650 V and a drift field of 450 V cm^{-1}.

Electron recoils likely make up a large proportion of the observed events with nuclear recoils making up a smaller fraction of the events. Nuclear recoils likely will have only a

single peak as they do not display the clustering that electron recoils do. Nuclear recoils will also likely span the energy range of observed events with generally shorter range than electron recoils. The resulting parameter space is still occupied by the electron recoil events observed during the ^{55}Fe runs however suggesting that it is impossible to discriminate on these two factors alone.

3.7.3 Head/tail effect

The presence of a directional signature within the induced recoils is of particular interest for neutron assay or dark matter detection applications. A nuclear recoil will deposit more energy ionising energy at one end of its track, resulting in an asymmetric distribution of charge in the event. This is known as the head/tail effect and is one of the key potential directional signatures in nuclear recoils, the head tail effect has not yet been convincingly observed in SF_6.

The parameters `roi_1` and `roi_2` are measurements of the charge contained in the first and last halves of the signal peak. The ratio between these two parameters, $\alpha = \frac{\texttt{roi\_1}}{\texttt{roi\_2}}$, can be used to measure the asymmetry of the signal [123] [87].

There is a difference in the shape of the pulses on the different channels due to the shaper electronics, this is controlled for by taking the difference between the mean values of α for each channel,

$$\Delta\alpha = \langle\alpha\rangle_A - \langle\alpha\rangle_B, \tag{3.4}$$

where $\langle\alpha\rangle_A$ is the average asymmetry parameter for ThGEM-A and $\langle\alpha\rangle_B$ is the average asymmetry for ThGEM-B. $\Delta\alpha$ is expected to be lower for the B-side exposure than for the A-side exposure if more charge is contained in the tail.

In order to select events which are expected to be majority nuclear recoils, only events with 1 identified peak and a maximum voltage of at least 350 mV selected. The long shaping time means that the peak voltage should be proportional to the maximum projected $\frac{dE}{dx}$ and as a result setting a high trigger threshold should select only nuclear recoil events. This way of selecting nuclear recoil events in negative ion drift gas is similar to the method in [124]. Table 3.1 shows the determined average asymmetry parameter for ThGEM-A and ThGEM-B and the value of $\Delta\alpha$ for the A-side and B-side runs.

Location	$\langle\alpha\rangle_A$	$\langle\alpha\rangle_B$	$\Delta\alpha$
A-side	1.444 ± 0.023	1.550 ± 0.029	-0.106 ± 0.037
B-side	1.383 ± 0.026	1.601 ± 0.028	-0.218 ± 0.039

Table 3.1: Asymmetry parameter for ^{252}Cf exposure of ThGEMs with ΔV_{ThGEM}=650 V and a drift field of 450 V cm^{-1}.

In each run $\langle\alpha\rangle_A$ is lower than $\langle\alpha\rangle_B$ and this can be attributed to the different shaping of the electronics. The back-to-back configuration enables the elimination of this systematic by comparing the value of $\Delta\alpha$ for the different exposure directions. The value of $\Delta\alpha$ is lower for B-side exposure than A-side exposure. This is consistent with the result reported in [125] and implies more charge at the start of the recoil than at the end. Although more energy is lost by a recoil at the end of its track than at the start a larger fraction of the lost energy contributes to ionisation at low energy. This effect is known as ionisation quenching and will be discussed more in Chapter 4.

3.7.4 Discussion

It was established that the ThGEM's were able to observe the ionising radiation interactions induced by the ^{252}Cf in the gas and make measurements of signal parameters. The ThGEM operating voltage established in Section 3.6 was initially used for the directed neutron run. It was quickly found that sparking made this voltage inoperable after only 2 hours of continuous operation so the voltage was reduced.

Some directionality was observed in the statistics of the `t_width`, `n_peaks` and α parameters consistent with what would be expected although populations of recoils from a given exposure direction were not clearly separable. The results for the directed neutron runs are consistent with those in [125], where it was suggested that the poor separation observed then might be partially attributed to neutron back-scatter and the asymmetric geometry of the vessel during the directed exposures. This directed neutron experiment had a more symmetric layout which suggests that the small asymmetry might be more fundamental to the recoils in the gas. Chapter 4 will use simulation to explore the contribution of back-scatter, electron recoils and other systematics to the observed signal.

3.8 ThGEM damage

After the neutron runs were completed, it was decided to investigate the sparking which had become a limiting factor in the achievable ThGEM bias. First the voltage threshold for sparking was established; each ThGEM was biased to 600 V in 20 Torr SF_6, the voltage was then increased in increments of 10 V in one minute steps until a spark was observed. The ThGEM bias at which a spark occurred was 660 V for ThGEM-A and 680 V for ThGEM-B.

After this the ThGEMs were removed from the vessel and visually inspected for defects and damage which might have contributed to or been inflicted by the observed sparking. Figure 3.23 shows a map of the identified defects and damage observed on the ThGEM anode side during the inspection. No defects were identified on the grounded side of the ThGEMs apart from the burned rims which were also visible on the anode side.

On ThGEM-A a strand of something resembling a hair or thin wire was found with a length of approximately 1 mm laying across about three holes. Also identified was a region where the copper layer between the two holes was missing, an area of about 0.2×0.5 mm. It is not known if this might be a manufacturing defect as a comprehensive visual inspection was not performed prior to the operation of the ThGEMs in the vessel. An unknown object was observed in one of the holes adjacent to the removed copper, although it did not appear to be the missing copper layer. No burn damage was observed on ThGEM-A even in the regions where other defects were identified.

On ThGEM-B there were no defects or foreign objects identified but there was a number of holes which had the rims blackened by apparent burns. A total of 13 holes with burned rims were found and they were all grouped towards one side of the ThGEM device. The affected holes had the rims on both sides of the ThGEM blackened. Sparks were observed on both of the ThGEMs, although burn marks were only visible on ThGEM-B. This might suggest that the mechanism that resulted in the blackening of the hole rims might not be simply the sparking.

One way to mitigate the effect of sparking might be to ensure that the ThGEMs operate below the threshold for sparking, preventing damage which might contribute to lowering the sparking threshold. Another processes which might help would be the imple-

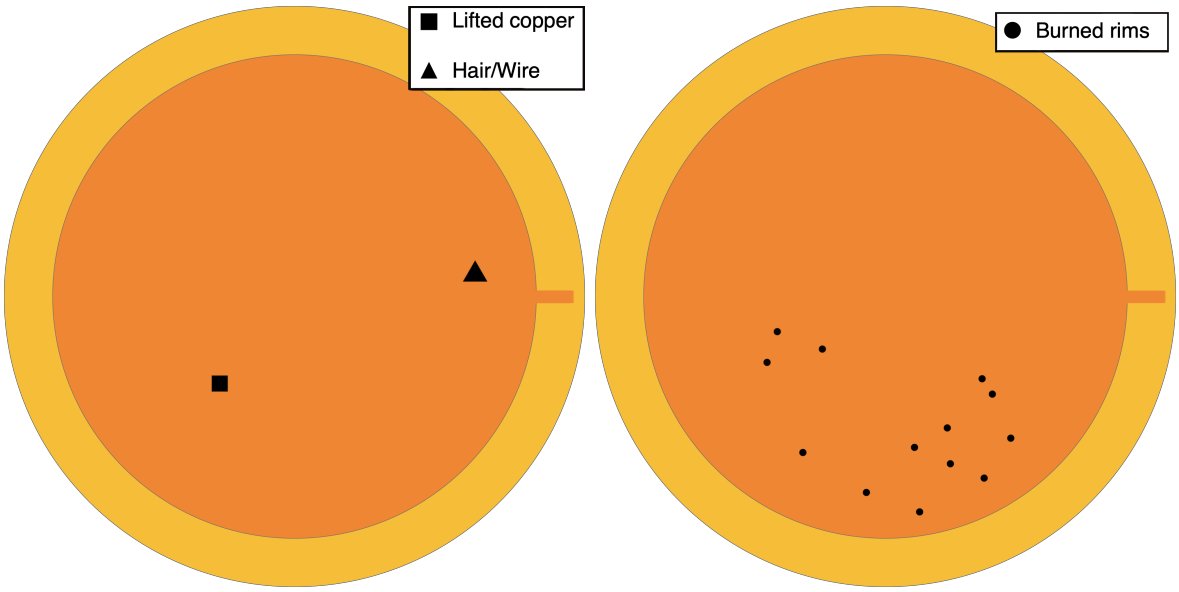

(a) ThGEM-A (b) ThGEM-B

Figure 3.23: Locations of defects identified during the visual inspection of ThGEMs. The triangle indicates the location of the hair/wire and the square indicates the location of the lifted copper on ThGEM-A. The burned rims on ThGEM-B are indicated by circles.

mentation of a ThGEM cleaning protocol for new or damaged ThGEMs. The COMPASS RICH-1 experiment implemented a cleaning regime for the ThGEMs which included a high pressure water rinse followed by an ultrasonic bath in a PCB cleaning solution [126]. The implementation of a similar protocol might assist in maintaining a more consistent level of operation and extend the lifetime of ThGEM detectors.

3.9 Conclusions for ThGEM operation in SF_6

The ThGEM design was hoped to present a device capable of producing significant gain in the negative ion drift gas SF_6. It was found that ThGEMs were able to operate in low pressure SF_6 and could produce gas gains of up to 1550, sufficient to observe 5.9 keV electrons. The electron events observed in SF_6 had significant observable structure, further investigation and characterisation of this structure might present a strong ability to discriminate electron and nuclear recoils and produce accurate measurement of track parameters. During neutron exposure, some correlations were found between the exposure direction and extracted parameters for event width and number of peaks. The observed differences in the asymmetry parameter was also consistent previous reports of the head/tail effect in SF_6. The ThGEMs however presented some significant operational issues; mainly the unexpectedly high gain variation between the devices and the presence of the sparking effect which limited the maximum operating voltages which could be achieved.

Establishing safety margins on the maximum operating voltage of the ThGEMs and cleaning protocol such as the one described in [126] might help mitigate the sparking issue. It might also be possible to slightly more optimise the electronics and ThGEM dimensions for SF_6 to reach a lower energy threshold for events.

Given the issues encountered in SF_6 with the ThGEM it was decided to focus de-

velopment effort on an amplification device which maintains the favourable properties of ThGEMs such as their rigidity and scalability but avoids the associated sparking and gain variation. Chapter 6 will describe the operation of the MM-ThGEM device, an iteration on the ThGEM design which is hoped to overcome some of the issues encountered with the ThGEM.

Also interesting was the features of ThGEM events in SF_6 gas which were identified in the ^{55}Fe and ^{252}Cf runs. To explore these features and their correspondence physical track effects Chapters 4 and 5 will use simulations to explore the attributes of recoils in low pressure SF_6 and the resultant signal.

Chapter 4

Simulation of nuclear and electron recoils in low pressure gas

A quantitative understanding of the interactions occurring in the detector gas is important to inform the analysis of the detector data from the last Chapter and for further detector designs using the same or similar gas targets.

Of particular importance for the applications of interest, discussed in Chapter 2, is the ability to discriminate electrons from nuclear recoils and the ability to extract directional information from the recoil tracks. This chapter covers development of Monte Carlo simulations of keV electrons and nuclear recoils. The goals include the extraction of some of the key parameters of interest in the detector development; particularly measurements of the ranges of electron and nuclear recoils and the expected distributions and types of recoils present in a simulated detector volume. The data generated in this chapter will also be utilised in Chapter 5 which will discuss in detail a model for the corresponding detector signal and the expected discrimination and directionality obtainable.

The three programs which will be discussed in this chapter are DEGRAD, SRIM and Geant4. There are a number of simulation tools available which are applicable in different domains, the three programs which are used here are selected as the most appropriate for the simulation of low energy electrons and ions in low pressure gas.

Geant4 is the most flexible of the programs, able to simulate complex geometries and transport particles with customisable physics packages for different energy domains and processes. DEGRAD and SRIM on the other hand are much less flexible but contain very detailed physics simulations for their specific problem domains. DEGRAD simulates the transport of electrons and photons in gas with comprehensive electronic shell models which Geant4 lacks. SRIM simulates the transport of ions in matter and like DEGRAD has more comprehensive low energy physics compared to Geant4 including corrections for chemical bonds and matter phases (solid, liquid and gas).

Section 4.1 describes the simulation of x-ray induced electron recoils in SF_6 using the DEGRAD simulation code. Section 4.2 describes the simulation of Fluorine recoils using the SRIM program and addresses how quenching was accounted for in the SRIM output. The accuracy and performance of different Geant4 physics modules is explored in Section 4.3 with the SRIM and DEGRAD simulations used as benchmarks. In Section 4.4 Geant4 is used to explore the systematics related to the exposure of the detector to an ^{55}Fe source and a ^{252}Cf source. Finally the overall conclusions of the chapter are presented in Section 4.5.

4.1 Electron ranges and ionisation with DEGRAD

WIMPs and neutrons do not have electromagnetic interactions and as a result do not directly transfer energy to electrons. As a consequence, electrons with keV scale energies constitute a type of noise in WIMP and neutron detectors. An accurate simulation of keV electrons can contribute to developing good discrimination between electrons and nuclear recoils in real detectors. Furthermore x-ray generated electrons are useful for the calibration of gas detectors and quantifying the range and other shape parameters can assist in the discrimination between genuine signal and artifacts in novel detector technologies.

DEGRAD is judged to be the best simulation tool to model the ionisation caused by high energy electrons in the detector gases. It is a Fortran program which performs detailed simulation of the interaction of photons, electrons, and minimum ionising particles with gas mixtures [127]. DEGRAD includes simulation of atomic/molecular cascades and de-excitation, photon absorption, auger shake-off, fluorescence and electron scattering [128]. At the time of writing it is the most comprehensive and accurate available simulation of the interaction of photons and electrons for the gases in its database [129]. DEGRAD version 3.2 is used for all simulations presented in this work.

DEGRAD is launched and interfaced through the command line with settings for a given simulation run set through input 'cards'. The input cards take the form of text files which are redirected to the DEGRAD executable at launch. The settings which can be initialised on the input cards include the gas, pressure, temperature, electric field, magnetic field and the incident radiation type and energy. The most detailed output of DEGRAD consists of the position in space of each of the thermalised electrons generated by the radiation interaction in the gas and the time at which they thermalised. This is in contrast to the output from SRIM and Geant4 for which the output in the setup used consists of the position and energy deposition of the tracked particle at each time step.

4.1.1 ^{55}Fe in SF_6

Characteristic X-rays from the decay of ^{55}Fe by Electron Capture are useful for low energy calibration of particle detectors. The majority of x-rays can be approximated as mono-energetic with an energy of 5.9 keV. DEGRAD is run with 10,000 events with an X-ray of energy 5.9 keV in 20, 30, 40 and 50 Torr SF_6. The gas temperature is set to 19 °C which is the normal temperature of the lab. One of these events from the 20 Torr run is shown in Figure 4.1. The x-ray interaction occurs at $(0, 0, 0)$ in the top right and the electron recoil leaves a track of ionised electrons shown as points on the figure.

There is slight variation in the number of electrons generated by the recoil with pressure, Figure 4.2a shows the total number of electrons generated by each recoil at each pressure. The distributions form Gaussians with means 157 e, 158 e, 159 e, and 159 e at 20, 30, 40 and 50 Torr respectively. The difference of 2 electrons between 50 and 20 Torr data could be attributed to the different kinematics at different pressures. The literature puts the w-value of SF_6 determined from ^{60}Co irradiation at 34 eV which would produce 173 electrons [130]. The difference might be attributed to the significantly different setups and pressures.

The radial distribution of electrons from the X-ray interaction point for different pressures is shown in Figure 4.2b. The recoils are much shorter in higher pressures as would be expected and this is reflected by a tighter radial distribution. Figure 4.3a shows a

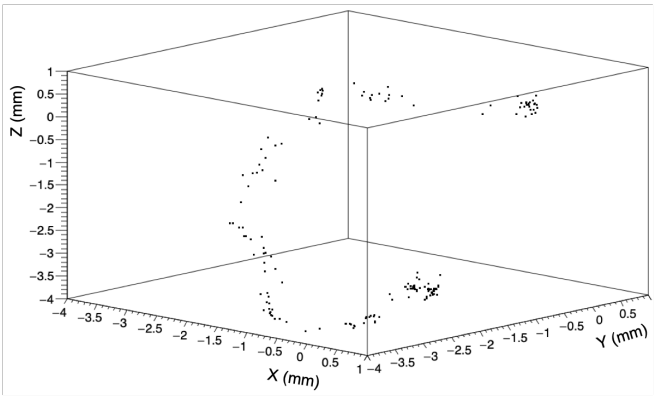

Figure 4.1: Locations in space for thermalised electrons from DEGRAD electron recoil in 20 Torr SF_6 induced by a 5.9 keV X-ray.

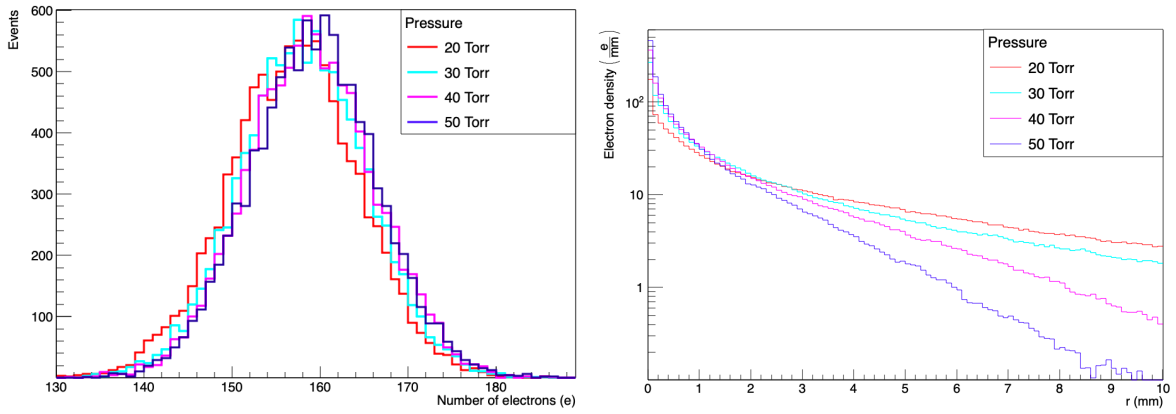

(a) Total number of ionised particles.

(b) Averaged radial electron density profile.

Figure 4.2: DEGRAD electron distribution data for 5.9 keV X-ray induced electron recoils in SF_6, for 10,000 events.

histogram of the radial range of the recoils measured from the X-ray interaction vertex to the furthest thermalised electron. The distribution has a long tail toward longer ranges, at 20 Torr the peak is at 2.4 mm and the average range is 3.4 mm.

The determination of the radial range requires knowledge of the initial location of the electron and accurate spatial data about each ionised charge. In a practical detector this knowledge is not available so another parameter for the range is also used which measures the width of the charge cloud. The charge cloud width is more relevant to the signal observed in a detector than the radial range although they are both useful.

To determine the width of the cloud, the electron locations are projected onto the x-axis and the width is taken to be the width of the inner 80% of the electrons. Figure 4.3b shows the distribution of charge cloud widths at different pressures determined in this way, the width is slightly less than half the ranges in Figure 4.3a. The expectation of structure on the order of millimeters is immediately relevant to the response of the detector and suggests the duration of charge collection will be on the order of tens of microseconds. A more detailed model of signal formation in a 1d detector is presented in Chapter 5.

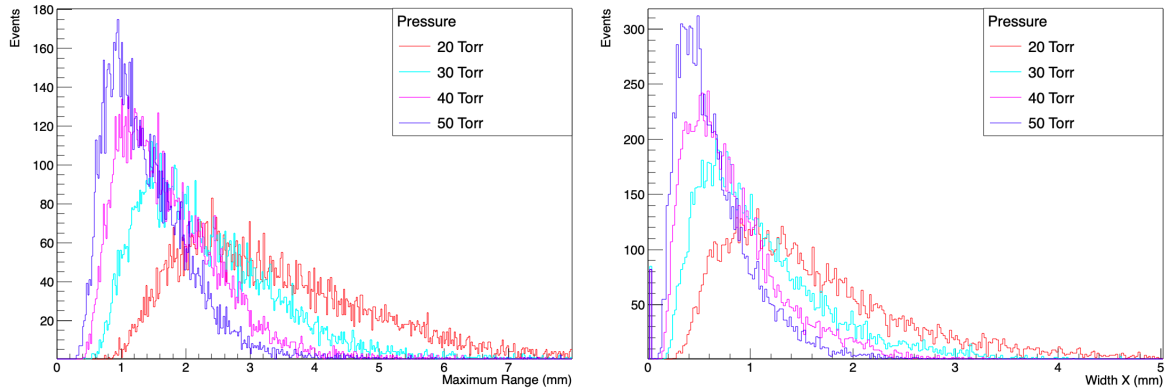

(a) Histogram of radial range of recoil measured from x-ray interaction vertex to furthest thermalised electron.

(b) Width of event in x axis as measured from 10^{th} to 90^{th} percentile of charge distribution.

Figure 4.3: DEGRAD electron range metrics for 5.9 keV X-ray induced electron recoils in SF_6, for 10,000 events.

4.1.2 Modeling keV electrons for CYGNUS

A feasibility study for a large nuclear recoil observatory based on gas TPC technology has been in preparation in the direction dark matter community for some time. At the time of writing the paper "CYGNUS: Feasibility of a nuclear recoil observatory with directional sensitivity to dark matter and neutrinos" [83] is submitted to Physical Review D and awaiting review. One of the key performance metrics for determining the ultimate sensitivity of such a detector is its ability to discriminated between electrons and nuclear recoils, its ER discrimination power. Because electrons form a significant background to WIMP detection experiments, the ability to reject them can define the low energy threshold of a detector.

To arrive at an estimation of the ER discrimination for an idealised detector a large amount of accurate electron recoil simulation data for a set of gas mixtures needed to be generated. The generation of this electron recoil data with DEGRAD was the author's main contribution to the CYGNUS paper.

One million electron recoils were generated at 1 keV increments over the energy range 1 keV to 20 keV. The simulation required the use of the University's HEP computing cluster and the raw output approached 1 TB of data. Runs were performed in different gases that were of interest for the CYGNUS observatory, one in 20 Torr SF_6 and one in 740:20 Torr He:SF_6, the Helium included as a target for the WIMP recoils.

The ionised electrons determined in DEGRAD were then subject to diffusion consistent with the drift in a TPC detector. The signal induced by the diffused charge on a set of idealised detector readouts was then modelled. Figure 4.4 shows a plot from the paper which displays a raw DEGRAD modelled 20 keV electron, the ion distribution after diffusion and the response of the modelled detector technologies to the recoil.

The modeled detector readouts were planar, wire, optical, pad, strip and pixel readouts. Planar readouts provide only information about the arrival time of drifting charge, the ThGEM discussed in Chapter 3 is a type of planar readout. The MWPCs discussed in Chapter 2 comprise wire type readouts and provide coarse position data in 2 dimensions. Pad type readouts consist of an array of millimeter scale charge sensitive pads which can provide a coarse 3D reconstructions of recoils. Strip readouts consist of an array of strips

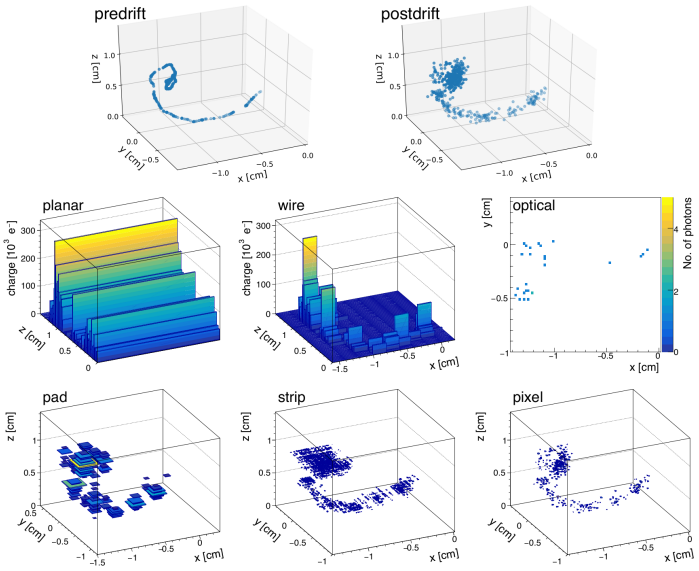

Figure 4.4: Distribution of ionisation for a 20 keV DEGRAD electron in 740:20 Torr He:SF_6 before (top left) and after 25 cm of drift (top right) and the signal from the readout measured on six different readout technologies.

in one or two directions which can provide a 3d reconstruction of recoils using the coincident arrival of signal on orthogonal strips. Finally pixel type readouts are similar to pad type readouts but with significantly smaller elements which are on the sub millimeter scale.

The diffused DEGRAD recoils were compared to SRIM generated nuclear recoils in the same gas mixture to arrive at the obtainable ER discrimination with the CYGNUS detector. The ER discrimination was parameterised by the electron rejection factor, R, defined by the ratio

$$R = \frac{N_{all}}{N_{surv}} \tag{4.1}$$

where N_{all} is the number of electron recoils in an energy bin and N_{surv} is the number of electrons which survive an electron rejection cut which preserves 50% of nuclear recoils. An electron rejection factor in excess of 6×10^4 was obtained at 3.5 keVee for fluorine recoils in atmospheric pressure He:SF_6. The ER discrimination factor defined the expected low energy threshold of the CYGNUS detector and therefore the projected exclusion limits for the CYGNUS detector.

The low energy threshold and other considerations including the event detection efficiency, the energy resolution, noise characteristics and the angular resolution were synthesised to arrive at the expected physics reach of each type of readout. Combining this result with the known costs of each readout enabled a determination of the directional sensitivity per unit cost of each readout technology and an evaluation of the most feasible for scaling to a large recoil observatory for WIMPs and neutrinos. A strip based readout was determined to be the most cost effective by a factor of three above any of the other evaluated readouts. This result informed the selection of the novel MM-ThGEM in combination with a resistive layer micromegas as a candidate for a scalable gas amplification and readout technology in SF_6 and other negative ion gases. The development of the micromegas-MMThGEM for use in SF_6 is the focus of Chapters 6, 7, 8, and 9.

The DEGRAD simulations of electron recoils were a important part of the determina-

tion of the feasibility of a the CYGNUS large scale recoil observatory. The detailed recoils contributed to the calculation of the expected ER discrimination factor and therefore to the low energy threshold of the observatory. The low energy threshold of the observatory dictates its sensitivity to WIMPs and neutrinos and consequently its overall physics reach.

4.2 Nuclear recoil ranges and ionisation with SRIM

The interactions of interest for WIMP detection and neutron assay produce nuclear recoils in the detector. Accurately modeling nuclear recoils to explore their ranges and any directional signatures which are encoded in the produced ionisation can help inform detector development and signal analysis. The comparison of simulated nuclear recoil data to electron recoil data is also anticipated to be useful for ER discrimination.

Stopping and Range of Ions in Matter (SRIM) is a software package for calculating a number of parameters related to the stopping of ions in matter and for simulating the transportation of ions. The SRIM package has very detailed physics which includes quantum mechanical treatment of ion-atom collisions, electron exchange and correlation interactions between electronic shells, and long range interactions described by electron excitations and plasmons within the target. Included in the SRIM package are two programs, SRIM and TRIM. The first program, confusingly also called SRIM, calculates electronic and nuclear stopping tables of an ion in a target. The other included program, Transport of Ions in Matter (TRIM), is the Monte-Carlo portion of the program which can be use to transport individual ions in multi layered targets. The distinction between the SRIM and TRIM sub-programs will be made in this section although elsewhere unless otherwise stated "SRIM" will refer to the overall package and calculations from either of the sub-programs. The version of SRIM used in this work is SRIM-2013.

Fluorine ions are expected to be the main nuclear recoil in SF_6 induced by both WIMPs and neutrons. As such this section will focus on the simulation of ^{19}F ions in SF_6

4.2.1 TRIM calculation modes

TRIM has a number of calculation modes available for performing Monte-Carlo simulations under different circumstances [69]. The modes include setups specifically for thin layers, biological materials and studying surface sputtering. The two settings of interest for us are the "detailed calculation with full cascades" and "ion distribution and quick calculation of damage" modes. A sample set of ten events in each mode for 20 keV Fluorine recoils in 30 Torr SF_6 is shown in Figure 4.5. The initial recoil track is in white, and the secondary recoils are in orange (Sulpher) and cyan (Fluorine).

The range and energy deposition distributions give similar results between the two simulation modes with the main difference being that the energy deposition from secondary nuclear recoils are effectively projected onto the primary track in the quick calculation. The SRIM manual explicitly states that the ionisation energy loss by the ion into the target, energy transferred to recoil atoms, and the final distribution of ions in the target will be correct in the quick calculation mode and furthermore that the ion range in the quick calculation mode and full cascade mode are identical. This is borne out by a quick test to compare the two modes in 30 Torr SF_6 with 1000 Fluorine ions with energy 20 keV. The secondary recoils in this test have lengths on the order of 100 µm which, as will be discussed in Chapter 5, is significantly below the scale at which event structure is expected to be visible to the detector. Due to the much slower run time of the full

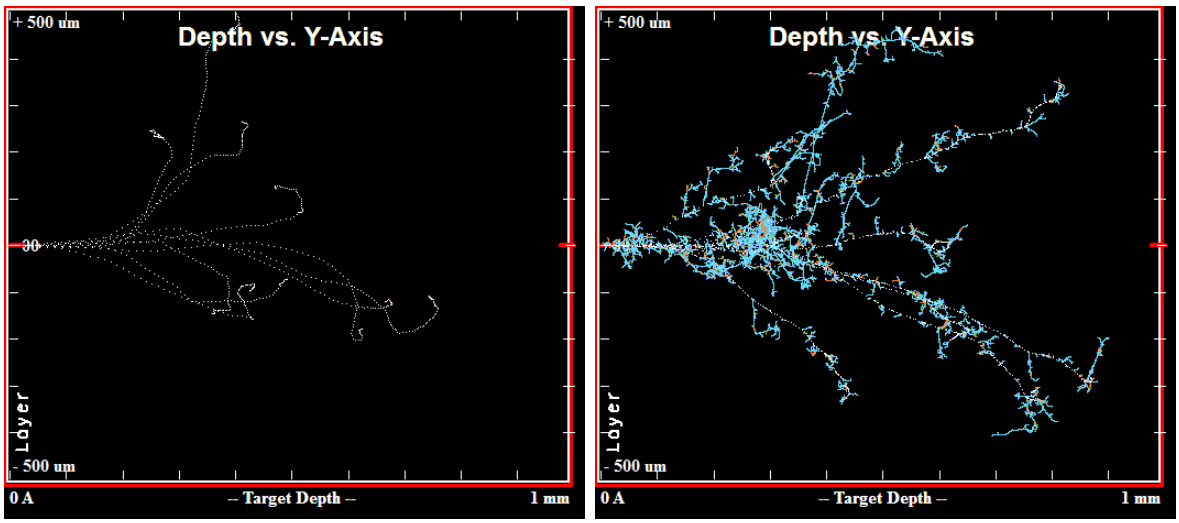

Figure 4.5: Sample set of ten 20 keV Fluorine recoils in 30 Torr SF_6 from TRIM, quick damage calculation (left) and full cascades (right). Primary recoil in white, secondary Sulpher recoils in orange and secondary Fluorine recoils in cyan.

cascade and the fact that the bulk properties of the recoil will be identical, it was decided that further calculations will be undertaken in the quick damage mode.

4.2.2 Compensating for quenching

The TRIM code is closed source and the information available to the user about each recoil is limited to what is available in the data files which TRIM outputs. A significant omission from the TRIM output files for our purposes is a measurement of the ionisation energy loss per step, with only total ionising energy loss accessible. This is significant because nuclear recoils, particularly at low energy, do not disperse all of their energy as ionisation and the fraction of energy lost to ionisation changes with energy. This effect is described by the Ionisation Quenching Factor (IQF) which is the fraction of the total recoil energy which is released by ionisation of the target material. A semi empirical expression for the IQF, f_n, is given by Lindhard *et al.* [73], and can be expressed as

$$f_n = \frac{kg(\epsilon)}{1 + kg(\epsilon)} \tag{4.2}$$

where the reduced energy, ϵ, and the constant, k, which is related to the stopping power can be determined for a nucleus of atomic number Z and mass number A, with

$$\epsilon = 11.5 E_R Z^{-\frac{7}{3}}, k = 0.133 Z^{\frac{2}{3}} A^{-\frac{1}{2}}, \tag{4.3}$$

and $g(\epsilon)$ can be parameterised by:

$$g(\epsilon) = 3\epsilon^{0.15} + 0.7\epsilon^{0.6} + \epsilon. \tag{4.4}$$

The Lindhard model neglects the atomic binding energy of electrons which means this model becomes quite crude at low reduced energies, with a lower limit of $\epsilon \sim 10^{-2}$, equivalent to ~ 0.2 keV for Fluorine [74]. This simplification of the Lindhard model also assumes the recoil is propagating in a medium made up of the same isotope, using this approximation for SF_6 would mean neglecting a seventh of the nuclei in the gas.

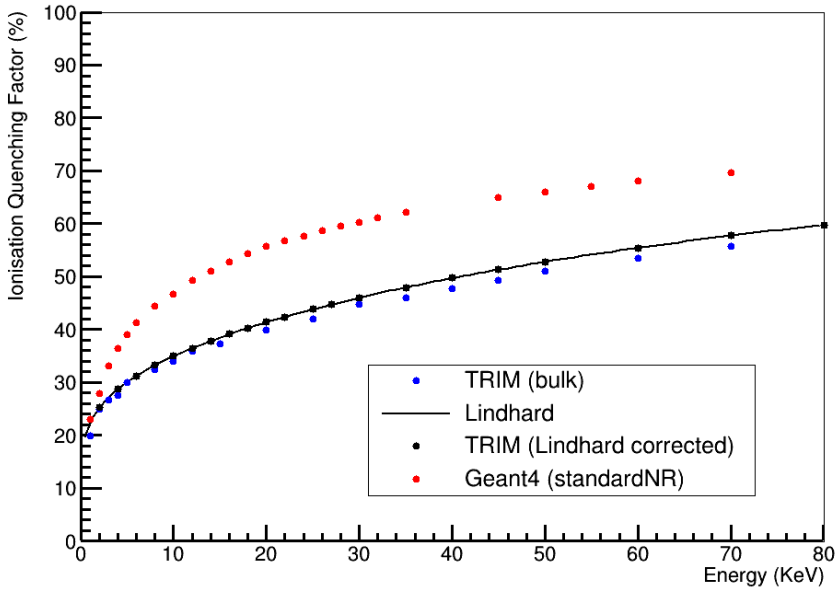

Figure 4.6: Simulated ionisation quenching factor of ^{19}F recoils in 20 Torr SF_6 from TRIM and Geant4, quenching expected in pure Fluorine from Lindhard model indicated.

As mentioned previously the IQF of individual recoils in inaccessible in TRIM, the total ionising energy loss for an entire run though is accessible and the IQF can be trivially obtained from that. The quenching factor for ^{19}F recoils in 20 Torr SF_6 from TRIM determined from the average ionising energy loss for 10000 recoils is shown in Figure 4.6, along with the results from the Geant4 `standardNR` physics list and the prediction from the Lindhard model for pure Fluorine.

The Lindhard model is very close to the prediction from SRIM while Geant4 predicts a significantly higher quenching factor. The reason for the divergence between Geant4 and the SRIM model is not clear although might simply be due to Geant4 having poorer low energy physics than SRIM, the physics of Geant4 will be covered in further detail in Section 4.4. The Lindhard model however agrees to within 5% with the results from SRIM despite neglecting the Sulpher atoms in the gas. While SRIM is probably the best tool at the time of writing for estimation of the quenching factor of a novel gas, it was shown to be out by a factor of 10-20% for the estimation of the quenching factor of the novel detector gas isobutane [131]. Given the possible error and the fact that no empirical measurement of the quenching factor of SF_6 currently exists, the Lindhard approximation is considered sufficiently accurate to the SRIM prediction to be used as a correction to the deposited energy.

To reconstruct the stepwise ionising energy loss in the gas the IQF determined from the Lindhard model is used as a modifier to the total energy loss, for other gases or nuclei, care should be taken when applying this correction to ensure that it matches the SRIM prediction to a high enough level of accuracy. The IQF on the event level in each of the TRIM runs after the Lindhard correction is applied also shown on the graph, it is perfectly coincident with Lindhard model as would be expected.

4.2.3 ^{19}F ion ranges

Figure 4.7a shows the radial range distribution for 20 keV Fluorine ions at different pressures in SF_6. Average radial ranges of 20 keV Fluorine recoils are 0.87 mm, 0.58 mm, 0.44 mm and 0.35 mm in 20, 30, 40 and 50 Torr SF_6 respectively. The radial range distribution is much more symmetric than seen for the electrons which might be attributed to the nuclear tracks being straighter. The width of the inner 80% of the charge projected onto an randomly oriented axis is shown in Figure 4.7b, the peak of the distribution increases and the tail to higher widths gets longer with decreasing pressure. The randomly projected widths of most events is less than 1 mm at all pressures, the difference from the radial range is indicative of most of the charge being concentrated in a single area of the projected track.

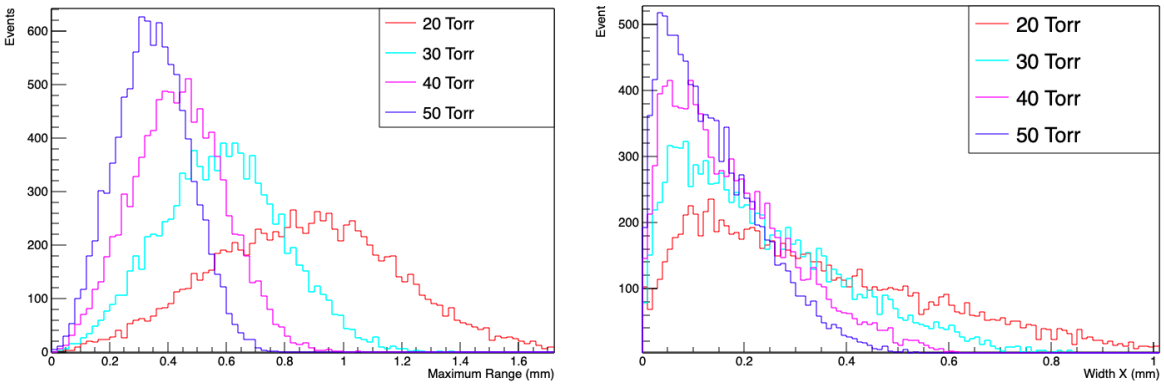

(a) Histogram of radial range of recoil measured from initial location to furthest point in Fluorine track

(b) Width of event in random axis as measured from 10^{th} to 90^{th} percentile of energy deposit

Figure 4.7: SRIM range metrics for 20 keV Fluorine recoils in SF_6.

When we instead look at how the range varies with energy we find that the radial range and the width of the event projected onto an axis is close to linear. Figure 4.8a shows how the average of the radial range and three projected widths for 10,000 events varies with initial energy.

The event widths are determined by the width of the inner 80% of the deposited ionising energy projected onto an axis, as in Section 4.1. The three axis which are used are the y-axis (parallel to the recoil direction), the x-axis (perpendicular to the recoil direction) and a randomly oriented axis. The perpendicular projected width does have a noticeable deviation from the linear fit at low energy ($E < 15$ keV), with the measured widths lower than the linear fit. The large difference between the parallel and perpendicular projected widths shows that directional information about the initial recoil direction is encoded in the distribution of deposited energy.

We can use the difference between the parallel and perpendicular projected widths to estimate the segmentation a perfect detector would need to be able to distinguish recoils perpendicular and parallel to the segmented direction. The difference is linear with constant 2.88 mm keV^{-1}, so for example an segmentation of 0.288 mm would be sensitive to the direction of 10 keV recoils in 20 Torr SF_6. This is simplistic and assumes no diffusion or other systematic effects whatsoever but it does immediately translate the ground truth result into something applicable to detector design.

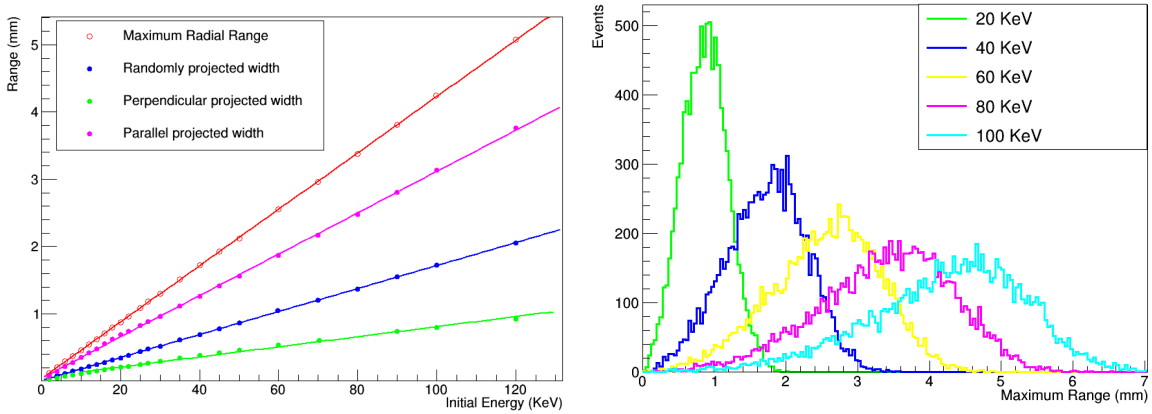

(a) Variation in the radial range and linear, perpendicular and randomly projected widths with energy, linear fits to the data plotted.

(b) Histogram of radial range of recoil measured from initial location to furthest point in Fluorine track.

Figure 4.8: SRIM range metrics for Fluorine recoils in 20 Torr SF_6.

Overall the simulation of nuclear recoils in SF_6 demonstrates that directional information is encoded in the recoil shape across energies as well as range information which distinguishes nuclear recoils from electrons. Converting this in to a form which has more meaningful implications for the detection of recoils requires modeling the diffusion of charge during drift and the effects of a detector readout. Chapter 5 presents a model for translating the simulated recoils into a detector-like signal and the resulting directionality and ER discrimination available to a 1d readout.

4.3 Accuracy and performance of Geant4 physics in low pressure gas

Accurately modeling electron and nuclear recoils in an infinitely extended volume of a given material is useful for the determination of the expected signal for an idealised detector. Real detectors are however finite and the signal from a source of radiation observed by a detector is subject to systematic effects from the geometry of the detector and the transport of the radiation in the surrounding environment. DEGRAD and SRIM provide the most complete models for electrons/x-rays and heavy ion recoils respectively [129], but only allow for the propagation of a specific set of particles and within basic geometries. The simulation toolkit Geant4 however can transport a diverse range of particles and enables the creation of much more complex geometries than either DEGRAD and SRIM. Consequently Geant4 allows access to the systematic effects of finite sensitive volumes and particle transport outside the detector which are unavailable in the DEGRAD or SRIM models.

The flexibility of Geant4 is a double edged sword; the ability to simulate particle transport on the scale of micrometers to kilometers at energies from hundreds of eV to TeV requires a range of models with different applicability to different regimes [132]. The selection of an inappropriate physics model for a specific use case can produce unphysical results due to approximations which work well in other cases. The transport of KeV energy particles in low pressure gases is an unusual enough application that specific care needs to be taken in the selection of Geant4 physics models. This section will compare the

performance of a number of physics lists with the available dedicated simulations, SRIM and DEGRAD, in order to conclude which will be most appropriate for our application. The results will inform the physics implemented in the Geant4 simulations in Section 4.4 which explores the systematics related to the ^{55}Fe and ^{252}Cf exposures of the ThGEM detector.

4.3.1 Description of Geant4 and simulation setup

Geant4 is a particle physics simulation toolkit which contains a comprehensive range of processes for particle transport at a range of energies from 250 eV to TeV [132]. The toolkit is written in C++ and consists of a set of C++ classes which are accessed and interfaced with each other through the user's own code. A comprehensive description of Geant4 can be found in its user guide [133].

The Geant4 toolkit provides access to a variety of "physics lists", sets of physical processes collected together to describe the physics of the simulation. The user can also select the components of their own physics list and even write their own physical processes. It is important to select a set of physics which has a good balance of speed and accuracy within the selected problem domain. This is particularly critical for use cases like ours which are near one of the limits of Geant4's applicable energy range, where not all of the models have been fully validated [134]. Geant4 version 10.0 is used for all the simulations presented in this work.

The Geant4 code and geometry for the test was based on the TestEm7 example which is designed to compare a very basic detector response to different physics lists. The geometry is simplified to a SF_6 gas filled cube and some functionality is added to give additional run time control over the gas pressure and the particle source. The program is set up to output the ionising energy deposit, particle location and particle type at each timestep. Each run consisted of 10,000 mono-energetic primary particles emitted from the origin in a beam along the x-axis.

The physics lists compared were selected based on their expected relevance to the relatively low energy ion and electron recoils of interest. The slowing and scattering of both types of recoil is entirely due to electromagnetic processes at this energy and as such focus is on electromagnetic physics lists. Here is presented a short description of the selected physics lists, more information is available at [134, 135]

standard The default set of electromagnetic physics processes used in the major reference Physics Lists (FTFP_BERT, FTF_BIC, QGSP_FTFP_BERT, etc.).

emstandard_opt3 A modification to the standard physics list for higher accuracy tracking of electrons, hadrons and ions. It increases the binning of physics tables and substitutes a number of scattering and ionisation models with more detailed ones [136].

standardSS A modification to the standard physics which which substitutes the multiple scattering processes for Single Scattering models for all coulomb interactions, simulating each individual coulomb interaction of a propagating charged particle.

ionGasModel A modification to the standard physics list with the Bragg and Bethe-Bloch ion Gas Models in addition to the standard processes.

emlivermore Substitution of a number of the electromagnetic physics processes for photons and electrons in the standard physics list with ones using interpolated data from the Livermore libraries (EADL-EEDL-EPDL).

empenelope Substitution of a number of the electromagnetic physics processes for photons, electrons and positrons in the standard physics list with processes derived from the PENELOPE Monte-Carlo code [137].

standardNR A modification of the standard physics list which uses the Urban multiple scattering model and screened nuclear recoils for ions. [136].

The Geant4 user has access to other parameters which effect the physics of the simulation, for example the tracking cut defines the energy below which a given particle type will stop being simulated. Another parameter which was anticipated to be important was the maximum step size, Geant4 simulates the transport of a particle in discrete time steps with the step size calculated based on the mean free path of the particle. As the target medium in these simulations is a low pressure gas, the mean free path of the particles is comparatively large, which might have a adverse affect on the physics performance of the simulation.

4.3.2 Comparison of 5.9 keV electrons in Geant4 and DEGRAD

Electron recoils with energy 5.9 keV are selected as the test case for the electron physics comparison between Geant4 and DEGRAD because of the importance of ^{55}Fe induced electrons of that energy. The target gas was 20 Torr SF_6 at 19 °C and the precipitating x-ray was not simulated for cleaner access to the range metrics which were used as a basis of the comparison. Each run consisted of 10,000 electrons starting at the origin in a focused beam along the x-axis, with the physics list and the step size limit changed across runs. An equivalent simulation was performed in DEGRAD and the results are used as a benchmark for the Geant4 physics.

Figure 4.9a shows the histogramed radial range for each physics list with automatic step sizing and for DEGRAD. Note that the `ionGasModel` physics list is not shown as it's output is identical to the results `standard` list (this is possible because the random number generator seed was the same at the start of each run and is indicative of none of the modifications from the `standard` list being called at any point in the run).

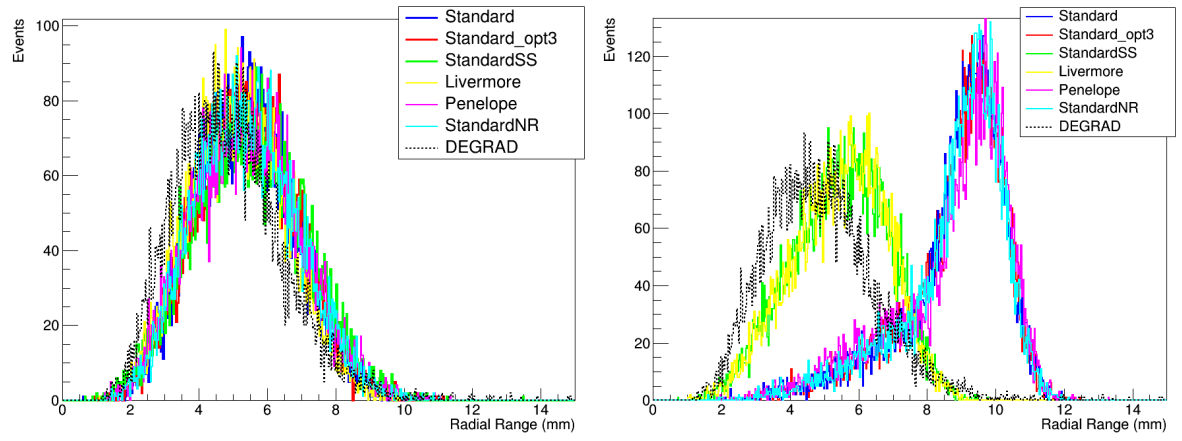

(a) Automatic step sizing

(b) Maximum step size 20 µm

Figure 4.9: Distribution of the e- radial range for 5.9 keV electrons in 20 Torr SF_6 for different Geant4 Physics and DEGRAD.

Without any step size limit, the Geant4 models all agree on the average radial range to within 4%, although they are all predict slightly longer ranges than DEGRAD. A

significant issue is that the automatically determined step sizes can be as large as 1 mm which is a significant fraction of the recoil length, as a consequence the average number of steps in each event is only 13 for all of the physics lists except `standard`, which averages 5.4 steps, and `standardSS` which averages 68 steps. This is problematic because the energy dependent physical processes simulated by Geant4 are dependent on the assumption that the steps are small enough that the energy can be assumed to be constant over the duration of the step. This assumption is not very accurate when the particle can lose more than 20% of its initial energy in a single step.

To counter the large steps and the expected degradation of the physics performance, a maximum step size was imposed which puts a limit on the maximum length of a step. With a step limit in place however a number of the physics lists diverge significantly from the DEGRAD prediction and from their un-limited predictions, as shown in Figure 4.9b the `standard`, `emstandard_opt3`, `empenelope` and `standardNR` physics lists all predict significantly longer ranges for forced 20 µm steps. Looking at the variation with maximum step size it was found that for these lists lower step sizes resulted in longer radial ranges, although the actual path length ends up being effectively equal for all the runs. The effect turns out to be related to the amount of scattering that the tracks undergo; smaller limits on step size result in tracks that scatter less, at step sizes of 1 µm the tracks are unphysically almost perfectly straight. Figure 4.10 shows a subset of the tracks from the `standard` and `emlivermore` runs with a 20 µm step size maximum illustrating this effect.

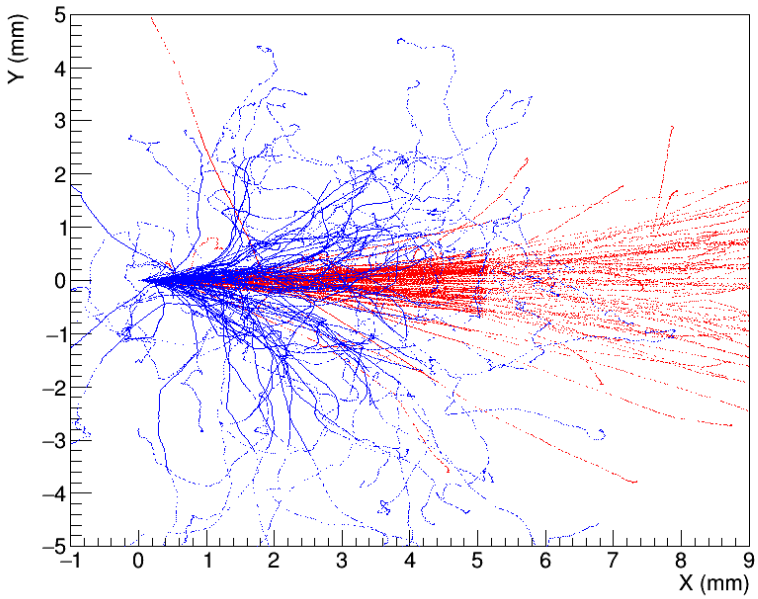

Figure 4.10: Subset of Geant4 5.9 keV electron tracks in 20 Torr SF_6 with a 20 µm maximum step size using `emlivermore` physics (blue) and `standard` physics (red).

The relative straightness of the electron tracks in the `standard` list is typical of most of the physics lists with the 20 µm step maximum. The modification to the total amount of scattering was present even with a maximum step size of 500 µm, a step size which also results in significant per step energy loss of the particle. The `emlivermore` and `standardSS` do not exhibit this behaviour and the scattering of the electrons with these lists does not seem to strongly depend on whether or not there is a maximum step size.

For a more granular examination of why the `emlivermore` and `standardSS` physics

lists do not diverge for forced shorter steps, the `standard` list is used with a step limit of 20 µm and the physical processes within the list are swapped out with those in the `emlivermore` and `standardSS` lists in different runs. The key processes contributing to the shorter range of electrons are found to be `G4LivermoreIonisationModel` for the `emlivermore` list and `G4CoulombScattering` for the `standardSS` list with the substitution of either of these routines into the standard physics list being enough to recreate the shorter range distribution with the step limit.

The reason `G4CoulombScattering` does not diverge at low step sizes can be attributed to the fact that it treats each scattering interaction discretely; the equivalent processes in the other physics lists use continuous multiple scattering approximations, which assume that there are many (soft) scattering interactions in a given step such that they can be treated collectively. In a low pressure gas with short step sizes this approximation doesn't hold and as a result the continuous multiple scattering approximation diverges from the expected behaviour. Some of the physics processes also mix the continuous and discrete models so that soft interactions are modelled collectively and hard interactions are modelled discretely. The `G4LivermoreIonisationModel` process uses a mixed model and seems to be able to handle the short steps where the other processes that use this model (e.g. `G4UrbanMscModel` in `standard_opt3`) are impaired by the continuous part of their physics. It's not clear that this can be attributed to anything other than better optimisation for our use case on the part of the `emlivermore` list.

To compare other shape parameters each recoil was projected onto three axis: the axis parallel to the recoil direction, an axis perpendicular to the recoil direction, and a randomly orientated axis. For each projection the width of the inner 80% of the deposited energy was used as a metric of the shape. For non limited step sizes it was found that Geant4 predicted longer electron ranges in all axis than DEGRAD for all the physics used. Rather than being a result of substantially different recoil shapes the difference in these metrics is more related to the energy deposition in different portions of the track. DEGRAD having the charge deposition more concentrated, particularly at the end of the track than in any of the Geant4 physics. Both with and without a step size limit the `emlivermore` and `standardSS` physics are closest to the DEGRAD prediction for all the metrics suggesting these are providing the best physics for electrons.

4.3.3 Comparison of ^{19}F recoils in Geant4 and SRIM

The other particle types of interest are nuclear recoils in the detector, the most common of which in SF_6 is expected to be Fluorine. In this case using SRIM as a benchmark, the same overall setup as the last section is used with the initial particle instead being 20 keV ^{19}F nuclei. The nuclei are initialised as fully ionised although the initial ionic charge is ignored by most physics lists in favour of the effective charge which is dependent on the ion's kinetic energy. The exception to this is the `ionGasModel` and `standardSS` physics lists which will actually model the charge initialised. The radial range distribution for 10,000 ions with each physics list with and without a 20 µm maximum step size is shown in Figure 4.11.

The most significant divergence between Geant4 and SRIM is in the `ionGasModel` and `standardSS` models which do not use an effective charge during the transport have significantly shorter ranges than the other physics in all cases. Doing further runs with singly charged ^{19}F ions results in a much longer range for both types of physics while leaving the range for the other physics lists unchanged, confirming the ionic charge is the

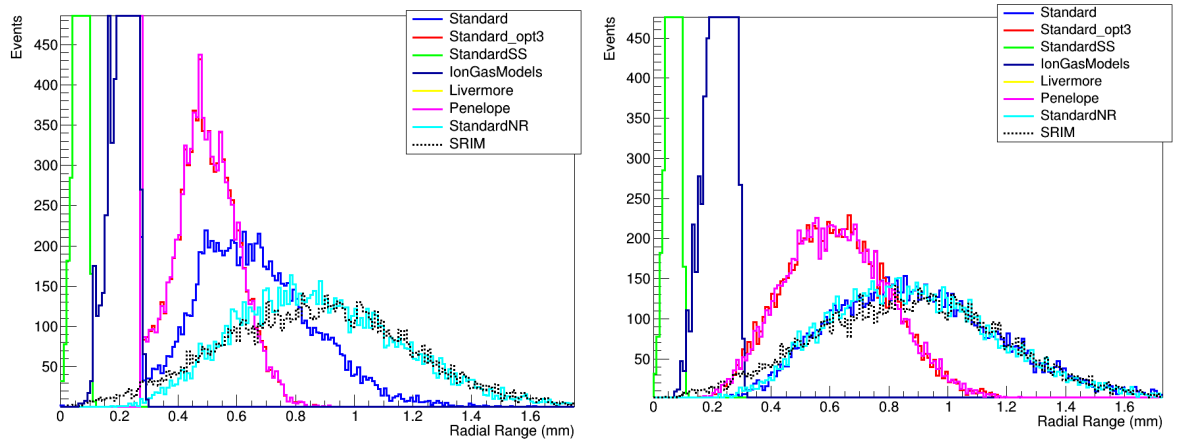

(a) Automatic step sizing

(b) Maximum step size 20 µm

Figure 4.11: Distribution of the ^{19}F radial range for 20 keV ions in 20 Torr SF_6 for different Geant4 Physics and SRIM.

source of the effect. As SRIM also uses an effective charge model for ion transport it is hard to compare either of the `ionGasModel` and `standardSS` models with it.

For the automatic step sizing in Figure 4.11a, the next shortest ranges belong to the `emlivermore`, `empenelope` and `emstandard_opt3` physics lists. The `emlivermore` and `empenelope` physics are perfectly identical (`emlivermore` is not visible in Figure 4.11 due to this) which shows their ion physics is the same and that no electron or photon physics is called during the run. The `standard` physics list produces even longer ion ranges and `standardNR` list produces the longest range of the Geant4 physics and is the most similar to SRIM.

As with the electrons, without any cap on the step size the steps can be very large relative to the full length of the recoil, in this case steps can be up to 100 µm long. The average number of steps for each event for the `emlivermore`, `empenelope` and `emstandard_opt3` physics lists is 10.4. The average number of steps for the `standard` and `standardNR` physics lists are 22.6 and 37.5 respectively, for comparison SRIM averages 65 steps.

When the maximum step size is set to 20 µm, the ranges for all of the physics lists increases compared to the automatic steps, although `standardNR` changes fairly little. With these step sizes `standard` physics is close to both SRIM and `standardNR` but the `emlivermore`, `empenelope` and `emstandard_opt3` runs still have a significantly shorter range than either. Significantly the straightening of the recoil tracks that was seen with the electrons is not observed for ^{19}F ions. Further decreasing the step size does not result in a significant change in the physics of the `emlivermore`, `empenelope` or `emstandard_opt3` lists.

The radial range provides a lot of information about the recoil shape but is not the only range metric of interest. Also of interest is the range of the recoil in a set of 1d projections measured as the width of the inner 80% of deposited ionising energy. The axes the the recoils are projected onto to obtain these metrics are parallel to the recoil direction, perpendicular to recoil direction and a randomly orientated axis. The difference between the average of the shape metrics for SRIM and each of the Geant4 physics lists with a 20 µm step maximum is shown in Figure 4.12.

The difference between the average radial ranges for SRIM and Geant4 are consistent with the analysis of Figure 4.11 with the `standard` and `standardNR` physics most similar

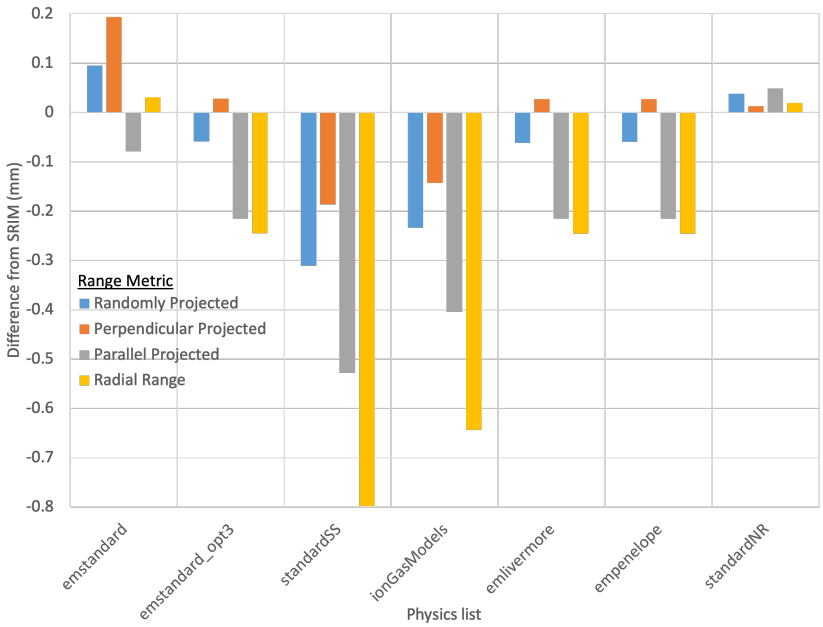

Figure 4.12: Difference between SRIM and different Geant4 physics lists with a 20 µm stepping maximum for a 20 keV Fluorine nucleus in 20 Torr SF_6.

to SRIM. For the projected ranges however the `standard` physics list has a much larger divergence from the SRIM predictions than the `standardNR` list which is most similar to SRIM across all metrics. For the other physics lists the divergence of the radial range from SRIM is a good predictor of the physics list's performance on the projected range metrics.

The ionisation quenching factor is also a significant consideration when it comes to obtaining an accurate model for nuclear recoils. The quenching factor as it applies to the SRIM recoils was previously discussed in Section 4.2.2. For 20 keV ^{19}F recoils in SF_6, the IQF determined from SRIM was 40% and the lindhard model gave a quenching factor of 41%. All of the Geant4 physics predicts a significantly higher quenching factor; for 20 µm steps the `emlivermore` and `empenelope` lists have a quenching factor of 52%, `emstandard_opt3` has a quenching factor of 53% and `standardNR` has 55%. The `standardSS` list has a quenching factor of 8% for fully ionised ^{19}F, but the absence of an effective charge model means there isn't a direct comparison that can be made with SRIM and the other lists. The `emstandard` and `ionGasModels` lists do not account for quenching at all, in the runs using those lists all deposited energy is accounted for as ionising energy deposit. When there is no step limit in place there is a slight change in the quenching factors of <1%. The systematic overestimation of the quenching factor by Geant4 by at least 10% compared to SRIM is consistent across the tested physics.

Overall the `standardNR` physics list appears to perform the best; it is the most similar to SRIM across all of the range metrics and the predicted ranges are robust to changes in maximum step size. The large divergence between the other physics lists and SRIM and their sensitivity to step size implies that some of the slowing approximations are breaking down in the relevant energy and density regimes in a similar way to that observed for electrons.

4.3.4 Comparison of execution times of Geant4 physics lists

In addition to accuracy an important consideration for the selection of the required physics is the execution time. While the 10,000 particles used in these comparison runs is fairly small and even the longest execution times are not a massive obstacle, further simulations might use millions or billions of events and the required resources for a run would be a significant concern.

To compare the execution times of each physics list the shell command `time` was used to measure the user CPU time of a run of 10001 particles and a run of 1 particle on a work station. The run with one particle is used to control for the time taken to initialise the geometry and all the physics and libraries which does not scale with number of events, the execution time per 10000 events is then taken to be the difference. The workstation used was running the CentOS 7 Linux distro on a i7-3820 CPU with 64 GiB of RAM and a GeForce GTX 550 Ti graphics card. Table 4.1 shows the determined execution time per event for electrons and Fluorine nuclei at 5.9 keV and 20 keV respectively with the 20 µm maximum step size. The execution times for DEGRAD and SRIM are also shown with the execution time for DEGRAD determined in the same way as for Geant4. SRIM couldn't be timed on the same work station or in the same way as it is a Windows program and furthermore does not have a command line interface, instead the duration of a 10000 event run was timed manually with a stopwatch, the reduction in precision is considered acceptable due to the fairly long execution time of the SRIM program.

Physics	^{19}F (ms/event)	e^- (ms/event)
emstandard_opt0	1.27	2.11
emstandard_opt3	0.73	2.08
standardSS	21.1	1.66
ionGasModels	0.29	2.11
emlivermore	0.80	2.33
empenelope	0.72	2.13
standardNR	1.05	2.40
SRIM	8.88	-
DEGRAD	-	39.7

Table 4.1: Per event execution time of different physics lists for 10000 20 keV ^{19}F and 10000 5.9 keV e^- in 20 Torr SF_6.

For the Fluorine recoils the physics which took the longest was the `standardSS` physics list which took 21 ms per event followed by SRIM which took less than half as long at 8.9 µs. The other physics were much faster with per-event times around 1 ms, and the `ionGasModels` list only took 0.29 ms per event although this is probably because of the incredibly short recoils caused by the preservation of the ionic charge with that physics.

With the exception of `standardSS`, the electron recoils exhibit fairly little variation in execution time between most of the physics lists with `emlivermore` and `standardNR` taking only slightly longer per event than the other lists. Surprisingly the `standardSS` list executes the fastest, in a reversal of the trend with the nuclear recoils. This might be because of the discrete nature of most of the processes in that list so that many of the functions are only called when a discrete interaction happens and not on every step. This explanation would track with the assumption that the adverse effects on the scattering for

most of the other processes are a result of the continuous approximations suffering from the low number of interactions per step. DEGRAD takes much longer than any of the Geant4 physics, which might be a reflection of its somewhat deeper physics of in terms of tracking the cascades in electron shells of ionised atoms and the thermalisation of ionised electrons.

4.3.5 Conclusions and Geant4 physics selection

The investigation into the most valid Geant4 physics for our use case was considered necessary because the particle energy and material density regions of interest are much lower than many of the applications of Geant4. The fact that the use case is close to the limit of applicability of most of the Geant4 physics is borne out by the behaviour of the electron physics studied with regards to limiting the step size. Automatic step sizing for electrons leaves the energy loss per step very large and the number of steps per event very low, which brings into question the validity of the constant energy approximation required for accurate physics over the length of a step. Limiting the step size however had an immediately adverse effect on the rate of scattering for the recoils, showing that another approximation (that the number of soft scattering interactions per step was enough to be treated collectively) was being made invalid. The `standardSS` and `emlivermore` physics seem to get around these two competing effects, and give fairly consistent physics at all step sizes and the most similar results to DEGRAD.

The automatic step sizing was also a significant issue for ^{19}F recoils for the same reasons, although in that case limiting the step size did not appear to run into the same issues with scattering. The enhanced ion physics of the `standardNR` physics list put the Geant4 results more in line with SRIM than the other physics lists and it also didn't suffer from significant changes to the track parameters from the step size changing. The `standardSS` and `ionGasModels` were unfortunately hard to evaluate in comparison with the other physics lists due to using the initial ionic charge and not an effective charge.

While a single physics list did not have the best performance across all the tested situations the modularity of Geant4 means that aspects of different physics lists can be mixed and matched. A custom physics list was constructed by using `standardNR` as a base and substituting the electron and photon physics of the `emlivermore` list, this set should provide stable physics with both automatic and limited step sizing for both electrons and nuclear recoils. The customised list was called `standardCE` and was it was found that the averages for the range metrics were the same as `standardNR` for ^{19}F recoils and `emlivermore` for e^- recoils indicating they were successfully integrated. Arriving at a set of physics which well models recoils in low pressure gas enables Geant4 to be used with confidence to explore the systematics related to the detector geometry.

4.4 Exploring systematics related to detector geometry in Geant4

As discussed in Section 4.3, Geant4 enables the creation of complex geometries through which particles can be transported. This enables an evaluation of systematic effects of a finite detector volume and the transport of radiation through the geometry of the detector. This kind of analysis is unavailable in DEGRAD or SRIM, although the individual recoils generated in those programs are expected to be higher quality.

This section uses Geant4 to explore the systematic effects of the detector geometry on the recoils generated by ^{55}Fe and ^{252}Cf in SF_6 in the sensitive volume of the ThGEM detector characterised in Chapter 3.

4.4.1 Detector model

To exploit the aspects of Geant4 which set it apart from the other simulation packages discussed and to examine some of the systematics which might be occurring in the real data collected, a virtual model of the vessel used for the evaluation of the ThGEM's discussed in Chapter 3 was constructed within the program. A side by side comparison of the vessel and Geant4 model is shown in Figure 4.13.

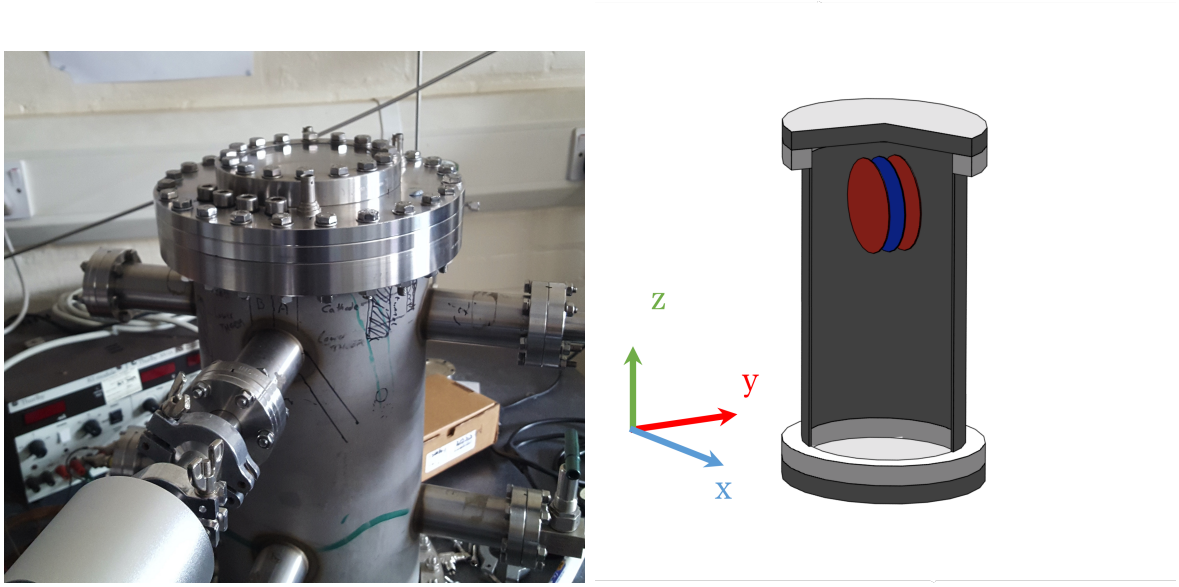

Figure 4.13: Rig image (left) and the Geant4 geometry with cut-away plane (right), the ThGEMs shown in red and the cathode in blue.

The virtual model consists of a cubic world volume, 1 m on a side, made of air (`G4_AIR`) at STP, within this volume is the vessel. The vessel consists of a hollow cylinder with circular collar and endcap at each end and is constructed of stainless steel (`G4_STAINLESS-STEEL`). The arms of the vessel are neglected as well as the electronics and nearby wall, table and gas system. Inside the vessel is the detector gas and the two back to back ThGEMs and the cathode. The ThGEMs and cathode consist of disks with 6 cm radius and 0.7 mm height made of the material FR4. The FR4 is manually constructed within Geant4 from SiO_2 and Epoxy (H_nC_n) in the ratio 1.12:1 and with total density 1.86 g/cm^3. The <100 µm thick copper layers on the face of each ThGEM and the cathode are neglected due to their thinness. As the cathode consisted of an old ThGEM in the experiment, the cathode and ThGEMs are identical. The separation between each ThGEM and the cathode is 2 cm and a cylinder of the detector gas with radius 5 cm in the region between each ThGEM and the cathode is designated as a sensitive detector. This corresponds to the radius of the region of the ThGEM which has drilled holes.

When a particle deposits ionising energy in one of the sensitive detector regions, the coordinates of the particle at the end of the timestep, the ionising energy deposited and the particle type enumerated according to the PDG Monte Carlo Particle Numbering Scheme [138] is output to file. A local coordinate system is used for the output where the

origin is located at the centre of the surface of the ThGEM and the z axis points towards the cathode. The `G4GeneralParticleSource` class is used to enable the position, energy and particle type of the source to be set at run time.

4.4.2 ^{55}Fe in SF_6

To simulate ^{55}Fe source in the vessel the particle source is positioned on the inside perimeter of the vessel at the midpoint between one of the ThGEM's and the cathode. This is to recreate the ^{55}Fe source location used with the ThGEMs in Chapter 3 when the source was positioned via magnet. Each event consists of a 5.9 keV photon emitted in a random direction from the particle source, although only events which result in energy deposit in the drift region are saved. Runs are performed at 20, 30, 40 and 50 Torr of SF_6 at 19 °C with one million initial photons emitted isotropically.

As would be expected most of the energy deposit in the sensitive region is due to electron recoils. Figure 4.14 shows one of the induced electron recoils in 20 Torr SF_6.

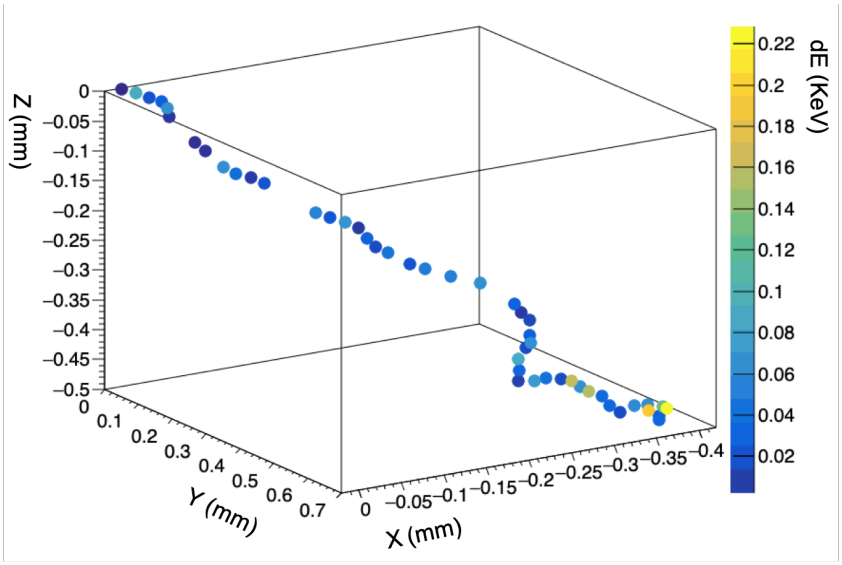

Figure 4.14: Particle location and ionising energy deposit at each timestep in Geant4 for an electron in 20 Torr SF_6 induced by a 5.9 keV X-ray.

The recoils are normally on the order of millimeters and exhibit significant scattering consistent with the observations from DEGRAD. For some events, Compton scatters of the x-ray photon in the gas also deposit energy at some distance away from the main electron recoil. This is fairly rare although it underlines one of the systematic effects that is missed by a simple simulation of 5.9 keV electrons. Figure 4.15 shows all the simulated electron recoils in the drift region for 1,000,000 initial photons in 20 Torr SF_6.

The circular region in which there are recoils corresponds to the sensitive region of the ThGEM. The track density is higher nearer the particle source which is located 97 mm from the center of the ThGEM, (this would be $(0, 97)$ on the graph). One of the systematics that is indicated by this plot is the significant amount of the tracks that aren't fully contained in the drift region. Table 4.2 shows the number of fully and partially contained tracks at each pressure.

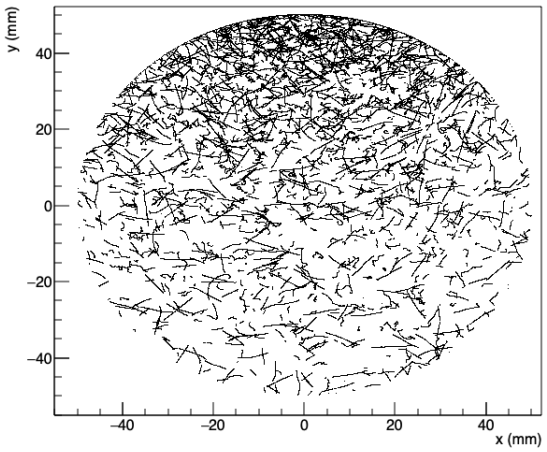

Figure 4.15: Recoil locations in x-y in Geant4 for electrons in 20 Torr SF_6 induced by a 5.9 keV X-ray.

Pressure (Torr)	Fully contained tracks	Partially contained tracks	Proportion contained (%)
20	1523	505	75.1
30	2781	465	83.3
40	3417	455	86.7
50	3552	465	88.4

Table 4.2: Total fully and partially contained events for one million photons at each pressure and percentage of saved events which are fully contained.

The events are classified as partially contained if the recoil is within 0.05 mm of any edge of the drift region at any timestep. The total number of recoils increases with pressure and the proportion of those recoils which are fully contained also increases. The increase in total events can be attributed to higher total cross section to x-rays at higher pressure. The higher proportion of contained recoils can be attributed to shorter tracks, which are less likely to cross the perimeter.

For partially contained events the visible energy to the detector is less than the full recoil energy, which could distort the 5.9 keV peak used for detector calibration. A plot of the energy spectrum of the events indicates that the contribution of the partially contained events to the energy spectrum is a fairly flat distribution from zero to 5.9 keV. Significantly there doesn't seem to be any distortion of the ^{55}Fe peak which means the effect of these partially contained events can be neglected in the experimental data.

In summary, the Geant4 simulation indicates that x-ray transport from the ^{55}Fe source and charge loss off the edges of the drift region do introduce a systematic distortion of the ^{55}Fe energy spectrum. Importantly this distortion does not result in a change in the average of the 5.9 keV peak and consequently these effects can be safely neglected for the experimental determination of the gas gain.

4.4.3 ^{252}Cf in SF_6

The ability of Geant4 to propagate many different types of particle through complex geometry enables the experiment undertaken in Section 3.7 to be simulated in a more sophisticated way. Because neutron interactions in the detector gas as well as the surrounding environment can contribute to the observed signal, a simulation which includes neutron transport through the detector geometry is necessary to explore the signal that would be observed. Aspects of the experimental data including the population of observed waveform peaks with 300 µs widths, the energy spectrum of events and the contribution of neutron back scattering to the head-tail measurement are might be resolved using simulation data.

To accurately model neutron interactions additional data files for neutron cross sections had to be loaded into the physics list, including the `G4NDL4.4`, `G4NEUTRONXS1.4` and `G4NEUTRONXS1.4` files. To model a ^{252}Cf source, the particle source is initialised to emit

neutrons with a range of energies from 0.1 MeV to 10 MeV with the spectrum modelled by the equation $\frac{dN}{dE} = \sqrt{E}e^{-\frac{E}{T}}$ with $T = 1.3$ MeV [51]

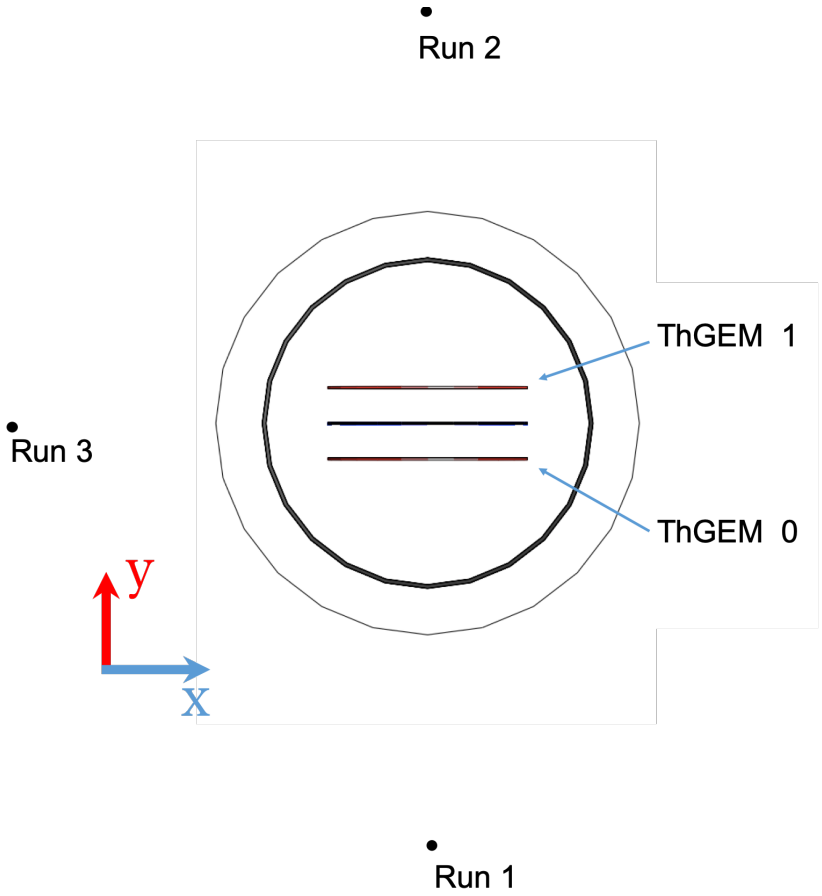

Figure 4.16: Particle source locations in the Geant4 model for the ^{252}Cf runs.

The spectrum of neutron energies is given by the equation

$$\frac{dN}{dE} = \sqrt{E}e^{-\frac{E}{T}}, \tag{4.5}$$

where a value of T of 1.3 MeV gives a good approximation of the ^{252}Cf spectrum [51,139]. The gamma-rays which are produced by ^{252}Cf during fission are neglected in this model.

Three runs of 100 million neutrons each are performed with the particle source offset 23 cm from the cathode in the locations shown in Figure 4.16. These locations are selected to be consistent with the experimental neutron source locations relative to the vessel in Section 3.7. The gas pressure in the vessel is set to 60 Torr of SF_6 to make the results comparable with the ^{252}Cf runs performed in Chapter 3 and in [125].

As discussed in Chapter 1, neutrons themselves are not observed by most detectors but are detected through the secondary recoils and other reactions they induce. There are a number of these reactions which can occur as well as a number of target nuclei besides the ones which comprise the detector gas. Consequently a number of the ionising interactions in the detector region might not originate from the S or F recoils of primary interest. Figure 4.17 shows the total count of each type of particle which deposited energy in the drift volumes in each run.

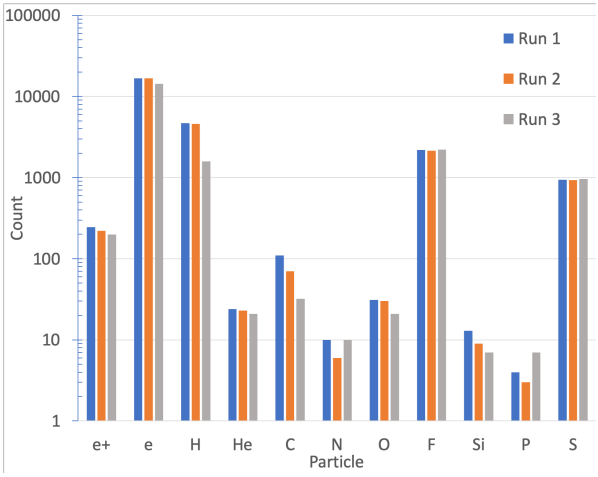

Figure 4.17: Count of ionising particles in the ThGEM 1 sensitive volume for each run.

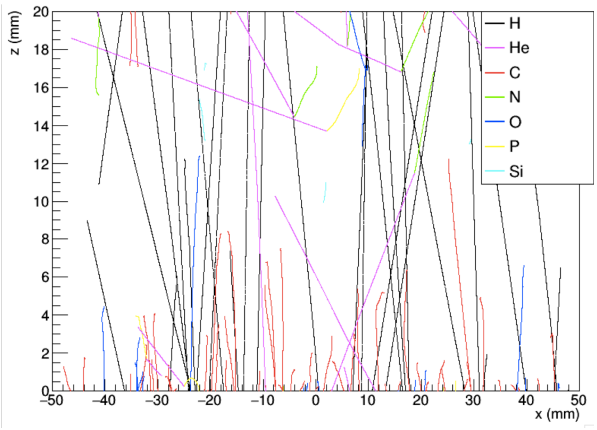

Figure 4.18: The ionising tracks of recoils excluding S, F, and $e^{\pm}$ in run 1, ThGEM 1, the Hydrogen recoils are downsampled by a factor of 100 for clarity.

The most commonly detected particle are electrons, which are the main secondary particles generated by gammas (photons aren't counted because of the way the simulation is set up) which are themselves are a secondary particles produced primarily by inelastic scattering of neutrons in matter. The gamma background in this case has enough energy that a significant amount of pair production occurs in the sensitive volume accounted for by the count of positrons (e+ in the figure).

There is a significant number of nuclear recoils that were not Sulpher or Fluorine nuclei. The spatial distribution of nuclear recoils excluding Sulpher and Fluorine in ThGEM 1, run 1 are shown in Figure 4.18. The primary nuclear recoil in the sensitive region is actually hydrogen for runs one and two, these hydrogen recoils originate from the ThGEMs and Cathode and can be attributed to the recoil of hydrogen in the epoxy of the FR4.

The Silicon, Carbon and Oxygen recoils are also mainly generated by recoils from the ThGEM, the significantly lower rates can be attributed to a mix of lower cross section to neutrons and to the thinner skin depth for the heavier ions. Helium, Phosphorus and Nitrogen on the other hand are not present in any of the materials used in the detector and are entirely created by neutron spallation and or the decay of excited nuclei, some of these reactions can be seen in Figure 4.18.

Before the analysis was performed it was assumed that the thin copper layer on the ThGEM and cathode could be neglected due to its low mass. The results however makes apparent the fact that surface recoils from the detector itself might make up a significant fraction of signal events, and the inclusion of the copper layer would likely significantly lower the number of hydrogen recoils as compared to this simulation.

The main particles of interest are Fluorine and Sulpher recoils as well as the signal from electrons for ER discrimination purposes. The range and energy deposition within the drift region of the Fluorine, Sulpher and electron recoils is shown in Figure 4.19. There is a peak in the deposited energy spectrum of fluorine at around 90 keV and at 25 keV for electrons, aside from those features the energy spectra show a generally exponentially declining rate with energy. The electrons are the dominant recoil below 60 keV of deposited ionising energy and Fluorine is dominant above that. One significant factor that is made clear by the use of the full geometry is that many of the electron recoils range out in the ThGEM or out of the edge of the drift region; this and the ionisation quenching contribute significantly to the measured energy and ranges.

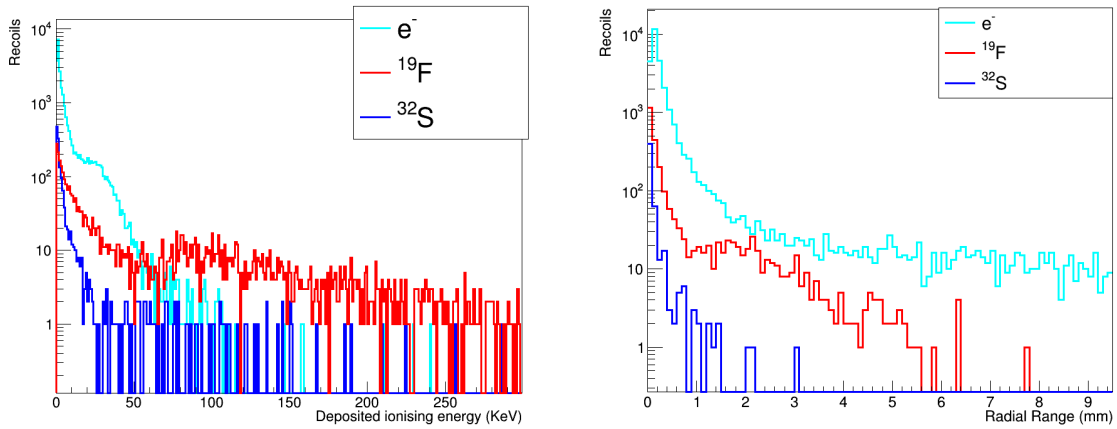

Figure 4.19: The ionising energy deposition (left) and radial range (right) distribution of recoils from Geant4 ^{252}Cf neutrons in ThGEM 1 in 60 Torr SF_6.

Another aspect of interest is the level of directionality which is preserved in the nuclear recoils. In a previous experiment studying the head tail effect of recoils in SF_6, exposure from one side resulted in an no reversal of the head/tail signal [125], part of the interest in performing this simulation is to determine the extent to which back scattering neutrons might contribute to the signal. Figure 4.20 shows the distribution of recoil direction by the azimuthal angle in global coordinates in each run for S and F recoils and for all other nuclear recoils.

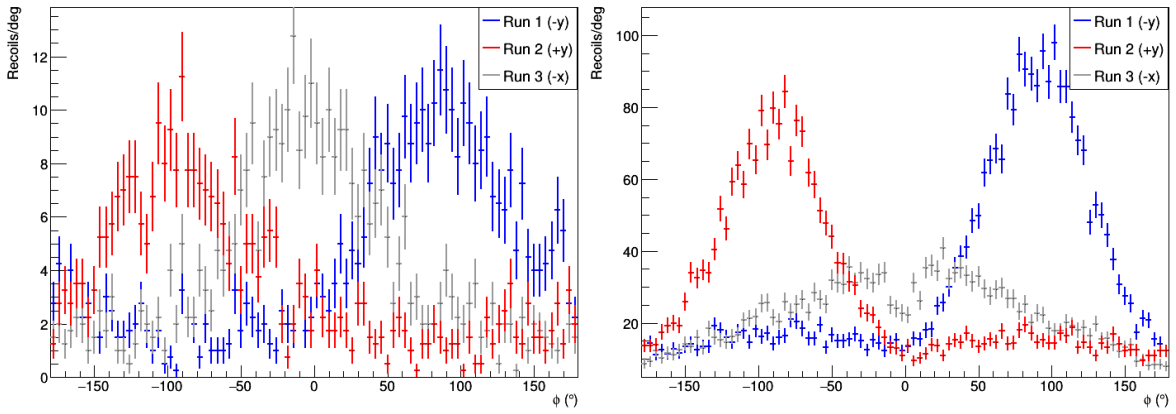

(a) Fluorine and Sulpher recoils (b) All other nuclear recoils

Figure 4.20: The distribution of azimuthal angle, θ, in global coordinates for the initial directions of recoils in ThGEM 0 for each run in 60 Torr SF_6.

The S and F recoils are broadly focused in the opposite of the source direction in each run as might be expected for a fairly columnated source of neutrons. An additional background of about 2 recoils/° is also present which indicates that there is some neutron back scatter contributing to observed recoil flux. The only major difference between the angular spectra for the -y, +y and -x source positions is the angle around which the recoils are focused, the shape remains broadly the same.

The angular distribution for the non-SF recoils has the same general shape as the SF recoils for the -y and +y source position runs, although with higher statistics. The non-SF recoils in -x run on the other hand have a much broader angular distribution with

a suppression in signal at $\theta \sim 0$. This can be attributed to the fact that the majority of non-SF recoils originate from the surface of the ThGEM or cathode and must have angles $\theta \neq 0$ to escape into the gas.

Figure 4.21 gives a more detailed view of the angular distribution of the signal recoils, showing the recoil directions of S and F ions in spherical coordinates for each run. As also seen in Figure 4.20a, the recoils are mostly distributed in the opposite direction to the source, with a small background of back scattered recoils as well. There is no vertical preference for the recoil direction which suggests that the vertical asymmetry of the vessel around the sensitive region is not contributing particularly to flux of scattered neutrons.

Overall the Geant4 simulations of the ThGEM vessel and gas under exposure to ^{252}Cf demonstrate that in addition to the S and F recoils of interest there is also significant flux of other mixed nuclei and electrons. Recoils from the material comprising the ThGEM and cathode comprise a significant portion of the non-SF recoils and likely form a significant part of the observed signal. The produced S and F recoils are distributed across a wide range of energies and corresponding ranges and the initial direction of the recoils well correlates with the source position. In Chapter 5 a model for the diffusion and readout of charge by the ThGEMs will be used to explore the relationship between the simulated data presented here and the experimental data from Chapter 3.

4.5 Conclusions

The main goals of this chapter were to use simulation tools to examine key characteristics of electrons and nuclear recoils and to explore the systematic effects of radiation transport and the limited detector geometry for the studies undertaken in Chapter 3. The simulations undertaken here will be used in Chapter 5 to explore the detector response to the different types of recoils and to arrive at quantitative conclusions about the ER discrimination power and directionality of a 1D ThGEM like readout.

High granularity simulations of electron nuclear recoils in low pressure SF_6 were provided by SRIM and DEGRAD. Using DEGRAD 5.9 keV electrons were found to have radial ranges from 0.5 mm to 7 mm at the pressures explored. Nuclear recoils explored in SRIM were significantly shorter, with radial ranges from 0.1 mm to 1.6 mm at 20 keV. It was also found that the range metrics used were all effectively linear with nuclear recoil energy up to at least 120 keV.

The SRIM and DEGRAD simulations also provided a benchmark for examining the recoil physics of Geant4 which, as was borne out in Section 4.3, is very close to the extreme limits of its physics capabilities in our problem domain. After establishing the Geant4 physics which was best suited to the use case, a model of the detector used in Chapter 3 was constructed to explore the systematics related to the detector geometry. Section 4.4.2 describes how this model was used to simulate the ^{55}Fe runs which were used to calibrate the detector. The main discovered systematic effect was the loss of charge from partially contained recoils which comprised between 12% and 25% of the detected recoils. A review of the energy spectrum of the contained charge showed that this should not adversely contribute to the final calibration results however.

The same setup was used to examine the ^{252}Cf neutron runs and likewise uncovered a number of systematics, particularly the high volume of recoils originating from the surface of the ThGEM and cathode and the angular distribution of the recoils. The S and F recoils comprised only 14% of the ionising energy depositing particles observed in the sensitive region with the majority of the rest of the particles being electron and protons.

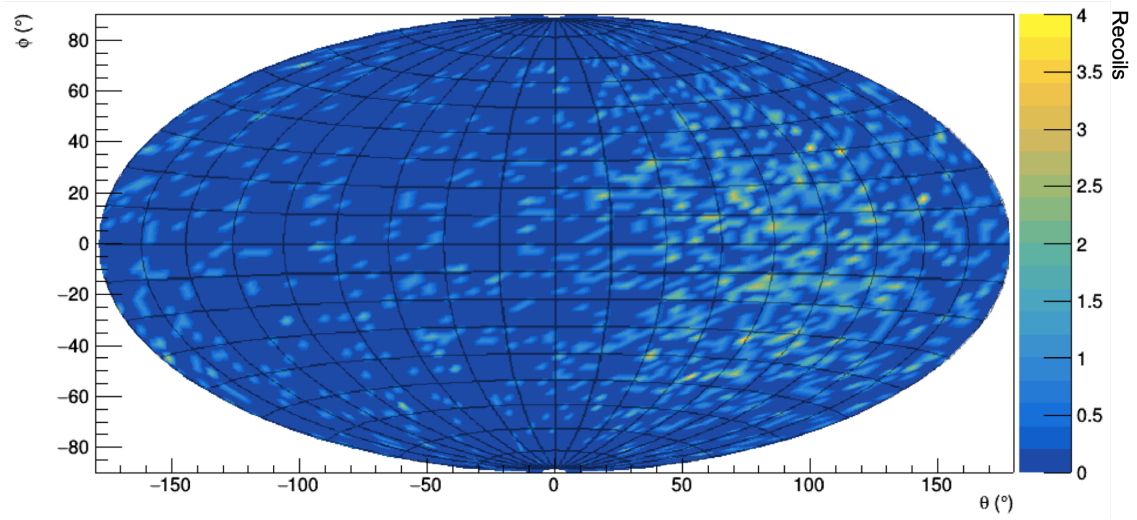

(a) Run 1 (-y)

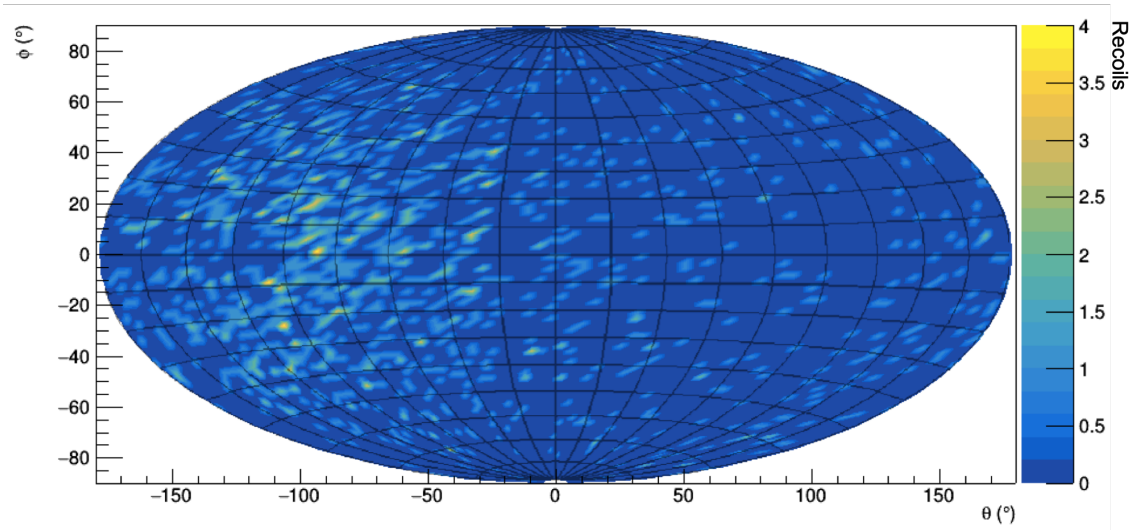

(b) Run 2 (+y)

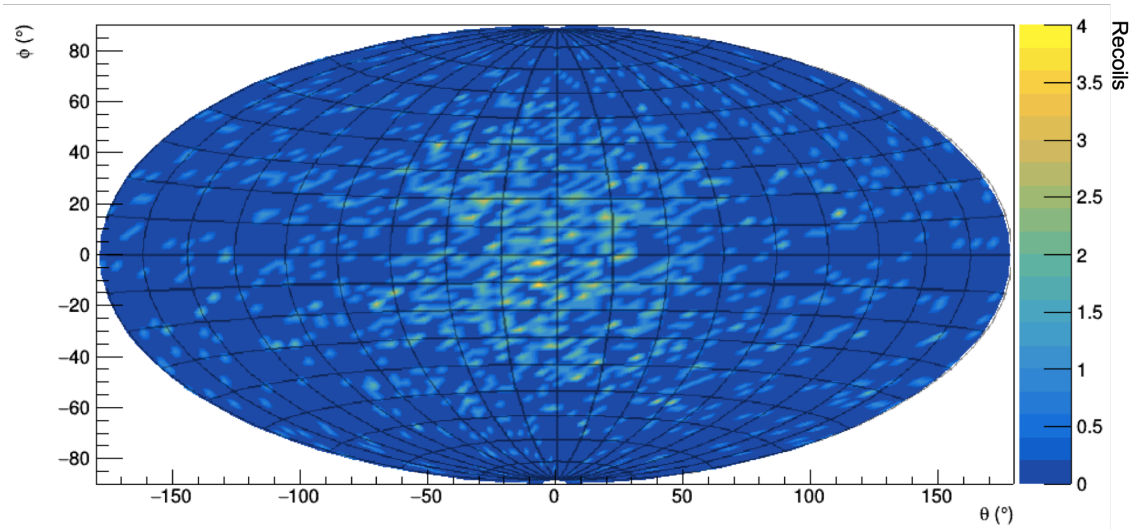

(c) Run 3 (-x)

Figure 4.21: Aitoff projection of the initial directions of Fluorine and Sulpher recoils in ThGEM 1 for each run in 60 Torr SF_6 in global coordinates.

The S and F recoils were shown to be fairly well directed away from the neutron source, with only a fairly small fraction directed toward the source attributed to back scatter.

This chapter focuses exclusively on analysis of the ground truth data from the simulations. Any real detector however will suffer from the limitations of its readout, diffusion in the gas and other detrimental effects on the final signal. The next chapter will use a model of those effects to examine how the generated events in this chapter might look to an actual detector.

Chapter 5

Modelling Detector Response

The simulations described in Chapter 4 produce data about the recoil shapes and the ionising energy deposit of electrons and nuclear recoils in low pressure gas relevant to the detectors that this work focuses on. The simulation output does not however directly translate to detector signal, this Chapter focuses on modelling the response of an idealised detector to the recoils simulated in the last chapter. Obtaining a modelled detector signal enables the analysis of simulation data with the same tools as experimental data, and provides insight into how signal parameters map to features of the recoil. The main objectives of modeling the detector response are to explore the ER-discrimination power available to an idealised 1d planar readout and to determine what directional signals are encoded in nuclear recoil data.

Section 5.1 describes how the output from the various simulation programs is unified into a common format and how the effects of diffusion and signal shaping are modelled to produce a detector equivalent signal. The detector modeling algorithm is applied to DEGRAD and Geant4 ^{55}Fe x-ray simulations in Section 5.2 and compared to experimental data from ThGEMs. Section 5.3 uses the SRIM and DEGRAD recoil data to examine Electron/Fluorine recoil discrimination in SF_6 using the signal parameters extracted from the modelled signal. In Section 5.4 the readout modelling is used to examine the signatures of directionality which are present in the 1d signal from Fluorine recoils in SF_6, with a focus on the SRIM data. The modelled signal from the Geant4 ^{252}Cf run is used in Section 5.5 to examine the electron/recoil rejection and the directional signatures that might be expected from a similar neutron source experiment. Finally the overall conclusions and important observations are discussed in Section 5.6.

5.1 Converting simulation data to detector signal

To convert the simulated charge deposition in the gas to an analogue of detector signal the transport of the charge in the drift field must be modelled. Tools like Garfield can model electron transport in the gas, and can loosely model negative ion transport with the workaround described in Section 6.3. However, the transport of each individual charge in an event takes significantly more computing power than the generation of the recoil event to begin with and furthermore the accuracy of the Garfield workaround is only as good as the available mobility data. Instead a simple model for the gaussian diffusion of the drifting charge is created based on empirical data.

To consistently model a response for all three of the simulation codes used in this work, the output of each code has to take a common format. A C++ module is written

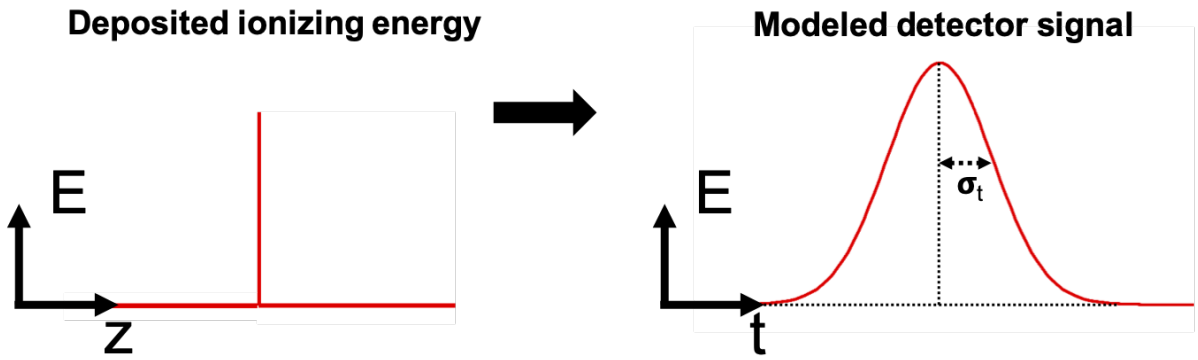

Figure 5.1: Diagram of the conversion of the simulated ionising energy deposit to detector signal.

for this task which takes as arguments the file name and file type of an output file from DEGRAD, SRIM or Geant4 programs and allows the user to access the data in the file event by event with a common interface. Common interface enables access to each event as a set of points with each point consisting of it's coordinates (x,y,z) in millimeters, an ionising energy deposit in KeV (de) and a particle type (ds) stored as an integer according to the PDG particle numbering Scheme [138]. In the case of DEGRAD where the output consists of thermalised electron locations, each electron is treated as an energy deposit equal to the w-value of the gas determined from DEGRAD (36.8 eV for SF_6).

With the data files unified into a single format, the diffusion modelling is then performed. The set of points corresponding to ionising energy deposits are rotated if required then offset along the z axis by a nominal "drift distance". In the Geant4 runs with the detector geometry the recoils are already located within the drift region of the detector model with the output z coordinate giving the offset from the ThGEM plane so no rotation or translation is performed.

To then convert to a detector response the space-energy distributions are projected onto the z axis. The z coordinate of a given timestep is converted to arrival time, t, at an anode on the x-y plane by division by the drift velocity v_d. The diffusion in time is then modelled by convolving the arrival time with a gaussian with width given by

$$\sigma_t = \sqrt{\frac{\sigma_z^2(z)}{v_d^2} + \sigma_{sys}^2}, \tag{5.1}$$

where σ_z is the diffusion determined by an interpolation using the values for reduced mobility reported in [140]. An interpolation to empirical data is used rather than the thermal limit described in Section 2.2.2 due to the divergence from the thermal limit that occurs at high drift fields [121]. An additional systematic width, σ_{sys}, is added to the diffusion width in quadrature, this accounting for the broadening of the signal due mostly to the shaping time. A diagram of the conversion of z-axis projected ionising energy deposit to modeled detector signal is shown in Figure 5.1.

The additional width, σ_{sys}, is determined empirically for the specific readout chain used with the ThGEMs by fitting a gaussian to the signal output from the calibration runs performed in Section 3.4. The calibration signal is generated from 100 mV square test pulses injected into the amplification chain through a 1 pF capacitor. A σ_{sys} of 6.37 µs was determined from the fitted width of the amplification chain output.

The resulting gaussian is normalised to have an area equal to the magnitude of the energy deposit of the point and is added to an array of time bins which represents the detector signal. The number of bins and bin size of the array is based on the sampling window and sampling time of the modelled detector, in the case of the ThGEM rig this means an array with 1 µs binning and 2000 bins. Each event is centered within the array based on the time of arrival of the first point in that event in the file. At the end of each event the array is output to a text file in the same format as the LabVeiw DAQ allowing analysis to be undertaken with the same tools as the ThGEM data. Consequently the following analysis will use the same signal parameters as described in Chapter 3. A notable difference is that the vertical scale in the case of the simulated signal has units of keV/bin as opposed to the shaper output in V of the experimental data.

5.2 Comparison of readout modeled ^{55}Fe electrons with experiment

The ^{55}Fe x-ray source is an important isotope for the gain calibration of low energy threshold gas detectors. The characteristic 5.9 keV electrons induced by the ^{55}Fe x-rays were observed using the ThGEMs in Section 3.6. These electron recoils exhibited significant structure on the scale of millimeters, with multiple peaks observed in the detector signal. Due to the known energy and significant discernible structure of these electron recoils, they present an opportunity to validate the simulation and readout modelling against data. It is furthermore useful to confirm that the multi-peaked structure observed in the ^{55}Fe signal in Section 3.6 corresponds to physical structure and not a systematic effect such as ringing.

The 5.9 keV x-ray induced electrons simulated in DEGRAD and Geant4 which are described in Sections 4.4.2 and 4.1 are used as the model for ^{55}Fe. The Geant4 data is split into two runs: one consisting of recoils in a beam at the origin in a simple gas volume and the other using the detector geometry as described in Section 4.4.1, with a 5.9 keV photon source on the vessel perimeter. For the DEGRAD and Geant4 gas only runs the recoils are randomly rotated and offset by 1 cm (the average drift distance in the ThGEM data) before diffusion modelling. Figure 5.2 shows a typical DEGRAD generated 5.9 keV electron recoil in 20 Torr SF_6 and the resulting modelled signal for 1 cm of drift in a 450 V cm^{-1} drift field.

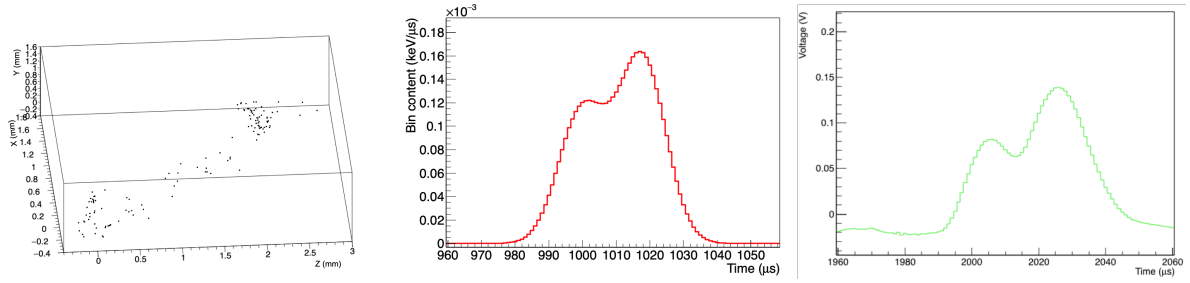

(a) (b) (c)

Figure 5.2: (a) Raw DEGRAD ^{55}Fe recoil in 20 Torr SF_6, (b) the same recoil after modeling diffusion to 1d readout at 450 V cm^{-1} drift and (c) an actual ThGEM event.

The clustering of the charge in the simulated recoil results in two merged peaks resolvable in the readout-modelled recoil with a separation on the order of 20 µs. Events

displaying similar structure to the displayed readout-modelled DEGRAD recoil are also present in the experimental data; the signal from a similar ^{55}Fe event observed on the ThGEM at the same pressure and drift field is shown in Figure 5.2c.

Using interpolated values for the diffusion constant, the thermal diffusion over the length of 1 cm in 20 Torr SF_6 with a 450 V cm^{-1} drift field is equivalent to a time width of 1.06 µs. As such broadening of the signal is dominated by the 6.37 µs width from the pulse shaping amplifier for the short drift distances in our experiments. For an electron track with a length of 1 mm the total collection time without diffusion in this electric field will be 14 µs so a significant amount of structure is preserved, as can be seen in the figure.

The readout modelled DEGRAD and Geant4 data and the ThGEM data from Chapter 3 are analysed using the analysis tools described in Section 3.3. The threshold for integration and width determination is set at 1/5 of the maximum signal amplitude for each event to make the results for the very different vertical scales of the experimental and simulated data comparable. The ThGEM data contains a number of noise events and recoils which aren't part of the 5.9 keV peak, as such a set of cuts is imposed to constrain the recoils to only signal like events which are contained in the identified 5.9 keV peak. The cuts constrain the time bin that the maximum voltage is reached in each event to a window from 1995 µs to 2500 µs to select only events consistent with the DAQ triggering on a signal like peak. Additionally, events where the minimum (pedestal subtracted) voltage was less than −0.02 V and events which saturated the digitiser (had peak voltage of 1 V) were rejected. Finally to select only events contained in the 5.9 keV peak the integral peak voltage, `q_peak`, was constrained to the window 2.5 V.µs to 6 V.µs.

The parameter `t_width` gives a measure of the width of the highest peak in units of sampling time (1 µs here), defined by number of contiguous samples which are over a given threshold. The distribution of the `t_width` parameter for each of the data sets is shown in Figure 5.3a, the simulation data histograms are normalised to 525 events to compare to the ThGEM data.

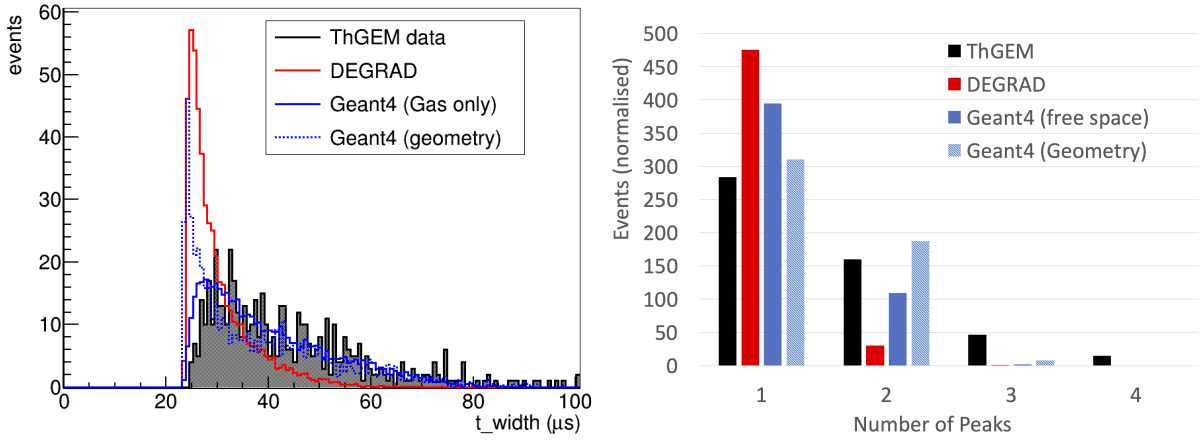

(a) The *t_width* parameter.

(b) The *n_peaks* parameter.

Figure 5.3: Signal shape paramters for ^{55}Fe induced electron recoils in 20 Torr SF_6 for DEGRAD, Geant4 and ThGEM data.

Both of the Geant4 runs give higher values for `t_width` than DEGRAD, matching more closely with the ThGEM data. Both the Geant4 with geometry and DEGRAD runs have `t_width` peaking around 25 µs, consistent with the majority of the signal width being due to added width from the readout modelling. The lower bound on the peak width due

to the readout is also evident in the ThGEM data, although there is less of a sharp peak at 25 µs than in the DEGRAD or Geant4 gas only runs. The difference between the results for the Geant4 run with the detector model and without it is mostly due to the orientation of the electron tracks; the modelled x-ray source in the detector geometry produces tracks oriented more parallel to the readout plane than the randomly oriented electrons in the gas only run. This might suggest that even though the randomly orientated gas-only data matches quite well with the ThGEM data, there is possibly another systematic in the modelled signal width which the random orientation is canceling out.

The multiple peaks observed in some events the ^{55}Fe data from the ThGEMs in Chapter 3 are also apparent in the simulation data after the diffusion modelling. An example of this type of multi-peaked event is shown in Figure 5.2. the observation of the multi-peaks in the simulation data confirms that the observed multi-peaks are most likely not due to any effect of the readout electronics but are an aspect of the structure of the recoils in the gas. The parameter `n_peaks` counts the number of distinct peaks which are above the event's integration threshold. Figure 5.3b shows the number of one, two, three and four peak events which are counted for each run, with the simulation data again normalised to 525 events.

The ThGEM run tends to have the more visible peaks than the simulated data, with the only observed quadruple-peak events and by far the most triple-peak events. All of the simulated runs however do exhibit events with as many as three peaks, the Geant4 (geometry) run having the most skew toward more peaks and being the most similar overall to the ThGEM runs by this metric. DEGRAD tends to show the fewest distinct peaks by this metric with the majority of events only having a single identified peak.

Metrics based on the signal height are not directly comparable to the ThGEM data due to the different vertical scales of the simulated and ThGEM data. Although a significant result from examining the modelled signal parameters is confirmation that `v_max` provides a very poor measure of the event energy due to the large width of the signal peak.

Overall there are some significant differences between the ThGEM and simulated data. The signal width introduced by the readout seems approximately correct, given the nearly coincident low edge of the respective `t_width` distributions. The experimentally observed distribution in `t_width` is consistent with a longer time of the charge collection, this might be attributed to more charge diffusion during drift, longer recoils or slower drift. If there were more charge diffusion than modelled however it would be expected to result in fewer visible peaks in the ThGEM waveforms relative to the simulated data. Conversely longer recoil ranges or slower drift speeds are consistent with more visible structure and therefore more peaks which is what is actually seen in the ThGEM data relative to the simulated data. Reducing the drift speed by a factor of 1.5 is found to bring the simulated data much more into agreement with the ThGEM data. This is equivalent to a reduced mobility of $38\,\mathrm{mm^2V^{-1}s^{-1}}$ rather than the literature $57\,\mathrm{mm^2V^{-1}s^{-1}}$ which was used. Notably the independent measurements of the drift speed of the primary charge carrier in the same vessel in sections 3.7.2 and 6.5.2 arrived at reduced mobilities of $35\,\mathrm{mm^2/V/s}$ and $(33.6 \pm 0.5)\,\mathrm{mm^2/V/s}$ respectively. These measurements are both much more consistent with a drift speed that well fits the simulation data.

The most significant outcome is the confirmation that the structure that is seen in the ThGEM ^{55}Fe data is consistent with electron recoils. The relative contribution of the shaping time to the event width is also of relevance to the design of future experiments and the analysis of electron recoil data.

5.3 ER discrimination using SRIM and DEGRAD

The ability of a detector to distinguish between electrons and nuclear recoils (its ER discrimination) is important for both neutron and dark matter detection applications. The main goals of this section are to use the simulation data to determine which signal shape parameters can be expected to be relevant for ER discrimination and to determine how good the discrimination of a 1d detector might be expected to be.

All of the electron and fluorine recoils in 20 Torr SF_6 generated by DEGRAD and SRIM data are used as the basic data set, with the recoils in each case randomly rotated and with 1 cm of drift in a 300 V cm^{-1} drift field. The DEGRAD data set contains 3×10^6 electron recoils at energies between 2 keV and 200 keV and the SRIM dataset contains 3×10^5 recoils with the same energy and binning. The parameters for the resulting modelled waveforms are extracted using the experimental analysis described in Section 3.3.

Examining the signal parameters for all of the recoils together, there are significant differences between the regions of the parameter space filled by the electron and fluorine recoils. The parameters which show the most significant separation between the electron and ^{19}F populations are the maximum value reached in the signal waveform, `v_max`, the time that the signal is above the integration threshold, `t_width`, and the ratio `q_peak/q_tot`, which is the fraction of the total deposited charge, `q_tot` which is contained in the identified signal peak, `q_peak`. Scatter plots for `v_max` against `t_width` and `v_max` against `q_peak/q_tot`, the two projections which show the best separation, are shown in Figure 5.4. Note that the stripes visible in the SRIM data are a consequence of the energy binning and are not indicative of any physical effect.

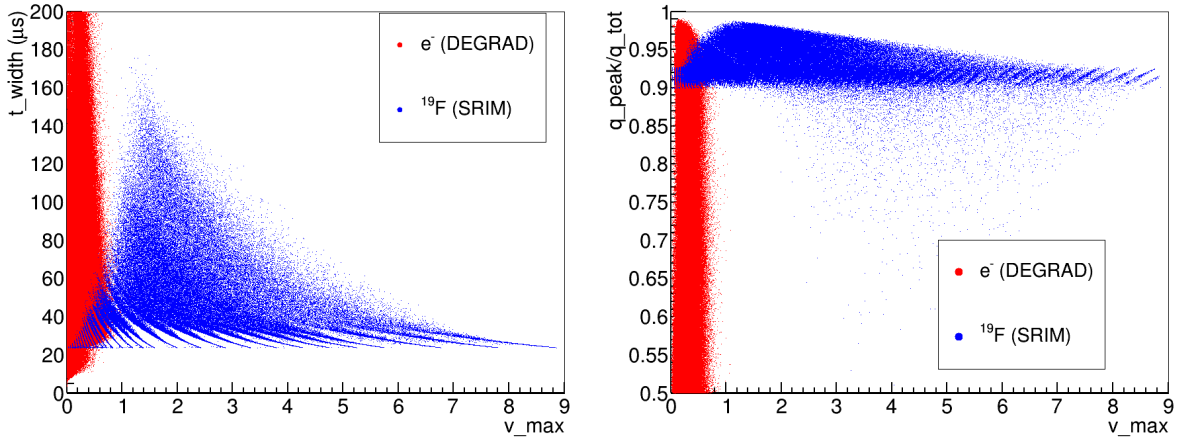

(a) `v_max:t_width` (b) `v_max:q_peak/q_tot`

Figure 5.4: Parameter scatter plots for electron and Fluorine recoils from DEGRAD and SRIM respectively in 20 Torr SF_6 with a 30 V cm^{-1} drift field

The parameter which give the strongest discrimination on its own for the detector model in this case is `v_max`, with all electron recoils having a `v_max` of less than 1.15. This means that high energy Fluorine recoils can be trivially discriminated from all electron recoils with a simple cut of `v_max`$>$ 1.15. The reason for this is the lower rate of energy deposition, $\frac{DE}{dx}$, of the electron recoils. The low rate of energy deposition also accounts for the generally higher `t_width` due to the longer range of electrons. The tendency of the electron recoils to create charge clusters on the other hand is responsible for the separation in `q_peak/q_tot`.

Parameter	Minimum	Maximum
q_peak/q_tot	0.9	$0.92 + 0.03 \times$ v_max
t_width	23.9	$23.4 + 24 \times$ v_max
roi_1/roi_2	$1 - 0.14 \times$ v_max	$1 + 0.14 \times$ v_max
rise_s	33	$35 + 14 \times$ v_max

Table 5.1: Electron veto cuts for simulated recoils in 20 Torr SF_6, minimal cuts in red.

With electron recoils, particularly at higher energy, the clusters are often separated enough that the signal falls below the threshold in between them, meaning a lot of the event charge isn't contained in the largest peak.

Examining how these differences translate into ER discrimination power, we quantify the discrimination power with the electron rejection factor, R, which we define as

$$R = \frac{N_{all}}{N_{surv}} \tag{5.2}$$

where N_{all} is the total number of background electron recoils and N_{surv} is the number of those recoils which survive an electron vetoing algorithm.

A simple electron veto can be defined by accepting events with v_max $> v_{50}$ where v_{50} is the value at which the 50% of nuclear recoils in a given energy bin are rejected by the veto. A set of cuts are defined on the other parameters which further reduce the number of electron recoils, these cuts are shown in Table 5.1. These cuts are arrived at manually to trim sections of the parameter space which contain primarily electrons. A subset of these cuts consisting of only the cuts on q_peak/q_tot and t_width is designated the 'minimal' set of cuts, indicated in red in the table. Cuts on q_peak and q_tot on their own are avoided as they are close to proportional to the deposited energy and are therefore sensitive to energy binning of the electron and fluorine recoils. The cuts are not applied to events with v_max$>$ 1.15 as no electron recoils at all pass that threshold.

Figure 5.5 shows the electron rejection factor of the simple electron veto with no, minimal and all cuts determined for each initial energy in the fluorine runs against all of the 3×10^6 DEGRAD electron recoils. Not shown on the graph are points where the electron rejection factor exceeds 3×10^6 (i.e. when all simulated electron recoils are rejected).

When discriminating on v_max alone the electron rejection factor increases exponentially with energy above 12 keV, below this the discrimination factor approaches unity (i.e. no electron rejection). The flattening of the slope at this point is a result of the parameter v_max becoming low enough that none of the electron recoils in the sample are rejected. The addition of the minimal cuts increases electron rejection by a factor of about 12 and the rest of the cuts provide a further improvement on the order of around 12 again. For nuclear recoils with energy 45 keV or above all electron recoils can be rejected based on v_max alone. For the minimal and full set of cuts the first Fluorine energy bins for which all electrons are rejected are 40 keV and 35 keV respectively. The best electron rejection factor achieved with these signal parameter at 2 keV is about 700.

The most comparable result might be from [83] which plots the simulated discrimination between Fluorine and electron recoils in 755:5 Torr He:SF_6 and displays a similar exponential increase off in the rejection factor with increasing energy. Overall however the discrimination determined in that case was better at higher energies and worse at lower energies; an electron rejection factor in excess of 1×10^6 was obtained at 10 keV and at

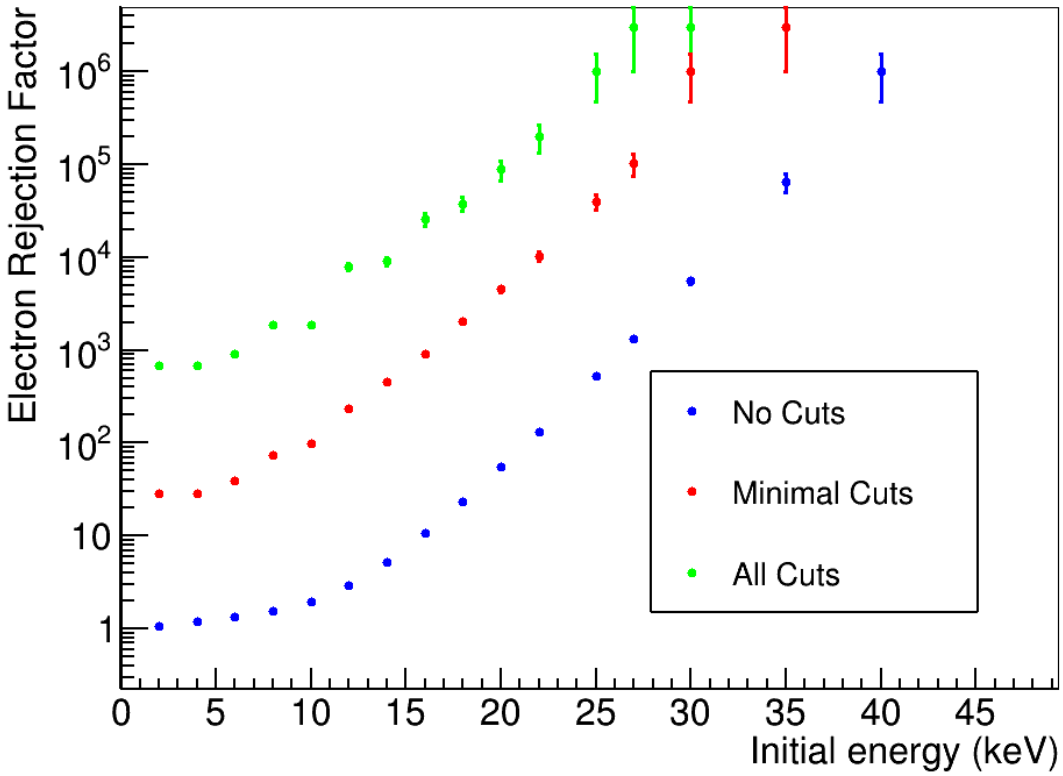

Figure 5.5: Simulated electron rejection factor for the acceptance of 50% of Fluorine recoils in an energy bin against all electron recoils in 20 Torr SF_6 with a 300 V cm^{-1} drift field.

2 keV the rejection factor was only 200. This can be partially attributed to the different methodology and gas pressure, discrimination result obtained in that case assumed reconstruction of the diffused charge in 3d, perfect knowledge of the deposited ionising energy and only discriminated based off a single parameter corresponding to the track length. In our case, the projection of the charge onto a 1d readout and then the use of multiple parameters results in better low energy discrimination and worse high energy discrimination.

Better discrimination might be achieved with our data with direct access to the `q_peak` and `q_tot` parameters which were neglected in this case as to not exploit the energy binning of the underlying recoils. A set of simulations with binning based on deposited rather than initial energy might be able to include these parameters in a veto without worrying about said binning.

Overall, the readout modelling has helped show the significance that might be expected of the `v_max`, `t_width`, `q_peak/q_tot`,`roi_1/roi_2` and `rise_s` parameters for discriminating electron and nuclear recoils. In addition the relationships between the parameters and how electron and nuclear recoils map to parameter space are things that could only have been discovered the readout modelling and are useful to inform the analysis of detector data where both electrons and nuclear recoils are present.

5.4 Signatures of directionality in Fluorine recoils

The signatures of directionality which might be obtained from the recoils of nuclei in gas is of particular interest in this work. This section will focus on the signatures of directionality that are present in the modelled signal for the simulated ^{19}F recoils, as such the two parameters which are scrutinised are the `t_width` and asymmetry parameters.

The parameter `t_width` provides a measurement of the width of the identified signal peak as described in the last section and is expected to give the strongest discrimination between recoils traveling horizontally (laterally) and recoils traveling vertically (up/down) relative to the readout plane. The asymmetry parameter, which is described in Chapter 3 and is used to discriminate between up- and down-going recoils, is defined by the fraction `roi_1/roi_2` where `roi_1` and `roi_2` are values equal to the integral of the signal over the first and second half of the time that the signal is over threshold. The asymmetry parameter increases when more ionising energy is deposited in the portion of the recoil which is closest to the readout plane. An asymmetry parameter of exactly 1 means the portion of the waveform which is over threshold is perfectly symmetric in time. The ability to identify the directional sense of the track is referred to as head-tail discrimination and as discussed in Section 2.3, is a powerful directional signal.

The readout modelling is performed on simulated recoils in SRIM offset by 1 cm from the readout plane and rotated into three different orientations. The three recoil orientations are +z (away from the readout plane), -z (towards the readout plane) and +x (parallel to the readout plane), these orientations are referred to as the 'up', 'down' and 'lateral' runs respectively.

Figure 5.6 shows the distributions of `t_width` and the asymmetry parameter for directed 20 keV Fluorine ions in 20 Torr SF_6 with a readout modelled with a 300 V cm^{-1} drift field. The distribution for down going recoils is excluded for clarity from the `t_width` plot as is the distribution for lateral recoils from the asymmetry plot.

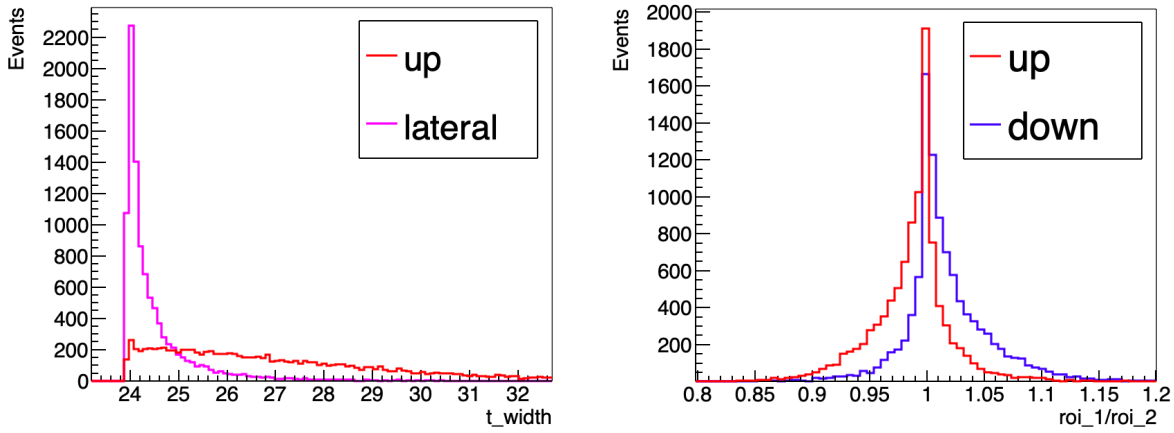

(a) Distribution of the `t_width` parameter. (b) Distribution of `roi_1/roi_2`.

Figure 5.6: Width and asymmetry distributions for directed 20 keV Fluorine ions in 20 Torr SF_6 from SRIM with readout modeling using a 300 V cm^{-1} drift field.

As with electron recoils, a lower bound on the distributions of `t_width` in Figure 5.6a is imposed by the signal width added by the modelled readout chain and drift. The vertical recoils (down-going recoils have the same `t_width` distribution as up-going recoils) share the same lower bound on the time width as lateral recoils but extend to significantly higher

widths, consistent with the contribution of the vertical track. The up-going and lateral recoils have significantly different form and average values for the `t_width` parameter, suggesting that discrimination between up-going and lateral recoils is possible at 20 keV.

The distribution of the asymmetry parameter shown in Figure 5.6b peaks a 1 for both up and down going recoils. Down-going recoils skew toward higher values of the asymmetry parameter and up-going recoils skew towards lower values which implies that most of the ionising energy of the recoil is deposited at the end of the track. One again the differences between the two distributions implies that discrimination between up and down going recoils is possible.

The fraction of recoils which can be correctly assigned to their orientation based on a cut on the `t_width` or asymmetry parameters is used to quantify the vertical/horizontal and up/down discrimination power respectively. The discrimination cut was equal to the mean of the parameter for all the events in the up/lateral or up/down data sets in a given energy bin. The sample of vertical recoils for vertical/horizontal discrimination includes only up-going recoils as the `t_width` distribution for up and down going recoils are identical. For vertical/horizontal assignment all events which had larger than the mean `t_width` were assigned as vertical recoils and all events with less were assigned as horizontal recoils. For up/down assignment all events which had larger than average asymmetry parameter were assigned as down-going and all other events were assigned up-going. Figure 5.7 shows how the fraction of correctly assigned vertical/horizontal and up/down recoils varies with energy using this method. Note that a completely random assignment would achieve a correct assignment half the time so a correct assignment fraction of 0.5 implies no sensitivity.

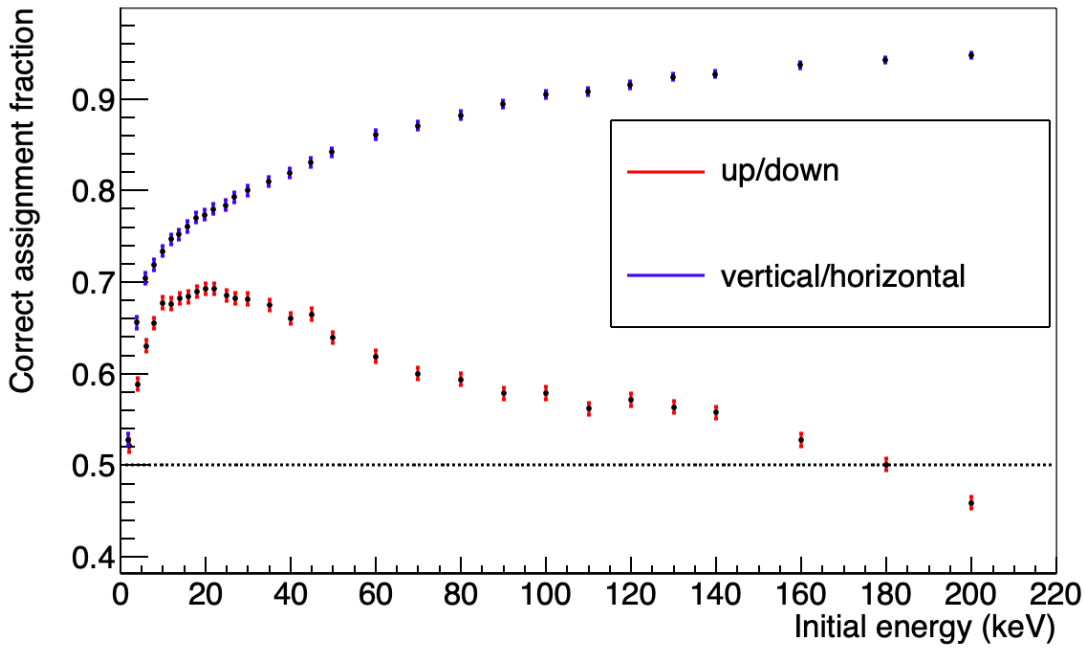

Figure 5.7: Fraction of SRIM Fluorine recoils in 20 Torr SF_6 correctly assigned as up/down and vertical/horizontal using the 1d detector parameters for asymmetry and recoil width respectively.

The vertical/horizontal assignment improves with increasing energy, asymptotically approaching one at high energy. This is a consequence of the distributions of the `t_width`

parameter for each direction becoming more distinct. The lowest rate of correct assignment, for 2 keV recoils, was $52.7 \pm 0.7\%$ while the at 200 keV recoils were correctly $94.7 \pm 0.3\%$ of the time. This is consistent with the increasing difference between the horizontally and vertically projected ranges of the SRIM recoils described in Section 4.2. The ability to discriminate between vertical and horizontal recoils shows that the ThGEM readout should be capable of the 2D axial directionality described in Section 2.3. A shorter shaping time might lower the minimum bound on `t_width` and assist with vertical/horizontal discrimination at low energy, although likely at a cost of energy resolution and signal/noise.

For discrimination between up- and down-going recoils (head/tail discrimination), the average asymmetry parameter which defines the difference between up and down going recoils is close to 1. The up/down assignment improves with increasing energy up to a correct assignment rate of $69.3 \pm 0.6\%$ at 22 keV when the trend reverses and the fraction of correctly assigned recoils gets worse. At 180 keV assigning up/down direction based on the asymmetry parameter is as good as random and at 200 keV correct assignment is achieved $45.9 \pm 0.7\%$ of the time, which is worse than random. These results imply that below 180 keV, most of the ionising energy of a recoil in the gas is deposited at the end of the track whereas above 180 keV this trend reverses and more ionising energy is deposited in the first half of the track.

A significant factor in the contributing to this effect is the ionisation quenching factor; while most of the energy loss of the particle occurs at the end of the track, this is offset by the reduction in the fraction of the energy deposited as ionising energy at the end. Figure 5.8a shows a 200 keV Fluorine recoil in 20 Torr SF_6 simulated with SRIM and corrosponding signal after detector modelling with and without quenching is shown in Figure 5.6b.

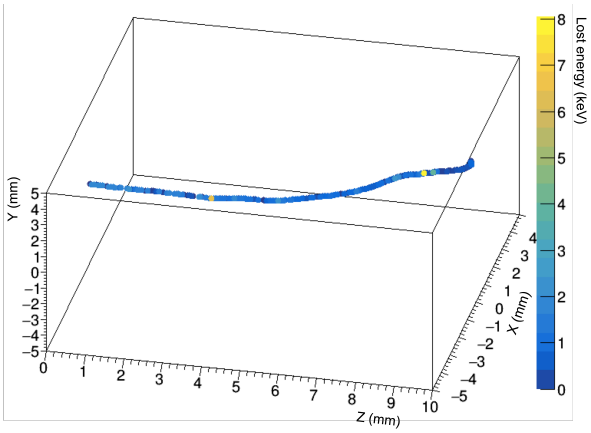

(a) Raw recoil in 3D.

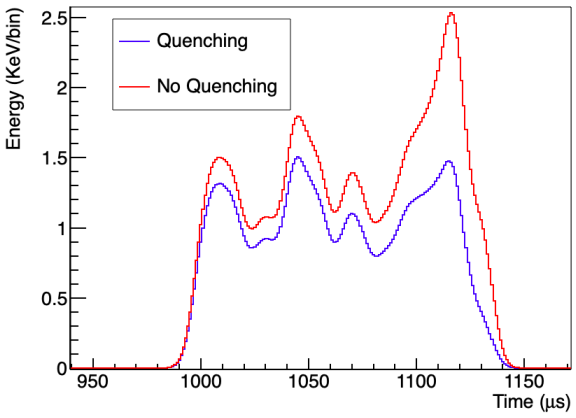

(b) Recoil after detector modelling with 300 V cm^{-1} drift field and 20 mm drift distance, with and without quenching.

Figure 5.8: Simulated recoil and modelled detector signal for Event 5 of the 200 keV ^{19}F SRIM run in 20 Torr SF_6, initial direction +Z.

If quenching is neglected there is a much more pronounced peak on the right hand side of the signal waveform in the figure, corresponding to the end of the track in this projection. When quenching is included the distribution becomes much more symmetric as less of the energy loss at the end of the track is ionising. A significant source of uncertainty in the determination of the level of head/tail discrimination which it might be possible for

a detector to achieve comes from the uncertainty in the ionisation quenching factor in SF_6. It has been shown in previous studies of novel gasses that the analytical and simulated IQF of novel gasses can deviate from the experimentally determined IQF by as much as 20% [131]. A variation of this magnitude in the IQF of SF_6 would significantly change the observed asymmetries and consequently the accuracy of the above results should be considered contingent on a measurement of the IQF of SF_6 which well matches the SRIM predictions.

Overall the results imply that vertical/horizontal discrimination between recoils should be possible with a 1d readout for KeV Fluorine recoils in SF_6. With increasing energy the discrimination improves up to $94.7 \pm 0.3\%$, showing the ability to reject a isotropic background with only a handful of events. A head/tail discrimination is also apparently possible with a maximum correct up/down assignment fraction of about 70%, although this result is significantly more conditional on the ionisation quenching being close to expectation. The combination of the ability of the readout to achieve vertical/horizontal and head/tail discrimination implies the ability to attain 2d vector directionality.

5.5 Signal from ^{252}Cf neutrons in Geant4

The Geant4 simulation of the ThGEM vessel with a ^{252}Cf neutron source described in Section 4.4 was a mock up of the experiment performed in Chapter 3. As discussed previously, the physics of Geant4 are not as comprehensive as SRIM or DEGRAD but the ability to create complex geometries and to transport a variety of particles enables a better exploration of some of the systematics of an experiment. Rather than examine isolated electron or Fluorine recoils, the Geant4 simulation of ^{252}Cf exposure of the ThGEM vessel explores all of the ionising interactions caused by neutrons in the detector volume. Using the simulated data in conjunction with the readout modeling to examine the signal that might be expected from this experiment is hoped to help resolve some of the features in the experimental data. Of particular interest is disentangling the contributions to the experimental neutron data from the different particles observed in Section 5.5 The exploration of the Geant4 data is also hoped to give a qualitative idea of what might be expected in the data from similar neutron experiments.

The readout modelling was applied to the data from the simulation runs described in Section 4.4 with a drift field of $450\,\mathrm{V\,cm^{-1}}$ to match that used in the experiment. No rotation or offset of the recoil data was required as the coordinates of the Geant4 output are such that the ThGEM is located on the x-y plane.

5.5.1 ER discrimination

In Section 5.3 the `v_max` against `t_width` and `v_max` against `q_peak/q_tot` scatter plots gave good separation for electron and Fluorine recoils. The equivalent two scatter plots for the signal in ThGEM 1 from secondary recoils due to ^{252}Cf neutrons is shown in Figure 5.9.

The portions of the parameter space filled by electrons and Fluorine recoils is very similar to that which was filled in the DEGRAD and SRIM runs for recoils at 20 Torr with $30\,\mathrm{V\,cm^{-1}}$ drift field in Figure 5.4. Electrons are confined to the low `v_max` region as a result of the generally lower charge density of electron tracks. The trend for nuclear recoils to have a high `q_peak/q_tot` as a consequence of their tendency not to form charge clusters and the triangle shape in `v_max-t_width` space seem to be consistent despite the

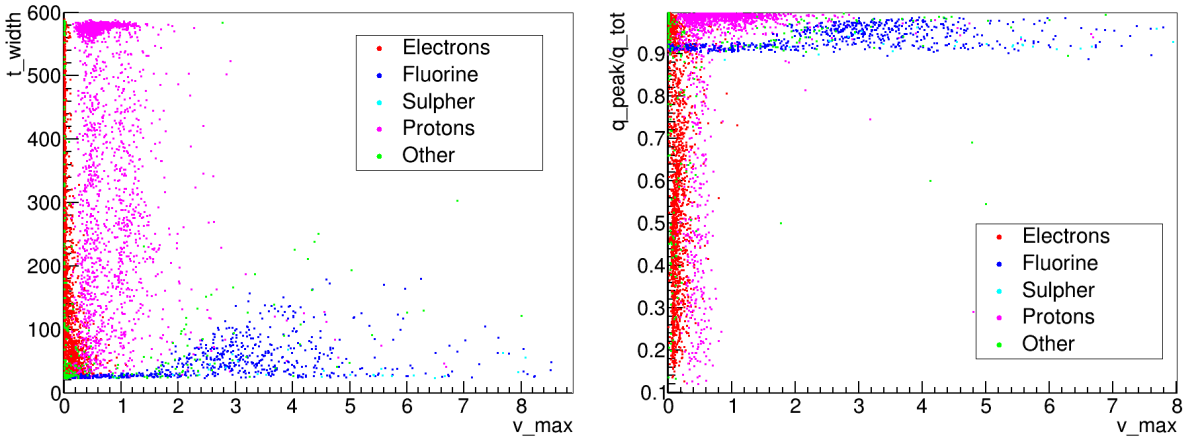

(a) `v_max:t_width`. (b) `v_max:q_peak/q_tot`.

Figure 5.9: Parameter scatter plots for signal in ThGEM 1 in the ^{252}Cf Geant4 run 1 in 60 Torr SF6 with 450 V cm^{-1} drift.

Parameter	Minimum	Maximum
`q_peak/q_tot`	0.9	0.93
`t_width`	23	28 + 4×`v_max`
`roi_1/roi_2`	1 − 0.14×`v_max`	1 + 0.14×`v_max`
`rise_s`	33	39 + 13×`v_max`

Table 5.2: Electron veto cuts for Geant4 simulated recoils in 20 Torr SF_6, minimal cuts in red.

different pressure, drift field, recoil energy spectrum and simulation code. Also occupying approximately the same portion of parameter space to the Fluorine recoils are Sulpher recoils, which are of course the other target atom for neutrons in the SF_6 gas.

As discussed in Section 5.5, there is also large proton recoil background from the surface of the ThGEM in addition to the electron background. This proton recoil background has generally higher `v_max` than the electron background which means that discrimination based on that parameter will be much poorer for protons. There is a clear upper limit on the `t_width` parameter at around 590 µs visible in the proton data, this corresponds to the negative ion drift time across the 2 cm drift gap. These events can be attributed to protons which cross the full width of the drift gap. A similar effect was observed in the experimental neutron data in Section 5.5 with events clustered around a maximum width. The points labeled 'other' on this plot consist of positrons and a mix of light nuclei produced by neutron induced reactions in the gas, as such they are located all over the parameter space in the scatter plots.

A modified version of the ER discrimination algorithm described in Section 5.3 is used to find the electron and proton rejection factor against Fluorine and Sulpher recoils. Unlike in Section 5.3 there is no energy binning of the initial recoils so the electron rejection cut value, v_{50}, which preserves 50% of the nuclear recoils is determined with the binning based on the parameter `q_tot`. The parameter `q_tot` is a measurement of the deposited ionising energy and will be lower than the initial recoil energy by the ionising quenching factor as well as any losses off the edge of the readout. The cuts presented in Table 5.1 are modified for the Geant4 data, the modified cuts are shown in Table 5.2.

The differences between the SRIM/DEGRAD cuts and the Geant4 cuts are both limits

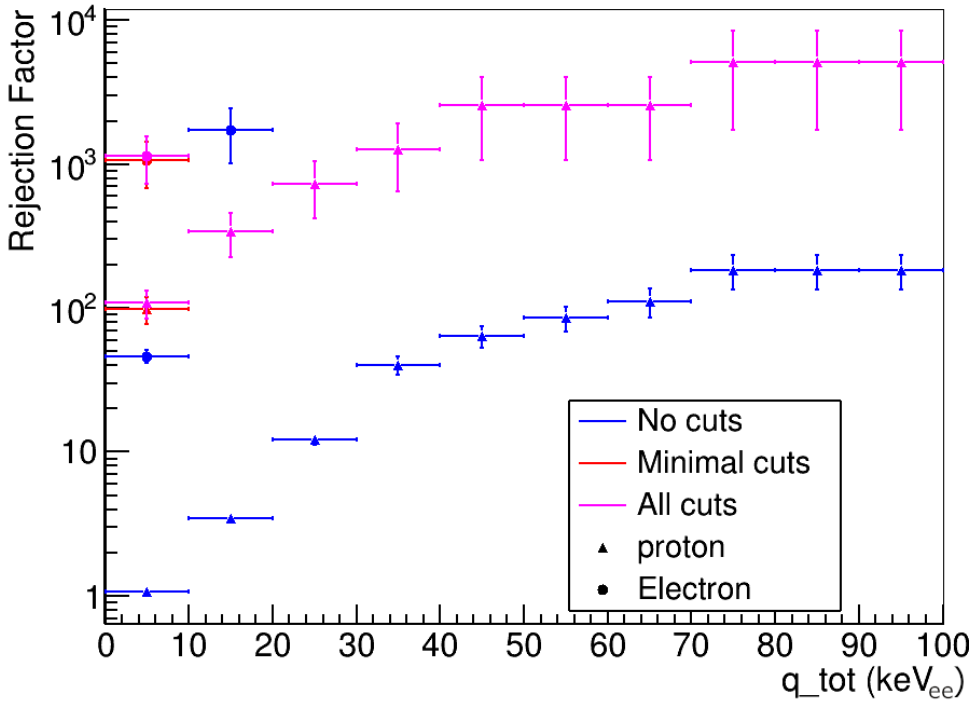

Figure 5.10: Simulated electron and proton rejection factors against S and F recoils in 20 Torr SF_6 for the Geant4 ^{252}Cf runs. The line colour indicates the applied cuts and the marker shape indicates electron or proton discrimination.

on `t_width`, the maximum of `q_peak/q_tot` and the maximum `rise_s`. These are to do with differences in the locations of the electron and recoil distributions in parameter space. Fluorine and Sulpher recoils are grouped together in this analysis due to their fairly similar signal parameters and to maximise statistics. The dataset used in this case consists of the recoils from ThGEM 1 in run 1 and from ThGEM 2 in run 2, (i.e. both up-going recoil runs).

Figure 5.10 shows the resulting electron rejection factor as well as the rejection factor of the same cuts for protons. The binning is much more coarse than in the SRIM and DEGRAD electron rejection data and the maximum electron rejection factor which can be determined for this data is ∼7000 due to the lower statistics.

When discriminating for S and F recoils the most difficult particles to reject are the protons. Discrimination against protons only on the `v_max` parameter obtains a rejection factor of 1 (no rejection) in the 0 keVee to 10 keVee energy bin. The proton rejection factor then increases with increasing energy up to 70 keVee and a rejection factor of about 100 which remains constant up to 100 keVee. The proton discrimination is worse compared to electrons mainly due to the higher $\frac{dE}{dx}$ of protons, which in turn makes `v_max` a significantly worse linear discriminant and contributes to the flattening of the discrimination rate at high energy. The addition of minimal cuts increases the rejection factor by about 100 compared to discriminating on `v_max` alone. The rejection factor for minimal cuts is coincident with that for full cuts over most of the energy range for protons which is why most of the minimal cut points are not visible in the figure. The lack of improvement when the full cuts are applied suggests that the asymmetry and `rise_s` parameters are not contributing significantly to the proton discrimination.

The electron rejection factor was higher than the proton rejection factor across the

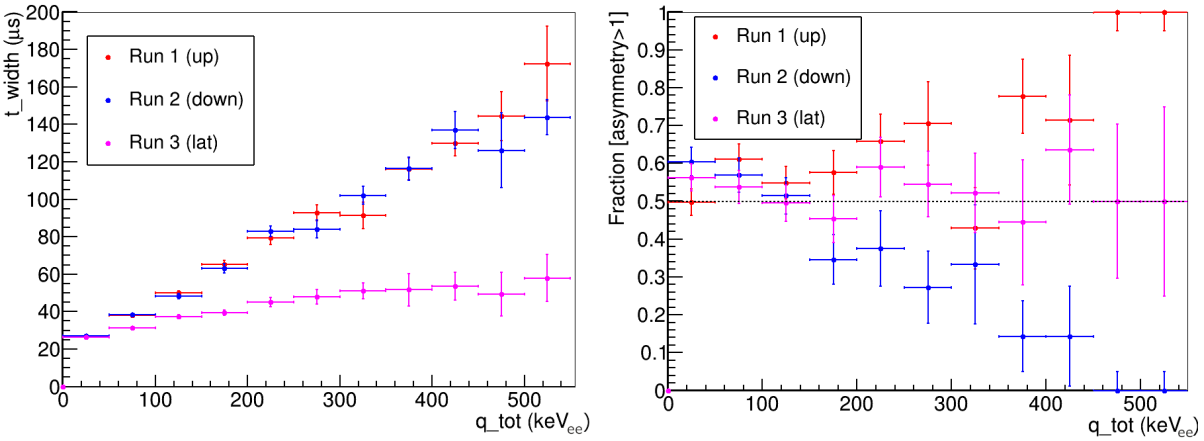

(a) Variation of average `t_width` with `q_tot`.

(b) Variation of the fraction of recoils with `roi_1/roi_2`> 1 with `q_tot`.

Figure 5.11: Direction sensitive parameters in ThGEM 1 for S and F recoils in 60 Torr SF_6 for the ^{252}Cf simulation runs in Geant4.

energy range. Discrimination only on the `v_max` parameter (no additional cuts) is sufficient to reject all electrons for recoils with deposited energy greater than 20 keVee. The addition of minimal cuts increases the electron rejection by a factor of 20 and the full cuts only produced a marginal improvement over this. With only two points of finite electron rejection it is hard to say anything definitive about the trend, the data is however consistent with the exponential relationship between the electron rejection factor and energy. These results are consistent with the DEGRAD-SRIM results when taking into account the difference between the energy binning and the handling of quenching.

Overall it is shown that it is possible to discriminate between electrons and SF-recoils and between protons and SF-recoils. The poorer discrimination between protons and SF recoils indicates that protons might form a background in the neutron runs that is more difficult to reduce in analysis than the electron background. The proton background also obfuscates the separation between the the electron and SF-recoil populations.

5.5.2 Directional signals in ^{252}Cf data

Another aspect of the modelled signal which is of interest is the presence of signatures of the direction of the neutron induced recoils. As in Section 5.4 the parameter `t_width` and the asymmetry parameter, `roi_1/roi2`, are used to quantify the detector ability to discriminate between up, down and lateral going recoils. The expected recoil directions for runs 1, 2 and 3 are up, down, and lateral relative to the ThGEM, although the recoils are not columned but instead form a distribution around the expected direction; the distribution of recoil directions in each run were discussed in Chapter 4. Figure 5.11a shows the variation of the `t_width` parameter with `q_tot` for the S and F recoils for the different ^{252}Cf runs.

The average `t_width` for recoils `q_tot`< 50 keVee is not significantly affected by the expected recoil direction. In the interval 50 keVee to 100 keVee differences in the average `t_width` become apparent and the difference increases with increasing energy. The fairly broad angular distributions of recoils likely contributes to the fairly high energy threshold required to discriminate between the horizontal and vertically directed runs.

The fraction of recoils in each run which have an asymmetry larger than 1 is shown in Figure 5.11b. At the lowest energy the down-going recoils have more of a tendency to have a more positive asymmetry than the up-going recoils. This trend reverses at in the 50 keVee to 100 keVee bin and for this and higher energies up directed recoils tend to have the more positive asymmetry. The overall trend is similar to that observed in SRIM, although in the SRIM data the crossing point was observed at 180 keV, equivalent to about 140 keV after quenching. The discrimination between up and down going recoils gets increasingly good as the recoil energy increases, although the lower statistics of recoils at this energy contributes to fairly large errors.

Overall, the broader angular spectrum of recoils generated by a neutron source contributes to worse discrimination between the source directions than for idealised directed recoils. Explorations of directionality in the ThGEM detector under exposure to ^{252}Cf should begin by focusing on the high energy recoils despite the overall lower statistics as the separation between the populations of up/down and lateral/horizontal recoils are much better.

5.6 Conclusions

Using a model of the diffusion and readout of ionised charge enables a analysis of simulation data using the analytical tools developed for the experimental data. Comparison between the simulated and experimental ^{55}Fe data showed that many of the features of signal waveforms observed experimentally could be recreated including the event widths and multi-peak events. The simulation data confirmed that the multiple peaks that were seen in the ThGEM data were physical and consistent with electron recoils from ^{55}Fe x-rays. The differences that were present between the simulated and experimental ThGEM data suggested a systematically slower drift speed, what this might be attributed to is not known.

The ER-discrimination available to a 1d readout was also explored with the most relevant waveform parameters found to be `v_max`, `t_width` and the ratio `q_peak/q_tot`. An electron rejection factor in excess of 1×10^6 was obtained for cuts which accepted half of fluorine recoils at an energy of 25 keV.

The 1-d parameters most relevant to particle direction were found to be the asymmetry parameter and `t_width` for head/tail and vertical/horizontal discrimination respectively. These two parameters were found to be sufficient to obtain directional information across keV energies for well directed recoils, although a reversal in the correspondence of the asymmetry parameter to direction was found at high energy. The reversal of the asymmetry was not expected or accounted for in the experiment performed in [125] or in Chapter 3, and might contribute to the ambiguous results in those cases. Further experiments examining the head/tail effect should consider the high energy reversal of the asymmetry, although it should be noted that fairly high statistics would likely be needed to confirm this effect.

The use of Geant4 enabled some of the practical systematics related to ^{252}Cf neutron exposures of a detector to be explored. The relationship between the 1-d parameters and the particle type remained consistent but the various other types of particle, particularly protons created by neutron interactions was demonstrated to make the separation of electron and nuclear recoils significantly more difficult in practice. Additionally the angular spread of the recoils resulted in a significant increase in the energy threshold at which head/tail and vertical/horizontal discrimination could be achieved.

Chapter 6

MultiMesh-ThickGEM

Gas based radiation detectors rely on electron amplification in the gas in order to turn ionisation interactions in the gas into detectable signal. The negative ion drift gas SF_6 in particular requires large electric fields in order to reach the threshold for electron amplification. ThGEMs are a device for generating avalanche fields in gases which were described in Chapter 3; they consist of a dielectric sheet with a thickness on the order a millimeter and a copper layer on both sides, the amplification field is formed in a set of holes drilled through the sheet. In Chapter 3 ThGEM's were explored as an electron amplification device in SF_6 and while sufficient gain was obtained there were issues with the stability of the device at the operating voltages.

The problems with using a single ThGEM motivated the search for a gas amplification device which has sufficient gas gain to achieve a low energy threshold and is less prone to damaging sparks. Various technologies were considered for this, including multiple ThGEM stages, Multilayer-ThGEMs, GEMs and μ-RWELL's. The detector design settled on after consultation with the CERN MPGD manufacturing facility was the MM-ThGEM.

The MultiMesh Thick-GEM (MM-ThGEM) is a novel gas amplification device which is a hybrid of a ThGEM and a multimesh micromegas. It was invented in 2017 as a self supporting amplification device to fill a similar role as a ThGEM or a double or triple GEM that might have better avalanche characteristics and better suppression of Ion Backflow (IBF) [141]. A MM-ThGEM has the same form as a ThGEM but with the addition of mesh planes layered into the dielectric sheet and across the holes which enable more control over the field shape within the holes.

This chapter will describe the operation of a MM-ThGEM device in SF_6, this is the first time that a MM-ThGEM has been operated in a negative ion gas. The MM-ThGEM was hoped to overcome some of the issues experienced with ThGEMs particularly the sparking issues and gain variation which is at least partially attributable to the dependence on the dielectric structure.

The electric field in the MM-ThGEM detector can be divided into five distinct field regions that are referred to as the drift field, the collection field, the first amplification field, the first transfer field, the second amplification field and the second transfer field. The MM-ThGEM field regions, gap seperations, and the sections that relate to each one are listed in Figure 6.1. The MM-ThGEM and the experimental set-up is described in more detail in Section 6.1.1. Section 6.2 describes how the collection field interacts with the drift field and the effect of changing it on the collection efficiency and energy resolution in CF_4. Section 6.3 explores the effect of the variation of the collection field in CF_4. Section 6.4 describes the variation in gain and energy resolution with the amplification

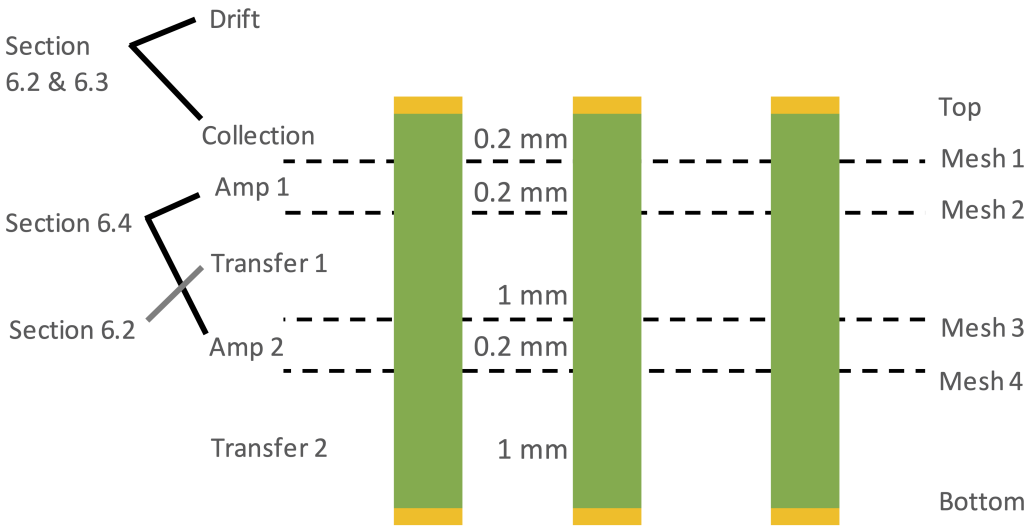

Figure 6.1: Cross-section of the MMThGEM with the field names (left), plane names (right) and the gap widths (centre-left). The sections which relate to each region are indicated on the left.

fields and an estimation of the Townsend coefficients in SF_6. The variation in ion drift speed and the gain of the device with the transfer field is discussed in Section 6.5. Finally the use of the device in the CF_4:SF_6 gas mixture is described in Section 6.7.

6.1 Device description and experimental setup

6.1.1 MM-ThGEM device

The MM-ThGEM detector was identified as a promising avenue for development following a discussion with the CERN micropattern detector production facility in 2018. The MM-ThGEM that was used in this work was fabricated CERN and delivered to Sheffield in February of 2019. The device consists of a dielectric layer with copper planes on the top and bottom with a lattice of drilled holes, a plan diagram of the MM-ThGEM and a close-up picture of the holes is shown in Figure 6.2.

Embedded in the dielectric layer are four meshes which are used to generate and shape the field in the holes. The four meshes are embedded at depths of 200 µm, 400 µm, 1400 µm and 1600 µm from the top of the device, the full thickness of the device is 2600 µm. The meshes are labeled one through four from top (cathode side) of the device to the bottom and the copper planes are referred to as the top and bottom planes. The holes have a diameter of 0.8 mm and are arranged in a hexagonal lattice with a pitch of 1.2 mm over the 10 x 10 cm active area of the device. The fact that the mesh spans the width of the hole separates this kind of detector from the Multilayer-ThGEM (M-ThGEM) which was first reported on in 2017 [142].

The meshes and copper planes divide the detector into a number of distinct regions, the labeling scheme for these regions is shown in Figure 6.1. The device is designed to be used in an amplify-drift-amplify configuration where the charge from the event is amplified in one high field region then drifted in a low field region before being amplified again in a second high field region. The amplification regions are generated in the gaps

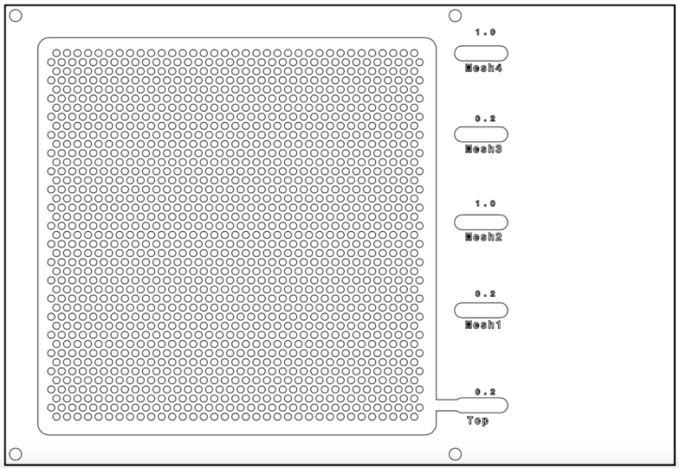

(a) Plan diagram of the MM-ThGEM.

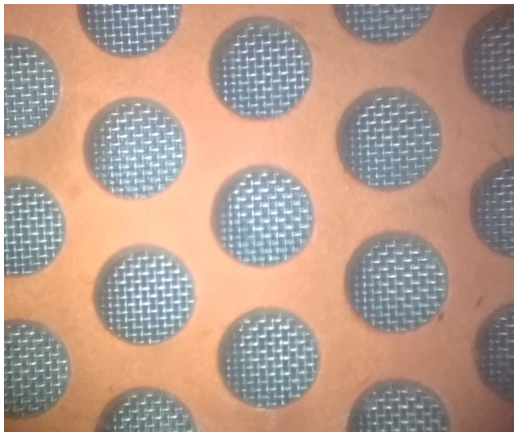

(b) Close-up picture of the MM-ThGEM holes from above.

Figure 6.2: A plan view of the MM-ThGEM detector and a close-up of the holes.

between meshes 1 & 2 and meshes 3 & 4, both of the gaps have a width of 200 µm. The other field regions are used for charge transport and are referred to as the drift field, the collection field and the first and second transfer fields. Each region is delimited by a mesh except the collection and drift fields which are separated by the top copper and are more interdependent than the other fields.

The inclusion of the mesh layers enables the generation of the electric fields to be decoupled from the dielectric layers. In conventional ThGEMs, charge up of the dielectric layer plays a significant role in field shaping [112]. Furthermore, sparking across the dielectric surface is believed to be a significant source of the damage that was observed to degrade the ThGEM performance in Chapter 3. It is hoped the MM-ThGEM will avoid these issues while maintaining the desirable properties of the ThGEM like their ability to self-support and to cover a large area. The division of the amplification region into two stages also reduces the potential difference across any single region which might help reduce the damage incurred from any sparks which do occur.

6.1.2 Experimental setup

The MM-ThGEM is placed inside a small steel vacuum vessel which is pumped to vacuum before filling with the drift gas, the vessel is shown in Figure 6.3. A cathode consisting of a square copper plate is located at 13 mm above the top plane of the MM-ThGEM and is held in position with nylon rods at the corners. Americium-241 and Iron-55 sources were sealed in the vessel and were manipulated with magnets so that the detector could be exposed to α or x-ray radiation. A number of additional high voltage feedthroughs were installed on the vessel, enabling the independent biasing of meshes 1, 2, 3 and 4 and the cathode.

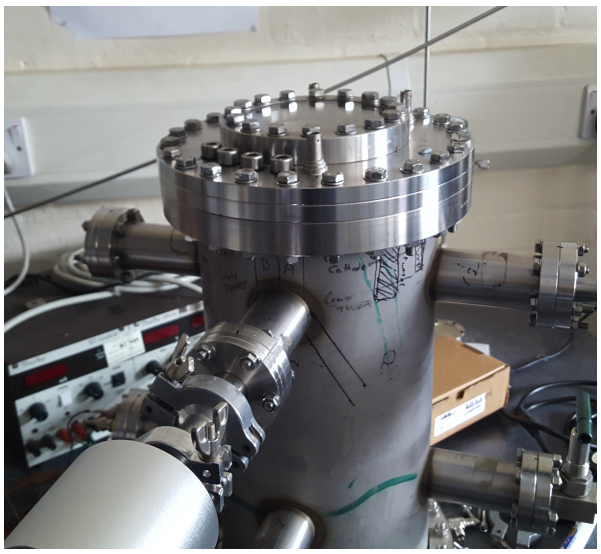

Figure 6.3: Picture of the vessel with the MMThGEM setup inside.

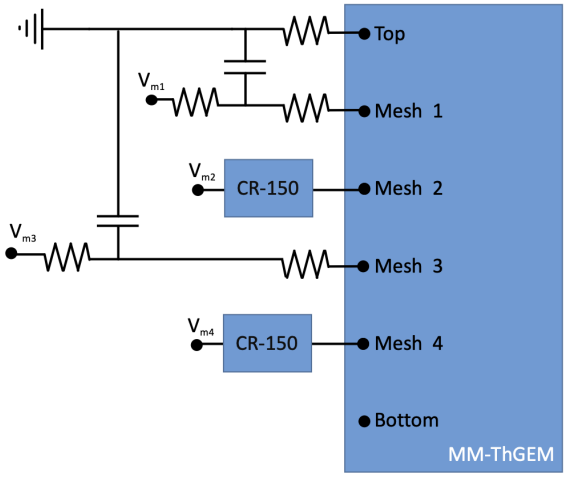

Figure 6.4: Circuit diagram of the bias scheme of the MM-ThGEM.

The biasing scheme of the MM-ThGEM is shown in Figure 6.4. Meshes 2 and 4 were biased and instrumented with CR-150 evaluation boards. The small separation and relatively large area of the meshes results in a significant capacitive coupling between them, as a consequence it was found that directly biasing meshes 1 and 3 resulted in significant noise on the instrumented meshes. To reduce the noise, a low-pass filter was implemented on the bias lines of meshes 1 and 3 as shown in the figure. Internally the bias line on the CR-150 board passes through a low-pass filter with the preamplifier uncoupled from the bias line through a capacitor so all the meshes are biased through low-pass filters.

The top plane of the MM-ThGEM was held at ground through a 100 MΩ resistor. The bottom of the MM-ThGEM was left floating due to the lack of feedthroughs and high voltage supplies to bias this plane as well.

The amplification chain for the instrumented meshes (2 and 4) consisted of a CR-111 preamplifier and the CR-200 4 µs shaping amplifier [114, 115]. The CR-150 boards and preamplifiers are located inside the vessel in order to reduce the noise as much as possible while the shapers are located outside the vessel. The output of both of the amplification chains digitised using a National Instruments NI-5751 digitiser. The digitiser is self-triggered with a threshold set in software, the digitisation window covers a range of ±1000 µs from the trigger time with the signal sampled every 1 µs.

6.1.3 Electronic calibration

If the detector is working correctly the signal observed at the digitiser is proportional to the ionisation in the gas with a constant of proportionality equal to the product of the gas gain and the electronic gain. Therefore in order to determine the gas gain associated with the MM-ThGEM device, the electronic gain associated with the amplification electronics needs to be determined.

Two metrics are considered for the measurement of the final signal; the maximum voltage of the signal peak and the integrated peak voltage. The maximum voltage is a suitable measurement of the signal when the collection time is faster than the shaping time of the electronics, with the 4 µs shaping time of the amplification chain this is suitable for electron drift gasses like CF_4. When the collection time is slower than the shaping

time not all of the collected charge contributes to the measured peak height, consequently integrating the peak signal provides a better measurement of the gain for negative ion drift gases such as SF_6.

These parameters are extracted with the same analysis described in Section 3.3. The integrated peak voltage is determined by integrating the signal which is over a threshold which is set the a quarter of the maximum voltage.

The electronic gain of the amplification chain is determined by injecting a test pulse into the amplification chain through the 15 pF capacitor integrated on the CR-150 test board. The variation in the maximum peak voltage and integral peak voltage with test pulse size for channel 2 is shown in Figure 6.5. The maximum peak voltage and integral peak voltage have different scales such that they fit on the same graph.

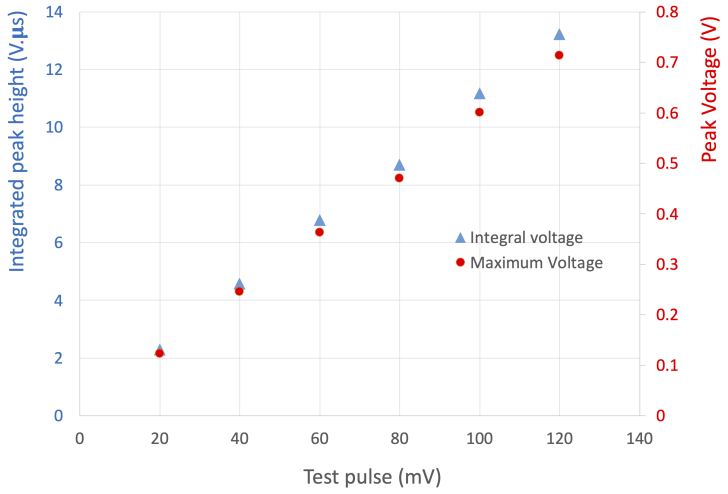

Figure 6.5: Peak height and integral voltage for a test pulse injected into channel 2 through a 15 pF capacitor.

Both of the gain metrics are proportional to the test pulse voltage which is expected. The electronic gain in terms of peak voltage of the amplification chain is determined to be $0.402 \pm 0.003\,\mathrm{V\,pC^{-1}}$. The electronic gain determined from the integral of the peak voltage is $7.46 \pm 0.06\,\mathrm{V\,\mu s\,pC^{-1}}$. These electronic gains are used for the gas gain determination in subsequent sections.

6.2 MM-ThGEM collection field in CF_4

In a conventional ThGEM the field which directs the charge into the holes of the device (the collection field) is part of the same field which is responsible for the amplification. In the MM-ThGEM device these fields are decoupled by the mesh layers and the collection field can be controlled separately from the amplification fields. The collection field is generated by the potential difference between the top plane and first mesh of the MM-ThGEM and is also affected by the drift field with which there is not a hard boundary. The collection field exists to focus as much of the charge from the drift region as possible into the holes of the MM-ThGEM. Efficient focusing of the charge is vital for the operation of the MM-ThGEM device and the collection field is unique in not being effectively linear, consequently undertaking a detailed study of the charge focusing in the holes is important for the consistent operation of the device.

6.2.1 Experimental measurement of gain and energy resolution

To explore how the potential difference between the first mesh and the top plane of the MM-ThGEM shapes the collection field and the effect of the collection field on channeling charge into the device, the MM-ThGEM is first operated in the electron drift gas CF_4. CF_4 was selected to use initially because it has significantly higher gas gain than SF_6 and, as an electron drift gas, is also far easier to model.

The radioactive source ^{55}Fe is useful for its generation of monoenergetic 5.9 keV x-rays which in turn produce significant electron recoils of the same energy in a target material. Producing electron recoils of a known energy is useful for the determination of the gas gain and energy resolution of a device making ^{55}Fe useful for the low energy calibration of gas TPCs. The vessel was pumped to vacuum and filled with 40 Torr of CF_4, it was found that sufficient gain was reached to observe ^{55}Fe x-ray induced electron recoils with only one of the two amplification fields. To study the collection of electrons a constant potential difference of 530 V was maintained between meshes 1 and 2, creating an amplification field of 26 500 V cm^{-1}. The 530 V bias was selected as it was sufficient to produce clear ^{55}Fe spectra. The detector was exposed to the ^{55}Fe source and the voltages of the cathode, V_{cath}, and mesh 1, V_{m1}, were varied from -100 V to -500 V and 10 V to 170 V respectively. Meshes 3 and 4 were not biased and were left at ground during these runs in order to minimise the charge amplification and transfer processes occurring which were not being studied.

The output of the amplification chain of mesh 2 was connected to an Ortec 926 ADCAM MCB which was used to histogram the maximum voltage of the ^{55}Fe events. Figure 6.6 shows the event energy spectrum generated for the device with $V_{m1} = 30$ V and $V_{cath} = -200$ V in 40 Torr CF_4 under ^{55}Fe exposure.

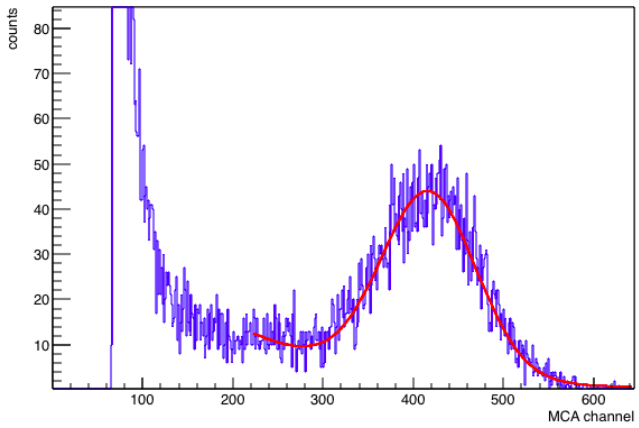

Figure 6.6: MM-ThGEM mesh 2 MCA spectrum (blue) and fitted peak (red) from an ^{55}Fe run in 40 Torr CF_4 with $V_{m1} = 30$ V, $V_{cath} = -200$ V and an amplification field of 26 500 V cm^{-1}.

The energy spectrum consists of an exponential drop off in event rate with increasing energy with an additional gaussian peak at the high energy end of the spectrum. This is consistent with the expected ^{55}Fe spectrum in addition to the ambient background radiation with the gaussian peak corresponding to 5.9 keV electron recoil events.

To determine the detector overall gain and energy resolution at each setting, a Gaussian was fitted to the 5.9 keV peak in each histogram. Additionally a term consisting

of an exponential was included in the fit to account for the background. The gaussian+exponential function fitted to the histogram is shown by the red line in Figure 6.6. The mean and width of the fitted Gaussian was used to determine the gain and energy resolution at each value of V_{m1} and V_{cath}. The energy resolution of the detector in this case is given by the FWHM of the gaussian divided by the mean of the gaussian function [51]. Figure 6.7 shows the effective gas gain and energy resolution determined over the range of cathode and mesh 1 voltages.

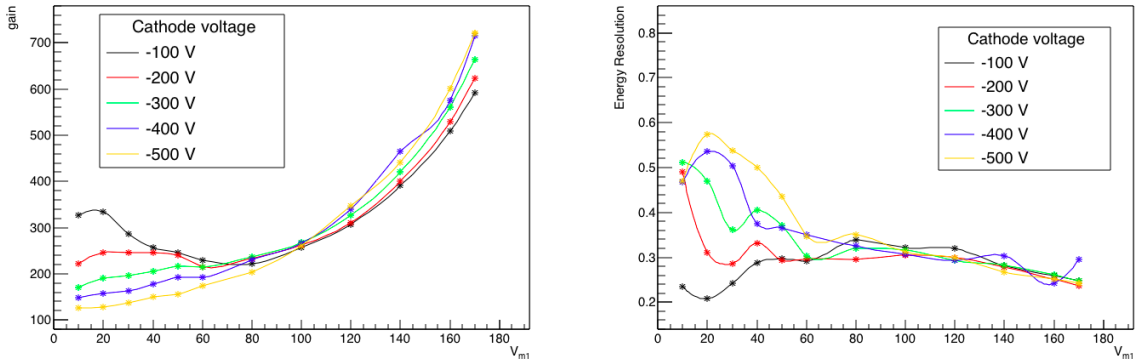

Figure 6.7: Mesh 1 voltage against the gain (left) and energy resolution (right) of the MM-ThGEM for different cathode voltages in 40 Torr CF_4 with a constant 26 500 V cm^{-1} amplification field.

There are two visible regimes in the gain: for $V_{m1} \lesssim 60$ V the gain is inversely related to the cathode voltage and close to flat with V_{m1}, conversely when $V_{m1} \gtrsim 100$ V this situation is more or less reversed and the gain is exponentially increasing with V_{m1}. There is significant spread in the energy resolutions of different cathode voltages at low collection fields, with higher cathode voltage having worse energy resolution. At higher collection fields the energy resolution becomes more similar for each value of the cathode voltage.

The non-linearity of the gain and energy resolution with the drift and collection fields suggests that a number of competing processes might be occurring. In order to understand the nature and contributions of these processes to the observed signal, a simulation of the charge transport in the MM-ThGEM holes is developed as described in the next section.

6.2.2 CF_4 charge transport simulation in Garfield++

Garfield++ is a simulation toolkit primarily focusing on the transport of electrons and ions in electric fields [143]. To understand the processes occurring in the transport and multiplication of the electrons in the holes of the MM-ThGEM a Garfield simulation of the region between the cathode and mesh 1 was created.

An electric field map was generated for each set of cathode and anode voltages with the finite element analysis program ANSYS. The volume of the field map was defined by the cathode and mesh 1 planes and a rectangle with opposite corners at the centre of adjacent holes (corresponding to the rectangle drawn in Figure 6.9), the map for the MM-ThGEM's hexagonal lattice of holes can then be created by reflection along each edge of the rectangle. Using Ansys is necessary because Garfield++ cannot generate field maps more complicated than simple linear geometries. A diagonal section of the field map volume for some sample voltages are shown in Figure 6.8.

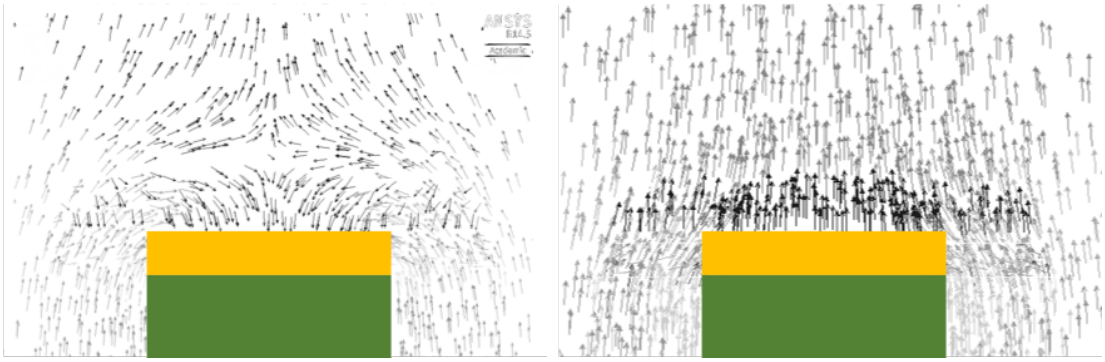

(a) $V_{m1} = 20\,V$, $V_{cath} = 100\,V$. (b) $V_{m1} = 20\,V$, $V_{cath} = 500\,V$.

Figure 6.8: Sample of Ansys field maps of the collection and drift fields at different cathode and mesh voltages generated for the MM-ThGEM.

The direction of the arrows in the field maps indicate the direction of the electric field and the length of the arrows indicates the field strength. The left and right edges of each map correspond to the centres of adjacent holes and the dielectric and metal between the holes is indicated in green and orange. The maps vary from having a dipole-like shape where the electric field exiting the hole loops back to be directed toward the metal as in Figure 6.8a to the field being close to linearly orientated in the cathode direction as in Figure 6.8b. The field shape is dependent on the ratio between the cathode and mesh 1 voltage, with larger V_{cath}/V_{m1} producing more linear field shapes and smaller V_{cath}/V_{m1} producing more dipole-like field shapes

The field maps were imported to Garfield++ and 10000 electrons were randomly placed within the boundaries of the field map rectangle cell at a constant height of 8 mm above the top plane of the MM-ThGEM. Garfield was then used to transport each of the electrons in 40 Torr CF_4 under the influence of the electric field and the endpoints were recorded. The position and status flag of each endpoint was used to determine whether the electron had been successfully collected by reaching the first mesh or if it had attached in the gas or ended up in the dielectric or top plane of copper. The spatial distribution of endpoints for an example run with $V_{m1} = 60\,V$ and $V_{cath} = 300\,V$ is shown in Figure 6.9.

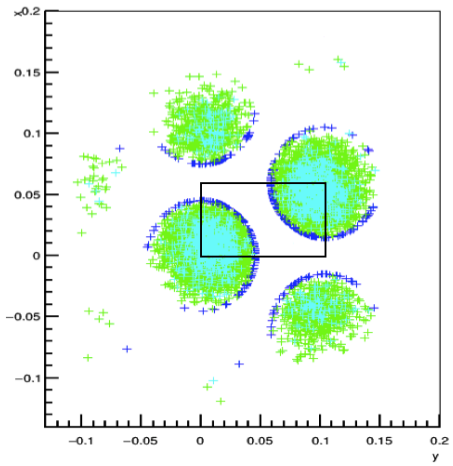

Figure 6.9: Electron endpoint distribution in space for $V_{m1} = 60\,V$, $V_{cath} = 300\,V$. Cyan: attached, Green: collected, Blue: embedded in dielectric.

The electrons embedded in the dielectric walls of the holes, in blue, outline the edges of the MM-THGEM holes near the electrons' starting location. The collected electrons, in green, are located at the bottoms of holes on the plane corresponding to mesh 1. Finally electrons which attach in the gas are indicated in cyan and are broadly localised to the middle of the holes. Electrons impacting on the copper top plane of the MM-ThGEM were not present at all at this voltage.

In addition to electron losses, electrons are also generated in an avalanche process at some of the voltages explored. Figure 6.10 shows the rates of electron generation and losses in the Garfield simulation with different field configurations.

Figure 6.10a shows the simulated gas gain which is determined by the total electron endpoints divided by the starting number of electrons. At mesh 1 voltages of 20 V and 40 V there is no electron multiplication in the gas at all. Electron multiplication starts at 60 V and the gain is exponential with mesh 1 voltage, there is also a slight proportionality to cathode voltage which can be attributed to the drift field contributing slightly to the field in the hole.

Figure 6.10b shows the fraction of endpoints which which were located on the copper of the top plane, were collected by the device, embedded in the dielectric and attached to ions in the gas. These four scenarios account for all of the electron endpoints in the simulation.

At low V_{m1} and high V_{cath} most of the electron losses are to the copper top plane, this can be explained by the geometry of the electric field; at low values of $\frac{V_{m1}}{V_{cath}}$ the field above the top plane is close to uniform and the electrons will move close to straight down from their starting positions with many ending up on the metal. When $\frac{V_{m1}}{V_{cath}}$ is higher the field above the hole takes on more of a dipole shape and better directs the electrons into the holes of the device reducing the fraction of electrons lost in this way to zero. The difference in field shapes is demonstrated by Figure 6.8b and Figure 6.8a.

Electron attachment in the gas dominates the losses for high V_{m1}, with fairly little dependence on the cathode voltage, except for $V_{cath} = -500$ V which has a enhanced amount of attachment as compared to the rest of the data. In CF_4 the electron attachment coefficient increases at high E/N starting at around 35×10^{-17}Vcm^2 [118], equivalent to around 495 V cm^{-1} or a cathode voltage of −380 V. The high fields generated in the holes

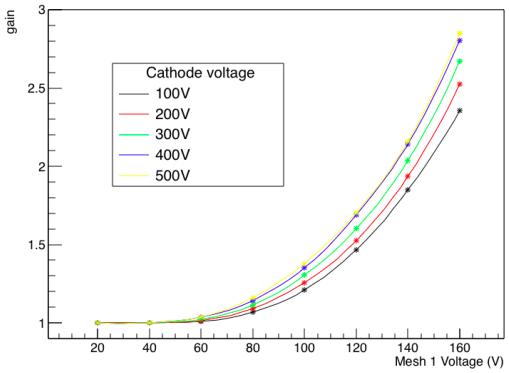

(a) The mesh 1 voltage vs gas gain.

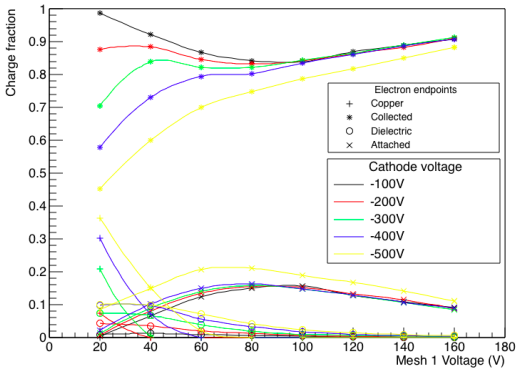

(b) The ratios of the electron endpoint locations against mesh 1 voltage.

Figure 6.10: Results for Garfield++ simulation of electron transport in the collection and drift fields of the MM-ThGEM in CF_4 for different cathode voltages.

are enough to cause significant electron attachment which increases with the collection field until the effect starts to be offset by the gas gain. In the case of $V_{cath} = -500\,\mathrm{V}$ the drift field is enough to cause significant attachment in the drift region causing additional losses as compared to lower cathode voltages. The dependence on field is reflected by the distribution of electron attachment endpoints in Figure 6.9, which are concentrated in the holes of the MM-ThGEM.

The last component of electron losses in Figure 6.10b is electrons embedding in the dielectric which forms the sides of the holes. The rate of losses to the dielectric decreases with increasing V_{m1} and shows an approximately linear relationship with cathode voltage. There is no rim on this device which means that in order to embed in the dielectric the charge needs to diffuse laterally within the hole. The lower proportion of electrons terminating in the dielectric at high V_{m1} and low V_{cath} is a result of better focusing of the electrons into the centre of the hole. Electrons embedding in the dielectric would have the effect of charging the dielectric and would have a focusing effect on charge in the hole, although back flowing positive ions will counteract this which could result in a net positive charge on this part of the hole wall [112]. Currently the effect of charge up on the MM-ThGEM device has not been investigated, although it might contribute to the shape of the collection field over long exposure times.

To compare the simulation to the data one can define the effective gain of the drift and collection fields of the MMThGEM as the number of electrons which arrive at the first mesh divided by the initial number of electrons. Figure 6.11 shows the effective gain determined in Garfield, it preserves a number of the features of the experimental data which is shown in Figure 6.7.

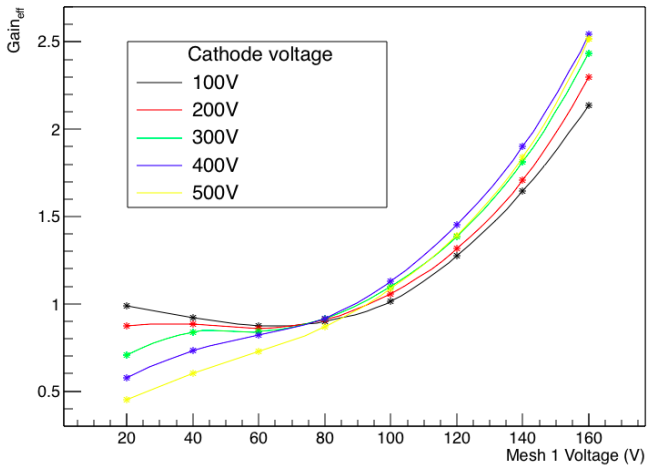

Figure 6.11: The simulated effective gain of the MMThGEM Drift and Collection fields.

The exponential nature of the gain with mesh 1 voltage is a common feature of the simulated and experimental data as is the proportionality of the gain with cathode voltage at high V_{m1} and the inversion of that proportionality at lower mesh 1 voltage. The most significant difference is in the region $V_{m1} < 60\,\mathrm{V}$, particularly for $V_{cath} = 100\,\mathrm{V}$ which in the data has a gain approximately 1.5 times higher for $V_{m1} = 20$ than for $V_{m1} = 80$ this is opposed to 1.1 times higher in the simulation. This difference might be attributed to better transport of the electrons through mesh 1 at lower collection fields in the experiment, a process not simulated in the simulation Garfield.

Another area of interest is the contribution of the collection field to the energy resolution. For our purposes the energy resolution is the variance in the number of electrons arriving at the anode for a recoil of a given energy. There are a number of contributions to the energy resolution of a detector including variations in the number of ionised electrons at a given energy and the number produced by the avalanche process.

The contribution of the collection field to the energy resolution is in the variation in the number of electrons which are collected at mesh 1. The simulation doesn't model the energy resolution of the device but it is likely that the main contributor to the energy resolution of the collection field is electrons lost to the metal and dielectric. The localised nature of the electron recoils that the system detects means that the alignment of an initial charge cloud with a hole would have a significant effect on the efficiency of the charge collection at low collection fields, the attachment rate on the other hand is not really dependent on the initial position and hence would contribute more to a lowering of the gain than degradation of the energy resolution. This is reflected in the experimental data by the generally larger energy resolution at low V_{m1}.

With some slight differences the simulated Garfield++ data reflects well the variation in the gain observed experimentally from the 5.9 keV peak. The simulation demonstrated the competing electron loss and multiplication processes which comprise the contribution of the collection field to the observed gain.

6.2.3 Conclusions

The experiments in CF_4 demonstrated that the collection field is an important factor contributing to the gain and resolution of the device. Requiring only one amplification field to observe ^{55}Fe enabled the collection efficiency to be studied disentangled from other systematic effects. The Garfield simulation assisted in the determination of the different contributing processes to the overall collection efficiency. Electron multiplication, attachment, and impact on the metal and dielectric were shown to all contribute to the final gain. The similarity between the variation in the simulated and experimental gain suggests that charge transport in the collection field is well modelled by Garfield++.

Having successfully confirmed that the device works as expected in the fairly well understood CF_4, the operation of the device in the more novel SF_6 negative ion drift gas is described in the following sections.

6.3 MM-ThGEM collection field in SF_6

The majority of the MM-ThGEM characterisation was performed with the negative ion drift gas SF_6. As discussed previously in Section 2.2, negative ion drift gases are useful mostly because of their ability to significantly reduce the diffusion of a drifted charge cloud. This is important for extending the size of a gas detector to volumes large enough to be competitive in fields like dark matter detection. The performance of the device will be considerably different for negative ion gasses as the charge carriers are ions rather than electrons. As discussed in Section 6.2, ensuring efficient collection of the charge by the collection field is important for optimal operation of the MM-ThGEM device. Although the insights gained from experience operating the detector in CF_4 are expected to be useful, the different behavior of drifting negative ions as compared electrons necessitates a re-evaluation of the effect of the collection field on the signal.

6.3.1 Experimental measurement of gain and energy resolution

In SF_6 it was found that using both amplification fields was required to get a clear gain measurement from ^{55}Fe. Consequently the signal in the SF_6 runs was taken from the last mesh plane of the device, mesh 4 in Figure 6.1. The gain was determined from the integral of the signal waveforms as discussed because SF_6 is a negative ion drift gas.

The detector was operated at 20, 30, 40 and 50 Torr, at each pressure a stable operating point was found and the collection field was varied with the other fields held constant. The operating point for the various electric fields at each pressure is shown in Table 6.1. Figure 6.12 shows the gain against the mesh 1 voltage determined for different SF_6 pressures.

The amplification fields required to observe ^{55}Fe were found to increase with increasing pressure. This is expected as the mean free path of the electrons being amplified gets shorter as the pressure increases which necessitates higher fields to produce the same gains. The effect of changing the the amplification fields on the gain and energy resolution will be discussed further in Section 6.4.

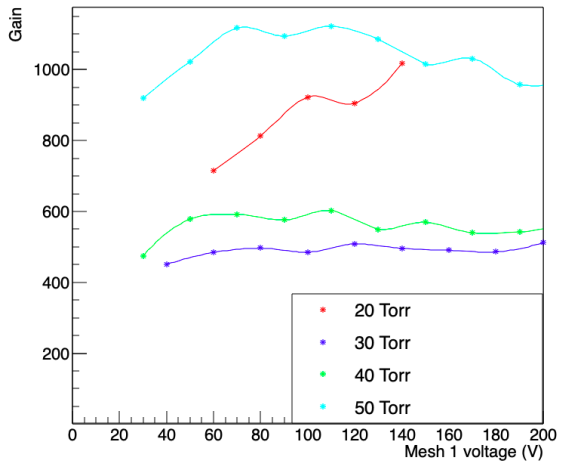

Figure 6.12: The mesh 1 voltage vs measured gain for different pressures of SF_6.

Pressure (Torr)	Transfer ($V\,cm^{-1}$)	Amp 1 ($V\,cm^{-1}$)	Amp 2 ($V\,cm^{-1}$)	Cathode (V)
20	400	22000	21000	500
30	600	23500	23500	500
40	600	25000	25500	600
50	600	28500	24500	600

Table 6.1: bias settings at each pressure when changing the collection field.

There is generally fairly little variation in the gain as the collection field is varied. The biggest exception being the 20 Torr run where the gain appears to consistently increase with collection field, the 20 Torr data shows some consistent irregularities in the measured gain and other parameters the main contributing reason for this will be discussed in Section 6.6. Overall the tendency for the gain to be flat with collection field suggests the charge is being collected fairly efficiently. The slight decrease from the trend in the gain at low voltages in the 40 and 50 Torr runs might suggest that the lower voltage limit for efficient collection might be in the range of 60 V to 80 V for the cathode voltages and pressures explored. This is because in a negative ion gas like this the charge collection efficiency is expected to be the only way that the collection field influences the gain.

6.3.2 SF_6 charge transport simulation in Garfield++

As with the CF_4 work (discussed in Section 6.2), exploring the contribution of the collection field to the observed gain can be assisted by simulation in Garfield. A significant

issue with performing an equivalent SF_6 simulation is that Garfield does not have code for the transport and amplification of negative ions. A work around for this is to use Garfield's positive ion transport code instead, reversing the electric fields and setting the ion mobility manually to that of SF_6^-. As a consequence of this 'hack' of Garfield, reattachment and amplification processes will not occur in the simulation, however these are expected to be negligible in SF_6 at the collection fields explored.

The same simulation methodology as described in Section 6.2 was employed with Garfield negative ion hack described above. Figure 6.13 shows the collection efficiency predicted by the Garfield simulation for charge transport into the holes for 40 Torr SF_6.

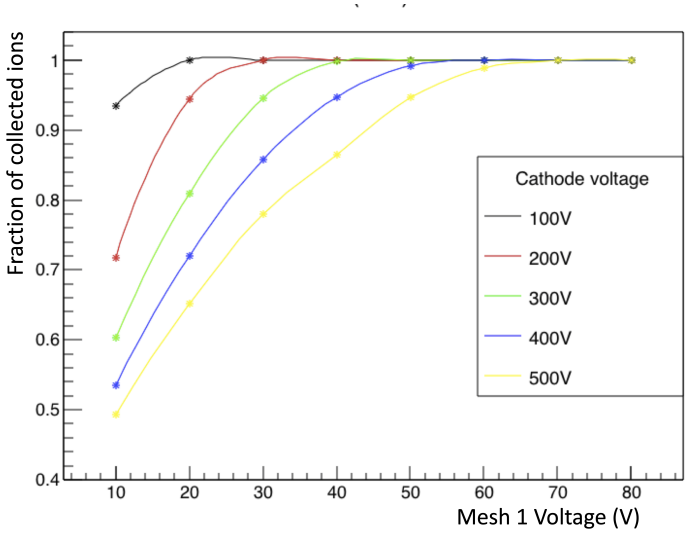

Figure 6.13: The simulated collection efficiency of the MM-ThGEM Drift and Collection fields in 40 Torr SF_6.

For a given cathode voltage the fraction of charge collected increases with mesh 1 voltage until all charge is collected. The mesh 1 voltage required to collect all the charge increases with cathode voltage consistent with the field shape rather than the strength being the determining factor in the collection efficiency. For each of the cathode voltages explored, total charge collection is achieved at a field ratio of around 10:1 between the collection and drift fields.

All of the uncollected ions in the simulation ended up on the metal top plane of the MM-ThGEM, unlike in the electron drift simulation of CF_4 where a significant fraction of the charge which was not collected and did not reattach ended in the dielectric. This could be attributed to the lower diffusion rate of the ions in the gas compared to electrons; once the charge has entered the hole it must diffuse laterally to reach the dielectric and embed, this happens at a lower rate for ions than electrons. The collection was close to 100% efficient at $V_{m1} > 60\,\mathrm{V}$ for all of the cathode voltages used in the Garfield runs.

The flat relationship for mesh voltages $V_{m1} > 60\,\mathrm{V}$ is consistent with flat relationship observed in the experimental data at pressures above 20 Torr. The lack of attachment, electron multiplication and charge embedding in the dielectric means that the amount of charge reaching the first mesh plane is equal to the amount of charge channeled into the holes.

6.3.3 Conclusions

The function of the collection field is to efficiently channel charge in to the holes of the MM-ThGEM. The purpose of exploring the variation of the gain with collection field was to arrive at a bias setting for the collection field which enabled all of the charge in the gas to be collected. The switch to negative ion drift significantly changes the charge transport in the collection field as compared to the CF_4 electron drift.

Both simulation and the experimental data suggest that a potential difference on the order of 70 V between mesh 1 and the top copper plane is sufficient to achieve near total charge collection for drift fields $\lesssim 400\,\mathrm{V\,cm^{-1}}$. No significant benefit in terms of effective gain or energy resolution appeared to be accrued in the experimental data by increasing the collection field beyond this point, which suggests that a mesh 1 voltage on the order of 70 V value is sufficient for the device operation.

6.4 MM-ThGEM amplification fields in SF_6

Having determined the collection field that needs to be applied to the MM-ThGEM to ensure efficient collection of charge in the gas, focus can move to the electron amplification fields. The amplification fields are vital to the operation of the MM-ThGEM device as they are the regions in which collected charge is multiplied and are therefore the source of the entirety of the device's gas gain. Two amplification fields are formed in the MM-ThGEM device: one between meshes 1 and 2 (amplification field 1), the other between meshes 3 and 4 (amplification field 2). In between these regions the charge is transported by a weaker field known as the transfer field. The locations of the MM-THGEM meshes and fields is shown in Figure 6.1.

The gain from a single amplification field was not found to be sufficient to observe the ^{55}Fe signal in SF_6, consequently all measurements of ^{55}Fe were taken from mesh 4 with both amplifcation fields contributing to the overall gain.

The need to use both fields is an anticipated consequence of using SF_6, it does however make disentangling the contributions to the gain from each of the two stages difficult. Several approaches to exploring the effect of the amplification fields on the gain are therefore used.

6.4.1 Gain of the MM-ThGEM from ^{55}Fe with equal amplification fields

Having both amplification fields held at the same magnitude has the advantage that the gain of each stage should be equal, it also reduces the number of bias parameters that need to be optimsed by one. During the equal amplification field runs the voltage on mesh 1, V_{m1}, was 30 V, the cathode voltage was 500 V and the transfer field was $500\,\mathrm{V\,cm^{-1}}$ at 20 Torr and $600\,\mathrm{V\,cm^{-1}}$ at 30 and 40 Torr. Amplification fields 1 and 2 were kept the same as each other and increased in tandem at each pressure. As in Section 6.3 the gain was determined by histograming the integrated mesh 4 signal and then fitting the ^{55}Fe 5.9 keV peak with a gaussian. Figure 6.14 shows the variation in gas gain determined for the MM-ThGEM with equal amplification fields at 20, 30 and 40 Torr SF_6.

The lowest field setting at each pressure was determined by the gain required to disentangle the ^{55}Fe signal peak from the noise, which was possible for gains in the hundreds.

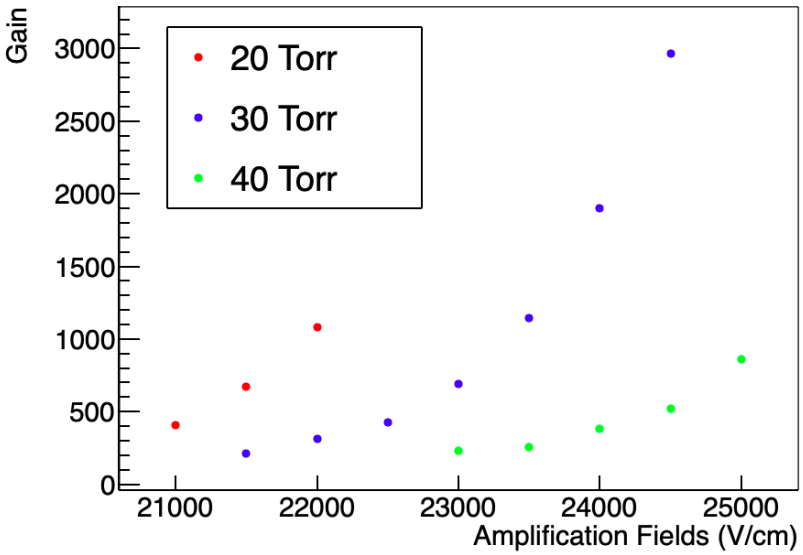

Figure 6.14: MM-ThGEM gas gain at 20, 30 and 40 Torr SF_6 against amplification field when amplification fields 1 and 2 are equal.

The limiting factor for high fields at 20 and 30 Torr was imposed by the onset of a continuous signal which represents the device's failure mode at high amplification fields. The characteristics and potential causes of this continuous signal will be discussed further in Section 6.6. At 40 Torr the amplification field were not ramped beyond 25 000 V cm^{-1} out of caution to not damage the device at this early stage.

The trend in Figure 6.14 is for an exponential increase in the gas gain with the amplification fields. At 20 Torr there is only a fairly narrow window of operating voltages from 21 000 V cm^{-1} to 22 000 V cm^{-1} at which the 5.9 keV peak can be observed. Conversely at 30 Torr the 5.9 keV peak can be observed over almost twice the voltage range, from 21 500 V cm^{-1} to 24 500 V cm^{-1}, and the 30 Torr runs also obtain the highest gas gain, approximately 3000.

6.4.2 Gain of amplification field 2 from ^{241}Am alphas

To determine the gas gain of a device, most calculations precede using the arrival of a known amount of charge at the device. Alpha particle are generally not useful in this regard because their long ranges make it hard to arrive at an accurate estimate of the total energy deposit in a detector. The MM-ThGEM however has two sequential separately instrumented amplification regions, this makes it possible to measure the gain of the second stage with an arbitrary charge deposit by gating the total deposited charge at mesh 2. This method extends the range of fields at which gain can be determined to significantly lower than possible with the 5.9 keV ^{55}Fe peak. It also further provides an independent measurement of the gas gain of a signal stage which is not dependent on effects in the collection field or on the calibration performed in Section 6.1.1 as the gain is simply the ratio between the signal observed on meshes 2 and 4.

An initial operating point was arrived at for each pressure by holding mesh 1 at 40 V with a drift field of 400 V cm^{-1}. The voltage on mesh 2 was then increased with the drift region exposed to ^{241}Am alpha particles until signal was observed with a magnitude of ∼30 mV. The voltage on meshes 3 and 4 were then increased such that the transfer field

had a strength of 500 V cm^{-1} and amplification field 2 had the same value as amplification field 1. Then the voltage on mesh 4 was increased incrementally while the voltages on the cathode and meshes 1, 2 and 3 were held constant. This meant amplification field 1 and the drift, collection, and transfer fields stayed constant while amplification field 2 was varied. Figure 6.15 shows the gas gain determined from the ratio between the signal on meshes 2 and 4 for ^{241}Am alpha particles in SF_6 using this method.

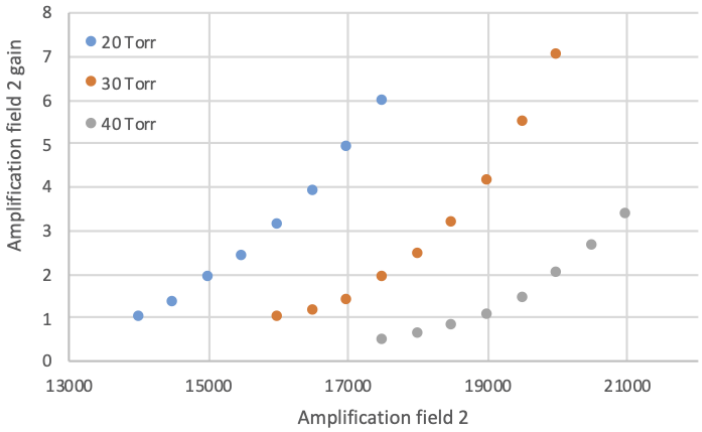

Figure 6.15: The gas gain in the region mesh 2 → mesh 4 determined from the ratio of the signal on mesh 2 to the signal on mesh 4 for alpha particles from ^{241}Am in 20, 30 and 40 Torr SF_6.

The relationship between amplification field and gain is close to exponential at each pressure and is constrained to the range 0.5 to 8. The upper limit on the determined gas gain is imposed by the requirement that the signal had to be large enough to measure on mesh 2 and small enough not to saturate the digitiser range mesh 4. At lower fields in 40 Torr SF_6 the gain is less than 1 which implies the net loss of charge between mesh 2 and mesh 4, these losses might occur in the transfer field or when the charge is transported through each mesh. The losses also likely contribute to the determined gain at higher fields although a consistent loss factor for the charge transport from mesh 2 to 4 could not be determined. The effect of the transfer field on the gain is explored in Section 6.5.

6.4.3 Gain of the MM-ThGEM from ^{55}Fe with constant amplification field 1

The gain for the entire device when the second amplification field was varied was also explored with ^{55}Fe. This necessitated significantly higher fields than were used to observed alpha particles, and the gas gain was determined from the ratio between the observed signal and the ionisation expected from the 5.9 keV peak.

The drift, transfer and collection fields were held constant at nominal values for each pressure as was the first amplification field. The transfer field was 600 V cm^{-1} for all runs, $V_{cathode}$ and V_{m1} were 500 V and 140 V respectively for the 20 and 30 Torr runs and 600 V and 150 V for the 40 and 50 Torr runs. The respective strengths of the first amplification field were 22 000 V cm^{-1}, 23 500 V cm^{-1}, 26 000 V cm^{-1} and 28 500 V cm^{-1} for the 20, 30, 40 and 50 Torr runs. Figure 6.16 shows the gain and energy resolution against the second amplification field for 20, 30, 40 and 50 Torr SF_6.

The gains for the entire device, seen in Figure 6.16a, were of the order of 100's suggesting that the per amplification field gain was on the order of tens. There is an increase in

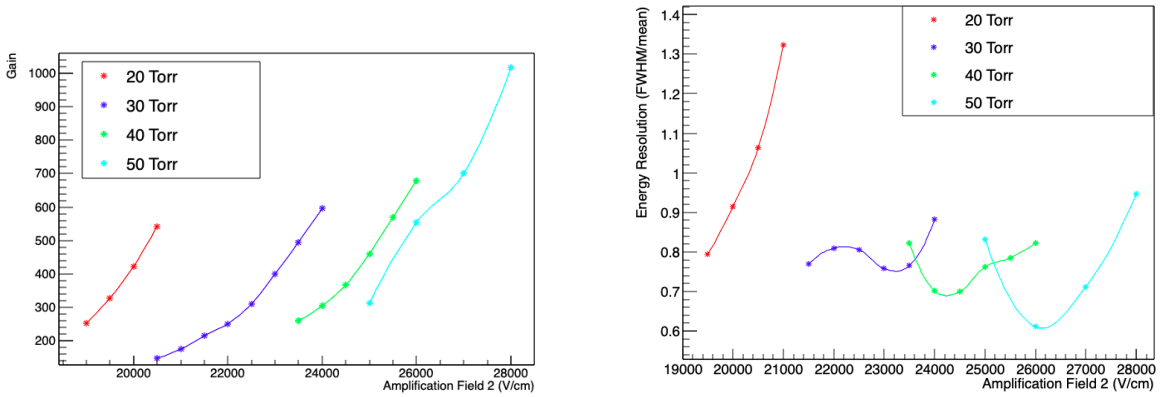

(a) The effective gain against second amplification field.

(b) The energy resolution vs amplification field 2.

Figure 6.16: Plots from variation of second amplification field of MM-ThGEM in low pressure SF_6 when first amplification field is held constant.

the gain with amplification field, although the shape is slightly different between pressures. At 50 Torr and in the higher field regions of the 30 and 40 Torr data, the relationship appears linear. At 20 Torr and at the low field regions of the 20 and 30 Torr data there is an upward curve suggestive of a exponential relationship.

Figure 6.16b shows a variation of in the determined energy resolution (defined by the FWHM divided by the mean of the gaussian fitted to the 5.9 keV peak) with amplification field 2. The energy resolution appears to reach a minimum in the range of scanned voltages for each pressure with the exception of the 20 Torr data where the resolution gets worse as amplification field increases. Furthermore the lowest obtained energy resolution decreases with increasing pressure, with the lowest energy resolution at about 60% obtained in 50 Torr SF_6. Low energy resolution is a desirable characteristic for particle detectors, so the locations of these minima are an important factor in the determination of an optimal operating point for the entire device. Significantly the lowest energy resolution at each pressure is not obtained when the amplification fields are equal but instead when the second amplification field is smaller than the first. The energy resolution minima might be related to the approach of the break The paper [77] suggests that such minima might be a result of a trade-off between the increased resolution of a larger amount of charge reaching the detection element and the degradation of consistent amplification associated with approaching the maximum operating voltage of a detector.

6.4.4 Extracting Townsend gas parameters

The gain of the device as a whole can be compared with the Townsend equation, an analytical model for gas gain in a linear electric field which was discussed in Section 2.2.1. The first order Townsend equation for a one stage device was formulated in Equation 2.4, which is re-stated here:

$$\ln(Gain) = dPAe^{-\frac{BP}{E}} \tag{6.1}$$

where d is the width of the amplification gap, P is the pressure, E is the amplification field, and A & B are the Townsend coefficients. The parameters A and B are associated with the gas in which the amplification is occurring. For a two stage device the total gain

will be a the multiple of the two gains:

$$\ln(Gain) = \ln(G_1 G_2) = \ln(G_1) + \ln(G_2) = d_1 P A e^{-\frac{BP}{E_1}} + d_2 P A e^{-\frac{BP}{E_2}} \tag{6.2}$$

this can be reformulated as a linear equation if $d_1 = d_2$ and $E_1 = E_2$ in the form of

$$\ln(\ln(Gain)) = \ln(2dPA) - \frac{BP}{E}. \tag{6.3}$$

assuming perfect collection and transfer of charge.

An alternate way to formulate Equation 6.3 is in terms of the mean free path of electrons, λ, and the effective ionisation coefficient, I_e using the Rose-Korff formulation given in Equation 2.5. This formulation provides parameters realted to physical quantities rather than the more abstract Townsend parameters.

For a detector well characterised by this Townsend equation, the double natural logarithm of the gain is linear with the inverse amplification field. Figure 6.17 shows the double natural logarithm of the gain against the inverse amplification field for the gains determined when both amplification fields were equal.

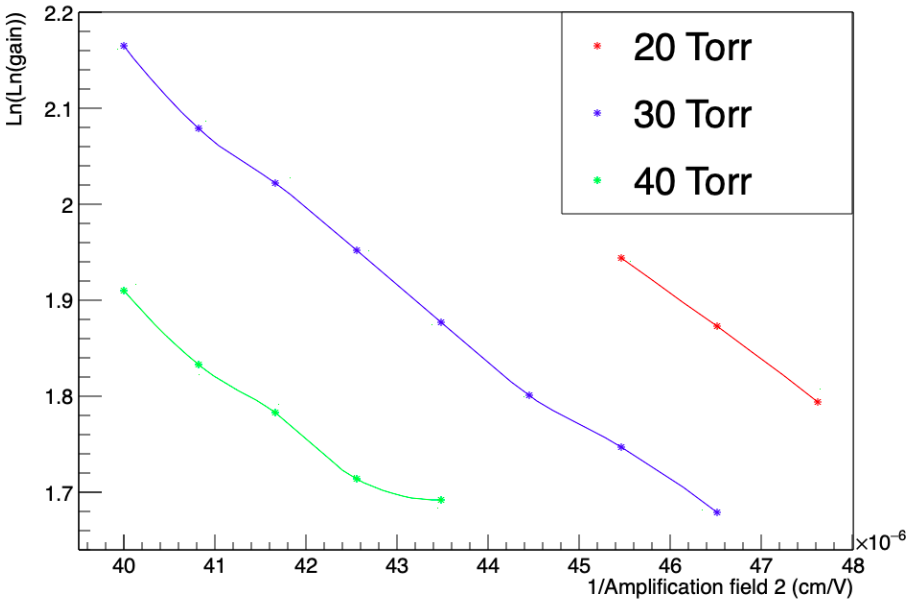

Figure 6.17: The double log of the effective gain of the MMThGEM in SF_6 against inverse amplification field where amplification field 1 equals amplification field 2.

The double logarithm of the gain is linear with the inverse amplification field, which is consistent with Townsend like gain of the device as in Equation 6.3. A linear fit to the points on Figure 6.17 obtains the values A, B, λ and I_e for each pressure, these values and the errors in the fit to the data are shown in Table 6.2.

The trend of the values of A and B to decrease with increasing pressure is consistent with the effect observed in the negative ion gas CS_2 in [144].

The effective ionisation energy, I_e, should be constant with pressure and the weighted average of the value determined at different pressures gives a value for I_e of 16.7(5) eV. The literature ionisation energy of SF_6 is 15.32(2) eV [145], which is fairly close to the weighted average. The effective ionisation is not expected to be exactly the same as the

Table 6.2: Values for the Townsend coefficients, mean free path and effective ionisation energy obtained with the MM-ThGEM.

Pressure (Torr)	**A ($\mathbf{cm^{-1}}$ $\mathbf{Torr^{-1}}$)**	**B ($\mathbf{V\ cm^{-1}}$ $\mathbf{Torr^{-1}}$)**	λ (μ**m**)	I_e **(eV)**
20	201 ± 10	3500 ± 50	2.49 ± 0.12	17.4 ± 0.9
30	176.5 ± 15	2666 ± 66	1.89 ± 0.16	15.1 ± 1.3
40	89.0 ± 30	1909 ± 120	2.81 ± 0.95	21.4 ± 7.4

ionisation energy because some of the energy obtained by the electrons accelerated in the amplification field is dissipated by prior collisions.

The estimated free path length, λ, should be inversely proportional to pressure although this relationship is not observed in the values extracted in Table 6.2. One factor neglected from this analysis is charge losses during the collection of the charge and the transfer of the charge from one amplification region to another. These losses would contribute additional terms to Equation 6.3 which are not accounted for.

6.4.5 Conclusions

The gain of the MM-ThGEM device originates from electron multiplication in the two amplification fields. The overall gas gain obtained was sufficient to observe the 5.9 keV ^{55}Fe peak at pressures from 20 to 50 Torr across a range of amplification fields. This is a significant improvement on the performance of the ThGEM described in Chapter 3 where the ^{55}Fe peak was only observed at one stable voltage. The highest gas gain obtained was about 3000 in 30 Torr SF_6 at matching amplification fields of $24\,500\,\mathrm{V\,cm^{-1}}$.

Characterising the gain of each amplification stage individually proved challenging as a result of the overall gain being the product of the contributions of both transfer fields as well as any loss factors in the collection and transfer of the charge. Operating the device with both amplification fields being equal demonstrated that the behavior of the MM-ThGEM is consistent with the first order Townsend equation and also enabled the extraction of the Townsend coefficients for SF_6.

The variation of the gain and energy resolution of the device with second amplification field was obtained with an ^{55}Fe source. It was demonstrated that there is space for optimisation of the energy resolution of the device, with distinct minima in the resolution observed at 30, 40 and 50 Torr. Using alpha particles to explore the gain of the second stage individually also indicated that there might be significant charge losses occurring in the transfer of charge from one amplification region to another at the $500\,\mathrm{V\,cm^{-1}}$ transfer field used. The effects of the transfer field on the gain are explored in the next section.

6.5 Transfer field

The Transfer field is formed between meshes 2 and 3 and transfers the charge from the first amplification field to the second amplification field. The field strength of the transfer field is too low for electron multiplication to occur and the main optimisation for this field is maximising the transfer efficiency between the two gain stages. Charge losses during the transfer are anticipated to originate from two sources; charge embedding in the walls of the holes and losses during the transfer of charge through the mesh planes.

Losses to the walls of the hole will be positively correlated to the diffusion of the charge in the hole; assuming no space charge effects and that all diffusion is thermal, the diffusion will be inversely proportional to the strength of the transfer field. Losses to the mesh planes are considerably harder to characterise theoretically, especially because the processes of electron attachment and detachment to negative ions is also occurring in the region of the mesh planes. The ratio between the fields on each side of the mesh have been shown to be correlated to the transparency of a mesh layer to electrons in pure electron drift gasses however [146].

6.5.1 Effect of the transfer field on gas gain

For pressures from 20 to 50 Torr of SF_6 the cathode, collection field and the amplification fields were set to nominal values and the transfer field was varied. The settings for the cathode, collection field and the amplification fields for each pressure are shown in Table 6.2. Figure 6.18 shows the variation of the gain measured at mesh 4 with transfer field in the device when all other fields are held constant.

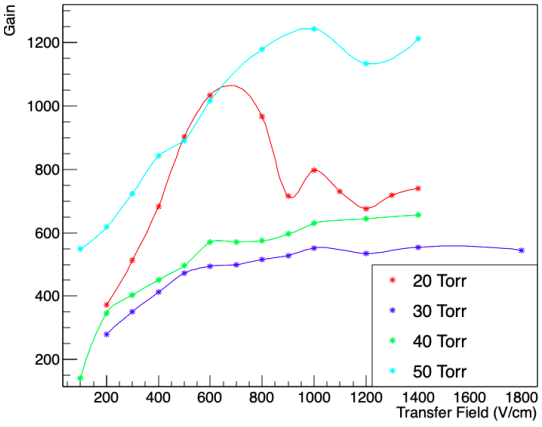

Figure 6.18: The gain vs transfer field in the MM-ThGEM.

Pressure (Torr)	**Cathode** (V)	V_{m1} (V)	**Amp 1** (V/cm)	**Amp 2** (V/cm)
20	500	140	22000	21500
30	500	140	23500	23500
40	600	150	26000	25500
50	600	150	28000	28000

Table 6.3: The field settings for each pressure when the transfer field is varied.

The general trend is that the gain increases asymptotically with the drift field up to an apparent limit. The gain does not show any significant increase with increasing voltage for transfer fields in excess of $1000\,\mathrm{V\,cm^{-1}}$.

As no electron multiplication occurs in the transfer field, the change in the observed gain can be attributed to better charge extraction through mesh 2 by the transfer field and to less losses to the hole edges. Consequently a transfer field in the range $600\,\mathrm{V\,cm^{-1}}$ to $1000\,\mathrm{V\,cm^{-1}}$ would be optimal for minimising these losses and therefore maximising gain.

The exception to the general trend is the 20 Torr run which exhibits an increase in the gain with transfer field up to $600\,\mathrm{V\,cm^{-1}}$ before the gain decreases significantly. This behavior might be attributed to the ringing effect discussed in Section 6.6.

6.5.2 Transfer times

The charge transfer in the gap is expected to be mediated by negative ions which will take a significant amount of time to drift across the gap on the order of tens of microseconds.

The determination of the transfer time enables an estimate of the mobility of the negative ions in the transfer gap to be obtained. The transfer time, $t_{m2\to m3}$, will be related to the transfer field, $E_{transfer}$, by the equation

$$t_{m2\to m3} = \frac{d}{\mu_0 E_{transfer}} \frac{PT_0}{P_0 T} \tag{6.4}$$

where d is the width of the transfer gap, μ_0 is the reduced mobility, P is the gas pressure, T is the gas temperature, and P_0 and T_0 are the pressure and temperature at STP. The amplification field is high enough that the electrons should detach from the negative ions and the travel time between meshes 3 and 4 should be $O(10\,\text{ns})$. Consequently the contribution of the transport of charge from mesh 3 to 4 can be neglected for calculation of the mobility

To determine the transfer time, the drift region was exposed to alpha particles from the ^{241}Am source with the amplification fields equal and set such that the detected signal on each instrumented mesh was approximately equal. Amplification fields 1 and 2 were equal and had strengths of $15\,500\,\text{V cm}^{-1}$, $17\,000\,\text{V cm}^{-1}$ and $19\,000\,\text{V cm}^{-1}$ at 20, 30 and 40 Torr respectively. Figure 6.19 shows typical events from the 30 Torr run for $400\,\text{V cm}^{-1}$ and $1700\,\text{V cm}^{-1}$ transfer fields.

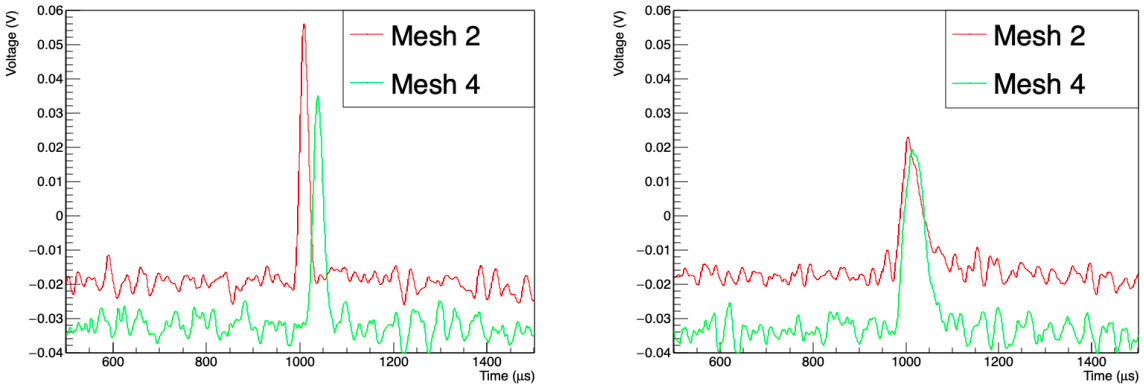

Figure 6.19: The alpha waveforms on meshes 2 and 4 for 30 Torr SF_6 with a $400\,\text{V cm}^{-1}$ transfer field (left) and $1700\,\text{V cm}^{-1}$ transfer field (right).

The signal on each mesh consists of a single peak which occurs later on mesh 4 than mesh 2, with the delay being shorter for the larger $1700\,\text{V cm}^{-1}$ transfer field. The delay between the peak on the two meshes can be attributed to the transfer time which is determined for each transfer field setting from the average of the difference between the peak times on meshes 2 and 4. Figure 6.20 shows the transfer time against reduced transfer field at 20, 30 and 40 Torr along with the best fit to the data using Equation 6.4.

The relationship between the determined transfer time and the reduced transfer field is well described by Equation 6.4 for all pressures. The reduced mobility is determined to be $\mu_0 = (33.6 \pm 0.5)\,\text{mm}^2/\text{V/s}$.

The literature value for the mobility of SF_6^- ions is around $53\,\text{mm}^2/\text{V/s}$ with variation of the order $5\,\text{mm}^2/\text{V/s}$ between experiments [121]. The value arrived at is significantly below this, possible reasons for this might be gas contamination, space-charge effects in the hole or a significant amount of the drifting charge not being SF_6^- ions. It should be noted that the sole canister of SF_6 available in the lab for these experiments is fairly old,

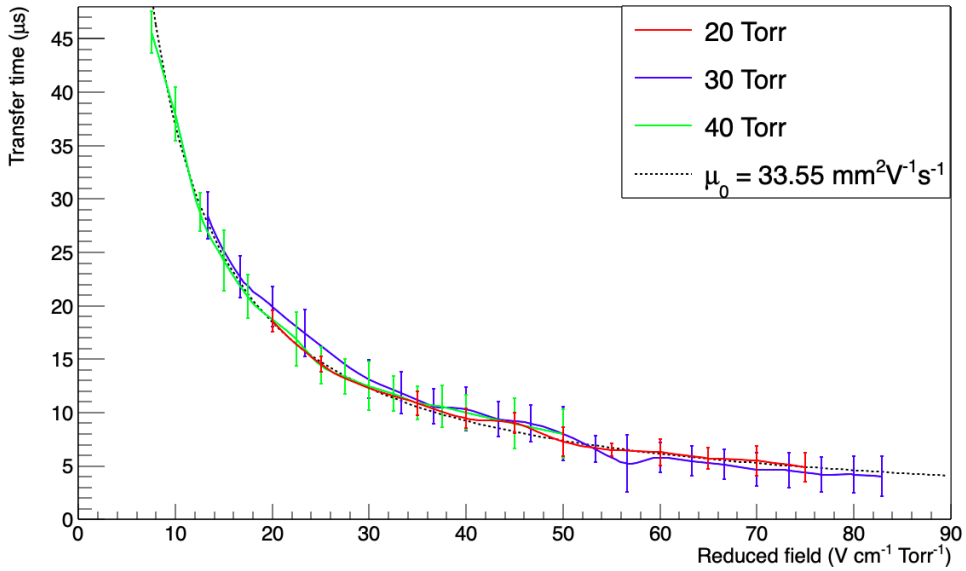

Figure 6.20: The transfer time from mesh 2 to mesh 4 in SF_6 against reduced drift field. Dotted line indicates the best fit to data ($\mu_0 = 33.55\,\mathrm{mm}^2/\mathrm{V/s}$).

and there is a potential that the contained gas has suffered some degradation. The short drift length and high charge density that should result from the first amplification stage might contribute to the second two factors.

6.5.3 Conclusions

The transfer field's purpose to transport charge from the first amplification stage to the second amplification stage. The charge survival rate in the transfer gap was shown to increase with transfer field, although with diminishing returns at higher fields. This is consistent with expectation as the main contributions to charge loss in the transfer gap is expected to be inefficient charge extraction through mesh 2 and losses to the hole walls. Both of the loss factors were expected to be ameliorated by higher transfer fields, which is reflected in the data. A transfer field in the region $600\,\mathrm{V\,cm^{-1}}$ to $1000\,\mathrm{V\,cm^{-1}}$ was determined to be sufficient to minimise losses during charge transfer.

Additionally using the delay between signal observed from alpha tracks on meshes 2 and 4, a measurement of the mobility of ions in the transfer gap in SF_6 was arrived at. The transfer times were found to be consistent with charge carriers with a reduced mobility of $(33.6 \pm 0.5)\,\mathrm{mm}^2/\mathrm{V/s}$.

6.6 Ion feedback effect in SF_6

During the ^{55}Fe runs in low pressure SF_6 irregularities in the detected waveforms were observed. Irregular waveforms exhibited a 'ringing' effect; two sample waveforms which exhibit this ringing are shown in Figure 6.21.

The waveforms exhibit periodic peaks in the voltage over an interval of about 200 µs after the initial signal peak. Multiple peaks are expected in electron recoil data due to the tendency of electron recoils to create clusters of charge, as was seen in Chapters 3

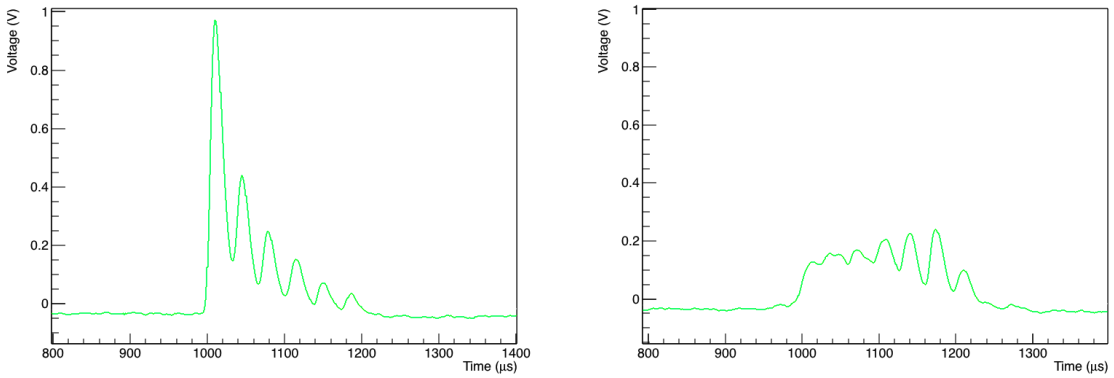

Figure 6.21: Sample ^{55}Fe events for 20 Torr SF_6 with 400 V cm^{-1} transfer field and 22 500 V cm^{-1} amplification fields, exhibiting the 'ringing' effect.

and 4. The number of peaks, the constant separations and the total width of the event are however not typical of 5.9 keV electron recoils at the pressure and drift field of the detector.

This ringing behaviour was not apparent in all the waveforms and was only observed in the 20 and 30 Torr runs. The absence of the ringing effect from the runs at higher pressure suggested that the ringing was caused by some physical effect outside the normal gas amplification and not due to an issue with the electronic set-up.

In order to investigate the origin and nature of these events a Fourier analysis of the signal waveforms was performed for runs with varying pressure and drift, transfer, collection and amplification fields. Fourier transforming the waveforms into the frequency domain enabled the characteristic frequency of the effect to be extracted disentangled from the non periodic underlying structure. For runs which did not exhibit the ringing effect, the frequency spectrum showed a smooth exponential-like drop off in the value of the transform with increasing frequency. Runs with the ringing effect additionally showed localised peaks in frequency, with the centre of the largest peak corresponding to the period of the observed ringing. An example of the frequency spectrum for a cumulative 500 events for a run displaying the ringing effect is shown in Figure 6.22.

The peaks in the frequency spectrum are centred at 28 kHz and 57 kHz on top of the exponential background. 28 kHz corresponds to a 36 µs period, which is consistent with the peak separations observed in the most well resolved events. The higher frequency peak, at 57 kHz, is the second harmonic of the first peak at 28 kHz. The second harmonic of the frequency associated with the ringing was consistently observable in the Fourier transform, as was the third harmonic sometimes. The relative height of the first peak in frequency space can be considered a measure of the strength of the ringing effect. The centre of the same peak gives a measure of the characteristic frequency of the ringing.

The strength and frequency of the ringing was found to be independent of the drift and collection fields. Conversely correlations between the amplification and the transfer fields were established.

The transfer field was found to have a relationship to the characteristic frequency of the ringing effect. The relationship between frequency and transfer field for runs where the ringing effect was observed is shown in Figure 6.23

The extracted characteristic frequency of the ringing effect is linear with the transfer field and also inversly proportional to pressure. The associated period corresponds to

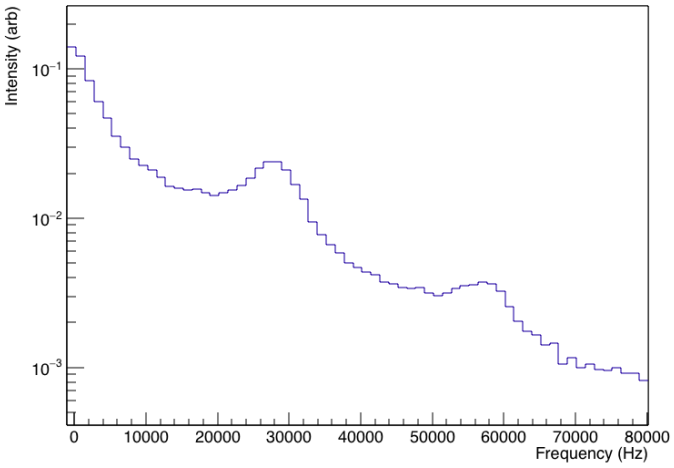

Figure 6.22: Fourier transform of 500 signal events in 20 Torr SF_6, 400 V cm^{-1} transfer field and 22 500 V cm^{-1} amplification fields.

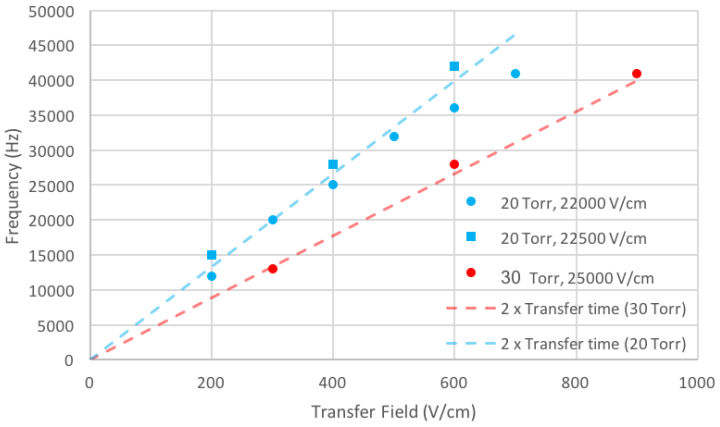

Figure 6.23: Average frequency of the ringing effect determined from Fourier transform against the transfer field for 20 and 30 Torr SF_6, amplification fields and pressures are indicated in the legend. The lines plotted are $\frac{1}{2t_{tr}}$ where t_{tr} is the transfer time calculated from the measured mobility, 33.6 mm^2/V/s.

twice the transfer time for negative ions in the transfer gap measured in Section 6.5.2.

The strength of the ringing, as measured by the height of the first peak above the background in frequency space, was proportional to the amplification fields. In 20 Torr SF_6 when both amplification fields were at or below 21 kV cm^{-1} the peak was not distinguishable, for voltages larger than this the peak became distinguishable in frequency space with increasing magnitude proportional to the voltage. The minimum amplification fields required to observe the effect at 30 Torr was 24 kV cm^{-1} and the effect was not observed at any of the applied voltages at higher pressures.

At the highest amplification field used in 20 Torr SF_6, the device can enter a regime where instead of decaying away, the ringing effect increases in magnitude. An example of an event displaying the behaviour is shown in Figure 6.24.

The initial small peak is followed by increasingly large peaks up to the saturation of the digitiser range, the signal then fluctuates between 0.5 V and digitiser saturation at 1 V while continuing to display separable peaks on the timescale of the ringing effect. The

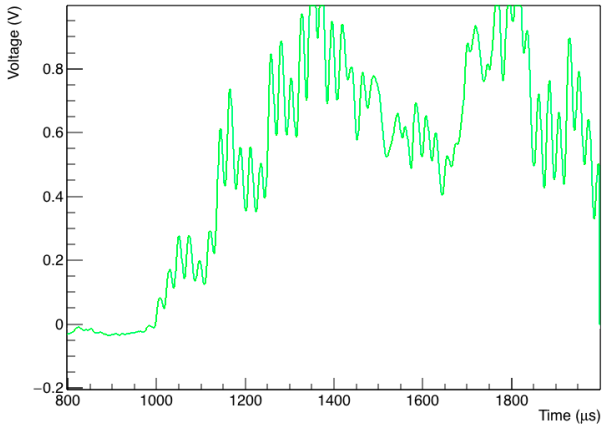

Figure 6.24: Onset of instability current 20 Torr SF_6 with 600 V cm^{-1} transfer field and 22 500 V cm^{-1} amplification fields.

waveform behavior on the right hand side of the figure was continuous after this event until the device voltage was reduced about ten seconds later. This suggests that the ringing effect is caused by some form of feedback where the initial signal is reproduced after a delay with a factor which scales the magnitude. In the runaway state in Figure 6.24, the reproduction factor exceeds one and the ringing gets increasingly large. The mechanism does however appear to be self-limiting, and the signal does not appear to significantly exceed the ±1 V range of the digitiser.

The potential mechanisms for the ringing effect which were considered included feedback in the electronic amplification, secondary photo-ionisation, and the liberation of secondary electrons by backflowing positive ions. To be consistent with the observed ringing effect, the mechanism must explain the relationship between the frequency of the ringing and the transfer field and the magnitude of the ringing and the amplification fields.

Electronic feedback would be caused if the output of some part of the electronic amplification chain were coupled to the input, the re-amplification of collected signal might result in feedback peaks following the initial signal arrival. The absence of the ringing effect from higher pressure data and the dependence on the transfer and amplification fields precludes electronic feedback and other mechanisms which were not reliant on charge transport in the gas.

The scintillation light produced by multiplication of charge can propagate in the gas and cause ionisation at another point in the gas, this photo-ionisation is a known source of secondary ionisation in gas detectors [147,148]. In the context of the MM-ThGEM most of the scintillation light would be produced in the second avalanche field, concurrent with the observation of signal. The scintillation photons would then ionise electrons nearer the top of the hole which would be transported back down to the second amplification field and would induce another avalanche. This model would explain the relationship between the amplification fields and the magnitude of the feedback as charge from secondary photo-ionisation would be multiplied by a factor controlled by the amplification fields of the detector. Secondary photo-ionisation however would not produce the subsequent peaks with observed time constant equal to twice the ion drift time and does not explain the absence of the effect at higher pressures when the gain is the same.

Another potential source of secondary ionisation and a mechanism for the creation of

the observed feedback effect is the backflow of positive ions. The impact of positive ions on certain surfaces can produce ionised electrons in a manner analogous to the photo-electric effect [149]. In the MM-ThGEM positive ions formed in the second amplification field could propagate back through the transfer region and the first amplification region and then impact on mesh 1 propelled by the high field of the first amplification region. The liberated electrons would then be multiplied in the first amplification stage before being traveling back through the transfer region and being multiplied again by the second amplification field. The second avalanche will produce its own positive ions which can start the cycle again, resulting in a feedback effect with the reproduction factor controlled by the amplification fields and period equal to the time taken for the charge to make a round trip. The mobility of the SF_6^+ ion is very similar to that of the SF_6^- ion, consequently the time taken for backflowing positive ions to cross the transfer gap should be about the same as the transfer time of negative ions going the other way [121]. The fact that the effect was not observed for higher pressures could be attributed to the lower velocities of the positive ions in the first amplification field which would reduce the probability of electron emission from the first mesh.

The only considered mechanism which well explains observed frequency of the ringing and its relationship with the amplification fields and pressure is the positive ion feedback effect. The period of the feedback effect in particular is not well explained by any model that doesn't require the transport of ions through the transfer field twice.

The feedback effect results in significant distortion of the signal and might contribute to the anomalous measurements of the detector performance at 20 Torr in Sections 6.4 and 6.5. In order to mitigate the feedback effect, care should be in future to avoid operating the MM-ThGEM in regimes where significant distortions from the effect are present in the signal. At more than 30 Torr the effect is not a concern, and at 20 and 30 Torr care should be taken to avoid operating the device at high amplification fields.

A positive aspect of the ion feedback effect is that it can be identified fairly easily before the runaway feedback occurs and it does not cause any discernible damage to the detector electronics or the MM-ThGEM itself. This is in contrast to the violent sparking events which characterise the limit of the ThGEM operating range which can damage the ThGEM and electronics and have a threshold which is hard to precisely determine without causing a sparking event.

6.7 The operation of the MM-ThGEM in CF_4:SF_6

Mixing a small amount of SF_6 into CF_4 has been shown to preserve the negative ion drift properties of SF_6 while enhancing the fraction minority charge carriers [150]. Maintaining the negative ion drift behaviour of SF_6 but reducing the overall SF_6 content of the fill gas is desirable due to the large global warming potential of SF_6. This is particularly important when it comes to scaling to a large detector such as the proposed Cygnus 1000 m^3 detector which will require significant quantities of gas. Enhancing the fraction of minority charge carriers would also make fiducialisation easier for large detectors, where the detection of minority carriers is vital for determining the offset of an event from the detector anode.

The operation of the MM-ThGEM detector in CF_4:SF_6 will be a useful benchmark if that gas is selected as the fill for a larger detector. It is also useful for exploring the use of the detector in a gas with ions that have significantly different mobilities to SF_6^-.

The performance of the MM-ThGEM was evaluated for CF_4:SF_6 mixtures at 30:2.2 Torr and 50:3.5 Torr, which are approximately 14:1 mixtures. The MM-ThGEM setup

inside the vessel and the instrumentation and bias scheme were identical to the setup described in Section 6.1.1. For all runs the first mesh was biased to 140 V and the cathode was biased to −500 V, the first amplification field 20 500 V cm^{-1} for the 30:22 Torr runs and 24 500 V cm^{-1} for the 50:35 Torr runs.

The varition in the device gain with the transfer and second amplification field were explored at both pressures. Figure 6.25a shows the gain of the device in the CF_4:SF_6 mixture against transfer field and Figure 6.25b shows the gain of the device against the second amplification field.

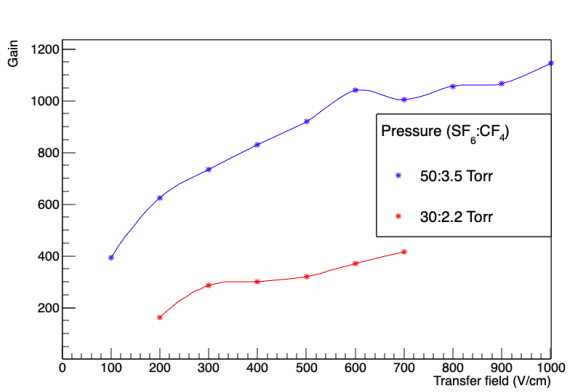

(a) Transfer field against gas gain.

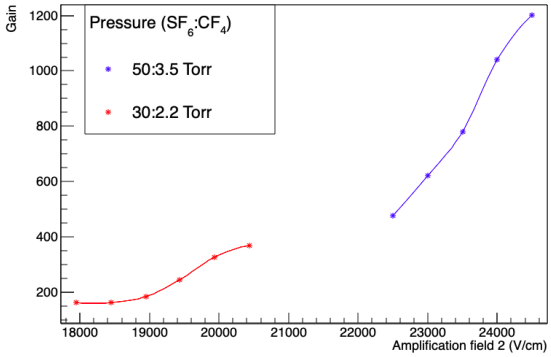

(b) Second amplification field against gas gain.

Figure 6.25: Variation in the gain with transfer field and second amplification field for the MM-ThGEM in CF_4:SF_6 mixtures at 30:2.2 Torr and 50:3.5 Torr.

When the second amplification field was varied in Figure 6.25b the transfer field was set to 600 V and The amplification field required to achieve a given gain is observed to be significantly lower in CF_4:SF_6 than in pure SF_6; for example the gain for matching amplification fields of 20 500 V cm^{-1} in 30:2.2 Torr CF_4:SF_6 is 370, to get an equivalent gain in 30 Torr of pure SF_6 requires amplification fields of ≈22 300 V cm^{-1}. The overall trend is for the gain to increase with increasing amplification field, although the relationship does not appear to be exponential as might be expected.

When the transfer field was varied as in Figure 6.25a, the second amplification field was set to 20 500 V cm^{-1} for the 30 Torr CF_4 run and 24 000 V cm^{-1} for the 50 Torr run. The variation of the gain with transfer field follows the same general shape as in pure SF_6, tending to plateau off at high transfer fields. The fact that the gain compares fairly similarly to the pure SF_6 data in Section 6.5 suggests that the exact mobility of the drifting ions might not be playing a significant role in the losses incurred in the transfer field.

The CF_4:SF_6 combination shows a significant amount of promise, although it was decided to push on to operating the MM-ThGEM-micromegas combination rather than continue to perform a more comprehensive characterisation of the operation of the MM-ThGEM in the gas mixture.

6.8 Conclusions

This section demonstrated the operation of the novel MM-ThGEM device in a negative ion gas for the first time. The device was initially operated in low pressure CF_4, which

demonstrated the importance of the collection field and the subsequent simulations of electron transport demonstrated a number of the competing the processes occurring during the charge transport in the gas. Moving to SF_6 considerably altered the dynamics of the charge transport, the range of collection fields explored were shown to be sufficient to collect the majority of the charge, consistent with simulation of ion drift in the gas.

The amplification fields enabled an estimation of the Townsend parameters of SF_6 and it was demonstrated that gains in excess of 1000 were achievable with fairly little tuning in low pressure SF_6. Varying the transfer field enabled a measurement of the mobility of negative ions in the gap, although the mobility arrived at was somewhat below the literature value which might point towards some more complex effects occurring in the gap than expected. A gradual increase of the gain in the gap with increasing transfer field over a range of voltages demonstrated that more efficient transfer of charge could be achieved by increasing the transfer field up to about $1000\,\mathrm{V\,cm^{-1}}$.

The device was found to be much more stable than a ThGEM, with none of the damaging sparks which are observed at the ThGEM operating point in SF_6. At 20 and 30 Torr the device's failure mode was a ringing effect identified as positive ions feedback, while this had a distorting effect on the detector signal at high amplification fields it was also considerably less destructive to both the electronics and MM-ThGEM than the sparks observed on ThGEMs.

A further gas mixture, CF_4:SF_6 was tentatively explored and demonstrated promise with significantly higher gains than were observed in SF_6 alone for similar pressures and field values.

Chapter 7

Characterisation of a Bulk Resistive Layer Micromegas with MM-ThGEM Amplification Stage

The ThGEM and MM-ThGEM discussed in previous chapters have simple planar readouts which are sensitive only to the arrival time of charge at the anode plane. If working well, these devices can provide a one dimensional projection of the ionised charge distribution in space. However, the charge ionised by electrons and nuclear recoils in the gas of a TPC is distributed in all three dimensions of space; a 1-D projection loses significant shape information which, if captured, can be useful for directionality and discrimination [83].

The advantages of reconstructing a recoil in three dimensions are however offset by the high cost of readouts capable of doing so. The one of most significant cost for large scale detectors is the instrumentation of the detector with sensitive electronics; readouts capable of full 3d reconstruction (like pixel readouts) require a significant number of electronics channels to capture the requisite detail.

An intermediate type of readout geometry is a strip based readout, where the readout elements consist of long strips in one or two directions on a plane. Strip based readouts can produce 2d projections of the charge distribution in space and require significantly less instrumentation, and are therefore much cheaper than pixel based 3d readouts. Strip based readouts have been determined to have the best trade off between sensitivity and cost for scaling into a large gas based recoil detector for WIMP detection [83].

A micromegas is a type of avalanche detector which uses a plane of mesh above an anode plane to create the amplification field [151]. Micromegas can be manufactured in bulk fairly cheaply and support strip readouts, as such they represent a scalable technology for high resolution recoil reconstruction [152].

The good cost-to-sensitivity ratio of strip based readouts, the economical micromegas device and the ability of negative ion gasses to extend the drift region available to a TPC is a combination which would have comparatively cheap volume cost for a TPC detector of a given sensitivity to nuclear recoils. The use of a micromegas strip readout in the negative ion drift gas SF_6 has been undertaken previously in [153], although the authors did not obtain gains sufficient to observe low energy recoils. The combination of a micromegas with an additional gain stage, such as the MM-ThGEM described in the last chapter, has the capability to obtain overall gains sufficient to observe low energy (keV) events on a strip based readout.

This Chapter describes the characterisation of a $10 \times 10\,\mathrm{cm}$ bulk resistive layer mi-

cromegas detector with a 256 µm amplification gap in low pressure gas at Sheffield in combination with the MM-ThGEM device described in Chapter 6. The main goals are to demonstrate the operation of the micromegas and MM-ThGEM combination, to obtain overall gains sufficient to observe KeV events on a strip based readout and to demonstrate the ability of the detector to reconstruct ionisation tracks which are extended in space.

Section 7.1 describes the micromegas detector and the electronic setup, and the calibration of the electronic channels as well as the radioactive source locations used for different characterisation runs. The operation of the micromegas as a stand-alone detector in SF_6 and CF_4 is discussed in Section 7.2. Section 7.3 discusses the micromegas-MM-ThGEM detector combination and its operation in CF_4, SF_6 and CF_4:SF_6 mixtures. Section 7.4 will present an analytic model of the charge dissipation effect in the resistive layer and compare it with data. Finally the overall conclusions are discussed in Section 7.5.

7.1 Micromegas design, experimental setup and calibration

7.1.1 Micromegas design

A micromegas is a type of parallel plate avalanche detector which uses a plane of mesh above an anode plane to create the amplification field [151]. The anode can be in the form of a plate, strips or pixels enabling one, two or three dimensional reconstruction of events in the detector. A further refinement to the micromegas is to protect the sensitive components with a layer of a resistive material, this helps protect the device and readout electronics from damage from sparks.

The defining characteristic of a given resistive layer is it's surface or sheet resistivity, R_s which can be determined for a rectangular sheet of material with electrode strips across opposite sides by the equation

$$R_s = \frac{V}{I}\frac{W}{L}, \tag{7.1}$$

where W and L are the width and length of the rectangle and electrodes are on the edges from which width is measured. The symbols V and I are the potential difference between electrodes and the current flowing between them; consequently the units for surface resistivity can be dimensionally reduced to $\Omega\,\mathrm{m/m}$. Rather than cancel away the length dimensions this is conventionally written $\Omega/\square$ with the unitless symbol $\square$ used to distinguish surface resistivity from conventional resistance which also has units of Ω.

The micromegas used for this work has a gap of 256 µm a sensitive area of $10\times10\,\mathrm{cm}$, the signal readout consists of two sets of orthogonal strips with each set having a pitch of 250 µm. The anode is a Diamond Like Carbon (DLC) bulk resistive layer with a resistivity of $50\,\mathrm{M\Omega/\square}$. The micromegas was manufactured to order along with the MM-ThGEM at the CERN MPGD production facility. A cross-sectional diagram and a picture of the micromegas is shown in Figure 7.1.

The left hand diagram in Figure 7.1 depicts a cross-section of the sensitive region of the micromegas device. The two sets of strips are embedded in the micromegas board, on top of which is deposited a thin resisitive layer. The two strip orientations are designated 'x' and 'y' with the y-strips embedded above the x-strips in the micromegas board. The x-strips have a width of 200 µm and the y-strips have a width of 80 µm, the smaller widths of the y-strips is to reduce the occlusion of the x-strips to the collected charge. The strips

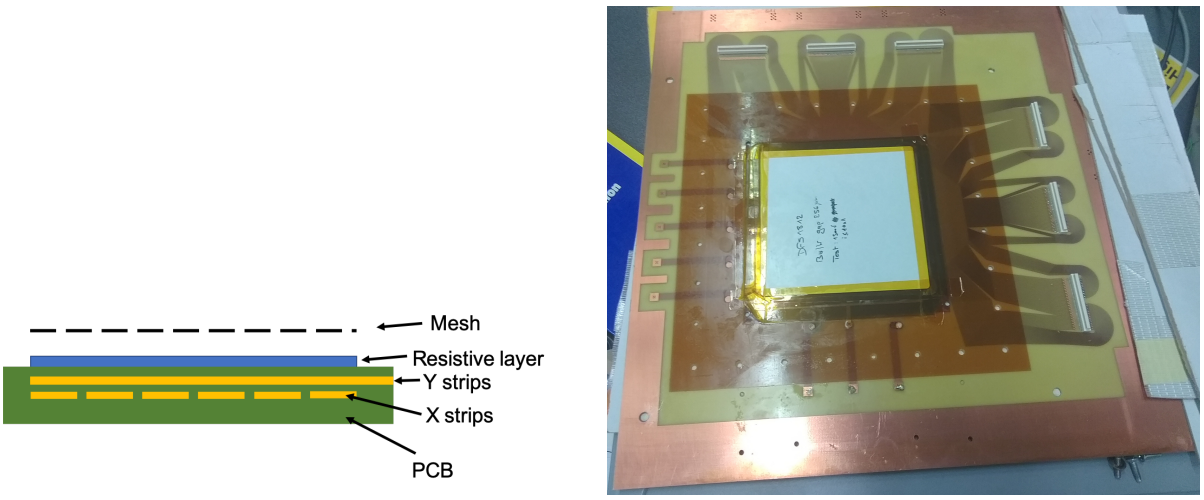

Figure 7.1: Cross sectional diagram (left) and image (right) of the micromegas with the sensitive area covered.

themselves are completely insulated from the resisitive layer and do not collect any charge, as such all the signal observed on the strips is induced by the motion of charge in the vicinity of the strips as in the Shockley-Ramo theorem [76]. The amplification field is formed by the mesh suspended above the resisitive layer which is supported by a series of pillars.

On the right in Figure 7.1 is a picture of the micromegas, in this picture the central sensitive region is covered to exclude dust which can degrade the performance of the device. The strip traces leading from the sensitive region to the board connectors are visible to the right and top of the sensitive region. Bias for the mesh and resisitive layer is applied through the solder pads below the sensitive region. The y-strips are orientated horizontally in the picture and the x strips are orientated vertically.

7.1.2 Cathode location and drift field geometry

A 10×10 cm square cathode was used to generate the drift field with a few different offsets from the micromegas/MM-ThGEM plane but generally around 2.7 cm. A solid copper cathode was used in most of the runs and a transparent mesh cathode of the same dimensions was used for runs where the ^{241}Am source was located behind the cathode to produce steeply angled alpha tracks.

The analytical software Ansys was used to explore the shape of the drift field to evaluate the optimal field cage design. For a 10×10 cm cathode at 3 cm or less from the collection plane it was found that the drift field in the centre of the micromegas was effectively linear without the presence of a field cage at operating voltages. As only a small fraction of the available strips could be instrumented, no loss of sensitivity was accrued by only instrumenting the central strips and avoiding the need for a field cage. A field cage would however be necessary if strips near the edge of the device were instrumented, distortions to the drift field for the implemented cathode geometry extended to $\sim$2 cm from the edge of the readout.

7.1.3 Instrumentation of the micromegas strips

The strips were instrumented with CR-111 charge sensitive preamplifiers and CR-200 4 µs shaping amplifiers [114, 115]. The resulting signal was converted to digital format with an NI 5751 digitiser and saved to disk on a connected PC running custom LabVIEW DAQ software; a diagram of the amplification and digitisation chain for the micromegas is shown in Figure 7.2. A voltage threshold on the input signal set in the LabVIEW software was used to trigger storage of discrete events with a window of ±1000 µs from the trigger time with a sampling time of 1 µs/bin.

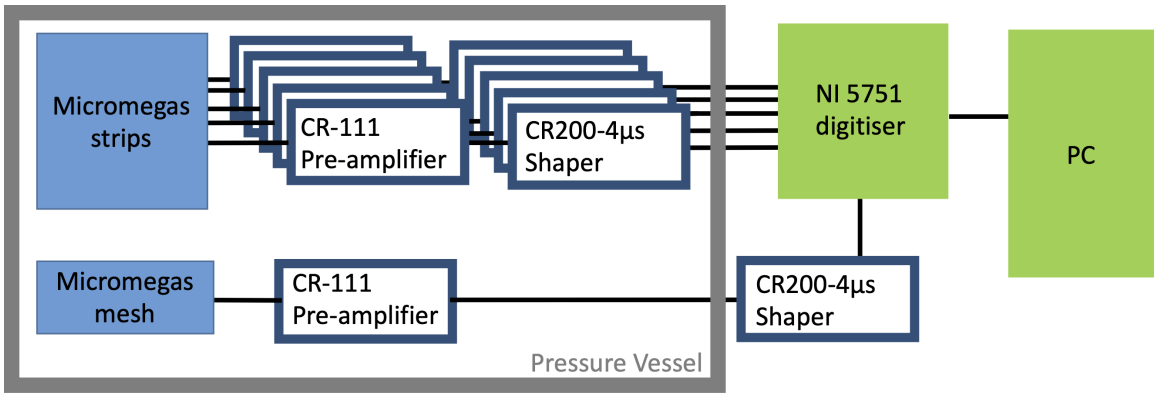

Figure 7.2: Diagram of the amplification and digitisation chain for the micromegas strips and mesh.

The signal from the micromegas mesh was also passed through an amplification chain, with the preamplifier decoupled from the bias voltage through a capacitor. Apart from the decoupling capacitor the readout and digitisation chain was the same as the strips. The output from the mesh amplification chain was either digitised (shown in diagram) or connected to an oscilloscope to monitor the detector.

Due to hardware constraints there were only 16 channels total which could be both amplified and digitised. If the available digitisation channels were evenly divided between x and y strips, the sensitive area at the strip pitch of 250 µm would be 2×2 mm. As shown in Chapter 4, ^{55}Fe electron recoils will have lengths on the order of 2 mm at low pressures so this sensitive area will only capture all the charge for very well centred events. To increase the sensitive area with the available electronics, adjacent strips were grouped into pairs and instrumented with the same channel giving an effective strip pitch of 500 µm and a sensitive area of 4×4 mm.

7.1.4 Test source position and handling

An ^{241}Am source and an ^{55}Fe source were used to characterise the device. A total of six ^{241}Am source locations were used in different runs for the bare micromegas and micromegas with MM-ThGEM for different gasses and pressures, Figure 7.3a shows the source locations for the x, y, x-y, and shutter runs. In the 'x' run all 16 channels were used to instrument the x strips, likewise in the 'y' runs only y strips were instrumented. In the 'x-y' and 'shutter' runs eight channels instrumented each of the x and y strips, in all runs the effective pitch was 500 µm. For both the 'x' and 'y' runs another run was performed with the source position reflected around the centre of the micromegas, these runs are designated 'xr' and 'yr'.

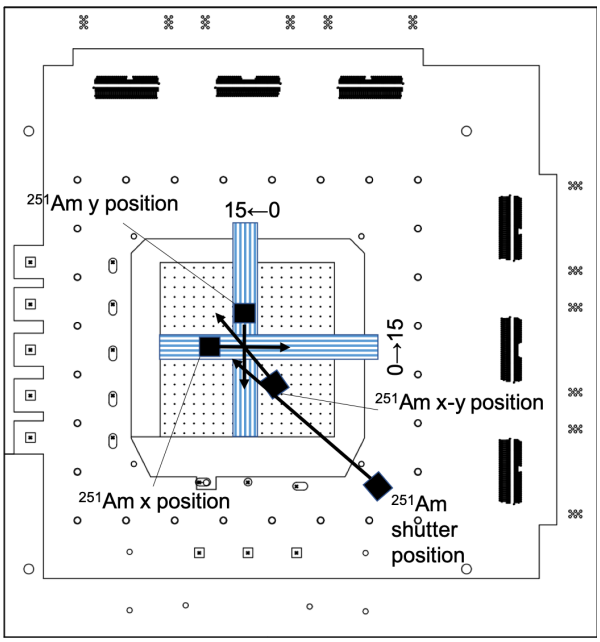

(a) Plan view of source location x, y, x-y and shutter runs. Instrumented strips and the channel numbering scheme for the 'x' (vertical strips) and 'y' (horizontal strips) runs indicated.

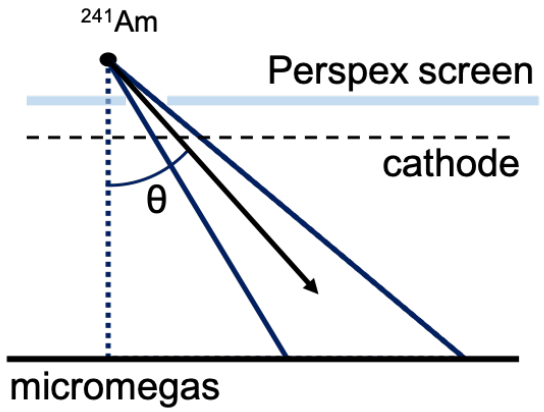

(b) Side view of source location for x, y, x-y runs, maximum and minimum incidence angle indicated by blue lines.

Figure 7.3: Diagrams of ^{241}Am source locations, alpha direction indicted by black arrows.

Figure 7.3b shows how the ^{241}Am source was positioned relative to the cathode and micromegas for the non shutter runs. For these runs a hole in a perspex screen between the cathode and source was used to constrain the angle of the incoming alphas from vertical (θ in Figure 7.3b). The alphas were constrained such that they cross between the instrumented strips and the cathode at a steep incidence angle. The minimum and maximum values of the angle θ in the x and y setups were measured to be 43° and 57° respectively. The maximum line of sight distance between the ^{241}Am source and the top plane of the detector was less than 7 cm which means the 5.5 MeV alphas should not be stopping in the gas at the pressures used.

The shutter run utilised a source shutter to enable the alpha source to be turned 'on' and 'off'. In these runs the alphas have considerably longer travel distance of ∼12 cm and are close horizontal relative to the micromegas. The direction of the alphas is not significantly constrained in the shutter runs except by the geometry of the drift region. The shutter runs were primarily used to confirm the detector was working correctly with an intense signal source which could be activated and deactivated in place.

7.1.5 Electronic gain of amplification chain

As described in Section 7.1.3, the signal on each of the instrumented readout strips is amplified by an individual electronic amplification chain. There is some variation in the gain between each of these data channels and to account for this a calibration run was performed before data taking began to allow for compensation for the gain variation in the analysis and to enable a determination of the gain of the device.

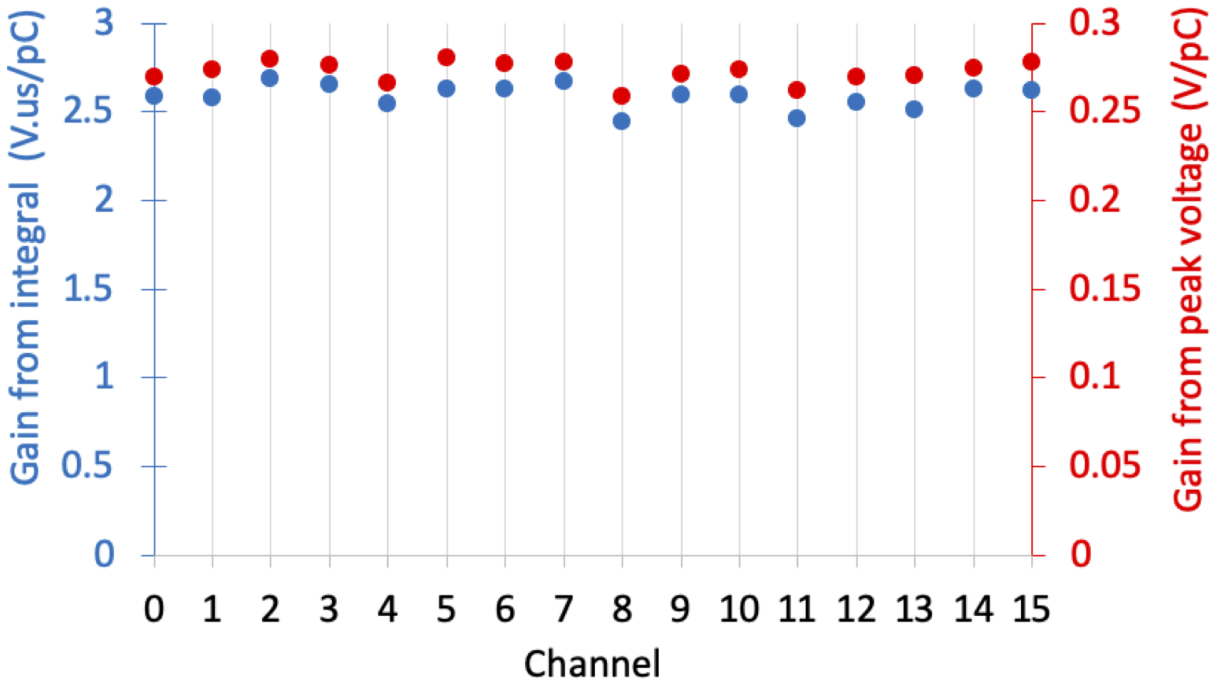

Figure 7.4: The electronic gain of each micromegas channel determined from the peak voltage (red) and integral (blue) from the injection of a 100 mV test pulse through a 15 pF capacitor.

To obtain an electronic calibration of a signal channel, test pulses of 100 mV from a TC-814 pulser were injected onto a 15 pF capacitor connected to the preamplifier input of the amplification chain and the signal output of the chain was recorded by the DAQ system. This process was repeated individually for each of the 16 signal channels.

As described previously in Chapters 3 and 6 there are two metrics which can be obtained for the signal magnitude, the peak voltage and the integral voltages. The applicability of each of these metrics is dependent on the relative speed of the signal shaping and charge collection. For charge collection which is fast on the timescale of the signal shaping, peak signal voltage is appropriate, whereas if charge is collected slowly on the timescale of the signal shaping the integral voltage is more appropriate.

The waveforms were processed with a simple pedestal subtraction and the maximum and integral peak voltage for each event was determined. The electronic gain of each channel was determined in terms of peak output voltage with $gain = \frac{V_{out}}{Q_{in}}$ where V_{out} is the peak output voltage and $Q_{in} = 1.5\,\text{pC}$ is the injected charge determined from the test pulse voltage and capacitance. The electronic gain in terms of integral voltage is determined in the same way as from peak voltage with the integral of the peak replacing V_{out}. The electronic gain in terms of peak voltage and integral voltage of each channel, determined from the average for all the events in the calibration run is shown in Figure 7.4.

As seen in the figure, the integral voltage is close to ten times larger than the peak voltage, with average integral gain being around 2.6 V.µs/pC and the average voltage gain being $0.27\,\text{V}\,\text{pC}^{-1}$. The standard deviation in the distribution of peak heights on an individual channel is around 1 mV and the standard deviation in the distribution of integral voltages is 10 mV.µs. As a consequence of the small standard deviations in the peak parameters across the calibration run, the random error is too small to be able to be seen in the figure.

The gain variation between channels on the order of 5% and the different gain on each channel is reflected by both the integral and peak methods. The gain on the shaper boards is controlled manually by a potentiometer so a small variation on the order of about 5% due to slightly different potentiometer settings is consistent with expectation.

7.1.6 Calibration with micromegas mesh capacitance

It is expected that there is significant capacitance between the mesh and the strips, this enables an in-situ calibration of the channels using the mesh as a capacitor. We can get a very approximate expected capacitance between the strips and mesh with the equation for the capacitance of a wire next to a plane which is

$$C = \frac{2\pi l\epsilon}{\ln\left(\frac{d}{a} + \sqrt{\frac{d^2}{a^2} - 1}\right)} \tag{7.2}$$

where l is the length of the wire, ϵ is the permittivity of the material in the gap, d is the distance between the plane and wire and a is the wire radius. Using $l = 10.5\,\text{cm}$, $d = 331\,\mu\text{m}$ and $a = 40\,\mu\text{m}$, and using the permittivity of free space gives a capacitance per strip of 2.1 pF for the y strips. The x-strips are wider (200 µm width) which is to counteract the larger distance between the strips and the mesh and the fact that parts of the x strips are occluded by the y strips. Using $l = 10.5\,\text{cm}$, $d = 360\,\mu\text{m}$ and $a = 100\,\mu\text{m}$ the capacitance found for the x strips is 3.6 pF. Although it should be noted that the fact the y strips are between the x strips and mesh would significantly reduce this value.

For the mesh calibration, a test pulse was injected onto the micromegas mesh and signal was read from the strips. The strips on the micromegas were paired into twos and channels 0-7 were connected to the central eight x-strip pairs and channels 8-15 to the central eight y-strip pairs. The peak voltages on each channel for the 150 mV and 200 mV test pulses is shown in Figure 7.5.

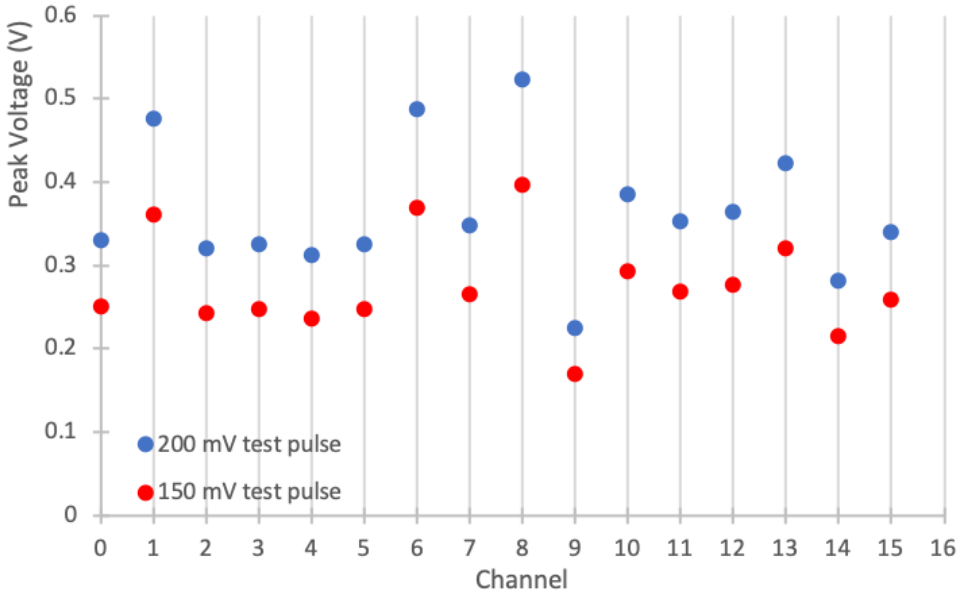

Figure 7.5: The pulse heights on each channel for a test pulse injected onto the micromegas mesh.

In this case there is a fairly large spread between channels and it is not accounted for by the different gains of the electronic chains shown in Figure 7.4 or by random error

which is again too small to be visible on this scale. The variation in the pulse heights might be attributed to poor connection between the channels and strips; the pitch of the channels on the connectors are extremely small and challenging to work with.

The average capacitance between the mesh and channels is 6.7 pF which assuming the strips are correctly grouped gives a per strip capacitance of about 3.4 pF. The determined capacitance of 3.4 pF is quite close to the analytical value of 3.6 pF estimated for the x strips, although further from the 2.1 pF estimated for the y-strips. The fairly crude approximation of the strips as wires and the neglection of the dielectric properties of the intervening resisitive layer might contribute to the difference between the analytic model and measurement. It is noticeable that there isn't a significant difference in the capacitance of the x (chn 0-7) and y (chn 8-15) strips, this can be attributed to the higher width of the x strips counteracting the longer distance from the mesh.

The variation between the pulse height on each of the channels from the pulse injection onto the mesh was found to translate to signal from events due to alpha and electron recoils as well. Rather than attempt hardware corrections for the signal variation it was decided that corrections in software would be more reliable. In order to obtain a uniform response from each strip, the data was scaled according to the mesh calibration. Each channel was scaled by the factor V_0^{calib}/V_n^{calib} where V_n^{calib} is the peak voltage in the mesh calibration for channel n which is the channel being scaled. For gain and threshold calculations it is then assumed that the scaled channels all have the same electronic gain as channel 0.

7.2 Micromegas with no gain stage

The micromegas was first operated without a MM-ThGEM amplification stage to explore the response of the micromegas on its own. The response of the detector to alphas from ^{241}Am and low energy electron recoils are explored to discover if the micromegas can demonstrate tracking and a low energy threshold. Also of interest is effect of the resistive layer on the response of the device to collected charge; as signal formation in this type of micromegas is reliant on the motion of charge in the vicinity of the strips the evacuation of charge through the resistive layer might have an effect on the signal. This is particularly relevant at the comparatively long timescales of charge collection from negative ion drift gases. It is anticipated that the gain of the micromegas device on its own will be extremely low in SF_6 so part of the characterisation is also undertaken in CF_4.

A mesh cathode was used with a drift gap of 2.7 cm between the cathode and micromegas mesh. The resisitive layer is grounded and the drift and amplification fields are generated by biasing the cathode and micromegas mesh to negative voltages. The bias voltages are applied through low pass filters to both the cathode and micromegas mesh to minimise the noise on the readout channels.

7.2.1 ^{241}Am in CF_4

The first runs were performed in CF_4 which has the advantage of having a far larger gas gain than the negative ion drift gasses and should enable a confirmation that the micromegas is working correctly before moving on to SF_6 and mixtures. The detector is exposed to an ^{241}Am source which produces 5.5 MeV alpha particles . The alpha particles provide extended tracks with a large amount of ionisation, these should be observable with fairly low gas gain and the observation of an extended track provides a demonstration of the micromegas response to spatially extended events.

The ^{241}Am source was placed in the x-y position with the x and y strips instrumented with 8 channels each, and the vessel was pumped down before filling with CF_4. Figure 7.6a shows the typical signal for an ^{241}Am generated alpha event on the micromegas in 28.7 Torr CF_4 in an x-y run, the signal from the x strips is in red and the signal from the y strips is in blue.

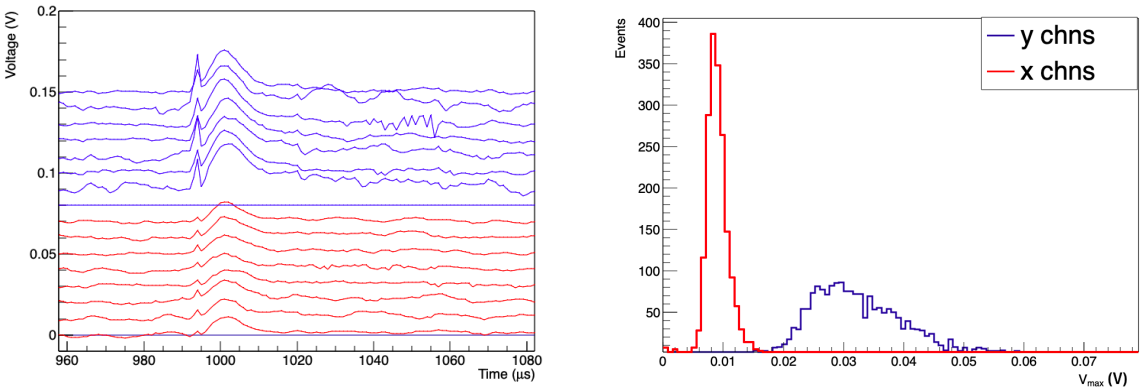

(a) Typical alpha event in CF_4 x-y run, x strips in red and y strips in blue.

(b) Histogramed peak voltages for the x channels and y channels.

Figure 7.6: ^{241}Am x-y run in 28.7 Torr CF_4 with micromegas voltage 485 V and cathode voltage of 1484 V.

The bulk of the signal consists of a single peak at the same time across all channels, this is consistent with what is expected from an electron drift gas. The electron drift in CF_4 at this pressure is expected to occur over a duration of a few hundred nanoseconds, meaning all the charge from an event will arrive at the readout effectively instantaneously at the timescale of the readout.

It can be seen in Figure 7.6a that the signal on the y strips is significantly larger than the signal observed on the x strips. To illustrate this more clearly, Figure 7.6b shows a histogram of the peak voltages for the y and x channels across an entire run. The average ratio between the peak voltage on the y and x channels is 3.45:1 over the entire run. The difference can be attributed to the geometry of the strips: the x strips are further from the amplification gap where the avalanche is formed and are also partially occluded by the y strips, which gives a smaller induced signal. This is consistent with what is observed on comparable micromegas devices [153, 154]. As was noted in Section 7.1.5 the capacitance between the x and y strips and the micromegas mesh isn't significantly different which implies that signal induced by moving charge in the amplification gap and signal induced by capacitive coupling to the mesh can be distinguished by the relative signal intensity on the x and y strips.

Another feature of the signal is a peak with a width of one bin preceding the main signal peak on all the channels, this feature is consistent across all the examined events and channels. This 'spike' can most likely be attributed to cross-talk though the shared ground from the pre-shaped signal which is concurrent with the actual charge collection, the signal from the shaper itself takes some time longer to catch up due to the longer shaping time. For negative ion drift gasses where the charge collection is slower the feature would be expected to disappear.

The collection of the track ionisation on the strips demonstrates the ability of the micromegas to respond to events extended in space. The 3.45:1 difference between the

signal magnitude on the x and y strips is an important factor which will help inform further analysis. The fast charge collection in CF_4 however meant that the time resolution of the readout was not sufficient to track the recoil. To obtain a demonstration of the position sensitivity of the strips the drift of ionised charge must be significantly slower, as in SF_6, or the events must by compact enough to be observed on only a few strips, like the ionisation produced by 5.9 keV electrons.

7.2.2 ^{55}Fe in CF_4

The 5.9 keV electron recoils induced by the ^{55}Fe x-rays are very short and produce a known amount of ionisation in the gas. We expect x-ray induced electron recoils from ^{55}Fe to be on the order of one or two millimeters at 30 Torr, this is equivalent to a width of 2-4 channels at the instrumented pitch. The observation of the 5.9 keV electron recoils is useful for the determination of the gas gain of the device and the compact nature of the recoils also enables a demonstration of the position sensitivity of the device.

Figure 7.7 shows an example ^{55}Fe event on the y strips in 30.0 Torr CF_4 with a micromegas voltage of 522 V, and a cathode voltage of 1322 V.

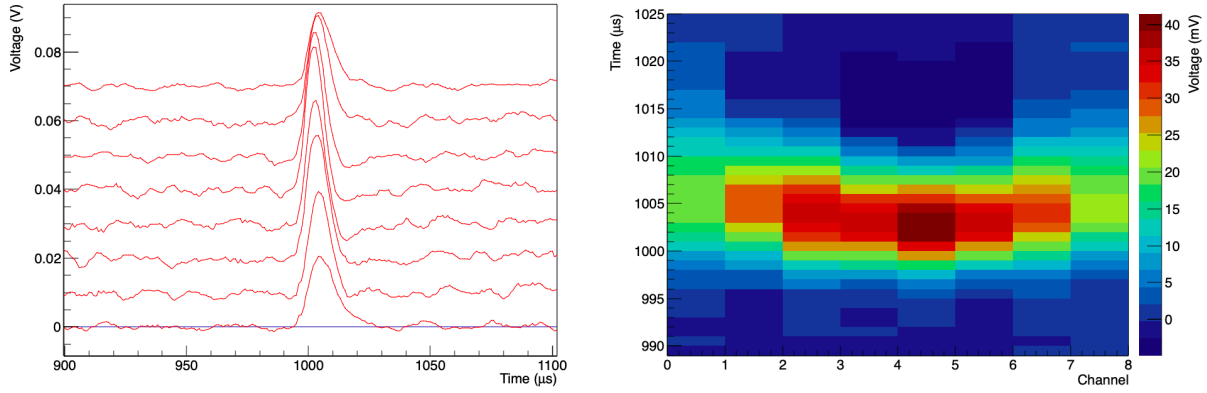

Figure 7.7: Raw waveforms (left) and 2d y-t projection of the signal (right) for a sample ^{55}Fe event on y strips for 30.0 Torr CF_4 with micromegas voltage of 522 V, and cathode voltage of 1322 V.

For the event in Figure 7.7 the highest signal voltage is reached on channel 4, with the peak voltage on channels 0 and 8 approximately half the magnitude of the peak on channel 4. Unlike in the alpha data there is a measurable time variation between the peak times on different strips with channel 4 peaking first and the other channels peaking in order of their offset from channel 4. This 'v' shaped structure is consistent across the observed ^{55}Fe events.

As the charge collection in CF_4 is expected to occur over a duration of less than a microsecond, the observed time variation cannot be attributed to the structure of the recoil itself. The 'v' shaped structure can instead be attributed to the charge collected on the resistive layer diffusing laterally away from the point of collection [154] [155]. Section 7.4 is dedicated to describing an analytic model of the charge dissipation in the resistive layer and comparing the analytic result with data.

The ^{55}Fe electron recoils are used to obtain a measurement of the effective gain of the device. This is less straight forward than for a 1d detector as the signal is spread over many channels. It was determined that the best way to get a measurement of the energy

deposited is to integrate the signal peak across all channels with the integration threshold set at a quarter of the maximum peak height. The net charge that is detected on the strips is then determined by dividing the integrated signal by the channel's electronic gain determined in Section 7.1.5. The effective gain is then equal to Q_{det}/Q_{55Fe} where Q_{det} is the detected charge and Q_{55Fe} is the charge ionised in the gas by the 5.9 keV ^{55}Fe x-ray.

Two types of cut were implemented on the data to obtain a gain measurement, a noise cut and a fiducialisation cut. Most of the events identified as noise consist of a peak of constant height and time across all channels, these are thought to be caused by high charge deposition events occurring outside the instrumented region with the signal picked up by capacitive coupling to the mesh. The noise cut removed all events where the peak height was close to constant across all the working channels. The fiducialisation cuts had to be implemented to ensure the peak was contained within the instrumented area and that the DAQ was not triggering on charge dissipation from events outside the area. The fiducialisation cut removed events where the largest peak on any channel occurs on either of the edge channels.

Using the events passing both the noise and fiducialisation cuts, a defined peak is observed in the distribution of the integrated peak charge across the y strips, the gain is determined from the average of this peak. The effective gain on the 8 y strips of the micromegas in 30.0 Torr CF_4 with a mesh voltage of 522 V was found to be 18830 ± 380. The magnitude of the signal on the x-strips on the other hand was not sufficient to obtain an ^{55}Fe peak, however the effective gain can be estimated indirectly. There are 3 only events which pass fiducialisation and noise cuts for both the x and y axis, the magnitude of the signal for these events on the x strips relative to the y strips is 0.27 ± 0.07, which is consistent with the ratio determined from the ^{241}Am runs. This indirect method suggests the effective gain on the x strips is around 5000.

It should be noted that the effective gain, determined here, which is the ratio between the charge ionised in the gas and the charge observed on the the strips is distinct from the gas gain, which is the ratio between the charge ionised in the gas and total charge produced in the amplification. Electrons collected on the resistive layer only induce a fraction of their charge on the strips, with the different couplings to the two strips accounting for the difference in the effective gains.

Overall, the observation of ^{55}Fe in CF_4 provides confirmation of the position sensitivity of the micromegas readout and demonstrates that gain sufficient to observe keV recoils can be obtained in low pressure CF_4. A difference in magnitude between the ^{55}Fe signal on the x and y strips was observed consistent with the ratios determined from alpha particles in Section 7.2.1. The evolution of the signal shape on the micromegas strips over the microsecond timescale demonstrated that a process besides the electron drift of charge is occurring in the signal formation on the strips. This is attributed to charge dissipation in the resistive layer which is explored in depth in Section 7.4.

7.2.3 ^{241}Am in SF_6

As stated in the introduction to this chapter the combination of a strip readout and a negative ion drift gas has the potential to be among the most cost effective technologies for directional detection in a large scale gas TPC. The demonstration of the operation of a micromegas strip readout in the negative ion drift gas SF_6 is one of the key motivations for this work. The slower negative ion drift is expected to result in the charge from recoils in SF_6 being collected over a long enough timescale that structure should be visible on

the microsecond timescale.

In this case the ^{241}Am source is positioned in the x and y positions described in Section 7.1.4 with all the channels instrumenting strips the associated direction. Due to the lower gas gain the voltage of the micromegas mesh had to be increased as high as was possible without the device sparking. The resistive layer protected the detector when the micromegas did spark and prevented damage to the device or electronics. The data presented in this section represents the limit of the gain performance of the micromegas device in low pressure SF_6. For the SF_6 alpha runs there are two main types of event topology, examples of which are shown in Figure 7.8.

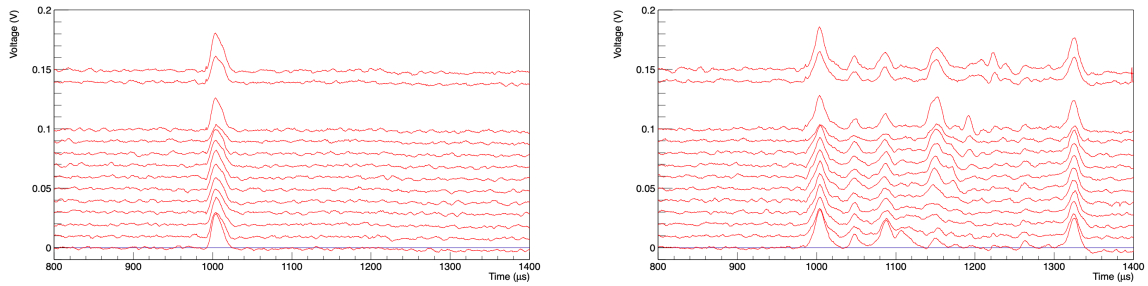

(a) (b)

Figure 7.8: Examples of the two main event topologies, 'x' run alphas in 20 Torr SF_6 on bare micromegas at mesh voltage −592 V and cathode voltage −2000 V.

The first type of event, in Figure 7.8a, has a static peak of constant height on all channels and the second type of event, in Figure 7.8b, has a number of peaks spread across several hundred microseconds. The second type of event has a number of static peaks which have equal height and timings across all the channels, for example the peaks at 1000 and 1330 µs in Figure 7.8b. There are also a number of non-static peaks where there is localised variation in the size of the peak across the channels, examples of these peaks are at 1110 and 1150 µs in Figure 7.8b.

The static peaks are most likely a result of capacitive coupling to the micromegas mesh; as was shown in Section 7.1.5 a change of the voltage on the mesh on the order of millivolts is enough to generate significant signal on the strips. Events where the charge collection occurs outside the instrumented region would create a voltage drop on the mesh which is capacitively picked up by all channels, resulting in the event type shown in Figure 7.8a. The non-static peaks on the other hands are thought to be induced by the moving charge in the amplification gap above the strips, actually corresponding to charge arriving from the drift region above the respective strips.

To remove the static peaks the difference was taken between the signal on each channel and the average signal on all channels, Figure 7.9a shows what the signal on the channels looks like after the average is subtracted for an example alpha event in the 'x' run. Figure 7.9b shows the time that the maximum voltage is reached on each channel after the average is subtracted. It can be seen in the figure that the peaking times determined in this way are approximately linear with channel number in the selected event.

The arrival time, t, of charge at the readout will be equal to its initial displacement from the readout plane, z, divided by its drift velocity, v_{drift}. If an alpha track is approximated as a straight line, the relationship between z and a horizontal coordinate, x, will also be linear and dependent on the angle of the track. The relationship between the

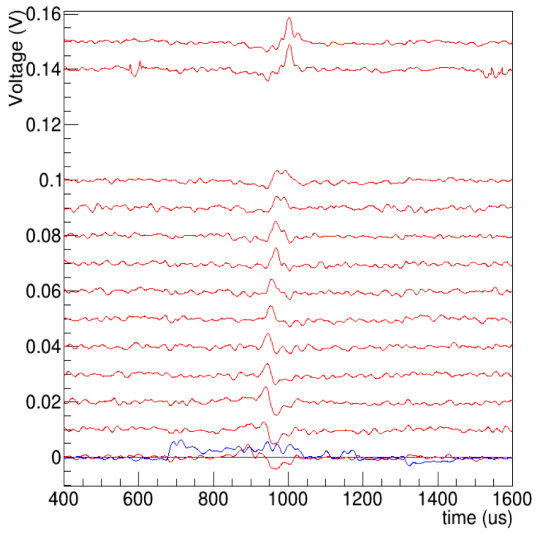

(a) Difference (red) between signal on each working channel and average of the signal on all working channels (blue).

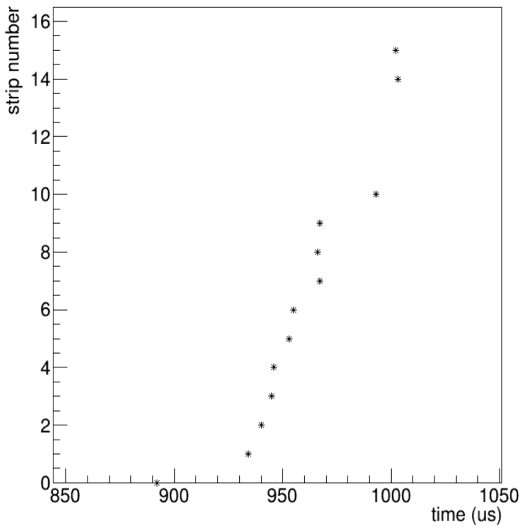

(b) Peak times on each channel after the average signal is subtracted.

Figure 7.9: Signal for 'x' run for an alpha event in 20 Torr SF_6 on bare micromegas at voltage $-592\,\mathrm{V}$ and cathode voltage $-2000\,\mathrm{V}$.

charge arrival time and the angle of a straight track can therefore be described by the equation

$$\frac{1}{\tan(\theta)} = \frac{dz}{dx} = \frac{dt}{dx}\frac{dz}{dt} = \frac{dt}{dx}v_{drift} \tag{7.3}$$

where θ is the angle between the track and the z axis in the x-z projection of the track as in Figure 7.3b. The drift velocity in the gas can be determined from the pressure, P, temperature, T, drift field, E, and reduced mobility, μ_0, of the ions in the gas by the equation

$$v_{drift} = \mu_0 E \frac{P_0 T}{P T_0} \tag{7.4}$$

where $P_0 = 760$ Torr and $T_0 = 273\,\mathrm{K}$ are the pressure and temperature at STP.

The alpha angle was constrained such that $43° < \theta < 57°$, assuming the SF_6 ions have the literature mobility of $53\,\mathrm{mm^2/V/s}$ the geometrically allowed $\frac{dt}{dx}$ for straight tracks are in the range 5.8 to $9.6\,\mathrm{\mu s\,mm^{-1}}$.

A straight line fit to the peak times on the channels after average subtraction is performed for each event to determine a $\frac{dt}{dx}$ for the alpha 'track'. After fitting, a cut is applied to select only events for which the relationship between peaking time and channel is well approximated by a linear fit. The cut implemented on the χ^2 of the fit, accepting only fits to events with $\chi^2 < 10^6$. Figure 7.10 shows the distribution of $\frac{dt}{dx}$ for the 'x' run with the described cuts.

There is a clear preference for positive $\frac{dt}{dx}$ with an average around $15\,\mathrm{\mu s\,mm^{-1}}$. Most of the events have gradients outside the expected range of $5.8 < \frac{dt}{dx} < 9.6\,\mathrm{\mu s\,mm^{-1}}$, although the distribution has a clear preference for the expected (positive) sign of the gradient. The correct sign of the overall distribution and the fact that a linear fit well described the average subtracted peaking times suggests that the charge deposited by the alpha track

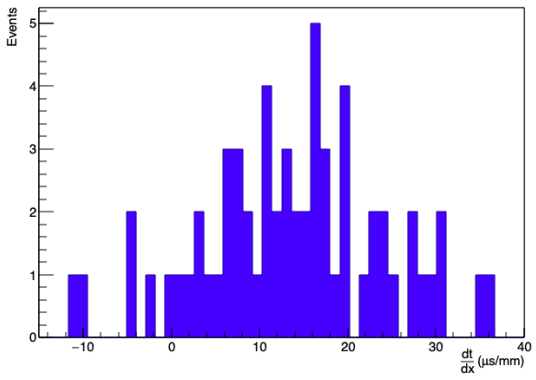

Figure 7.10: Gradient of linear fit to peak times of average subtracted waveforms against channel centre for an 'x' run in 20 Torr SF_6 on bare micromegas at mesh voltage −592 V and cathode voltage −2000 V.

is translating to position sensitive signal on the strips, the very wide distribution of signal suggests a fairly poor angular resolution for the micromegas with no amplification stage. The subtraction of the average waveform will result in distortion of the non capacitive signal which might contribute to the apparent poor angular resolution. The ability to instrument more strips and obtain signal from strips outside the range of the alpha track would enable the capacitive (static) signal to be entirely isolated from the induced signal and might enable a better reconstruction.

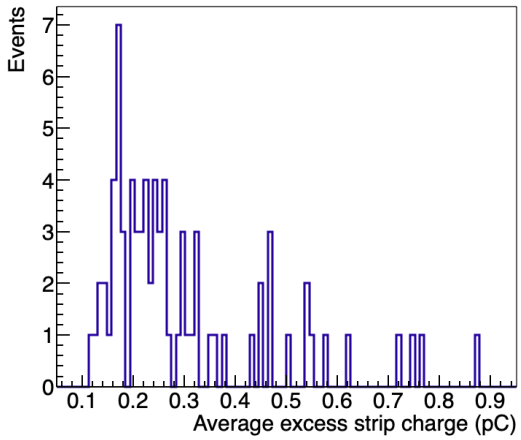

Figure 7.11: Average of the charge collected on each strip determined by the peak excess signal for 'x' run in 20 Torr SF_6 on bare micromegas at mesh voltage −592 V and cathode voltage −2000 V.

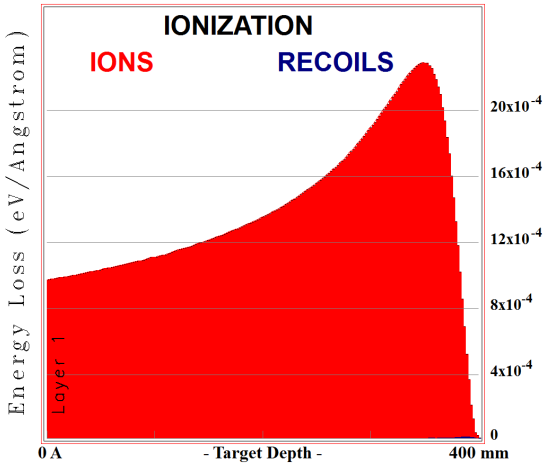

Figure 7.12: The average ionisation profile of 5.5 MeV alpha particles in 20 Torr SF_6 determined in SRIM.

It is preferable to use the known amount of ionisation produced by a source such as ^{55}Fe to obtain a measurement of the gain of a device. The gain of the micromegas was not high enough to observe the 5.9 keV electrons from ^{55}Fe however so an estimation of the gain is instead determined from the alpha signal. To obtain an estimate of the effective gain, the average charge collected by each strip is compared with the charge deposit of the alpha particle from simulation.

The signal associated with the arrival of charge from a segment of alpha track above each strip is determined from the peak excess voltage on a strip (the maximum signal voltage in the average subtracted waveform). The associated charge is then calculated using the electronic gains determined in Section 7.1.5 and the average per-strip charge for each event is calculated. The distribution in the average charge collected per strip for each event passing the $\chi^2 < 10^6$ cut described for the track fitting is shown in Figure 7.11.

Most of the events have per-strip detected charge between 0.1 and 0.3 pC although events with averages of up to 8.8 pC are observed. The lowest end of this distribution is defined by the point at which the electronic noise overwhelms the alpha signal at a strip peak signal of 3 mV. The average charge collection for all events passing the χ^2 cut is 0.29 pC/strip.

In order to determine the charge ionised in the gas above the strips, the slowing of 5.5 MeV alpha particles in 20 Torr SF_6 is simulated in SRIM. The details of the SRIM software package were discussed in Chapter 4. The average ionising energy loss profile for alpha particles in 20 Torr SF_6 is shown Figure 7.12.

There are approximately 4 cm of travel between the ^{241}Am source and the volume of the drift region above the instrumented strips. SRIM estimates an ionising energy loss of approximately 10×10^{-4} eV Å^{-1} at 4 cm along a 5.5 MeV alpha track in SF_6. Using the w-value of SF_6 of 34 eV [130], the ionisation energy loss can be converted to the charge ionised in the gas per unit length, obtaining 0.0544 pC mm^{-1} at 4 cm. To account for the angle of the alpha tracks, this number is multiplied by the factor $1/\sin(\theta_{avg})$ where θ_{avg} is the average angle of the alpha tracks which is 50°. Multiplying then by the strip pitch arrives at the average charge ionised in the track segment above each strip, which is 0.035 pC/strip.

An estimate of the gain can be determined from the ratio between the per-strip charge deposit in the gas determined from simulation and the average charge observed on the strips. The ratio is 8.3, given the extremely large unquantified systematic error related to the truncation of the strip signal by the electronic noise this is rounded to give the effective gain of 10. The gas gain is expected to be higher than this due to the inefficiencies associated with the coupling of the charge ionised in the gas to the charge on the strips.

In summary, the micromegas must operate very close to its maximum operating voltage in order to obtain any significant signal, even from the fairly high energy ^{241}Am alphas. After some processing the data obtained from the strips was shown to have a time dependence which was consistent with charge arriving from alpha tracks from the ^{241}Am source. This provides confirmation that the strips are providing position sensitivity and are capable of tracking although the angular resolution and efficiency of this process is fairly poor. The effective gain of the micromegas in 20 Torr SF_6 is estimated to be on the order of 10, underlining the need for an amplification stage to provide more gain.

7.2.4 ^{55}Fe in SF_6

As discussed, the 5.9 keV electrons produced by ^{55}Fe are useful for the gain calibration of gas detectors at low energy. The gain of the micromegas was not sufficient to observe any signal from 5.9 keV electron recoils on the strips in SF_6. It was possible however to observe ^{55}Fe events in the signal collected from the micromegas mesh which reduces the micromegas to an effectively 1d readout.

The micromegas in this setup has instrumentation of both the strips and the micromegas mesh which, as shown in Figure 7.2, has its own amplification chain consisting

of a CR-111 preamplifier and a CR200-4 µs shaper. When the micromegas is collecting sufficient charge for signal to be observed on the strips, the mesh signal is too large to observe any significant detail. Conversly for ^{55}Fe on the bare micromegas the signal available on the mesh is sufficant to observe 5.9 keV electrons without digitiser saturation. Two example ^{55}Fe signal events observed on the micromegas mesh in 30 Torr SF_6 with a mesh voltage of −560 V and drift field 306 V cm^{-1} is shown in Figure 7.13.

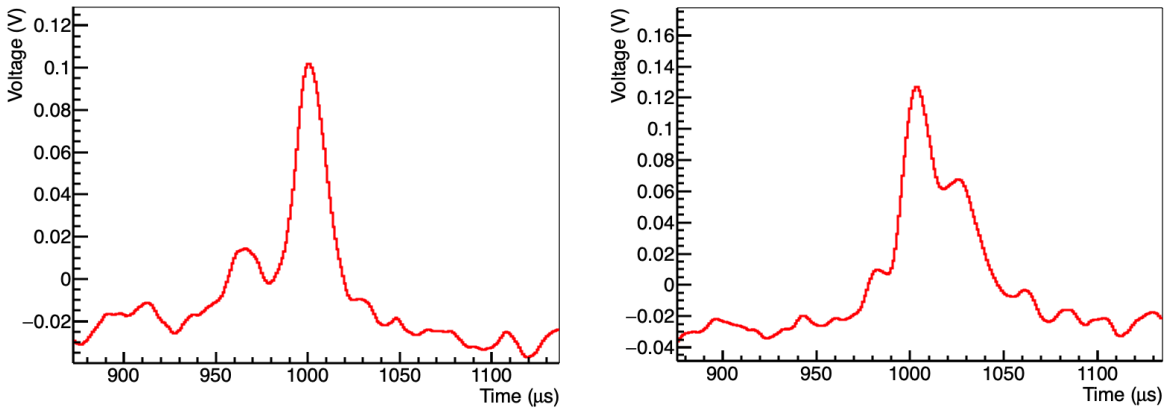

(a) Event 3.

(b) Event 7.

Figure 7.13: Example events observed on the micromegas mesh in 30 Torr SF_6 with mesh voltage −560 V and drift field 306 V cm^{-1}.

The events show multiple merged peaks with separations on the order of 30 µs and the total signal arrival occurs over a time on the order of 50 µs. The signal event shape is consistent with the low pressure ^{55}Fe events in SF_6 observed with the ThGEM, in simulations and with the MM-THGEM in respective Chapters 3, 4 and 6.

The mesh gain was determined using the integration of the signal and scaling by the electronic calibration of the signal channel. The mesh gain in 30 Torr SF_6 with a mesh voltage of −560 V and cathode voltage 1385 V was determined to be 2540 ± 200 with an energy resolution expressed by the FWHM/mean of the peak of 0.80 ± 0.05. This gain is over 200 times larger than the effective gain on the strips estimated for ^{241}Am alpha tracks which was the order of ten. This shows that the signal formation on the mesh is significantly more efficient than on the strips, this is consistent with what would be expected due to the different relative sizes and geometry of the mesh and strip sensitive elements. The gain obtained from the mesh is considered to be closer to the gas gain, the multiplication factor of electrons in the gas, than the strips where the coupling to the signal is worse. The gain measured on the strips can be considered a better characterisation of the practical detector performance as a strip based detector.

The measurement of ^{55}Fe signal on the mesh demonstrates that 1d and energy data is available to the micromegas mesh at significantly lower energies than are available on the strips. This also provides a demonstration that the micromegas mesh stage is producing significant gas gain even in the regime where low energy events cannot be observed in the strip data.

7.3 Micromegas and MM-ThGEM

The micromegas operating as a stand alone device can only just obtain gas gains sufficient to observe alpha particles in SF_6 on the strips and cannot observe recoils of significantly lower energy. Using the MM-ThGEM described in Chapter 6 as an amplification stage for the micromegas is hoped to give better overall gain and enable lower energy events to be observed in SF_6. This section describes the operation of the micromegas and MM-ThGEM coupled together, with an objective of demonstrating improvements in tracking and energy threshold.

7.3.1 Setup of the micromegas and MM-ThGEM

A cross-sectional diagram and image of the experimental setup of the micromegas with MM-ThGEM is shown in Figure 7.14.

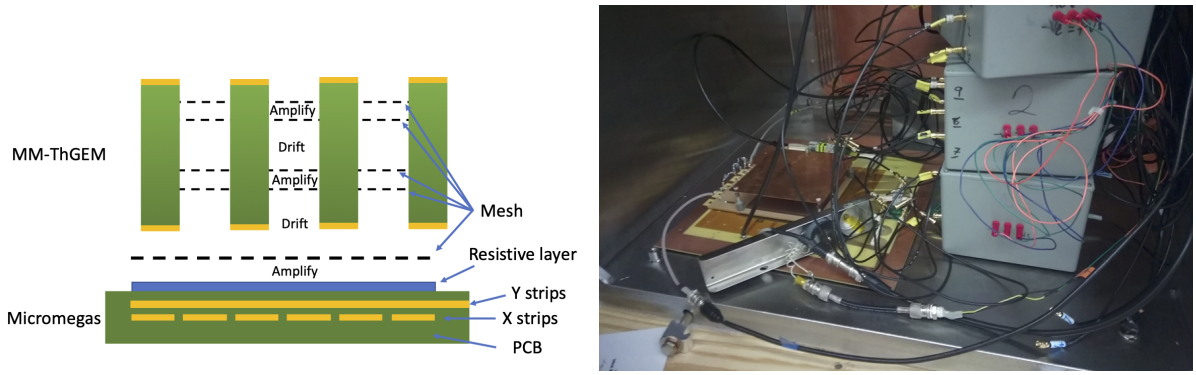

(a) Cross-sectional diagram with field type indicated in centre.

(b) Picture of the experimental setup inside the vessel.

Figure 7.14: Micromegas and MM-THGEM setup.

The MM-ThGEM was positioned in front of the sensitive region of the micromegas with a separation between the back plane of the MM-ThGEM and the micromegas mesh of 2.1 mm. The addition of the MM-ThGEM to the micromegas brings the total number of amplification stages up to three, separated by respective transfer regions of 1 mm and 3.1 mm.

A resistor chain was used to bias the MM-ThGEM enabling the four meshes and two copper planes to be biased with the application of just two voltages, the voltage division of the chain was based off field ratios determined in Chapter 6 to provide a good operating point. The resistance values of resistors in the chain and a diagram of the chain are shown in Figure 7.15.

Additionally it was found that it was necessary to add 10 MΩ resistors in series between each detector element and the resistor chain in order to reduce the noise on the output channels, these series resistors are designated as R_s in the diagram. The value ΔV_{MM} is used in the analysis to reference the voltage on the MM-ThGEM, it refers to the difference in voltage between the top and bottom copper plane of the MM-ThGEM. The transfer, collection and amplification fields are therefore defined by the voltage division of ΔV_{MM} by the resistor chain, excluding the 200 MΩ filter resistor on the return line. The ratio of ΔV_{MM} which is divided into each interval is also shown in the table in Figure 7.15.

The resistive layer and strips were held at ground and all other elements had a negative voltage. The source locations used in the micromegas-MMThGEM characterisation were

Interval	Resistance (MΩ)	Divider ratio (%)
$top \rightarrow m1$	11.4	7.39
$m1 \rightarrow m2$	66.4	43.1
$m2 \rightarrow m3$	6.67	4.32
$m3 \rightarrow m4$	61.4	39.8
$m4 \rightarrow bot$	8.34	5.4
$bot \rightarrow out$	200	-

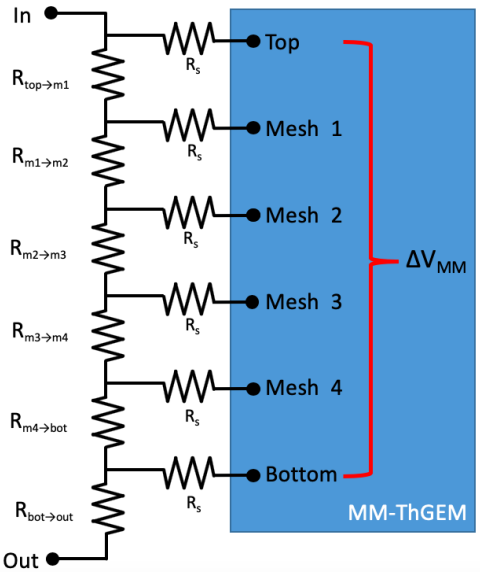

Figure 7.15: Resistance values (left) and diagram (right) for MM-ThGEM resistor chain.

as described in Section 7.1. The drift field was generated by a square cathode with a drift gap of 2.7 cm between the cathode and the top plane of the MM-ThGEM.

7.3.2 Response of the micromegas-MMThGEM in CF_4

It was shown in Section 7.2 that the micromegas has sufficient gain to perform well with no amplification stage in CF_4. The micromegas-MMThGEM combination is also tested in CF_4 to evaluate the effect of the additional of the MM-ThGEM on the event topology and overall gain on the strips.

The micromegas-MMThGEM combination was exposed sequentially to ^{241}Am alpha particles and ^{55}Fe. The ^{241}Am alpha events and the ^{55}Fe both showed the same topologies as the events observed in CF_4 on the bare micromegas. Figure 7.16 shows a typical ^{55}Fe event on the y-strips for the micromegas-MMThGEM combination in CF_4.

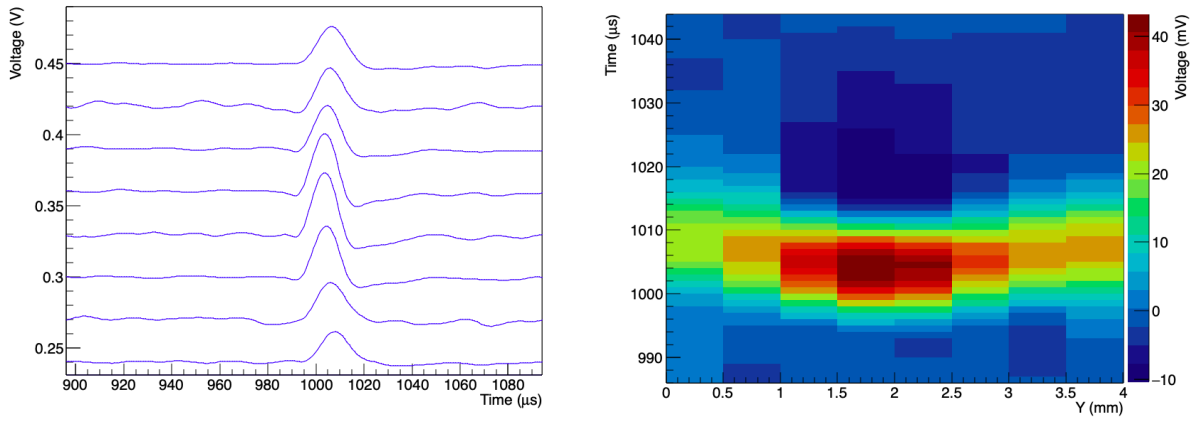

Figure 7.16: Raw waveforms (left) and 2d y-t projection of the signal (right) for a sample ^{55}Fe event on y strips of micromegas-MMThGEM for 30.0 Torr CF_4 with $\Delta V_{MM} = 784\,\mathrm{V}$, $V_{micromegas} = 460\,\mathrm{V}$ and a drift field of $307\,\mathrm{V\,cm^{-1}}$.

The event shows the characteristic charge dissipation observed for the ^{55}Fe events on the bare micromegas as exemplified by the event in Figure 7.7. The centre of the charge in the event can be distinguished which shows that the micromegas remains sensitive to the spatial position of charge above the readout, any distortion of the events shape due to the MM-ThGEM is not apparent. The near instantaneous arrival of charge in the electron drift gas means that distinguishing the z coordinate remains impossible with the readout electronics. It was found that the addition of the MM-ThGEM significantly increased the overall gas gain as compared to the bare micromegas and enabled operation of the micromegas at a lower mesh voltage. For ΔV_{MM} of 784 V and $V_{micromegas}$ of 460 V in 30 Torr CF_4, the overall effective gas gain on the y strips was 29600 ± 1400. This is a $\sim 50\%$ increase in the gain compared to the bare micromegas run where the micromegas mesh voltage 60 V higher.

The CF_4 data demonstrates that the MM-ThGEM is enhancing the overall gain observed on the strips and that the positional information observed in the initial runs with the micromegas only is preserved. This result is promising for the use of the micromegas-MMThGEM in SF_6 where the enhanced gain is necessary for the observation of lower energy recoils.

7.3.3 ^{241}Am tracking in SF_6

The demonstration of the good tracking with a strip readout in a negative ion gas is an important development goal for the micromegas-MMThGEM. The operation of the micromegas on its own in SF_6 in Section 7.2.3 demonstrated that directional information can be extracted from high energy alpha tracks without an amplification stage but also underlined some of the limitations of the micromegas on its own. The work with CF_4 above established basic functionality of the micromegas-MMThGEM set-up and the ability of the MM-ThGEM to enhance the overall gain of the device.

This section explores the overall tracking functionality of the micromegas-MMThGEM combination in SF_6 using ^{241}Am alpha particles. The ability to track alpha particles in three dimensions would be a strong demonstration of the readout's ability to track recoils and therefore to provide directional information.

The micromegas-MMThGEM was exposed to alpha particles in the x, y and x-y configurations. As shown in Figure 7.3b, the x runs consist of an alpha source orientated to emit alphas at a steep angle in the x-z plane with all 16 channels instrumenting the x strips and the y run consists of the source orientated in the y-z plane with 16 channels instrumenting the y strips. The x-y configuration has the source collimated to produce alpha particles traveling in the (+x,+y,-z) direction and has 8 channels instrumenting both the x and y strips. The addition of the MM-ThGEM significantly changes the event topology of alpha events in SF_6 as compared to the bare micromegas. Sample events from the x and y runs in 30 Torr SF_6 are shown in Figure 7.17.

The alpha events on both sets of strips show a fairly consistent shape with two peaks visible in the waveform. The first peak in each event occurs at the same time on all the channels with the same height. This is followed by a second peak which tends to occur at different times, with peak time having a close to linear relationship with channel number. The second peak is consistently much larger on the y strips than on the x strips whereas the first peak has the same height on both. The magnitude of the second peak also appears to grow faster with the gain than the first peak.

The different rates at which the relative sizes of the peaks changes with the device

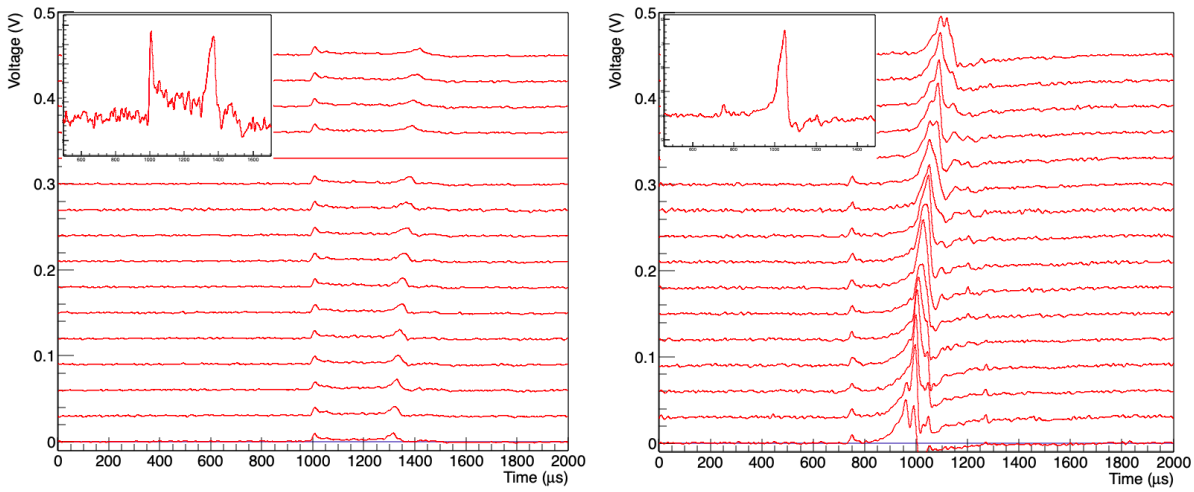

(a) x run event.

(b) y run event.

Figure 7.17: Typical alpha events in 30 Torr SF_6 with $\Delta V_{MM} = 1097\,\mathrm{V}$, $V_{micromegas} = 530\,\mathrm{V}$ and a drift field of $300\,\mathrm{V\,cm^{-1}}$. Detailed waveform from channel 8 inset.

gain suggests that they are created by different mechanisms. The constant height of the first peak and the lack of any correlation to strip location suggests it is from capacitive coupling to the mesh as was observed in Section 7.2.3. Assuming the capacitive coupling explanation is correct the first peak will correspond to the time of arrival of charge from the end of the alpha track which will be at the top plane of the MM-ThGEM in the x, y and x-y runs.

Looking at the detail of the waveforms, a plateau in the voltage starting at the first peak and continuing until after the second peak is visible in most events. This is also thought to be a capacitive effect, corresponding to the continued arrival of charge on the mesh from the alpha track. The second peak corresponds to the charge arrival at the strip from the alpha track in the gas and is the part of the waveform which is useful for tracking. It is the location of the second peak were the expected time delay between peak arrival times on successive channels due to the negative ion operation is observed.

The capacitive component doesn't correspond to charge in the space above the strip, therefore removing it is desirable for tracking and other analysis of the data. A baseline subtraction algorithm was created to preserve the track features while removing the capacitive component of the signal. In a fully instrumented detector this would not be necessary as the capacitive features could be extracted from the signals on a veto strip at the edge of the detector or similar.

To achieve this the baseline was determined by taking the average waveform over all channels as in Section 7.2.3. The root mean square deviation of the raw waveforms from the average waveform was then determined for each time bin. All time bins in the average waveform where the RMS deviation exceeded a threshold (i.e. region where there was significant non-capacitive signal) were emptied. The empty bins were then filled with a linear interpolation between the adjacent non empty bins. This baseline is then subtracted from the signal on each channel. This method reduced the distortion to the final waveform compared to the average subtraction method for steep alphas in the setup used. When both x and y strips were instrumented the algorithm was performed separately on each set of strips. Figure 7.18a shows the baseline subtracted waveforms as well as a 3-d plot

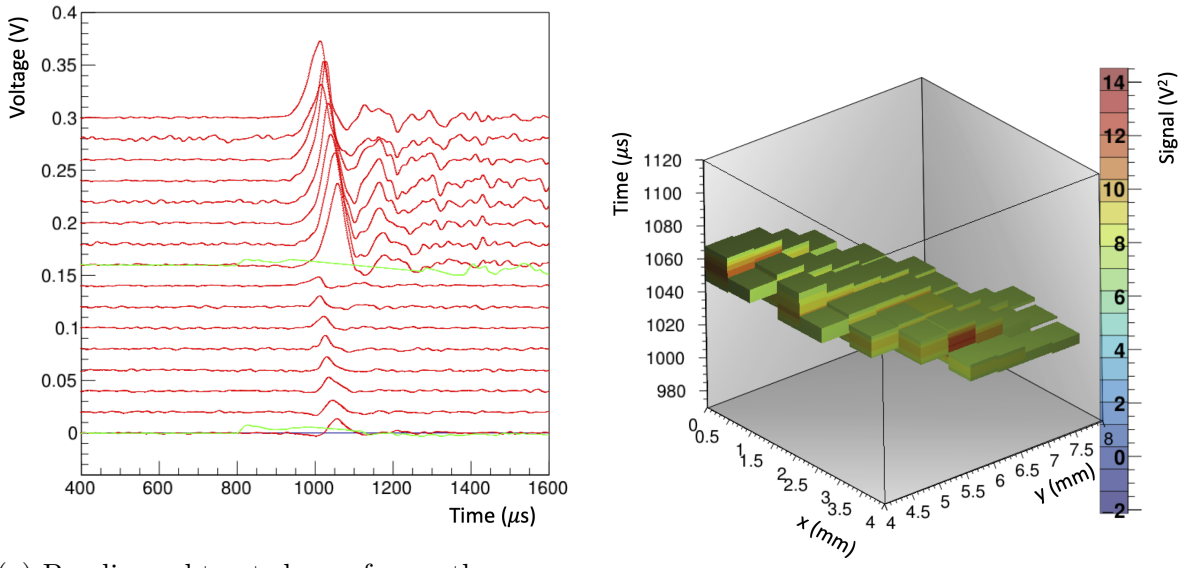

(a) Baseline subtracted waveforms, the bottom 8 channels instrument x strips and the top 8 channel instrument y strips, the baselines determined for each set of channels are in green.

(b) 3D plot obtained by the multiplication of the baseline subtracted voltage on each x channel by the voltage on each y channel for each time bin.

Figure 7.18: Baseline subtracted waveforms and 3d plot for example x-y run alpha in 30 Torr SF_6 with $\Delta V_{MM} = 1097\,\mathrm{V}$, $V_{micromegas} = 530\,\mathrm{V}$ and a drift field of $300\,\mathrm{V\,cm^{-1}}$.

of an alpha track for an example event from an x-y run.

The baseline subtraction neatly eliminates the first peak in the waveforms and pedestal between the first peak and second peak. The remaining signal peaks demonstrate offsets in time which are consistent with a straight track orientated in the (+x,+y,-z) source direction. This kind of track reconstruction was not possible with the bare micromegas where there was no clear 'track' in most events and a determination of a track direction was only possible with significant processing. The different event topology might be attributed to the lower gain of the micromegas without the MM-ThGEM, in that case signal from the capacitive coupling dominates. When the gain is increased by the addition of the MM-ThGEM the signal induced by arriving charge (the non static peaks) increases faster than the capacitive signal resulting in the much more clearly defined tracks observed with the amplification stage.

The x-t and y-t projections of the signal obtained from the x and y strips can be multiplied together to obtain a xyt reconstruction of the track. The xyt plot for the example event generated by multiplication of the baseline subtracted voltage on each x channel by the voltage on each y channel for each time bin is shown in Figure 7.18b. To make the track visible, all bins which have values less than half the maximum are set to transparent.

Because this method of event reconstruction is the synthesis of two 2D projections it works well only when there isn't any degeneracy in the signal arrival in time. If charge arrives at two distinct sets of x and y strips at the same time there is no way to determine which x strips correspond to the signal on which y strips and there are two sets of degenerate charge configurations which would produce the same signal. For angled alpha tracks like the one displayed where the charge arrival at a given time is localised to only a

few adjacent strips however this method provides good reconstruction of the orientation of the track in space.

The effect of the drift field on the observed tracks can be explored to arrive at a measurement of the mobility. As stated in Section 7.2.3, the angle from vertical, θ of the alpha track can be related to the signal arrival time on a strip, t, and the strip offset, x by the equation

$$\frac{1}{\tan(\theta)} = \frac{dz}{dx} = \frac{dt}{dx}\frac{dz}{dt} = \frac{dt}{dx}v_{drift} \tag{7.5}$$

the drift velocity in the gas, v_{drift}, can be determined from the pressure, P, temperature, T, drift field, E, and reduced mobility, μ_0, of the ions in the gas by the equation

$$v_{drift} = \mu_0 E \frac{P_0 T}{P T_0} \tag{7.6}$$

where $P_0 = 760$ Torr and $T_0 = 273\,\mathrm{K}$ are the pressure and temperature at STP.

Figure 7.19a shows the $\frac{dt}{dx}$ of the x-t and y-t projected alpha tracks for the x and y runs at different drift fields determined from a linear fit to baseline subtracted signal peaking times.

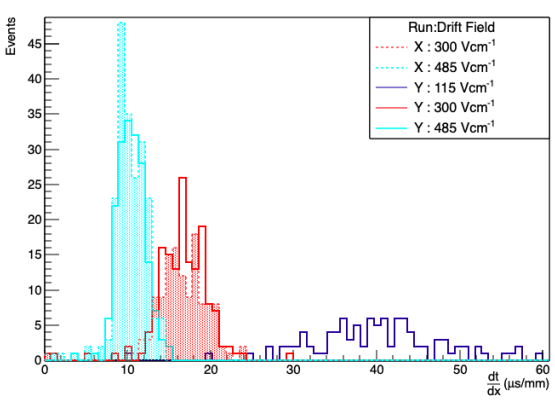

(a) $\frac{dt}{dx}$ for x runs (shaded) and $\frac{dt}{dy}$ for y runs (solid lines) for different drift fields.

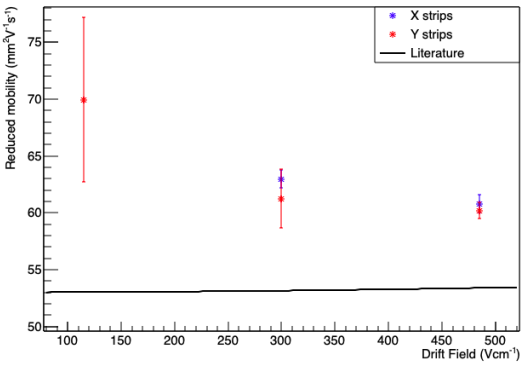

(b) Values for the reduced mobility determined from $\frac{dt}{dx}$ or $\frac{dt}{dy}$ for each run and value from literature [121].

Figure 7.19: Track data from x and y runs at 30 Torr SF_6 for micromegas-MMThGEM with $\Delta V_{MM} = 1097\,\mathrm{V}$, $V_{micromegas} = 530\,\mathrm{V}$.

There isn't a significant difference between the gradient determined for the x- and y-strips at a given field which suggests that the tracking is consistent between the two dimensions. The higher drift fields produce lower values of $\frac{dt}{dx}$ which is consistent with the expected increase in ion drift velocity. It is also notable that the relative widths of the distributions are considerably narrower than the distribution of determined $\frac{dt}{dx}$ observed on the bare micromegas in Figure 7.10, suggesting that the angular resolution has improved.

As the alpha exposure angle is constrained $43° < \theta < 57°$ and the electric field and gas parameters are known, the distribution of $\frac{dt}{dx}$ and $\frac{dt}{dy}$ can be used to determine the reduced mobility of the charge carriers by rearranging Equation 7.4 and 7.5 to get

$$\mu_0 = \frac{1}{\tan(\theta_{exp})\frac{dt}{dx}|_{POI} E \frac{P_0 T}{P T_0}} \tag{7.7}$$

where θ_{exp} is the expected angle of a Point of Interest, $\frac{dt}{dx}|_{POI}$, in the distribution. The three POI's we define are the minimum, maximum and average of the distribution which correspond to alpha angles 57°, 43° and 50° respectively. The mobility for each run and drift field determined from Equation 7.7 for the average of the $\frac{dt}{dx}$ distribution is shown in Figure 7.19b. The errors are determined from the values obtained for the minimum and maximum, defined as the $\frac{dt}{dx}$ of the 10th and 90th percentiles of the normalised cumulative distribution of events. The similarity between the mobility determined for each POI in the distribution suggests that the majority of the distribution width originates from the variation in the alpha track angle.

There are significantly larger errors for the lower drift fields which might be attributed to the higher diffusion and slower charge collection at those fields. The mobility from [121] is also plotted in Figure 7.19b which is below the determined mobilities. The systematic errors are not included in the error bars shown, propagating estimated errors in T, P, E and θ_{exp} gives a systematic error in the calculated values of μ_0 of $5\,\mathrm{mm}^2/\mathrm{V/s}$. The largest source of error is in the measurement of θ_{exp} which is estimated to have an error of around 2°. Taking the weighted mean of the measurements at different drift fields, a reduced mobility of $61.3 \pm 5(\mathrm{sys}) \pm 0.2(\mathrm{stat})\,\mathrm{mm}^2/\mathrm{V/s}$ is obtained for SF_6 ions in the gas. It should be noted that this is in opposition to the mobility values determined in Chapters 3 and 6 where figures closer to$35\,\mathrm{mm}^2/\mathrm{V/s}$ were consistantly determined. The reason for the sudden difference is not clear although both of the earlier mobility measurements were made in the same, smaller vessel while this one was made in a larger vessel containing more electrical components. The change to the larger vessel with different internal make up might be resulting in a different fraction of contaminants which is having an effect on the species of drifting negative ions.

The micromegas-MMThGEM combination has demonstrated the ability to track alpha particles in 3 dimensions in the negative ion drift gas SF_6. The measured delays in the signal peaking times on the strips are consistent with the drift of negative ions from a straight alpha track to within expected errors. The addition of the MM-ThGEM significantly improved the magnitude and quality of the strip signal and enabled the component contributions to be disentangled to the benefit of the tracking performance. This is demonstrated by the tighter distribution of $\frac{dt}{dx}$ consistent with the expected underlying distribution of alpha angles. Additionally the considerably larger signals that were obtained with the micromegas-MMThGEM should enable the observation of considerably lower energy events than previously accessible by the micromegas in SF_6.

7.3.4 ^{55}Fe in SF_6

Obtaining a low energy threshold is important for dark matter detection and neutron assay. The determination of the gain of the micromegas-MMThGEM is an important part of the characterisation of the overall detector. Additionally the demonstration that structure can be observed in low energy events is important for demonstrating the viability of obtaining directional signal at low energy thresholds. As discussed previously the ^{55}Fe x-ray source can be used to produce 5.9 keV electrons in a gas volume which are useful for the determination of the gain of the detector as well as for the generation of compact events displaying millimeter scale structure.

For the characterisation of the MM-ThGEM with ^{55}Fe the source is placed behind the mesh cathode directly above the instrumented area to maximise the number of recoils contained in the instrumented region. Figure 7.20 shows an example ^{55}Fe electron event

in 30 Torr SF_6 with $\Delta V_{MM} = 1106\,\mathrm{V}$, $V_{micromegas} = 540\,\mathrm{V}$ and $E_{drift} = 480\,\mathrm{V\,cm^{-1}}$.

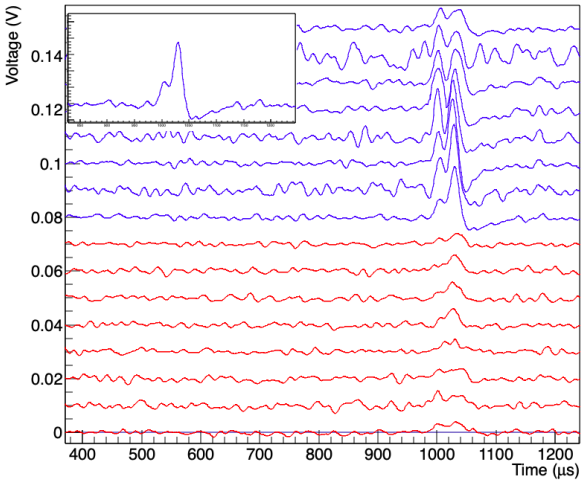

(a) Waveforms on x (red) and y (blue) channels with a detailed view of the channel 8 waveform inset.

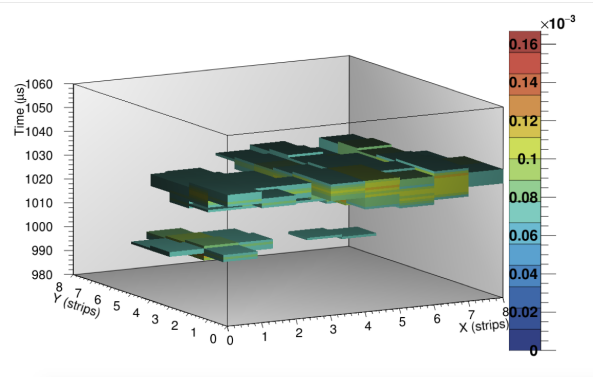

(b) 3d plot of the signal in xyt, colour scale is in $\mathrm{V^2}$ and the transparency threshold is $67\,\mathrm{mV^2}$.

Figure 7.20: Plots of an event on the y-strips in 30 Torr SF_6 with $\Delta V_{MM} = 1106\,\mathrm{V}$, $V_{micromegas} = 540\,\mathrm{V}$ and $E_{drift} = 480\,\mathrm{V\,cm^{-1}}$.

In this event there are multiple peaks consistent with the arrival of multiple charge clusters at different coordinates in x,y and z. This can be seen as the 3d extension of the multiple peaks observed in the 1-d projections of the ^{55}Fe event charge distribution observed in Chapters 3 and 6. This clustering was consistent with the ionisation produced by keV electron tracks in the simulations performed in Chapters 4 and 5.

The spatial separation between identifiable clusters in figure is equivalent to about 2 mm which is around the expected range of ^{55}Fe electrons in the gas at this pressure. Each signal peak appears to spread across multiple strips over time in a way which is consistent with the effect observed in the ^{55}Fe event signal on the strips in CF_4 in Sections 7.2.2 and 7.3.2. This effect is attributed to charge dissipating in the resisitive layer and is discussed further in Section 7.4. This charge dissipation dominates the signal for some events and obscures some of what might have been visible of the underlying recoil shape.

The 5.9 keV energy peak can be used to obtain the gain on the strips in the same way as in Section 7.2.2 The effective gain on the y strips at $\Delta V_{MM} = 1106\,\mathrm{V}$ and micromegas voltage 540 V is calculated to be 42513 ± 1000. The gain on the x-strips is still much lower than on the y-strips, using the integral charge the gain is 8100 ± 1200, with the large relative error due to the large signal to noise ratio at this gain. This is significantly more than the gain obtained with the stand alone micromegas in SF_6 in Section 7.2.3 where the effective gain on the strips was estimated to be on the order of 10.

As discussed on Section 7.2.4 the signal obtained from the micromegas mesh can provide a more accurate estimate of the gas gain than can be determined from the strips due to the better coupling to the charge in the gas. When running in combination with the MM-ThGEM this requires the voltage on the micromegas and MM-ThGEM to be significantly lower. In order to explore the contributions to the detector gain from the MM-ThGEM and micromegas gas amplification each was varied separately and the gain was determined from the signal on the micromegas mesh. When ΔV_{MM} was varied the micromegas mesh voltage, $V_{micromegas}$, was held at $-500\,\mathrm{V}$, and when varying $V_{micromegas}$,

ΔV_{MM} was held constant at 958 V. The drift field was 300 V cm^{-1} and the potential difference between the back of the MM-ThGEM and micromegas mesh was 100 V in all runs. The variation in the gain determined from the micromegas mesh against ΔV_{MM} and $V_{micromegas}$ in 30 Torr SF_6 is shown in Figure 7.21.

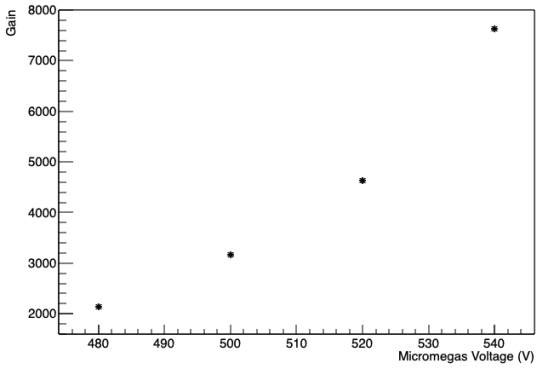

(a) Variation in overall gain with micromegas voltage and constant $\Delta V_{MM} = 958$ V.

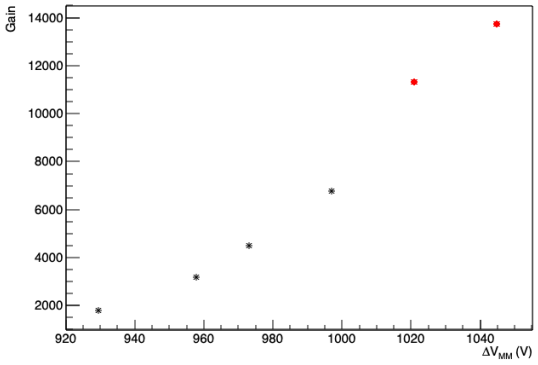

(b) Variation in overall gain with MM-THGEM voltage and constant $V_{micromegas} = -500$ V.

Figure 7.21: Effective gain of the micromegas-MMThGEM measured on the micromegas mesh in 30 Torr SF_6 with a 300 V cm^{-1} drift field.

Both the MM-ThGEM and micromegas bias individually show an exponential relationship with the overall gain measured on the mesh. The digitiser starts to saturate for measured gains above 9000, the measurements affected by the saturation are indicated by red markers, the saturation will tend to reduce the measured gain relative to the actual gain. the saturation of the mesh signal was the limiting factor in the applied biases. This demonstrates that at operating voltages both the MM-ThGEM and micromegas contribute significantly to the overall detector gain. As observed in Section 7.2.4 the instrumentation of the micromegas mesh enables the observation of signal at significantly lower energies than can be seen on the strips at a given detector bias setting. At a mesh voltage of $V_{micromegas} = -560$ V, the bare micromegas attained a mesh gain in 30 Torr SF_6 of 2500, the micromegas-MMThGEM would obtain this gain at about $V_{micromegas} = -500$ V, $\Delta V_{MM} = 940$ V and this is at the low end of the observed gains.

Overall the operation of the micromegas-MMThGEM has shown a the ability to observe low energy ~5.9 keV electron recoils on a strip based readout in the negative ion drift gas SF_6. The strip readout has sufficient spatial resolution to distinguish structure from these recoils consistent with expectation. The observation of this structure will be useful for the discrimination between electron and nuclear recoils and is also promising for the extraction of directional information from events in the detector. An effective gain of 42000 was obtained for the y strips and a gain of 8000 was obtained for the x-strips from ^{55}Fe data, this over 1000 times the effective gain that was estimated to be obtained with the micromegas on its own. Both the MM-ThGEM and micromegas were shown to contribute to the overall charge amplification indicating that the device is working as intended.

7.3.5 ^{241}Am in CF_4:SF_6

An alternative to pure SF_6 as a negative ion drift gas is the mixture CF_4:SF_6 which also has negative ion charge carriers and was shown in Chapter 6 to enable the MM-ThGEM to reach high gains at lower bias voltages relative to pure SF_6. As the MM-ThGEM performed well in CF_4:SF_6 and it presents a viable gas mixture for large detectors, the performance of the micromegas-MMThGEM is also explored in the gas.

The alpha source location and strip instrumentation is as described in Section 7.1; in the x runs only the x strips are instrumented and in the y runs only the y strips are instrumented. The x and y runs were performed in CF_4:SF_6 at pressures 28.7:1.3 Torr and 28.6:1.6 Torr respectively. Figure 7.22 shows typical events from the x and y runs in CF_4:SF_6.

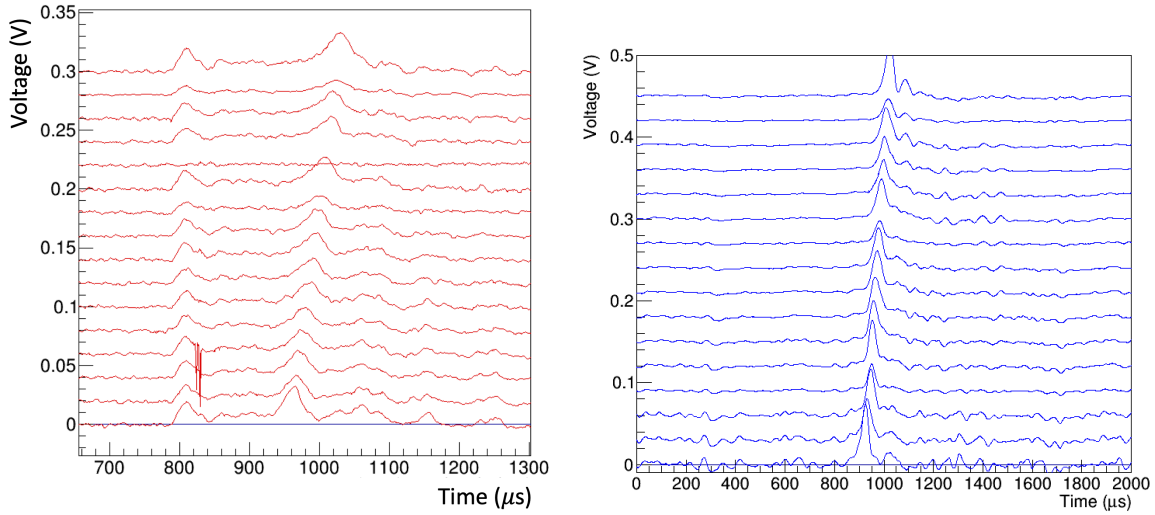

(a) x run event 26, with CF_4:SF_6 at 28.7:1.3 Torr.

(b) y run event 30, with CF_4:SF_6 at 28.6:1.6 Torr.

Figure 7.22: Typical alpha events in CF_4:SF_6 with $\Delta V_{MM} = 1014\,\mathrm{V}$, $V_{micromegas} = 500\,\mathrm{V}$ and a drift field of $352\,\mathrm{V\,cm^{-1}}$.

The event topologies for the alpha tracks in CF_4:SF_6 are very similar to those seen in SF_6, this can be attributed to the similar charge transport in the respective gasses. Like in SF_6 the signal on the x strips is considerably lower on the x strips than on the y strips and artifacts from the capacitive portion of the signal are more visible. The bias voltage that had to be applied to the micromegas-MMThGEM combination to observe the tracks was also lower than in pure SF_6.

Apart from the gain characteristics a major difference between the SF_6 and CF_4:SF_6 mixture is the mobility of the primary charge carriers. Figure 7.23a shows the distribution of projected alpha angles, $\frac{dt}{dx}$ and $\frac{dt}{dy}$ in CF_4:SF_6 determined with the same baseline subtraction and fitting described in Section 7.3.3.

As would be expected in a negative ion drift gas, rate of arrival of charge from the alpha track is faster for larger drift fields. The drift velocity of the main charge carriers is determined using Equation 7.5 using the minimum, maximum and average of the $\frac{dt}{dx}$ distributions and the corresponding measured alpha angles. Figure 7.23b shows the determined drift velocity against reduced drift field for the x and y runs and the best fit mobility.

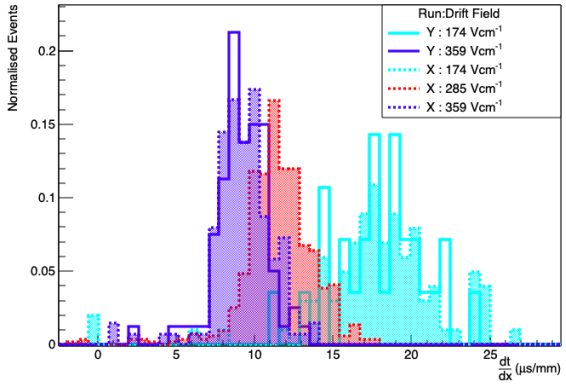

(a) $\frac{dt}{dx}$ for x runs (shaded) and $\frac{dt}{dy}$ for y runs (solid lines) for different drift fields.

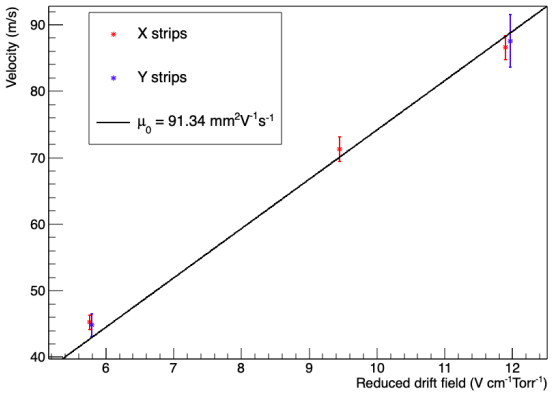

(b) Calculated velocity of primary charge carriers determined from alpha runs against reduced drift field, with best fit mobility.

Figure 7.23: Track data from x and y runs at ~30 Torr CF_4:SF_6 for micromegas-MMThGEM with $\Delta V_{MM} = 1006\,\text{V}$, $V_{micromegas} = 500\,\text{V}$.

Using the same method as in Section 7.3.3 the reduced mobility is found to be $91.3 \pm 8(\text{sys}) \pm 0.2(\text{stat})\,\text{mm}^2/\text{V/s}$. Previous work in CF_4:SF_6 identifies the primary charge carrier as SF_6^- at this pressure and field and its the reduced mobility as $79\,\text{mm}^2/\text{V/s}$ [150]. Interestingly the ratio between the literature and measured mobility here is 1:1.157, in SF_6 that ratio was 1:1.156. This is consistent with the main source of error being systematic, as reflected in the calculated errors.

The micromegas-MMThGEM displays very consistent tracking across both pure SF_6 and CF_4:SF_6 despite the different gas properties and operating point used. The ^{241}Am data demonstrates that the micromegas-MMThGEM and CF_4:SF_6 is a viable strip detector and negative ion drift gas combination for high energy recoil tracking and event reconstruction.

7.3.6 ^{55}Fe in CF_4:SF_6

As in the previous sections, ^{55}Fe can be used to test the abilty of the detector and gas combination to reconstruct low energy recoils and determine the achievable effective gain on the strips. Quantifying the ability of the micromegas-MMThGEM and CF_4:SF_6 combination to achieve this is important for demonstrating the low energy threshold and tracking capabilities. Figure 7.24 shows a typical ^{55}Fe event in 38.7:1.3 Torr CF_4:SF_6 on the micromegas-MMThGEM with $\Delta V_{MM} = 1047\,\text{V}$, $V_{micromegas} = 515\,\text{V}$.

As with the alpha events, the topology of the ^{55}Fe events in CF_4:SF_6 is very similar to in pure SF_6. Charge dissipation makes up a significant amount of structure on both the x and y strips, with a timescale on the order of microseconds. The effective gain on the strips is determined as previously described in Section 7.2.2. The gain on the y strips in 38.7:1.3 Torr CF_4:SF_6 with $\Delta V_{MM} = 1034\,\text{V}$, $V_{micromegas} = 506\,\text{V}$ is calculated to be 52600 ± 1500 and the gain on the x strips in the same run is found to be 8900 ± 1300. As seen with the stand alone MM-ThGEM the gain in CF_4:SF_6 is significantly higher than for similar voltages than in SF_6.

The observation of small scale structure and the determination of sufficient gains to observe low energy recoils demonstrates that, in addition to showing good tracking at high

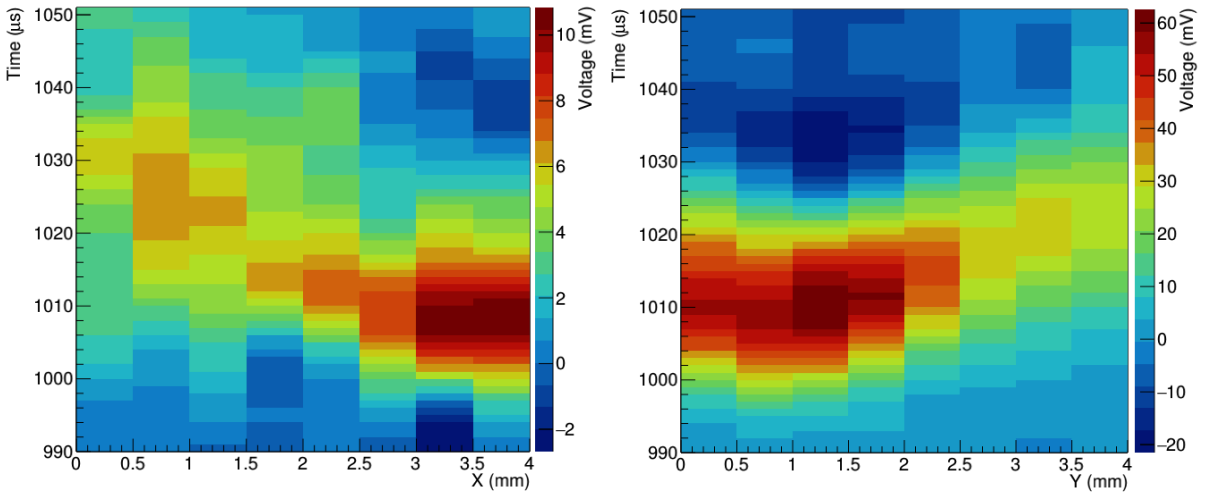

Figure 7.24: x-t and y-t plots of an ^{55}Fe event in 38.7:1.3 Torr CF_4:SF_6 for micromegas-MMThGEM with $\Delta V_{MM} = 1047\,\mathrm{V}$, $V_{micromegas} = 515\,\mathrm{V}$.

energy, the micromegas-MMThGEM and CF_4:SF_6 is a viable combination for low energy directionality work at KeV energies. The persistent observation of the spreading-out of the signal across the strips in ^{55}Fe data attributed to charge dissipating in the resisitive layer remains a large part of the signal. The exact cause of this effect and its relationship to the fundamental structure of the micromegas bears closer study.

7.4 Charge dissipation

As described in Sections 7.2.2, 7.2.4 and 7.3.6, a persistent characteristic of events on the micromegas is the spreading of the signal over several strips over a period of tens of microseconds. The effects of this are illustrated in Figures 7.7 and 7.24. The consistent observation of the effect on the micromegas in gasses with very different characteristics and in experimental setups with and without the MM-ThGEM show that is is intrinsic to the micromegas readout. This effect is attributed to the lateral dissipation of charge in the resisitive layer of the micromegas. To understand the dissipation better an analytical model was developed based on a simplified model of the detector. This section describes the developed model and compares the the results with the observed effect in the detector. The full derivations of the charge density equations presented here can be found in [156].

The simplest model is to describe the system as initially a point charge dissipating on an infinite resisitive plane in free space. This is derived by determination of the potential field of a spontaneously appearing point charge in a three layer geometry where the middle layer represents the resistive layer and the other two layers are free space. The thickness of the central layer is taken to zero and the outer layers to infinity. Determining the co-dependent evolution of the charge distribution and the potential field in each layer then requires the definition of characteristic functions for each region and the integration of each of these to infinity. The application of boundary conditions and some derived identities enables the charge density on the resistive plane to be determined in the form

$$q(r,t) = \frac{Q}{2\pi} \frac{vt}{(r^2 + v^2t^2)^{\frac{3}{2}}} \tag{7.8}$$

where $q(r,t)$ is the charge density as a function of radius, r, and time, t, where a point charge, Q, is initially at $(0,0)$. The rate of diffusion depends on characteristic velocity $v = \frac{1}{2\epsilon_0 R}$, where R is the resistivity of the resisitive layer ($50\,\mathrm{M\Omega/\square}$ for the micromegas in this work). However, this model neglects any of the other components in the micromegas and it can be shown that the capacitance of the resisitive layer to other elements in the detector will have a significant effect on the time evolution of the charge density at long times. If we instead approximate the micromegas as an infinite resisitive layer parallel to a grounded plane then we can define a characteristic time constant

$$T = 2b\epsilon_0 R \tag{7.9}$$

where b is the separation between the infinite resisitive plane and a parallel infinite grounded plane. For $t \lesssim T$, Equation 7.8 is a good approximation of the diffusion in the resistive layer. For longer time scales, $t >> T$, however a more appropriate model of diffusion is given by the equation

$$q(r,t) = \frac{Q}{b^2\pi}\frac{T}{8t}e^{\frac{-r^2}{8b^2t/T}} \tag{7.10}$$

Taking b to be $75\,\mu\mathrm{m}$ which is the separation between the resistive layer and the y-strips ($50\,\mu\mathrm{m}$ polymide+$25\,\mu\mathrm{m}$ glue), gives a value of T of $0.0664\,\mu\mathrm{s}$. As the sampling time of the DAQ is $1\,\mu\mathrm{s}$ the relevant domain for the experimental data is $t >> T$. Note that the use of electron drift gasses with collection and sampling times $O(10\,\mathrm{ns})$ is much more common in the literature and for those detectors Equation 7.8 is more appropriate.

If we treat the signal on the strips as created capacitively with charge density on the strips as equal and opposite to the charge density on the resistive layer above it then we can arrive at an approximation of the signal on strip n from the integral of the charge density over the strip area

$$Q_{strip}(t,n) = \int_{y_n - w/2}^{y_n + w/2}\int_{-\infty}^{\infty} q(x,y,t)dxdy \tag{7.11}$$

where y_n is the centre of strip n, w is the strip width and q is the charge density on the resistive layer. Taking the charge density on the resistive layer to be equal to $q(r,t)$ from Equation 7.10 in cartesian coordinates this integral evaluates to

$$Q_{strip}(t,n) = \frac{Q}{2}\left[\mathrm{erf}\left(\frac{y_n + \frac{w}{2}}{2b\sqrt{2t/T}}\right) - \mathrm{erf}\left(\frac{y_n - \frac{w}{2}}{2b\sqrt{2t/T}}\right)\right]. \tag{7.12}$$

As the strips are grouped into pairs to each readout channel the charge arriving at each preamp would be the sum of the charge on two adjacent strips. The charge arriving at the input of channel k is then $Q_{chn}(t,k) = Q_{strip}(t,2k) + Q_{strip}(t,2k+1)$. The charge evolution on eight channels with strip width and spacing consistent with 'y' on the micromegas is shown in Figure 7.25. The initial position of the charge is the centre of channel 0 (between strips -1 and 1) at $t = 0$. The charge dissipation visible on the strips with this model occurs over a time on the order of $10\,\mu\mathrm{s}$, which is consistent with what is seen in the ^{55}Fe data.

Of interest is how the time at which the most signal is observed on a given strip varies with the strip distance from the initial charge location. To obtain this signal peaking time on each channel the time differential of Q_{strip} is found to locate the turning points.

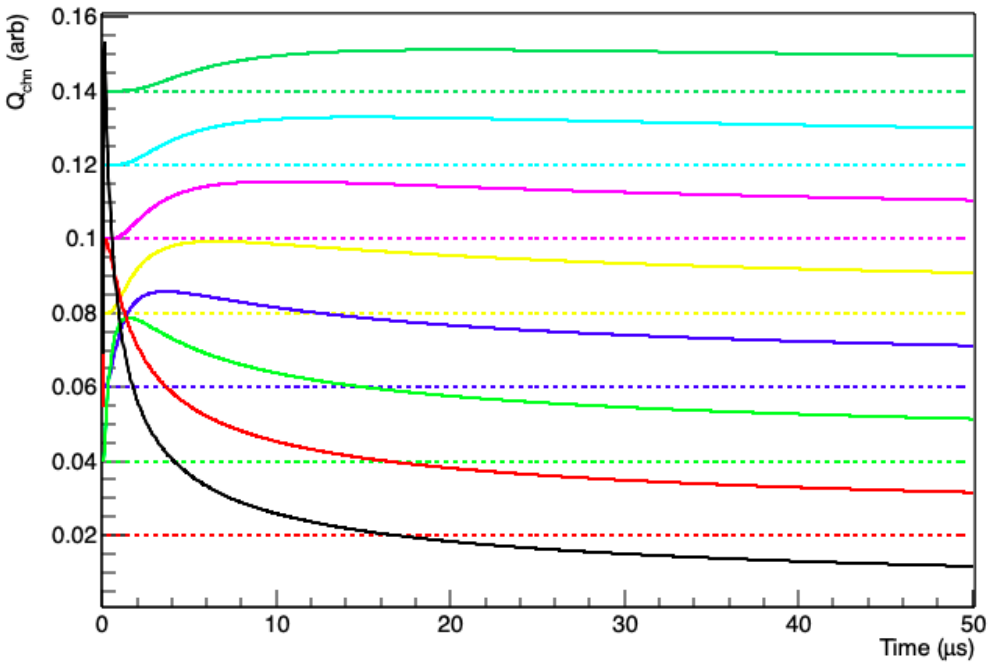

Figure 7.25: Charge on channels 0-7 for analytic model of unit charge dissipating in a resistive layer from centre of channel 0. Channels offset for clarity with dotted line indicating baseline.

The time differential of the signal on the strips is

$$\frac{\partial Q_{strip}}{\partial t} = \frac{\sqrt{T}t^{-\frac{3}{2}}}{b\sqrt{8\pi}} \left[\left(y_n - \frac{w}{2}\right) e^{-\left(\frac{y_n - \frac{w}{2}}{b\sqrt{\frac{8t}{T}}}\right)^2} - \left(y_n + \frac{w}{2}\right) e^{-\left(\frac{y_n + \frac{w}{2}}{b\sqrt{\frac{8t}{T}}}\right)^2} \right] \tag{7.13}$$

setting $\frac{\partial Q_{strip}}{\partial t} = 0$, the solution for finite time is the peaking time

$$t_{peak}(n) = \frac{w y_n T}{4b^2 \ln\left(\frac{y_n + \frac{w}{2}}{y_n - \frac{w}{2}}\right)} \tag{7.14}$$

in the limit of a thin strip such that $w << y_n$ this can be simplified to

$$\lim_{w<<y} t_{peak}(y) = \frac{T}{4b^2} y^2 \tag{7.15}$$

This result can also be found by the integration then differentiation of equation 7.10. The prefactor $\frac{T}{4b^2}$ reduces to $\frac{\epsilon_0 R}{2b}$ which has a value of $2.9\,\mathrm{s/m^2}$ for the R and b of the micromegas in this work.

Note that there are a number of simplifications and assumptions made in this model which include:

- All signal induced by the motion of charge is neglected
- The micromegas mesh and x-strips are omitted as elements

- The y strips are approximated as a contiguous grounded plane
- The input impedance of preamp and other effects of the amplifier chain are ignored
- The different Permittivities of elements in the detector is ignored
- The resisitive layer is treated as an infinite plane of zero thickness

Due to the complexity of the geometry a complete treatment would require finite element analysis or similar tools, as such the value $2.9\,\mathrm{s/m^2}$ should be considered closer to an order-of-magnitude estimation of the diffusion rate.

Equation 7.15 was fitted to the peaking times on each of the y strips from ^{55}Fe data in CF_4 and SF_6, an example event and fit is shown in Figure 7.26a. Figure 7.26b shows the distribution of the value of the fit constant, equal to $\frac{\epsilon_0 R}{2b}$, for the CF_4 and SF_6 runs.

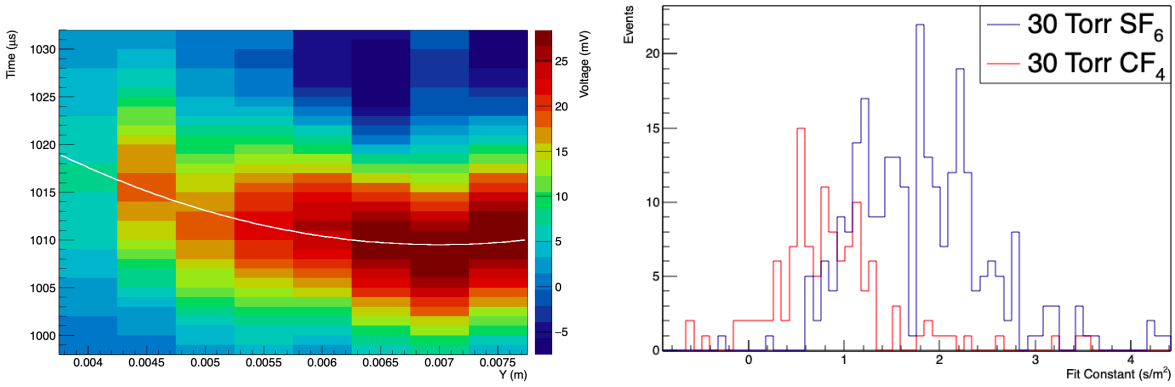

(a) Fit to channel peaking time (white) for an SF_6 event.

(b) Distribution of fit constant in 30 Torr CF_4 and SF_6.

Figure 7.26: Quadratic fit to charge dissipation in the resistive layer for ^{55}Fe data collected with the micromegas-MMThGEM combination.

The average fit constant was $0.87 \pm 0.67\,\mathrm{s/m^2}$ for CF_4 and $1.88 \pm 0.90\,\mathrm{s/m^2}$ for SF_6. The discrepancy between the two gasses might be attributed to the slower charge transport in SF_6 as the width of the ^{55}Fe event will tend to broaden the distribution more if all the charge arrives at approximately the same time as in CF_4. Despite the difference between the fit constant for the data and the value arrived at for the analytic model, the quadratic relationship between the channel peaking time and offset appears to well describe the diffusion that we observe.

As an aside, if the effect of the parallel grounded layer is neglected (i.e. charge dissipates as in Equation 7.8), the equation for peaking time is instead

$$t_{peak} = \left|\frac{y}{v}\right| \tag{7.16}$$

This model predicts a straight line relationship between signal peaking time and offset from the charge collection with a characteristic velocity of $v = 1.1\,\mathrm{mm\,\mu s^{-1}}$. The best fit of Equation 7.16 to the data instead arrives at a characteristic velocity of $v = 13.6\,\mathrm{mm\,\mu s^{-1}}$. The large difference between the analytic model and best fit to the data shows that the inclusion of a grounded plane in the model is important to obtain result which well describes the dissipation.

Overall charge dissipation in the resistive layer is shown to well describe the charge spreading effect observed in the micromegas strip data. The timescale of the signal measurement is shown to be a significant factor in the shape of the charge dissipation. On the microsecond timescale of negative ion charge collection, a quadratic relationship between signal peaking time and strip offset from the charge collection point is predicted by the analytic model and this is consistent with strip data. Understanding this signal formation process is important for disentangling contributions to the signal from ionisation in the gas volume and the motion of charge in the resistive layer. Approaches to mitigating the effect of the charge dissipation on the signal will be discussed further in Chapter 9.

7.5 Conclusions

The main goals of this chapter were to explore the use of the micromegas as a strip readout capable of event reconstruction in multiple dimensions at a low energy threshold in negative ion drift gases. It was found that the micromegas on its own performed well in the electron drift gas CF_4, with signal from alpha tracks and ^{55}Fe electrons resolvable on the strips. In SF_6 measurements of ^{55}Fe made on the micromegas mesh showed that significant gas gain was achieved, although it was not sufficient to observe the 5.9 keV electrons on the strips. With processing alpha tracks were distinguished, although the ratio of capacitive noise to track-like signal contributed to relatively poor track reconstruction.

The new MM-ThGEM technology was successfully used to enhance the signal observed by the micromegas. Adding the MM-ThGEM to the micromegas increased the gain without significant distortion to the event shape in CF_4. In SF_6 and CF_4:SF_6 mixtures the additional gain from the MM-ThGEM amplification stage resulted in a much more defined alpha track which enabled better tracking resolution and less distortion from processing. The more defined alpha tracks made possible a measurement of the reduced mobility of the negative ion gases, with values of $61.3 \pm 5(\text{sys}) \pm 0.2(\text{stat})\,\text{mm}^2/\text{V/s}$ and $91.3 \pm 8(\text{sys}) \pm 0.2(\text{stat})\,\text{mm}^2/\text{V/s}$ for the SF_6 and CF_4:SF_6 primary charge carriers respectively. These mobilities were within likely systematic errors of the negative ion mobilities determined by others with significantly different setups.

The addition of the MM-ThGEM also enabled ^{55}Fe to be observed on a micromegas in SF_6 and CF_4:SF_6 for the first time and a gain measurement to be obtained from the strips. It was possible to reconstruct three dimensional structure from electron and alpha events in the negative ion gasses, although the charge dissipation in the resistive layer introduced some artifacts into the reconstructed shape. The charge dissipation appears to be fairly well described by the analytic model presented in Section 7.4 when the effect of a parallel grounded plane is accounted for.

Chapter 8

Towards Scaling up the Readout

One of the major obstacles to scaling a detector for a deployment in a neutron assay or Dark Matter detection role is the instrumentation cost. The electronics to amplify and digitise a set of signals from a micromegas with sufficient gain and noise characteristics are a very significant component of the cost of the system. The Cremat amplification chain used in the previous chapter for example costs $\sim$ £50 /channel which would put the cost of instrumenting the entire 10×10 cm of the micromegas at £40 000, or approximately ten times the cost of the micromegas-MMThGEM combination itself. Implementing cheap electronics system with sufficient gain and low noise is an important step towards a realistic design for large area readout for this technology.

This Chapter will describe the operation of the micromegas-MMThGEM detector with the Negative Ion Data Acquisition (NI-DAQ) system, a scalable readout system for signal on the time scale of negative ion drift gas TPC's developed primarily in Kobe University, Japan. The aim is to demonstrate of alpha track reconstruction, neutron detection and a level of ER discrimination using a scalable readout system in combination with the micromegas-MMThGEM detector. Demonstrating the suitability of the DAQ system for operation with a diverse set of negative ion gas based detectors is an objective for the team developing the NI-DAQ system and the work presented here is expected to help contribute to the continued development of the NI-DAQ system. Moreover the ability to operate with significantly more channels than were available in the previous runs will help capture events with a larger spatial extent and better characterise the charge dissipation.

In the following, Section 8.1 describes the NI-DAQ amplification and digitisation system. Section 8.2 covers the detector setup in Kobe describing the vessel, bias and instrumentation of the detector. The signal processing used in the subsequent analysis is described in Section 8.3 as well as some of the noise species that are observed. The detector response to alpha tracks generated by ^{241}Am exposure of the drift region is described in Section 8.4, and the response of the detector to electron recoils from ^{55}Fe source is described in Section 8.5. Section 8.6 describes the detector response to neutron exposure from a ^{252}Cf source and the obtained discrimination and directionality.

8.1 Kobe NI-DAQ

The NI-DAQ system is the result of a project to develop scalable electronics for the NEWAGE directional dark matter detection experiment [153]. The readout system is developed specifically for negative ion gas detectors and as such has ideal characteristics for the instrumentation of the micromegas-MMThGEM combination in SF_6. The NI-

DAQ system encompasses the hardware and software architecture for the amplification, digitisation and digital storage signal.

The hardware component of the NI-DAQ system consists of a set of amplification boards and a digitisation board as well as a separate computer for saving the signal. The computer hosts a virtual machine which provides user interface and control of the digitisation board, with data transfer mediated by the DAQ-Middleware software framework [157, 158].

The amplification boards are an implementation of the Low-Temperature Analog Readout System (LTARS) and the digitiser is custom built around an FPGA, each of these components is described in more detail in the following sections. The per-channel cost for the initial production run of 10 000 channels for the LTARS system is around \$1.00 /channel, this is already comparable with significantly more mature scalable DAQ systems like the APV25-SRS system developed by [159].

8.1.1 Front-end electronics: LTARS

The LTARS is a custom analog front-end electronics system developed by a collaboration between Japan's national high energy physics laboratory, KEK, and Kobe University for amplification of signal from TPC type detectors with signal development on the order of microseconds. The main experimental applications for the LTARS system are liquid Argon or negative ion drift gas based TPCs. The current iteration of the LTARS system consists of an ASIC (Application Specific Integrated Circuit), which is integrated onto a *TOSHIZOU v2* PCB test board which mounts the relevant connectors and supporting circuitry. A picture of the *TOSHIZOU v2* PCB test board is shown in Figure 8.1a, the ASIC and relevant connectors labeled.

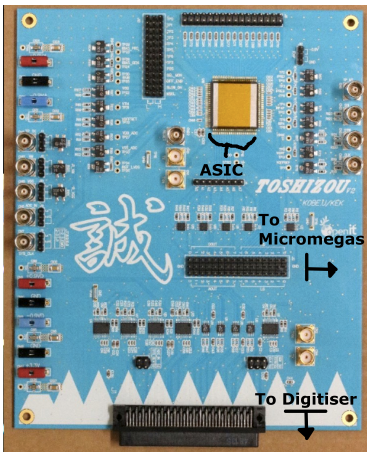

(a) The TOSHIZOU v2 ASIC board.

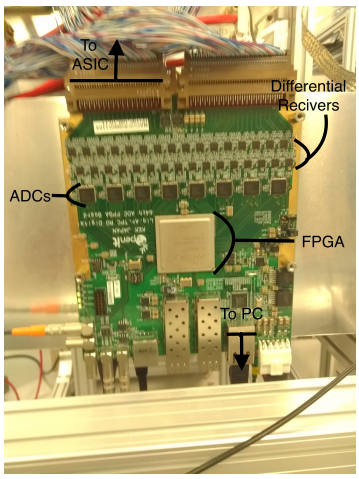

(b) The Digitiser board.

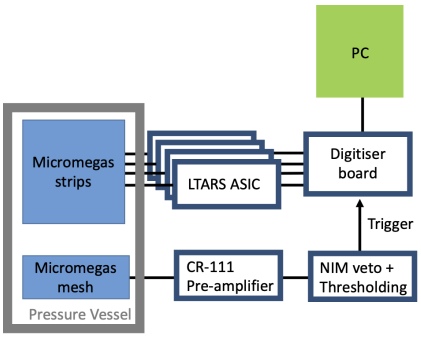

(c) Electronic DAQ setup using the Kobe electronics.

Figure 8.1: The NI-DAQ setup used with the micromegas-MMThGEM.

The individual ASIC units are fabricated with Silterra 180-nm CMOS process for the low noise and energy dissipation characteristics of that technology. Each of the ASIC units implement a preamplifier and CR-RC shaper stage for 8 channels. After the preamplification and first shaping stage each channel is split and amplified through additional individual shaping amplifiers with different gains. Consequently for each input channel

there are two output channels, designated the 'high gain' and 'low gain' signals, this enables the ASIC to operate over a wider range of signal intensity than a single shaper stage would provide. The design gain of the LTARS is $0.5\,\mathrm{mV\,fC^{-1}}$ for the low gain stage and $10\,\mathrm{mV\,fC^{-1}}$ for the high gain stage. The shaping time is $7\,\mu\mathrm{s}$ for the negative ion version which is used here, for operation with liquid Argon detectors there is also a $4\,\mu\mathrm{s}$ shaping option. The ASIC also has architecture to implement a dynamic gain stage although that is not implemented on the *TOSHIZOU v2* boards.

8.1.2 Digitiser board: FPGA

After amplification, the signal is digitised on a customised PCB board which is fabricated from off-the-shelf components. The digitisation board consists of a set of ADC units and a single FPGA, a picture of the board is shown in Figure 8.1b. The ADC units convert the Analog signal into a 12 bit integer representing the voltage. The FPGA collates the ADC signals into data frames which are exported via Ethernet to a PC using the DAQ-Middleware software framework. The digitisation board requires an external trigger which consists of a NIM logic pulse, enabling trigger thresholding and vetoing to be undertaken with standard NIM units.

8.2 Micromegas-MMThGEM setup with Kobe DAQ

Figure 8.2 shows the micromegas and MM-ThGEM setup inside the small steel vessel that is used for the runs in Kobe The micromegas is orientated such that the 'x' strips are aligned vertically, the 'y' strips are horizontal, and the cathode is towards the door of the rectangular steel vessel. The door of the vessel has a thin kapton window integrated into it, this and the steel mesh cathode allows the drift region to be exposed to an external ^{55}Fe or ^{60}Co source.

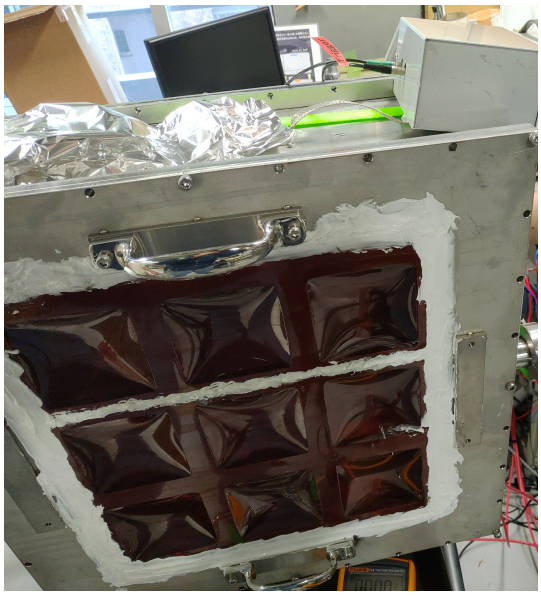

(a) Sealed vessel showing thin kapton window at the front.

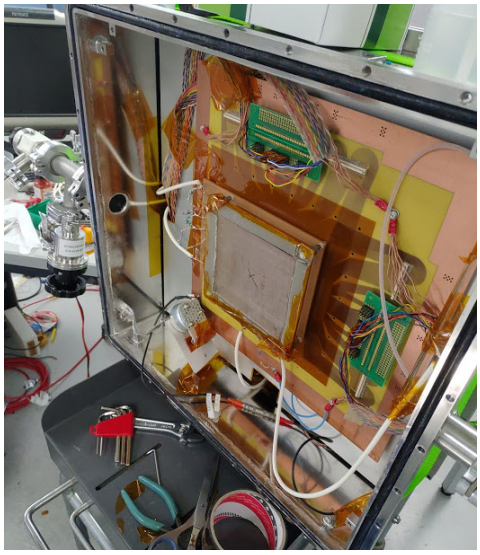

(b) Vessel with door removed showing micromegas-MMThGEM combination.

Figure 8.2: Pictures of the Kobe Micromegas vessel.

An ^{241}Am source is situated inside the vessel with alpha exposure of the drift region controlled by a source shutter, the alpha source and shutter are visible to the bottom left of the micromegas in the figure. A diagram of the micromegas-MMThGEM setup and relative source locations is shown in Figure 8.3. The MM-ThGEM is offset from the micromegas by a gap of 2 mm from the back plane of the MM-ThGEM to the micromegas mesh. The drift gap between the cathode and the top plane of the MM-ThGEM is 24 mm with no field cage. The MM-ThGEM is biased through the same resistor chain described in Chapter 7, allowing the top and bottom planes and the four intermediate meshes to biased with only two voltages.

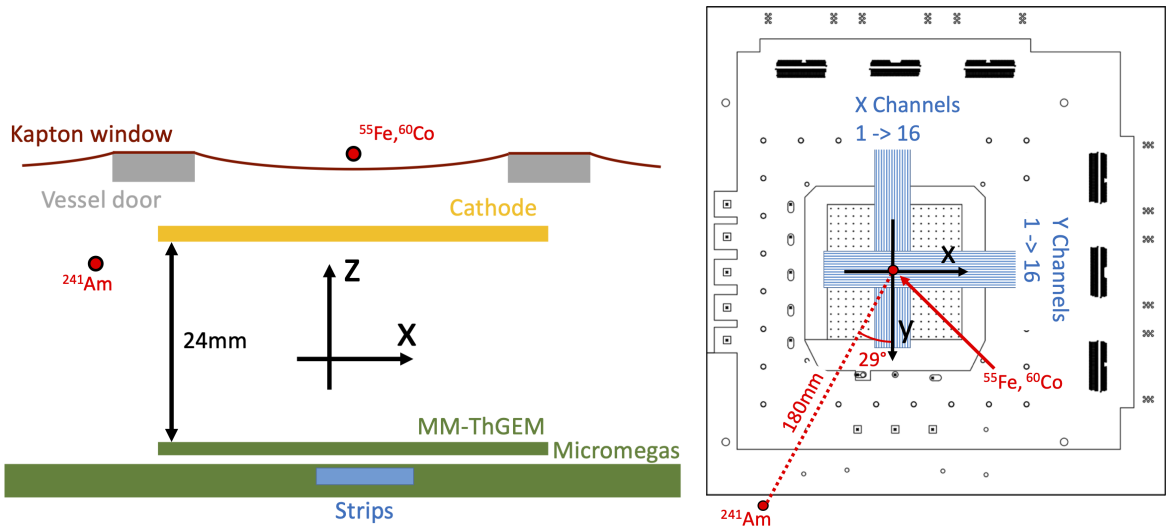

(a) x-y view.

(b) x-z view.

Figure 8.3: Diagram of the x-y and x-z projections of the micromegas-MMThGEM in Kobe.

On the micromegas, alternate strips are instrumented resulting in an effective pitch of 500 µm, this is slightly different from the set up in Chapter 7 where each channel instrumented two strips although the effective pitch remains the same. A set of ribbon cables are used to run the strip signal to four D-SUB DE-9 connectors on the rear of the vessel and then to the ASICs on a table next to the vessel. An effort was made to minimise the distance between the ASICs and the instrumented strips, the ∼50 cm total cable run between the micromegas and ASICs however likely still contributes significantly to the noise on the channels.

The micromegas mesh, cathode and the top and bottom of the MM-ThGEM resistor chain are biased through BNC connectors at the rear of the vessel. A CR-150 preamplifier is used to amplify the signal from the micromegas mesh. A thresholding module is used to convert preamplifier pulses into NIM logic pulses which are used to trigger the digitisation board. A NIM logic module and pulse generator is used to veto additional pulses from the thresholding module in a 5 ms window after a trigger pulse to prevent multiple triggers on the long tail of the preamplifier pulse.

The vessel is pumped to vacuum prior to filling with either SF_6 or an SF_6:CF_4 mixture. There are a number of runs performed over the duration of the deployment in Kobe, to keep track of each run an automatic naming convention is used based on the date and time of the run delimited by a 'T'. So for example run 20200228T164235 is the run starting on the 28^{th} of February in 2020 at 35 seconds past 16:42.

8.3 Signal processing

In preliminary runs it was found that the raw signal obtained from the strips includes a significant amount of noise both random and sinusoidal. Additionally a large fraction of the events obtained do not correspond to signal from interactions in the gas well centred above the strips or contain artifacts. This section describes the noise mitigation strategies which were implemented for the data analysis, the signal parameters which were extracted and describes the main populations of observed noise events.

8.3.1 Fourier notch cuts

During the data collection large sinusoidal noise was observed which on average effected about half of the instrumented channels. An example of the sinusoidal noise signal on one of the channels is shown in red in Figure 8.4a. The ASIC DAQ boards were unsheilded apart from the PCB ground planes integrated into them and this likely contributed to the issue. The hypothesis that noise is related to the setup of as individual ASIC board is supported by the fact that if sinusoidal noise was present it would effect all channels on a given ASIC board. This sinusoidal noise is particularly problematic on the channels instrumenting the x strips as frequently the signal is of a similar magnitude to this type of noise.

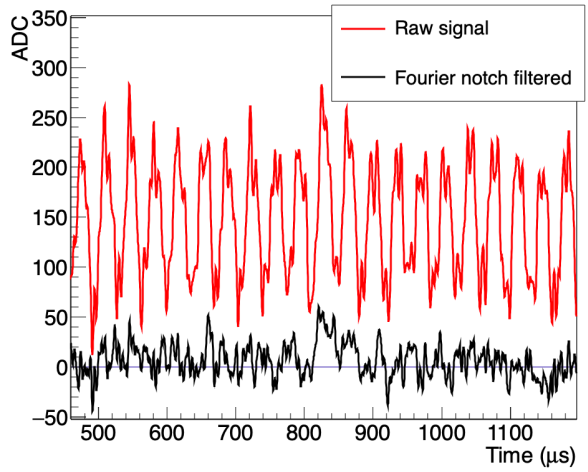

(a) Zoomed view of raw waveform and the waveform after notch cut and pedestal subtraction.

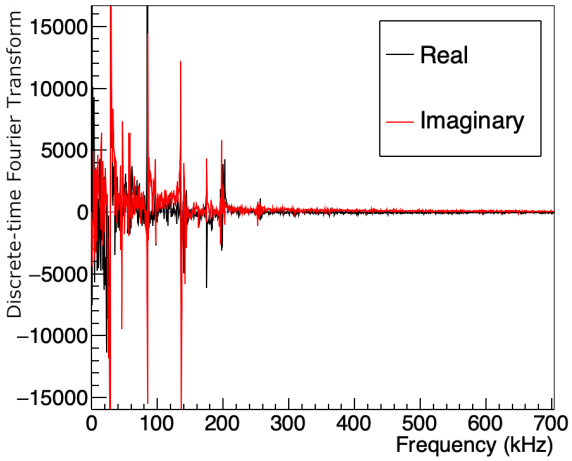

(b) Truncated Discrete-time Fourier transform of raw waveform.

Figure 8.4: Signal on Channel 14, Event 5 in run 20200229T103730.

To examine the sinusoidal noise a discrete Fourier transform was applied to the signal waveforms. An example Fourier transform of a single y channel is shown in Figure 8.4b, frequencies contributing to the noise are identified at approximately 28 kHz, 87.5 kHz and 137.5 kHz. The presence of these frequencies is intermittent and not all frequencies are present in all runs, furthermore the value of the noise frequencies seem to wander slightly. It's not known what the source of these noise frequencies is; the upper end of the frequency range is high enough to reach the low end of the AM radio band, although the 28 kHz frequency is too low for that.

To eliminate this noise an algorithm was written which applies a Fourier notch filter to the noise frequencies present on a given channel. The Fourier transforms are implemented

through the C based FFTW library, which provides the fastest available open source implementation of Fourier transforms. To apply the Fourier notch filter a discrete Fourier transform is performed on each of the signal channels individually. Bins in the resulting discrete-time Fourier transform corresponding to nuisance frequencies are then set to zero and the inverse transform is performed to recover the signal with those frequencies removed. The range of frequencies removed by the notch filter were 25.6 kHz to 31.9 kHz (DTFT bins 41-51 and 3948-3958), 84.4 kHz to 90.6 kHz (bins 135-145 and 3854-3864) and 131.3 kHz to 143.7 kHz (bins 210-230 and 3769-3789). The effect of the notch filter on a noisy channel is illustrated in Figure 8.4a.

This filter is very effective at removing this sinusoidal noise from the data and is vital for recovering small signals. There are some artifacts introduced by the filter; for instance ripples are sometimes visible at the edges of the signal window in the first and last $\sim$ 700 bins (280 µs), low level rippling effects are also noted near large magnitude peaks. These artifacts are uniformly much smaller than the sinusoidal noise itself and furthermore can be excluded from the analysis by constraining the analysis time window and careful thresholding. Even with the relatively small magnitude of such features, care is taken in the analysis to ensure that notch filter artifacts do not bias any of the results. Furthermore the notch filter is not applied to channels where there is not significant sinusoidal noise in a given run.

8.3.2 Savitzky–Golay smoothing

A significant amount of the random noise in the collected data has a timescale shorter than that of the signal. To help alleviate this noise a Savitzky–Golay filter was implemented to smooth the signal waveforms. The effect of a Savitzky–Golay filter of order 3 and length 20 on the signal from one of the micromegas y channels is shown in Figure 8.5.

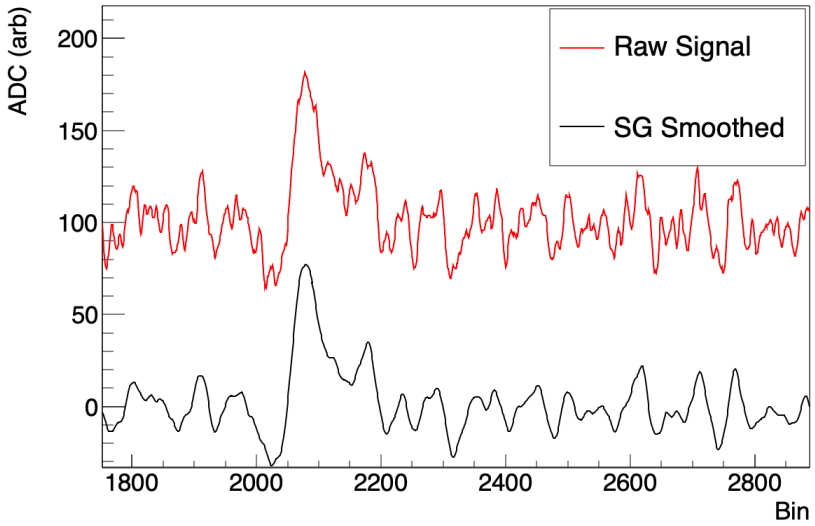

Figure 8.5: Signal on Channel 16, Event 5 in run 20200229T103730, raw waveform and waveform after smoothing with a Savitzky–Golay filter of order 3 and length 20.

The Savitzky–Golay filter involves fitting a polynomial of a given order to successive subsets of adjacent data points; the smoothed version of the waveform then derived from these fits. More detail about SG smoothing can be found in [160]. The optimal length and order of the SG smoothing is dependent on the specific task and the expected signal

features, as such the analysis code was set up such that the length and order of the SG smoothing can be set from the command line at run time. If a Fourier notch filter is applied to a given channel the SG smoothing is performed after it.

8.3.3 Interpolation of dead channels

Another issue that was encountered was that a number of channels in each run did not have any signal present on them in any of the events. The cause of this was determined to be a mix between physical disconnections between the ASIC and FPGA channels and individual ASIC channels being non functional. Attempts to fix the physical disconnections which were present did reduce the number of dead channels, although frequently fixing a disconnected channel would result in a different channel being similarly disconnected. Consequently over the duration of the experimental campaign there were five separate configurations of working channels over different days of the detector operation.

The connection issue can be partially attributed to the design of one of the intermediate connectors which was well suited for quick attachment and on-the-fly re-configuration but we learned did not have especially reliable continuity. The short detector deployment in Kobe limited the amount of time that could be devoted to reducing the number of affected channels, although all efforts were made to do so with the time available.

To mitigate the effect of the dead channels in software a simple one dimensional linear interpolation across those channels was implemented. An example of signal on the y-channels with and without the interpolation of dead channels is shown in Figure 8.6.

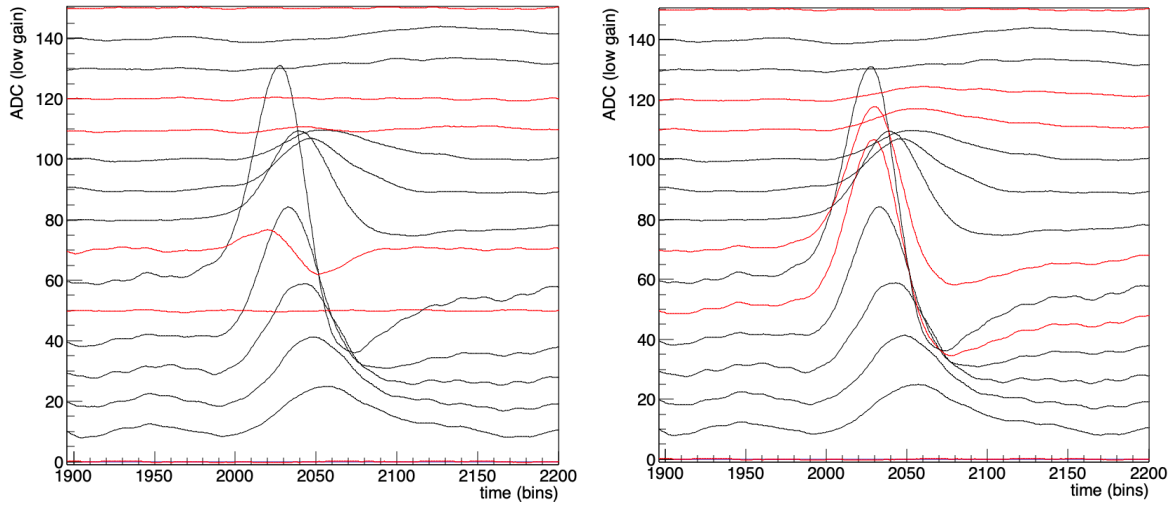

(a) No interpolation across dead channels. (b) Interpolation across dead channels.

Figure 8.6: Signal on low gain y channels, Event 105 in run 20200302T134917 with and without interpolation. Dead channels indicated in red.

The charge dissipation means that there is generally a smooth variation in signal across strips which facilitates the interpolation. The interpolation is necessary because several of the signal parameters are based on the integration of the signal peak and its width and excluding rather than interpolating the non-functional channels would more significantly alter these metrics. Interpolation is performed after the notch filter and SG-smoothing if those are applied, dead channels which occurred on the edge of the readout were not interpolated as there were not channels on both sides to interpolate across.

8.3.4 Noise event types

In addition to events which are triggered by charge arriving at the strips, a number of events for which the arrival of drifting charge is not a physical explanation are observed. A number of different species of these noise events are seen in the detector; the primary identified noise event types are described below and examples of each type are shown in Figure 8.7.

Cross-channel peak A signal consisting usually of a single peak observed on all the channels in a given dimension with the same size and timing across the channels. This is identified as pick up of capacitive signal from large magnitude events occurring elsewhere above the readout as in Chapter 7.

ASIC Discontinuity A discontinuity in the signal between different ASIC boards which instrument adjacent strips (i.e. between the first and last 8 channels in a given dimension). The signal on one of the ASICs sometimes appears to be physical while the other ASIC will not register any apparent signal. Discontinuities between the ASICs are also frequently present in other types of unphysical noise events.

Bipolar peak A large negative swing followed by a large positive swing in signal, with a tendency to have the same time and magnitude across all the channels on a given ASIC.

Wavepacket A burst of oscillatory signal, the burst of signal is typically around 80 µs long and the period of the oscillations is typically 13 µs.

With the exception of the cross-channel peaks there is a tendency for the noise events to be confined to a single ASIC. It is possible that the noise events are caused by the ASICs although the fact that they are frequently localised to a certain ASIC doesn't preclude the signal from originating inside the detector vessel as the signal wires going to each ASIC are bundled together inside the vessel.

These events are removed for the analysis of the data by cuts on the signal parameters. The ratio between the maximum and minimum pedestal-subtracted ADC value is sufficient to reject the wavepacket and bipolar peaks. The ASIC discontinuity effect and cross-channel peaks on the other hand can be distinguished by fiducialisation of the largest signal peak and by the lack of the charge dissipation effect observed in Section 7.4.

8.3.5 Waveform parameters

The analysis of the micromegas events requires extracting parameters from the strip waveforms. Signal parameters are first extracted for each individual channel using the same 1-d analysis described in Section 3.3 that was used for the ThGEM and MM-ThGEM data. The most important parameters from each channel are `v_max`, which is the maximum ADC value reached on the channel, `t_peak` which is the timebin at which maximum ADC value is reached and `t_width` which is the number of timebins that the 1d waveform is above a threshold. In addition the same signal parameters are extracted for a waveform constructed by summing the signal from all of the readout channels.

In this case the units of the parameters are different due to the different DAQ, the parameters extracted are in the base units of the digitisation: 'timebin', 'chn' and 'ADC'. The timebin is the sample in the digitisation window of a data point, each unit of timebin is equal to 0.4 µs in all the data presented here. The chn is the digitisation channel of

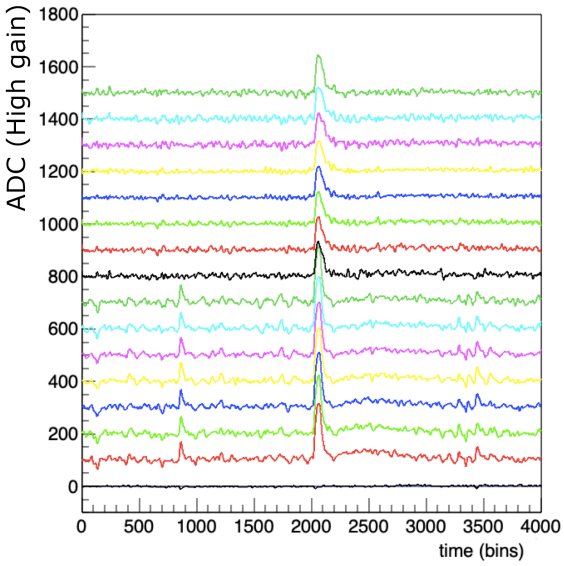

(a) Constant magnitude peak

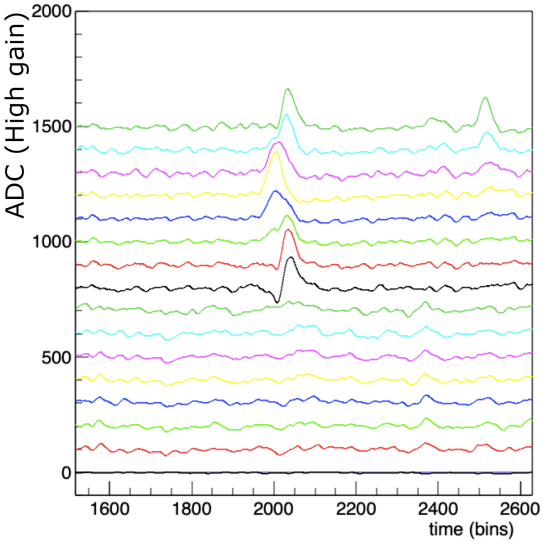

(b) Discontinuity across ASICs

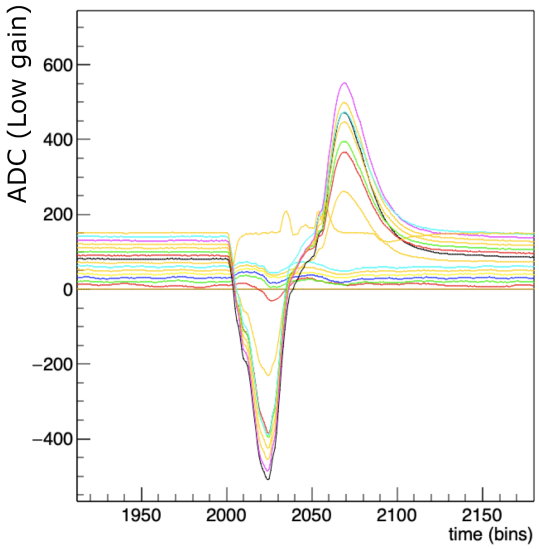

(c) Bipolar peak

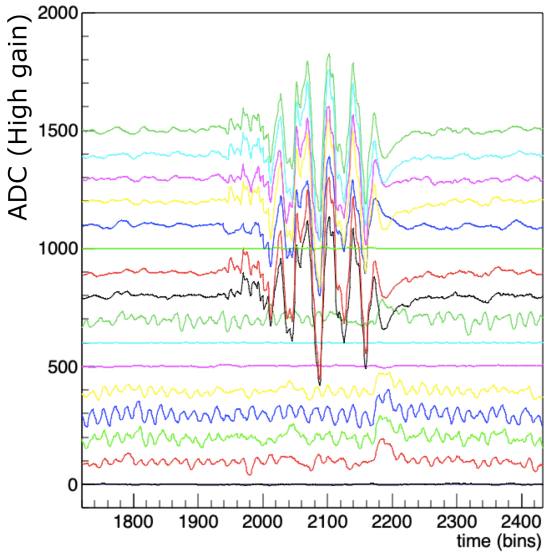

(d) Wavepacket

Figure 8.7: Examples of the main identified noise event types.

a data point, there are 64 total digitisation channels which are divided into four groups of 16; high and low gain for the x and y strips. The channel indexes at digitisation are 0-63 although in the analysis they are grouped into high or low gain for the x or y strips remapped within each group to channel numbers 0-15. For contiguous channels each unit of chn is equal to 500 µm spatial separation in x or y. Finally the unit ADC is the integer value of the voltage digitisation, each unit of ADC is equivalent to a difference in ASIC output of 1.024 mV.

In addition to the 1D parameters extracted for each strip, a set of 2D parameters describing the signal on all of the strips in a given dimension are extracted. These are either calculated from the 1D parameters or from the entire array of ADC values in a given dimension taken together. A short description of the 2D parameters extracted for the x channels are as follows, the set extracted for the y channels are calculated identically

and have the prefix 'y' instead of 'x'. The units of a given parameter are indicated in square brackets.

xthres [ADC]: A threshold set for several of the signal analysis algorithms, generally a fraction of `xv_max`

xv_max [ADC]: Highest value of the `v_max` parameter on any of the channels

xmaxchn [chn]: The channel which has the highest `v_max` parameter

xpeakt [timebin]: The value of the `t_peak` parameter for channel `xmaxchn`

xmeanv_max [ADC]: Average value of the `v_max` parameter for all channels

xt_mean [timebin]: The average value of the `t_peak` parameter for all channels

xq_peak [timebin.chn.ADC]: Integration in two dimensions of the contiguous bins with content larger than `thres` around the bin containing the highest ADC value in the event

xq_tot [timebin.chn.ADC]: Integration in two dimensions of all channels and time bins inside the analysis window

xstripsfwhm [chn]: FWHM of the distribution of `v_max` across the channels

xasym [chn]: The asymmetry of the distribution of `v_max` across the channels

edgexpeak [timebin]: The number of bins which have and ADC value larger than `thres` and are on either of the strips on the edge of the instrumented readout.

xntriggered [chn]: The number of strips with a `v_max` parameter exceeding the value of `thres`

Additionally fits to the peaking times against channel number are performed dependent on the incident particle type. For ^{241}Am runs a linear fit to the peak times is performed to obtain the gradient of a presumed straight track in the x-t and y-t projections.

For runs with a more point-like energy deposition, charge dissipation in the resistive layer was observed to dominate the signal in Chapter 7. In Section 7.4 the analytical solution for charge dissipation in a resistive layer parallel to a grounded plane produced a good fit to the observed peaking times on the micromegas device. Using this analytical solution for the charge dissipation the relationship between peaking time and strip number is expected to be quadratic. The time constant of this quadratic relationship is determined from fitting equation

$$(\texttt{t\_peak}(\texttt{chn}) - t_0) = A(\texttt{chn} - x_0)^2 \tag{8.1}$$

to the peaking times. In the analytical solution the prefactor A is equal to $\frac{\epsilon_0 R}{2b}$ where ϵ_0 is the permittivity of free space, R is the resistivity of the resistive layer and b is the separation between the resistive layer and grounded plane in the analytic model. For the micromegas used the resistivity is $50\,\mathrm{M\Omega/\square}$ and b is taken to be the same as the separation between the resistive layer and y-strips which is about $75\,\mu\mathrm{m}$, this gives an expected prefactor, A of $2.9\,\mathrm{s/m^2}$ or equivalently $0.625\,\mathrm{timebin\,chn^{-2}}$. The factors x_0,t_0 and A are extracted from the fit, the initial values of x_0 and t_0 are set to the location of the peak (equal to parameters `xmaxchn` and `t_peak` respectively).

The parameters which are extracted by these fits are as follows:

dtdx [timebin/chn]: Value of the gradient of a linear fit to channel number against `t_peak` for channels with `v_max>thres`

dtdx_chi2 The χ^2 of the fit which obtains `dtdx`

xfiteR_2b [timebin.chn^{-2}]: The value of the prefactor A in the fit to equation 8.1

xfitx0 [chn]: The value of the parameter x_0 in the fit to equation 8.1

xfitt0 [timebins]: The value of the parameter t_0 in the fit to equation 8.1

xfitchi2 The χ^2 of the fit to the equation 8.1

The fit parameters are used to determine the alpha direction and to study the charge dissipation.

More generally the parameters presented here are used for noise vetoing, discrimination and gain measurements.

8.4 Micromegas-MMThGEM - alpha tracking with ^{241}Am

The Americium α source inside the micromegas vessel is used to demonstrate the tracking capabilities of the micromegas-MMThGEM detector with the NI-DAQ backend. The Americium source is located in the bottom left of the detector vessel which means it is in the (-x,+y) direction in the scheme of channel ordering. The channels are ordered such that the +x direction is orientated toward the right hand side of the vessel and +y is downwards in the lab frame; x and y will always refer to directions in the channel ordering scheme. Figure 8.8 shows the location of the alpha source relative to the centre of the readout in the x-y and y-z projections. The source was not columnated in any way and the alpha angle is only constrained by the location of the sensitive strips relative to the source.

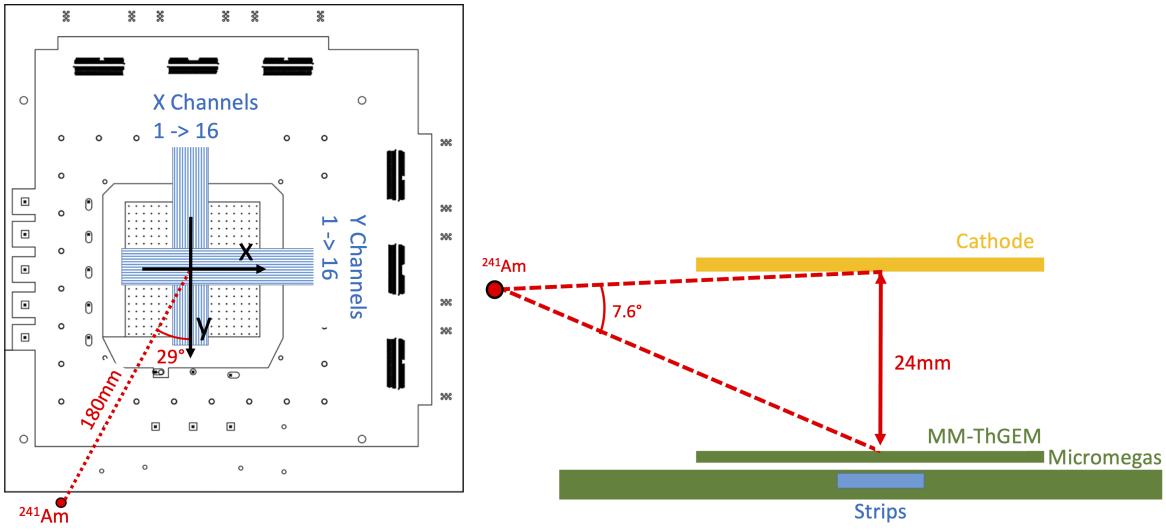

(a) x-y view. (b) y-z view.

Figure 8.8: ^{241}Am source location relative to the micromegas in Kobe.

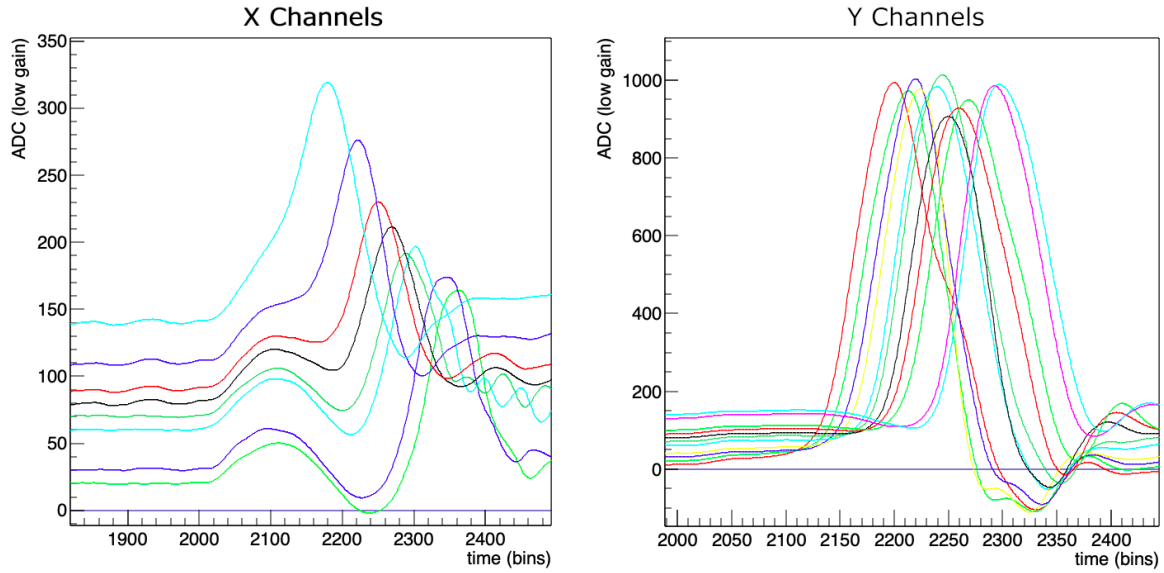

(a) Smoothed waveforms from x and y channels, offset for clarity and with dead channels removed.

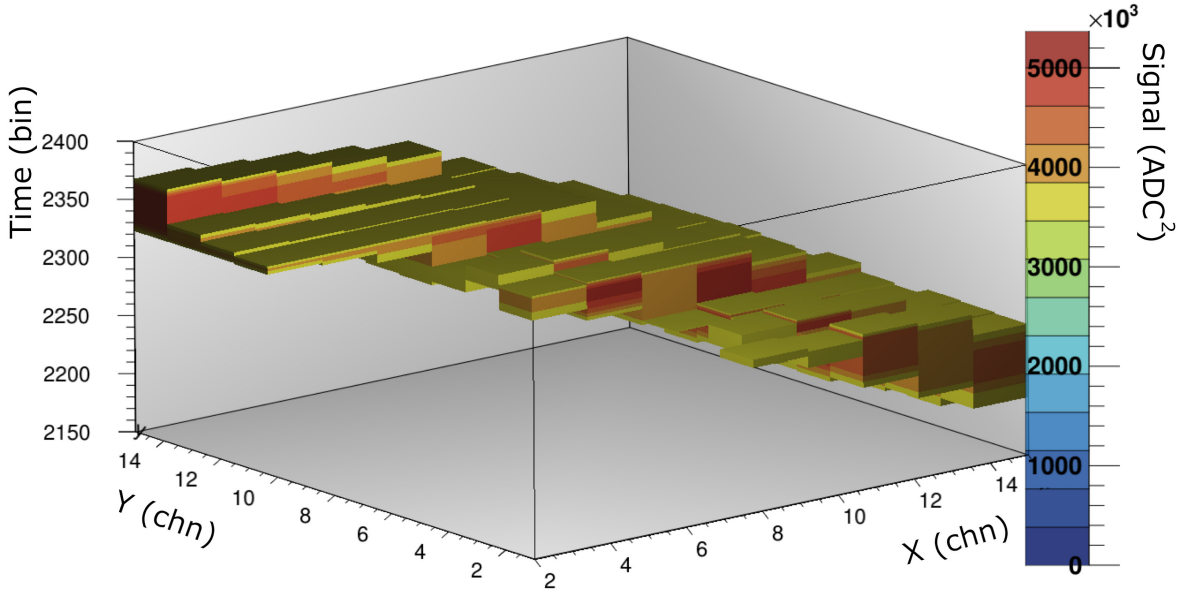

(b) Three dimensional plot

Figure 8.9: Event 233 in run 20200228T164235: ^{241}Am exposure of micromegas-MMThGEM in 39:1.8 Torr CF_4:SF_6 with $\Delta V_{MM} = 1045\,\mathrm{V}$, $V_{micromegas} = 515\,\mathrm{V}$ and a drift field of $360\,\mathrm{V\,cm^{-1}}$.

The two ^{241}Am runs which are examined here are run 20200228T164235 and run 20200302T181705. Run 20200228T164235 consists of ^{241}Am exposure of the drift region in 39:1.8 Torr CF_4:SF_6 with $\Delta V_{MM} = 1045\,\mathrm{V}$, $V_{micromegas} = 515\,\mathrm{V}$ and a drift field of $360\,\mathrm{V\,cm^{-1}}$. Run 20200302T181705 is an ^{241}Am exposure in 40.0 Torr SF_6 with $\Delta V_{MM} = 1170\,\mathrm{V}$, $V_{micromegas} = 575\,\mathrm{V}$ and a drift field of $312.5\,\mathrm{V\,cm^{-1}}$.

The fact that the angle of the tracks aren't constrained means that only a fraction of the events have coincident signal on both the x- and y-strips (i.e. the track passes over the crossing point of the channels). The artifact in the signal data which was consistent with capacitive signal noted in Chapter 7 is also present in this data, although the magnitude is small enough relative to the peak height to be ignored.

A typical example of a readout-crossing event from the CF_4:SF_6 run is shown in Figure 8.9. The waveforms, shown in in Figure 8.9a, consist of peaks on all the working channels with the peaking time roughly linear with channel number. The peak heights on the x-channels are significantly lower than on the y-channels, an additional static peak at bin 2100 is visible on the x-channels which is attributed to capacitive pickup. A three dimensional reconstruction of the event constructed by multiplication of the x and y-channels is shown in Figure 8.9b demonstrating a nearly straight track consistent with an alpha traveling in the (+x,-y,-z) direction. The low gain channels are used for the alpha runs due to the high gain channels saturating with the large deposited signal.

For events where track features are identified on both sets of strips the gradient of the track in the x-y projection can be obtained from the fitted 2d parameters using $\frac{dy}{dx}$ =`dtdx/dtdy`. The distribution of $\frac{dy}{dx}$ calculated by this method for the two ^{241}Am runs is shown in Figure 8.10. The expectation value of $\frac{dy}{dx}$ for straight tracks originating from the Americium source is $-\tan^{-1}(29°) = -1.8$ and is indicated by a red line on the figures. The values of $\frac{dy}{dx}$ in each run show a distribution which is centred around the expectation value indicating the tracking is consistent with an alpha source in approximately the expected location. As the alpha tracks are not perfectly straight and the angle is only constrained by the requirement it cross both sets of strips, the fairly wide angular distribution observed is consistent with what might be expected.

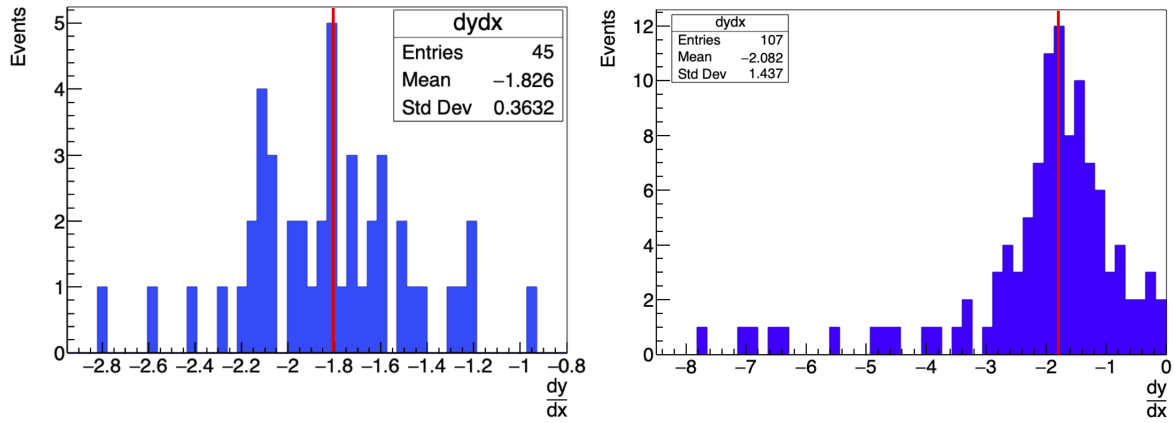

(a) Run 20200228T164235 (39:1.8 Torr CF_4:SF_6).

(b) Run 20200302T181705 (40 Torr SF_6).

Figure 8.10: The $\frac{dy}{dx}$ of cut passing tracks from ^{241}Am source runs on the micromegas with the expectation value (-1.804) indicated with a red line.

Some of the ^{241}Am events capture an alpha track stopping above the instrumented strips, Figure 8.11 shows one such event in the 40 Torr SF_6 run. The presence of a

track-like signal on the x-strips, which the alpha crosses prior to stopping, confirms that the y-strip signal in this event is from the end of an alpha track originating from the Americium source. The end of the track shows a large amount of clustering in the charge deposition by the alpha, the signal is dominated by charge dissipation in the resistive layer. Events with similar shape to this are observed in subsequent non-^{241}Am runs and knowing the topology of those events is consistent with an alpha track end is helpful for classification of those events.

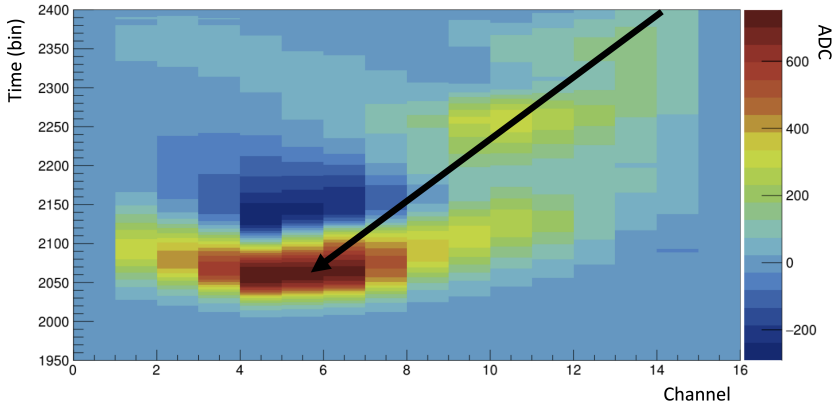

Figure 8.11: Signal on low gain y-channels for Event 17 in run 20200302T181705 (40 Torr SF_6), capturing an alpha track stopping. The rough path of the alpha is indicated by the arrow.

Overall, the micromegas-MMThGEM and NI-TPC readout combination shows good tracking of alpha particles with the ability to reconstruct 3-dimensional tracks from the x and y strip signal. The determined direction of the tracks in the x-y plane is consistent with the measured location of the alpha source. It was also observed that the end of alpha tracks exhibit a large degree of clustering and that charge dissipation in the resistive layer plays a significant role in the signal at the end of the track.

8.5 Micromegas-MMThGEM - determination of gas gain with ^{55}Fe

X-rays from an ^{55}Fe source can be used to generate consistent 5.9 keV electron recoils for the determination of the detector gas gain at a given pressure and voltage. Exploring the detector response and gas gain in this energy range is important for dark matter and neutron assay applications. Exposure of the detector to the x-rays is performed by taping an ^{55}Fe button source to the central pane of the kapton window on the door of the vessel.

Processed waveforms and 2d plots for an example ^{55}Fe event in 39:1.8 Torr CF_4:SF_6 are shown in Figure 8.12. The signal is processed with the Fourier notch cut described in Section 8.3.1, an SG-smooth with order 3 and length 20, and dead channel interpolation with interpolated channels shown in orange in the figure. In this event there is a significant amount of structure visible, with multiple charge clusters visible which are coincident in time across the x and y strips. The charge dissipation remains prominent in both of the x- and y-channels and is most visible in the main peak. The waveforms imply two main clusters with a separation of about one millimeter in both the y and z directions. This is consistent with the simulation of electron recoils with DEGRAD performed in Chapter 4.

In many of the ^{55}Fe events any structure is washed out by the charge dissipation leaving only a single identifiable peak.

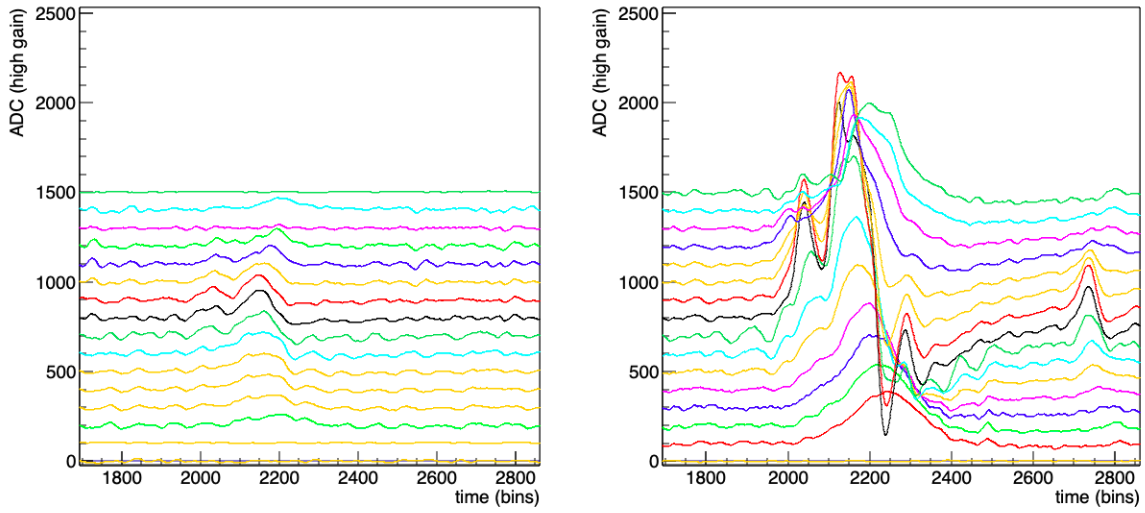

(a) Smoothed waveforms from x channels (left) and y channels (right), offset for clarity with interpolated channels in orange.

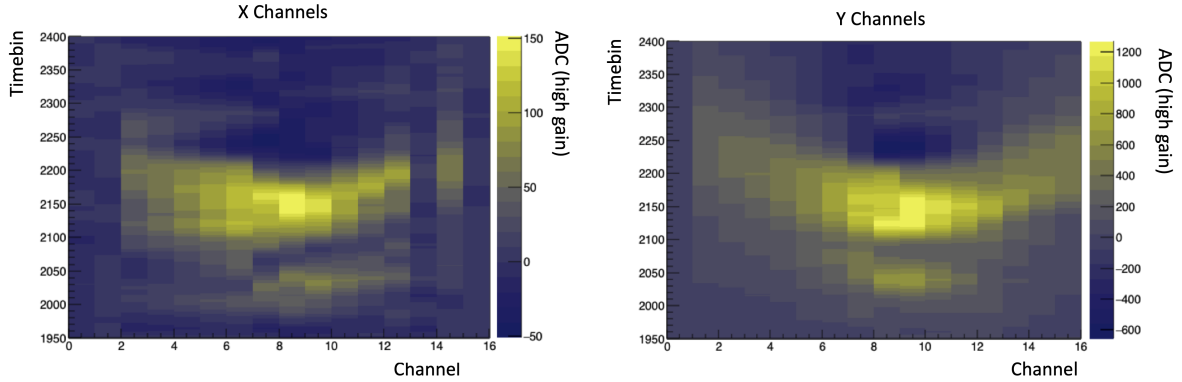

(b) Two dimensional x-t (left) and y-t (right) plots of signal on strips.

Figure 8.12: Event 1968 in run 20200229T172918: ^{55}Fe exposure of micromegas in 39:1.8 Torr CF_4:SF_6 with $\Delta V_{MM} = 1045\,\mathrm{V}$, $V_{micromegas} = 515\,\mathrm{V}$ and a drift field of $360\,\mathrm{V\,cm^{-1}}$.

As was seen in Chapter 7 the signal on the x strips is considerably less than observed on the y strips. As the strips only instrument a fraction of the area of the micromegas and the digitiser is triggered on signal from the micromegas mesh, only a small fraction of the events have signal on both the x and y strips as in Figure 8.12. Fiducialisation cuts are used to constrain the peaks in the dataset to well centred ones. The parameters `ymaxchn` and `edgeypeak` are found to be useful for fiducialisation.

The `ymaxchn` parameter identifies the channel which has the highest ADC value and can be used to constrain events to near the centre of the instrumented strips. Vetoing events where `ymaxchn` is one of the edge strips will remove those events where the observed signal is the tail of the charge dissipation from an interaction outside the instrumented area which pass cuts based simply on the threshold.

The `edgeypeak` parameter counts the bins on the edge channels which are above the

integration threshold for `yq_peak` and can be considered an estimate of the signal lost off the edge of the instrumented region. The integral of the signal peak over the strips, `yq_peak`, is used as a measurement of the effective gain on the strips and therefore removing events where significant signal is lost due to the finite readout is vital. Figure 8.13a shows a scatter plot of `edgeypeak` against `yq_peak` for run 20200229T172918. There are two populations visible in the scatter plot, events in the group which trends toward high `edgeypeak` are identified as ones which have significant signal lost off the edge of the readout. The population of events distributed in the region `edgeypeak<500` are significantly better contained on the readout with only a fairly small fraction of charge lost off the edge.

Figure 8.13b shows how basic fiducialisation cuts differentiates a 5.9 keV peak from the distribution of the `yq_peak` parameter. With no fiducialisation there is a drop off in rate with increasing energy and no peak can be differentiated from the low energy noise events. When a cut on `ymaxchn` which vetoes events peaking on an edge strip is implemented a peak in the high energy tail can be resolved at about 500 ADC · timebin · chn. The addition of the cut `edgeypeak<400` removes an even larger proportion of the lower energy events leaving the 5.9 keV peak well separated from the lower energy noise.

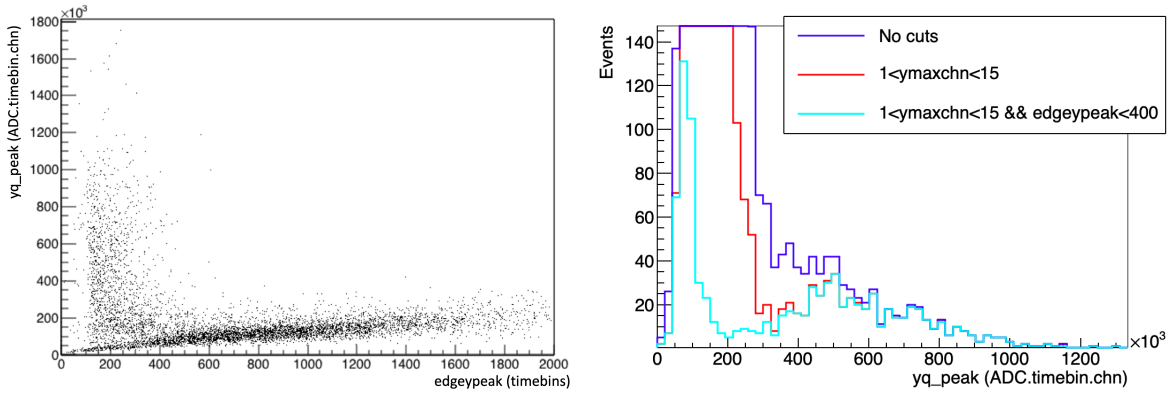

(a) Scatter plot of `yq_peak` against `edgeypeak`.

(b) Effect of fiducialisation cuts on the distribution of the `yq_peak` parameter.

Figure 8.13: Plots for Run 20200229T172918: ^{55}Fe exposure of micromegas in 39:1.8 Torr CF_4:SF_6 with $\Delta V_{MM} = 1045$ V, $V_{micromegas} = 515$ V and a drift field of 360 V cm^{-1}. High gain strips.

The micromegas and MM-ThGEM voltage are varied separately in the 39:1.8 Torr CF_4:SF_6 mixture with a constant drift field of 360 V cm^{-1} and detector exposure to the ^{55}Fe source. The fiducialisation cut `2<ymaxchn<14 && edgeypeak<yq_peak*0.001` is applied to the data and a Gaussian is fitted to the resulting distribution of `yq_peak`. The average of the gaussian fit is used to determine the effective gain of the device which is used for the energy calibration of later runs.

A calibration of the high gain channels determined the gain to be 370 ADC · timebin/fC. This translates to an expected integral charge of 10.27 ADC.bin for the collection of the unamplified ionised electrons from a 5.9 keV x-ray. The effective gain is then determined by dividing the `yq_peak` parameter by this expected signal.

The variation with ΔV_{MM} and $V_{micromegas}$ of the effective gain on the high gain strips determined in this way is shown in Figure 8.14. Both ΔV_{MM} and $V_{micromegas}$ show an apparently exponential relationship with gain as would be expected. When $V_{micromegas}$

is varied the MM-ThGEM voltage is held at a constant 1045 V, the upper limit of the micromegas voltage is set by the point at which events start to saturate the ADC of the high gain channels. When ΔV_{MM} is varied the micromegas voltage is held constant at 515 V, the MM-ThGEM voltage is limited by the runaway feedback effect similar to that described in Chapter 6 for the MM-ThGEM on its own. Gain curves in Figure 8.14 is consistent with the gain determined for the micromegas-MMThGEM device with the Cremat readout in Chapter 7 where the gain on the y strips in 38.7 : 1.3 Torr CF_4:SF_6 with $V_{micromegas} = 506$ V with $\Delta V_{MM} = 1034$ V was determined to be 52600 ± 1500.

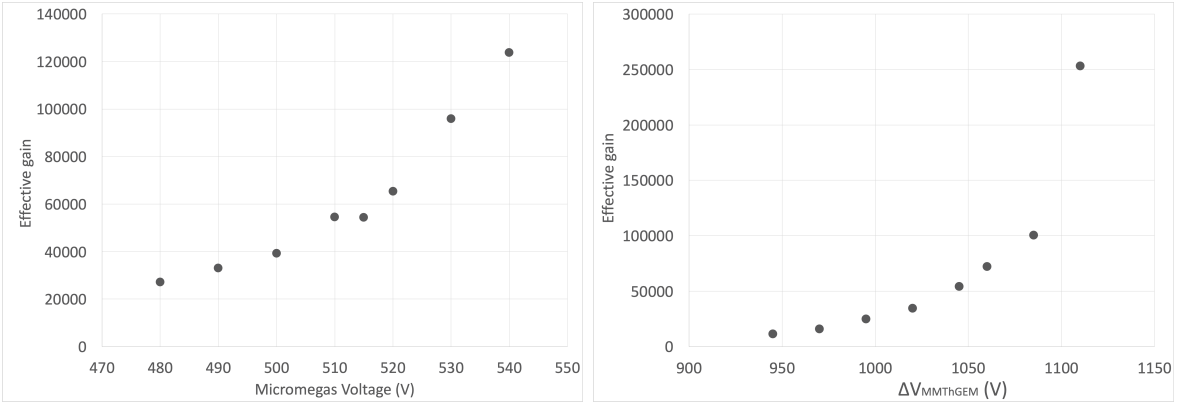

(a) Variation of effective gain on strips with micromegas voltage, constant $\Delta V_{MMThGEM} = 1045$ V and drift field of 360 V cm^{-1}.

(b) Variation of effective gain on strips with MMThGEM voltage, constant $V_{micromegas} = 515$ V and drift field of 360 V cm^{-1}.

Figure 8.14: Gains determined by peak integration on high gain strips for ^{55}Fe runs in 39:1.8 Torr CF_4:SF_6.

The maximum determined effective gain is 2.5×10^5 and is reached at $V_{micromegas} = 515$ V and $\Delta V_{MM} = 1110$ V. The gain might be increased further than this by increasing the micromegas voltage but the gain obtained at the midpoint is sufficient for obtaining signal.

For events where only a small amount charge is deposited, the electronic noise dominates the integrated signal. The threshold at which the signal can be separated from the noise is an important characteristic of the detector at a given operating point. The electronic noise and therefore threshold varies slightly depending on the setup, during the ^{5}5Fe calibration runs starting 20200229T, the electronic noise was approximately ±5ADC.

The operating point that was selected for further runs in CF_4:SF_6 was $\Delta V_{MM} = 1045$ V and $V_{micromegas} = 515$ V. The low energy threshold at this operating point is estimated to be about 0.7 keV on the y-strips and 4.6 keV on the x strips. In pure SF_6 the selected operating point was $\Delta V_{MM} = 1170$ V and $V_{micromegas} = 575$ V. The low energy threshold in SF_6 at this operating point is estimated to be about 1.5 keV on the y-strips and 8.2 keV on the x strips.

In addition to these gain measurements, an ^{55}Fe gain measurement was made before and after each set of neutron runs, the time elapsed between the gain measurements in these cases was around 24 hours of continuous detector operation. The determined difference in the gain over 24 hours is on the order of 3% which is around the expected statistical error in the gain measurement.

In summary, the runs with ^{55}Fe demonstrated that the readout could resolve structure on the scale of millimeters from low energy electron recoils in the instrumented gas volume.

Fiducialisation cuts were determined to be vital to obtain a resolvable 5.9 keV peak and it was established that gas gains in the range of 1×10^5 to 2.5×10^5 could be obtained with the micromegas-MMThGEM combination with the NI-DAQ readout. Operating points for the detector were established with a low energy threshold of 0.7 keV in CF_4:SF_6 and 1.5 keV in SF_6. The gains obtained were consistent with those determined in Sheffield with Cremat instrumentation and were seen to be stable over a significant time period. This demonstration of low energy operation and determination of the detector gain is vital for proceeding to the neutron exposure described in the following section.

8.6 Micromegas-MMThGEM - observation of nuclear recoils with ^{252}Cf

To explore the detector response to neutron induced nuclear recoils, the detector is exposed to a ^{252}Cf source. The spontaneous fission of ^{252}Cf can produce neutrons in the energy range 0 MeV to 13 MeV with an average of about 2.7 MeV. The neutron energy spectrum from ^{252}Cf neutrons source was discussed in Section 3.7 and in Chapter 4. In addition a significant flux of gamma-rays is the produced by the fission of ^{252}Cf as well as by neutron interactions in the environment so a significant number of electron recoils will be present in the ^{252}Cf data.

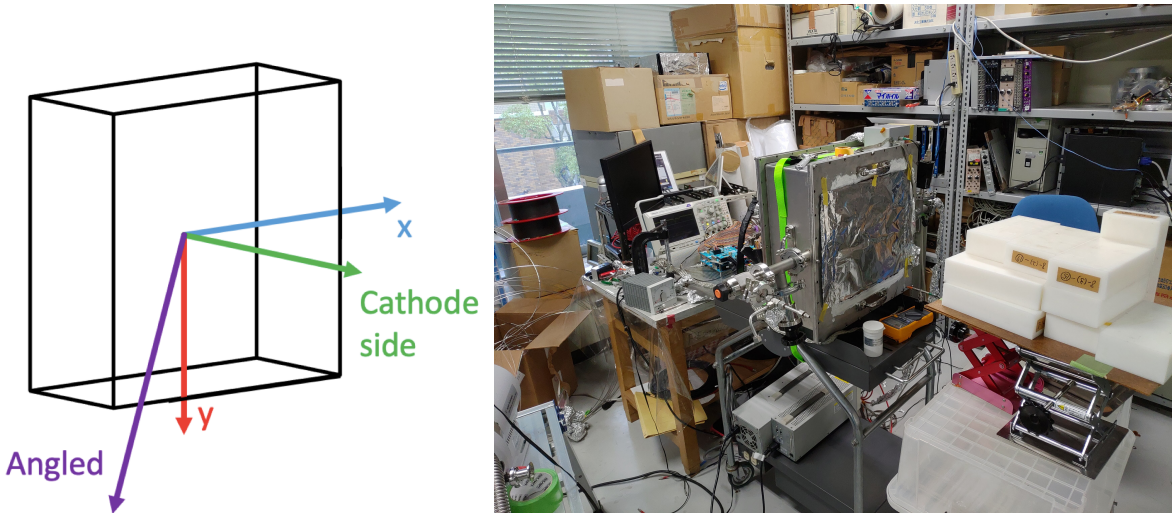

(a) Wireframe with source directions. (b) Picture of cathode-side source setup.

Figure 8.15: Kobe vessel set up during the ^{252}Cf runs.

The source is positioned in four locations relative to the vessel, we refer to the locations as the *x*, *y*, *cathode-side* and *angled* positions. The direction of the source relative to the centre of the drift region in each position is shown in Figure 8.15a. A picture of the vessel and source in the *cathode-side* set-up is shown in Figure 8.15b. In each case a small cave is constructed out of High Density Polyethylene (HDPE) blocks around the source to reduce the neutron exposure of the rest of the lab. The *x*, *y* and *cathode-side* locations the ^{252}Cf source was located at 55 cm from the centre of the drift region. In the *angled* position the source was located at (-57,93,44) centimeters in the (x,y,cathode) directions relative to the centre of the drift region.

8.6.1 ER discrimination with ^{60}Co

As discussed previously, ER discrimination is an important metric in itself and it is furthermore required to eliminate the large electron background present in the data due to gamma rays generated by the ^{252}Cf source and neutron interactions in the air and vessel. A ^{60}Co button source is used as a gamma emitter to generate electron recoils for comparison with the ^{252}Cf runs which contain both electron and nuclear recoils. During the decay of ^{60}Co to a stable isomer of ^{60}Ni gamma rays of energy 1.17 and 1.33 MeV are emitted. In the ^{60}Co runs the ^{252}Cf source is removed from the lab and the Cobalt source is positioned on the outside of the kapton window of the vessel.

As in the ^{55}Fe runs and in the simulations performed in Chapter 4, a defining feature of electron recoils is the presence of multiple charge clusters of thermalised electrons. The best linear discriminant was found to be the parameter `yq_peak` which is a measurement of the charge contained in the main peak of the event, due to electron recoils depositing far less energy per cluster.

Using an ^{55}Fe calibration performed before the neutron runs, and assuming the parameter `yq_peak` is linear with energy, the discrimination based on `yq_peak` (and noise cuts) is sufficient to veto all events in the cobalt run down to 35 keVee. This separation is visible in Figure 8.16a where the highest value of `yq_peak` for the ^{60}Co runs is 31×10^3 ADC · timebin · chn while during exposure to ^{252}Cf the energy extends well beyond this. Note that the finite width of the readout may contribute to a significant fraction of the electron recoil charge not being captured and likely contributes to the efficacy of this parameter as a discriminant.

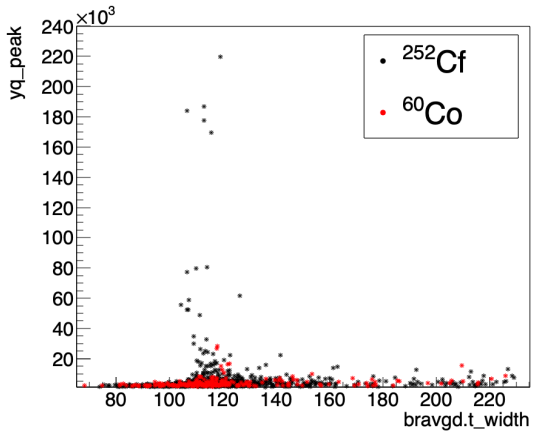

(a) Plot for runs 20200301T1319-20200302T1558: 40 Torr SF_6 with $\Delta V_{MM} = 1170$ V, $V_{micromegas} = 575$ V and a drift field of 312 V cm^{-1}.

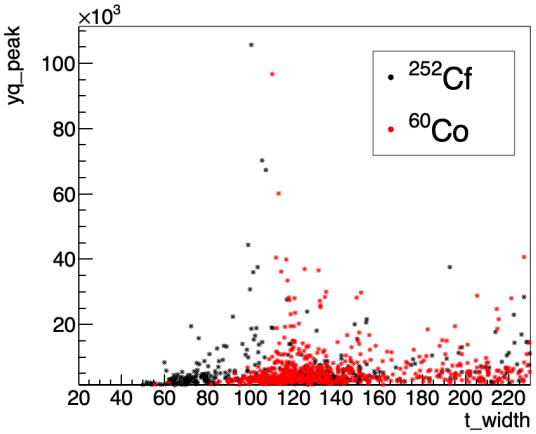

(b) Plot for runs 20200229T1037-20200229T1650: 39:1.8 Torr CF4:SF6 with $\Delta V_{MM} = 1045$ V, $V_{micromegas} = 515$ V and a drift field of 360 V cm^{-1}.

Figure 8.16: Scatter plot of `yq_peak` against `t_width` calculated from the summed y channels for combined ^{252}Cf and ^{60}Co runs.

For discrimination below 35 keVee additional parameters have to be included in the analysis. The `t_width` parameter determined for the summed y-strip waveforms was determined to show some separation for ^{252}Cf and ^{60}Co events below this energy. The `t_width` parameter is a count of the number of contiguous time bins that the ADC is over the threshold value, which in these runs is 1/4 of the maximum ADC value. Scatter plots

of the y_qpeak parameter against the t_width in pure SF_6 and CF_4:SF_6 for ^{252}Cf and ^{60}Co exposure is shown in Figure 8.16. In this case the cut ymaxchn>6 && ymaxchn<10 is added to constrain the signal to well centred waveforms which is important as the peak width for the summed waveforms is sensitive to charge loss from the readout edge.

For the plot generated from the pure SF_6 runs in Figure 8.16a, the bulk of the population of both ^{252}Cf and ^{60}Co events has y_qpeak$< 10^4$ and extends across a fairly wide range in the t_width parameter. Events with y_qpeak$> 10^4$ are mostly confined into a small region of the t_width parameter space between 100 and 130 bins. In the ^{60}Co runs the high y_qpeak events are confined to the the region 117<t_width<123 whereas the population of ^{252}Cf events extends down to t_width=105. The lower time width of the ^{252}Cf events as compared to events from the ^{60}Co data is consistent with the more compact neutron recoils as compared to electron recoils.

A simple linear cut of t_width<117 is enough to veto all of the electron recoil events down to y_qpeak$= 9 \times 10^4$ADC.bin, which is equivalent to an energy of about 10 keVee. The rejection factor that can be determined for this cut is 1×10^3 as only a small fraction of the ^{60}Co recoils are centred sufficiently to pass the fiducialisation cuts.

Attempts were made to include the ystripsfwhm parameter in the analysis which is a measurement of the event width in a different dimension but no significant correlations were found, this might be attributed to a combination of the coarseness of the readout pitch, the dead channels and to the charge dissipation, which effectively imposes a minimum width to a given peak.

Performing a similar analysis on the runs performed in CF_4:SF_6 produces the scatter plot shown in Figure 8.16b. As in the case with the pure SF_6 data, only fiducialisation, threshold and basic noise cuts are implemented. In this case the trend of the ^{252}Cf events tending to lower t_width is the same but the separation extends to significantly lower energy, the highest energy ^{60}Co event in the region t_width<80 is only about 2 keV. The fairly low statistics of electron recoils in this region (only two events) makes it hard to make a definitive statement about the lowest energy threshold of this discrimination cut. The reason for the better separation is likely related to the different mobility of the negative ions in CF_4:SF_6; as was shown in the alpha data the CF_4:SF_6 primary charge carriers are significantly faster which will result in a shorter collection time.

The cuts so far described are to veto electron events, however a population of events with a more track-like topology was observed in the ^{252}Cf data along side the more compact events which are anticipated to originate from neutron recoils in the gas. Figure 8.17 shows a scatter plot of the parameters yq_peak and yq_tot for the combined ^{252}Cf and ^{60}Co runs in 40 Torr SF_6 with $\Delta V_{MM} = 1170$ V, $V_{micromegas} = 575$ V and a drift field of 312 V cm^{-1}. The points in the ^{252}Cf data set consist of the combined events from all exposure directions. The population of compact neutron recoil candidates forms a line near the bottom of the graph, and have yq_peak>yq_tot. These events are fairly compact with only one identifiable peak, an example of the events in this population is shown in Figure 8.18a. There is very little structure visible in the events in the identified neutron population with the events dominated by charge dissipation.

Events which have a large amount of deposited energy but have yq_peak<yq_tot have multiple large peaks in the analysis window. These events appear to be consistent with long tracks from alpha particles or other light nuclei, frequently having similar signal topology to the stopping alpha track observed in Figure 8.11. An example event from this population is shown in Figure 8.18b. Events in this population deposit energies from 0.5 MeVee to 3.5 MeVee above the y-strips estimated from the yq_tot parameter, although

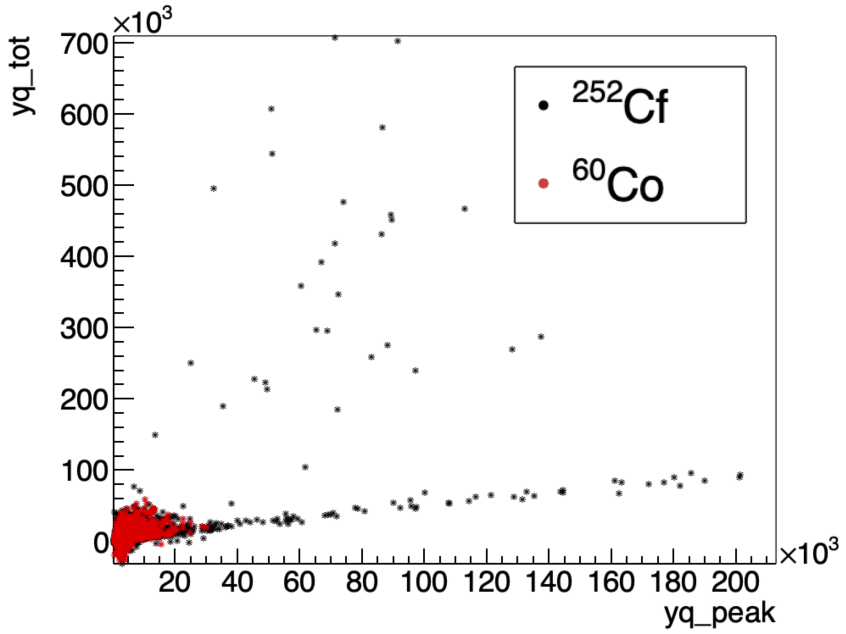

Figure 8.17: Scatter plot of the `yq_tot` and `yq_peak` parameters after noise cuts for the ^{252}Cf and ^{60}Co runs in 40 Torr SF_6 with $\Delta V_{MM} = 1170\,\text{V}$, $V_{micromegas} = 575\,\text{V}$ and a drift field of $312\,\text{V cm}^{-1}$.

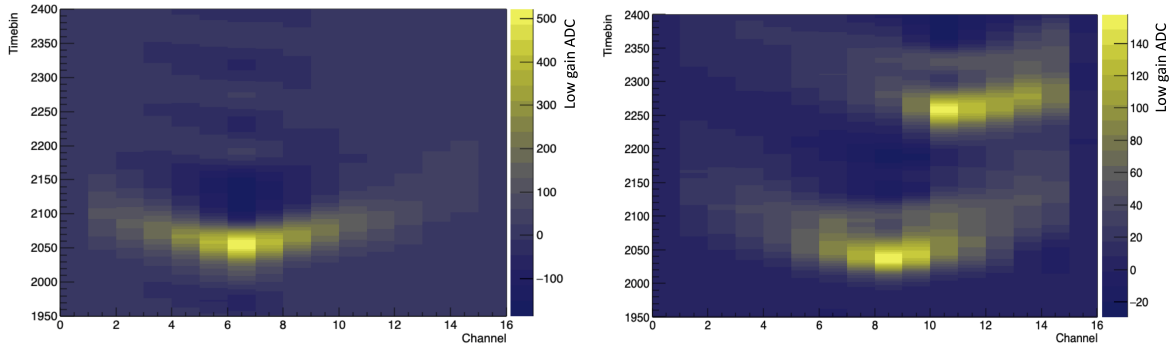

(a) High energy event with `yq_tot`<`yq_peak`. (b) High energy event with `yq_tot`>`yq_peak`.

Figure 8.18: High energy candidate nuclear recoil events for run 20200301T143151 (^{252}Cf in 40 Torr SF_6 with $\Delta V_{MM} = 1170\,\text{V}$, $V_{micromegas} = 575\,\text{V}$ and a drift field of $312\,\text{V cm}^{-1}$).

they are likely more energetic still. The source of these tracks may be neutron induced nuclear recoils from detector materials as was observed in the simulations performed in Chapter 4.

In summary, it was shown that the response of the micromegas-MMThGEM combination to electron and nuclear recoils is significantly different enough for discrimination between the populations. The best discriminants out of the parameters extracted were found to be `yq_peak` and `t_width`, with nuclear recoil events tending to have higher `yq_peak` and lower `t_width` as compared to electron recoil events. The observed difference between the ^{252}Cf electron+nuclear recoil data and the ^{60}Co electron recoil data is consistent with the expectation that nuclear recoils are shorter and produce denser clouds of ionisation as compared to electron recoils. Total rejection of electron recoil events from the ^{60}Co runs was possible down to 10 keVee in SF_6 and down to 2 keVee in CF_4:SF_6

although larger electron recoil statistics would be desirable to better quantify the electron rejection factor. Additionally a population of track-like events within the ^{252}Cf dataset were identified which are thought to correspond to light nuclear recoils. Having identified the population of likely nuclear recoil candidates within the data, the next step is attempting to obtain a directional signal from those recoils.

8.6.2 Directional signals in ^{242}Cf data

As discussed in Chapter 2, one of the main reasons for operating a detector with low pressure gas is that recoils are extended in space enabling the initial direction of the recoil to be determined. Exploring the directional signals associated with nuclear recoils in the gas is one of the main motivations for this work.

High energy events which are extended in space do show a level of directionality, Figure 8.19 shows two events which appear to have directional features. The green arrows in the sub-figures indicate the source direction, assuming literature ion mobility. The event in Figure 8.19a shows a track like event terminating at approximately channel 5 originating from the top right of the figure, consistent with a track from the source direction. Charge dissipation makes up a significant amount of the signal with the characteristic 'v' shape dissipation visible originating at the end and midpoint of the track. The estimated total energy deposit detected on the y-strips for this event is 580(50) keV, although there is expected to be a considerable amount of unobserved signal above uninstrumented strips.

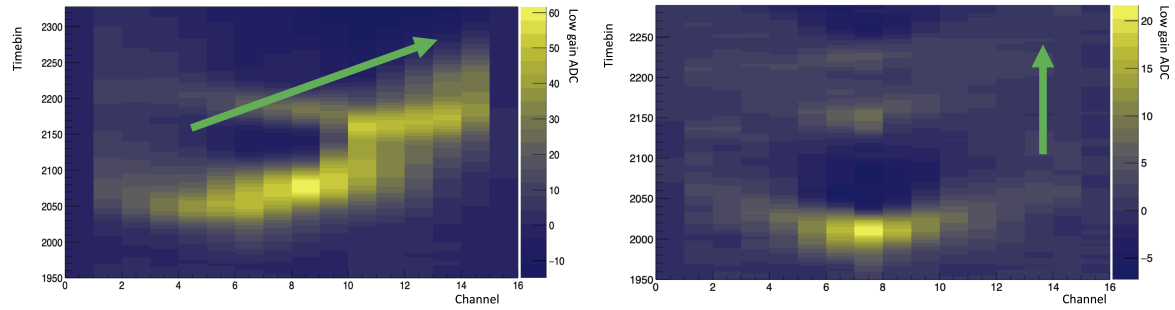

(a) Event from Run 20200301T143151, source in angled position, source direction indicated by green arrow.

(b) Event from Run 20200302T114059, source in cathode-side position, source direction indicated by green arrow.

Figure 8.19: High energy candidate nuclear recoil events in ^{252}Cf runs in 40 Torr SF_6 with $\Delta V_{MM} = 1170\,\mathrm{V}$, $V_{micromegas} = 575\,\mathrm{V}$ and a drift field of $312\,\mathrm{V\,cm^{-1}}$.

The event in Figure 8.19b shows a more point like event which exhibits the characteristic charge dissipation. Approximately 150 timebins after the first peak there is a smaller magnitude peak and another at about 70 timebins after that. This is consistent with charge clusters of separation 2.1 mm and 1.0 mm which might be caused by a track originating from the cathode direction. This event demonstrates one of the issues with the time scale of the charge dissipation, following the main peak there is significant baseline undershoot which is a consequence of the net motion of charge during the dissipation being away from the collection point. This undershoot obscures or depresses the signal from any charge arriving immediately after the primary cluster.

The fairly low statistics of sufficiently well centred track-like events and the difficulty in analysing the event shape present under the charge dissipation in a systematic way makes it hard to draw any definitive conclusions about the pointing ability of the detector.

For events which are compact there are some parameters which have significant differences in runs with different exposure directions. For example Figure 8.20 shows the distribution of the `yv_max` parameter for different exposure directions in the SF_6 and CF_4:SF_6 runs after fiducialisation and noise cuts. In both cases the runs are consecutive with change in the field strengths or gas and the trigger threshold and applied fiducialisation and noise cuts are identical for each exposure direction. Note that no ER discrimination cuts are applied in this case due to the very low statistics of discrimination cut passing events so the results might be significantly biased by the electron background. In both cases the `yv_max` parameter is lower for the y-side exposure, although the difference is significantly smaller in the CF_4:SF_6 runs. This might be attributed to the recoils traveling across the y-strips in the y-side exposure case resulting the amount of charge a recoil deposits on a single strip being lower.

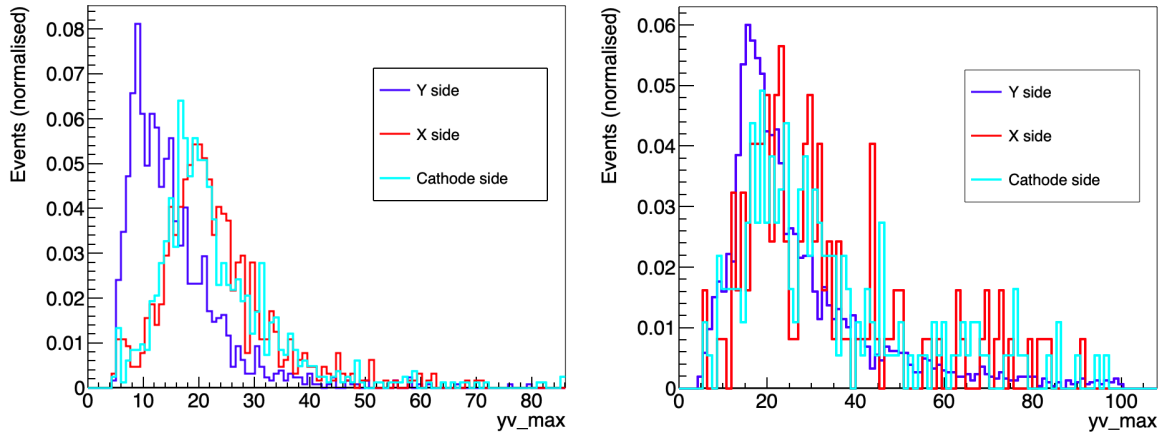

(a) Plot for runs 20200228T1833 to 20200229T1140: 39:1.8 Torr CF4:SF6 with $\Delta V_{MM} = 1045\,\mathrm{V}$, $V_{micromegas} = 515\,\mathrm{V}$ and a drift field of $360\,\mathrm{V\,cm^{-1}}$.

(b) Plot for runs 20200302T1140 to 20200302T1558: 40 Torr SF_6 with $\Delta V_{MM} = 1170\,\mathrm{V}$, $V_{micromegas} = 575\,\mathrm{V}$ and a drift field of $312\,\mathrm{V\,cm^{-1}}$.

Figure 8.20: Distribution of the `yv_max` parameter for different neutron exposure directions.

There were no other significant correlations with exposure direction obtained from other parameters which were consistent across multiple runs or with convincingly high statistics. The `t_width` and `ystripsfwhm` were expected to show some differences for different exposure directions but this was not observed. It is thought that the charge dissipation and the various dead channels might both have contributed significantly to reducing the directional performance of these parameters.

8.7 Observed charge dissipation

The charge dissipation in the resistive layer remains a significant part of the observed signal, the Kobe readout has significantly more channels than previously used which enables the dissipation to be measured over a wider area. As discussed previously in Section 7.4, the analytical expression for signal peaking time, t_{peak}, on a strip at offset y from the charge collection point due to charge dissipation in a bulk resistive layer parallel

to a grounded plane is

$$t_{peak}(y) = \frac{\epsilon_0 R}{2b} y^2. \tag{8.2}$$

Where R is the resistivity, ϵ_0 is the permittivity of free space and b is the separation between the resistive layer and the grounded plane. This prefactor reduces $2.9\,\mathrm{s/m^2}$ for the micromegas used in this experiment.

Fitting Equation 8.1 to the peaking time on the working y channels which are above the threshold enables this prefactor to be found. Cuts are applied to remove the noise events discussed in Section 8.3.4 and to constrain the peak to close to the trigger time and centre of the strips. After fitting Equation 8.1 to the peaking times, the cuts `-3<yfitx0-ymaxchn<3 && 10<yfitt0-ypeakt<10` are used to constrain the dataset to events where the peak of the event is close to the turning point of the fitted equation. The quadratic fit prefactor obtained by this method for events in the ^{60}Co and ^{252}Cf runs in CF_4:SF_6 and SF_6 are shown in Figure 8.21.

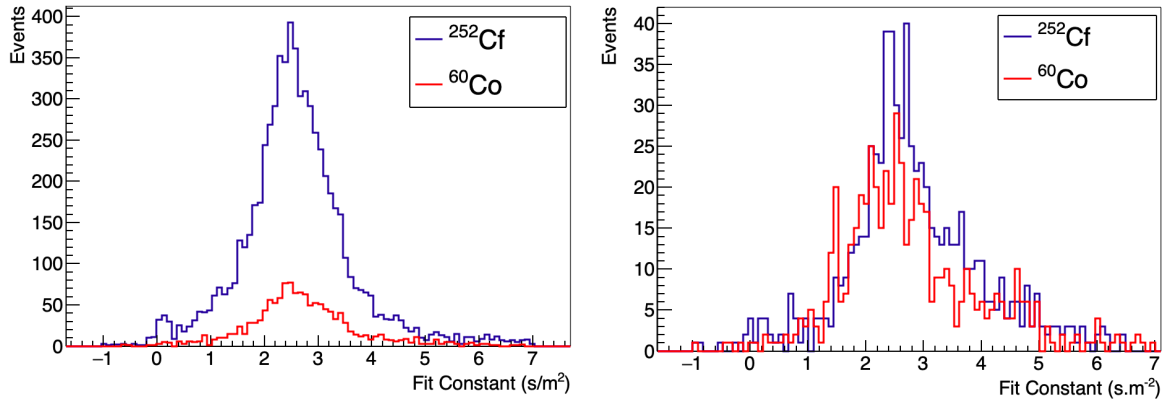

(a) Fit constant for 39:1.8 Torr CF_4:SF_6. (b) Fit constant for 40 Torr SF_6.

Figure 8.21: Fit constant to quadratic charge dissipation in the resistive layer.

The distribution of the prefactor in each case forms an approximate gaussian centred at about $2.5\,\mathrm{s/m^2}$. There aren't significant differences between the ^{60}Co and ^{252}Cf and the CF_4:SF_6 and SF_6 runs apart from the statistics. The average prefactor in this case is much closer to the analytical solution than observed in the Sheffield runs, this might be attributed to a wider readout which enables a more accurate measurement of the diffusion.

8.8 Conclusions

This Chapter described the operation of the micromegas-MMThGEM combination in low pressure SF_6 and CF_4:SF_6 with the NI-DAQ system. Using the NI-DAQ system enabled significantly more channels to be deployed on the micromegas than previously available and the micromegas-MMThGEM provided a testbed for the NI-DAQ system.

The ^{241}Am runs demonstrated x-y-t tracking of alpha particles with more strips than used in Sheffield, with the track angle forming a close to symmetrical distribution around the source direction. The additional readout width also enabled the positive identification of an alpha track stopping above the readout which displayed significant charge clustering and the dissipation characteristic of the micromegas.

The effective gas gain was determined with ^{55}Fe with an approximately exponential relationship with both ΔV_{MM} and $V_{micromegas}$ in SF_6:CF_4 and a maximum value of around 2.5×10^5. The ^{55}Fe calibrations were also performed before and after long neutron runs to confirm the gain remained consistent.

The operation of the detector in Kobe also consisted of the first operation of the micromegas-MMThGEM detector under neutron exposure. The integrated peak signal on the y strips `yq_peak` appeared to be a sufficient parameter on it's own to veto electron recoils down to an estimated 30 keV of deposited energy. Including the time width of the averaged y strip signal enabled the rejection of electron recoils down to approximately 10 keV in SF_6. In CF_4:SF_6, separation between the ^{252}Cf and ^{60}Co runs appeared to extend down to 2 keV although the determined rejection factor was limited by the statistics of the ^{60}Co runs.

Also noted in the ^{252}Cf runs was the presence of high energy, extended events similar to those observed in the alpha runs. These appear to be well discriminated by the ratio between the peak and total integrated charge. Extended track-like events demonstrated a directional tendency although the low statistics of these events and the obfuscation effect of the charge dissipation prevented a systematic analysis of them. For compact events, some statistical differences between exposure from different directions were observed, once again the charge dissipation appeared to be an exacerbating factor.

Some significant suggestions for improvements and issues to look into for the NI-DAQ system were arrived at, most significantly looking into the source of the unphysical noise events observed in Section 8.3.4 and the use of a more reliable connector between the ASIC and FPGA boards. Steps like enclosing the ASIC boards in an electrically shielded box and better insulating the readout cables would also improve the noise observed but neglecting these steps is more an artifact of the fairly fast deployment required than a design decision for the NI-DAQ system. The NI-DAQ otherwise functioned extremely well, running for the duration of the experimental campaign without significant degradation in performance and with sufficient gain for ^{55}Fe to be consistently observed. Runs lasting up to 23 hours and comprising up to 83 GB of data were executed successfully without interruption, demonstrating the stability of both the micromegas-MMThGEM detector and the NI-DAQ system.

Overall the main success of the micromegas-MMThGEM detector was the good gas gain and reliability in SF_6 based negative ion drift gasses. The combination shows significant promise as a scalable technology for directional recoil detection in negative ion gasses. The main factors which might be improved are the energy resolution of the detector combination and mitigating or removing the effect of the charge dissipation, some strategies for this will be discussed in Chapter 9.

Chapter 9

Outlook for Micromegas Data Analysis with Deconvolution

When charge is collected by a bulk resistive micromegas, it dissipates in the resistive layer which results in a systematic distortion of the signal observed on the position sensitive readout elements. Charge dissipation in the resistive layer of the micromegas was observed in Chapter 7 and 8 and was found to be characteristic of events on that micromegas. The charge dissipation is thought to degrade the micromegas discrimination and directionality results as it obscures the underlying structure of events which have a small extent in space. This chapter explores deconvolution as an approach to mitigating the effect of charge dissipation in the resistive layer on the data.

Section 9.1 gives an introduction to charge dissipation in resistive layers and describes an analytic model for the process in the micromegas detector. The basics of deconvolution are described in Section 9.2 with a focus on the Richardson-Lucy deconvolution. Section 9.3 describes the implementation of the Richardson-Lucy deconvolution for the analysis of the micromegas data. A qualitative discussion of the effects of the application of the Richardson-Lucy deconvolution on the micromegas data is presented in Section 9.4. Section 9.5 explores the alternate solution of modifying or removing the resistive layer. Finally, the chapter is concluded in Section 9.6 with a discussion of the recommendations for further development.

9.1 Introduction to charge dissipation

Micromegas detectors consist of a mesh used to delimit the amplification and drift regions and the charge collection occurs on an anode element. Resistive layer micromegas detectors are a version of the micromegas design where the charge is collected by a layer of resistive materials which has the advantage of decoupling the charge collection from the sensitive elements. The resistivity of the layer must be selected such that charge evacuation is slow enough that the charge can be observed by the electronics and fast enough that the resistive layer does not charge-up under irradiation.

The micromegas used in this work has a DLC bulk resistive layer of resistivity $50\,\mathrm{M\Omega/\square}$. The selection of a bulk resistive layer micromegas was partially motivated by the sparking damage observed on ThGEMs in SF_6 in Chapter 3; the resistive layer provides protection for the device and electronics that was anticipated to be necessary due to the ThGEM damage.

Charge collected by a resistive layer dissipates over time and is evacuated through

the layer's connection to an electrode, often at the perimeter of the layer. The charge dissipation is a significant factor in the formation of the signal on the micromegas strips and has a visible effect on the observed signal. A sample micromegas event exhibiting the characteristic charge dissipation in the resistive layer is shown in Figure 9.1.

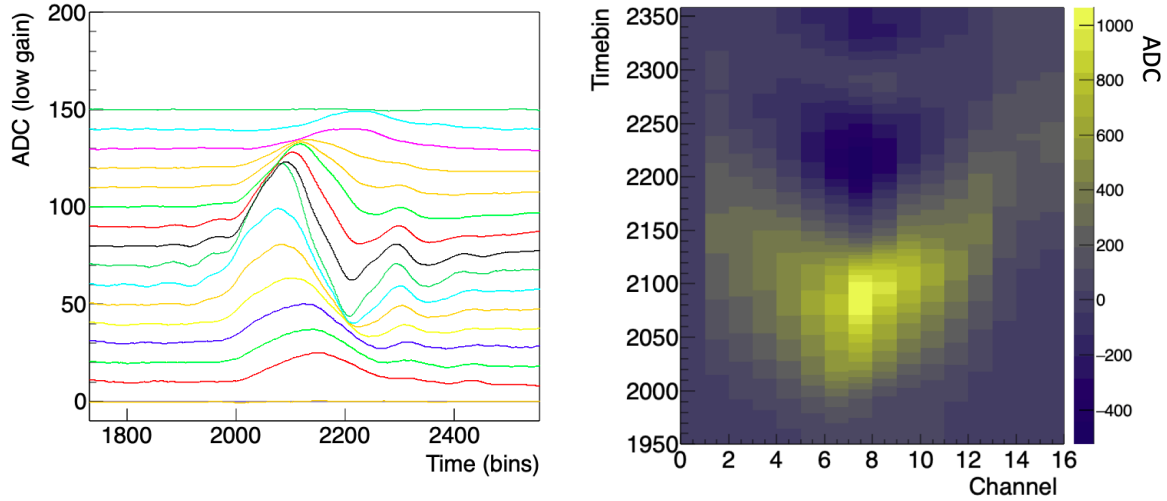

(a) y-strip waveforms, offset for clarity. (b) y-strip 2d plot.

Figure 9.1: Event 391 from run 20200229T172918: ^{55}Fe exposure of micromegas-MMThGEM in 39:1.8 Torr CF_4:SF_6 with $\Delta V_{MM} = 1045\,\mathrm{V}$, $V_{micromegas} = 515\,\mathrm{V}$ and a drift field of $360\,\mathrm{V\,cm^{-1}}$.

In the region of charge dissipation, a resistive layer micromegas can be approximated as an infinite plane of zero thickness and resistivity R parallel to a grounded plane at a distance b. As explored in Section 7.4, the parallel grounded plane is a necessary component as charge induced on other elements of the detector has an effect on the development of the charge density profile on the resistive layer at long times, $t >> T$, with a characteristic time given by the expression $T = 2b\epsilon_0 R$. The process of charge dissipating in a resistive layer in this model is illustrated in Figure 9.2.

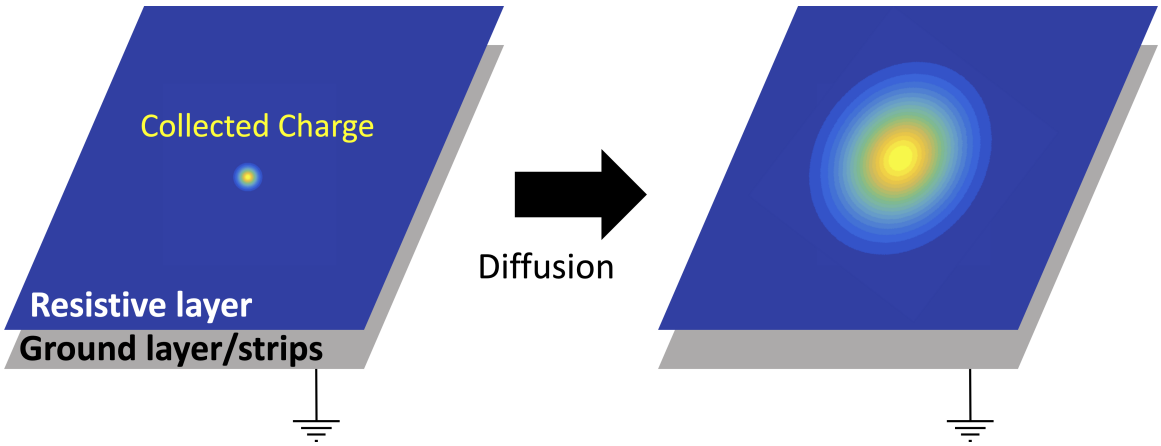

Figure 9.2: Diagram of the diffusion of charge in the resistive layer of a micromegas.

For the micromegas used in this work the resistivity R is $50\,\mathrm{M\Omega/\square}$ and the closest grounded component to the resistive layer is the y-strips, which are approximately 75 µm

from the resistive layer. Taken together the characteristic time constant of the micromegas is expected to be $T = 0.0664\,\mu s$.

Approximating charge collection as the appearance at $t = 0$ of a point charge of magnitude Q and at the origin of the resistive plane, the radial charge density on the plane as the charge dissipates is given by Equation 7.10, which is restated here:

$$q(r,t) = \frac{Q}{b^2\pi}\frac{T}{8t}e^{\frac{-r^2}{8b^2t/T}}. \tag{9.1}$$

The radial profile of the charge density in this analytic model at 1, 2, 5 and 10 µs for a unit charge dissipating with $T = 0.0664\,\mu s$ is shown in Figure 9.3.

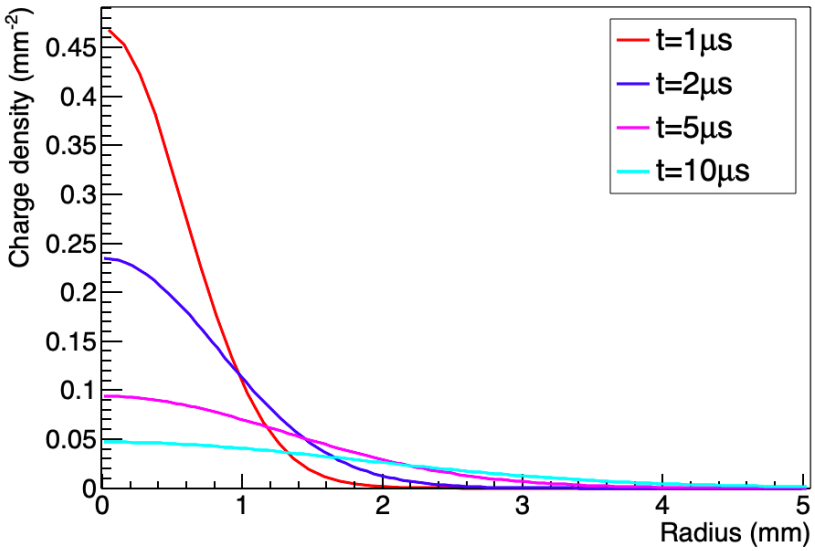

Figure 9.3: The radial profile for a unit charge dissipating on a resistive layer parallel to a grounded plane with $T = 0.0664\,\mu s$.

Consistent with Equation 9.1, the spatial distribution of the charge is gaussian with a variance proportional to the time after the initial point charge arrival.

The charge on the resistive layer induces an equal and opposite charge on the adjacent strips, which is a major component in the formation of signal in the detector. As was derrived in Section 7.4 and illustrated in Figure 7.25, the total charge present on a given strip in the analytic model increases over a duration which is larger for strips further from the collection point. After reaching a maximum the charge then decreases over time with an apparently exponential tail off.

In the limit of a thin strip (when strip width, w, is much smaller than the strip offset from charge colleciton point, y) the time at which the maximum charge is reached can be written

$$\lim_{w<<y} t_{peak}(y) = \frac{T}{4b^2}y^2 \tag{9.2}$$

The prefactor $\frac{T}{4b^2}$ reduces to $\frac{\epsilon_0 R}{2b}$ which has a value of $2.9\,s/m^2$ for the R and b of the micromegas in this work.

As was shown in Chapters 7 and 8, a quadratic of the form of Equation 9.2 well fits the peaking times observed on the strips for compact events on the micromegas. The fit constant for the quadratic was further found to be very close to the prediction from the analytic model; a constant of $1.9(9)\,s/m^2$ was obtained for ^{55}Fe events in SF_6 in Chapter 7 and a constant of $2.5(3)\,s/m^2$ was obtained for ^{252}Cf events in SF_6 in Chapter 8.

9.2 Introduction to deconvolution

Convolution refers to the modification of one function by another, where the value of the produced function is equal to the integral of the product of the two functions where one function is reflected and shifted [161]. Mathematically a convolution is described by the equation

$$f * g = \int_{-\infty}^{\infty} f(\tau)g(t-\tau)d\tau = h(t) \tag{9.3}$$

where f and g are the functions which are convolved and the result of the convolution is $h(t)$, which is a function of t. The parameter t is equal to the 'shift' of the function g relative to f when the integral is taken to obtain the value of $h(t)$. Convolution can be generalised to more dimensions and to discrete valued and finite functions.

In digital signal and image processing convolutions come up fairly often in the form of digital filters, which are used to blur or enhance an image or for smoothing among other tasks. In these applications, the function convolved with the signal is sometimes called a filter, kernel or transfer function depending on the context. Boxcar smoothing is an example of a simple convolution where the function convolved with the signal is a normalised rectangle function. Convolutions also well describe certain systematic distortions which can be present in collected signal.

Deconvolution refers to the process of reversing the effects of a convolution, obtaining one or both of the original functions from the convolved one. If the components of Equation 9.3 are considered in the context of deconvolution in signal processing, function h is the recorded signal and the function g is a distortion convolved with the signal that wants to be recovered which is f. In an image processing context, the function convolved with the signal is referred to as the Point Spread Function (PSF), which describes the detector response to a single 'pixel' of signal.

One significant problem in practical applications for deconvolution is the presence of noise in recorded signal. This has the effect of adding an additional noise term, ϵ, to the deconvolution equation,

$$f * g + \epsilon = h(t). \tag{9.4}$$

Consequently deconvolution algorithms often contain terms for the damping of, or compensation for, additive noise.

The Richardson-Lucy algorithm is an iterative maximum likelihood algorithm for deconvolution frequently used in astronomy [162] [163]. As formulated by Richardson, the iterative form of the algorithm in 1-dimension takes the form

$$F_i^{(r+1)} = F_i^{(r)} \sum_{k=i}^{c} \frac{G_{k-i+1}H_k}{\sum_{j=a}^{b} G_{k-j+1}F_j^{(r)}}. \tag{9.5}$$

Where F is the deconvolved signal array, G is the PSF and H is the originally observed signal. The subscripts refer to the position of the value in the respective array, so G_k is the k^{th} element in array G. The superscript on F refers to the iteration number, for the first iteration $F = H$ and the array F converges on the deconvolved signal with increasing iterations. The limits of the sums are given by the equations $a = (1, k - J + 1)_{max}$, $b = (k, I)_{min}$, and $c = i + J - 1$ where I and J are the dimensions of the arrays F and S respectively. In image processing the 2D form of the Richardson-Lucy algorithm is used alongside techniques to damp noise and boost the convergence rate.

The consistent and predictable nature of the charge dissipation on the resistive strip micromegas means that the resulting signal might be treated as the convolution of the

arriving charge location and a charge dissipation transfer function. Deconvolution could enable the recovery of a signal which more closely resembles arrival of charge at the micromegas plane without dissipation.

9.3 Implementation of the deconvolution

To explore the effect of deconvolution on micromegas data the Richardson-Lucy algorithm is selected as it is robust to noise and requires no prior assumptions about deconvolved signal or noise spectrum. The implementation of the Richardson-Lucy algorithm in the image processing toolbox of the MATLAB programming language is used to apply the deconvolution to the micromegas data.

MATLAB implements the Richardson-Lucy algorithm in the function `deconvlucy` which includes a number of refinements to the basic Richardson-Lucy algorithm [164].In addition to optimised computational performance, the MATLAB implementation allows the pixels of the input array to be assigned relative weights in the deconvolution, this is useful for excluding dead channels from the deconvolution and for removing potential edge effects.

Applying the function `deconvlucy` to the micromegas data requires importing the detector signal to MATLAB in an appropriate format, creating a PSF, and selecting an appropriate number of iterations to perform.

9.3.1 Importing events to MATLAB

Data analysis in previous chapters was undertaken in C++/ROOT and the data format needed only to be compatible with the custom analysis code written specifically for that data. Importing the events into MATLAB required both the conversion of the digital format of the data and shaping of the signal array into a form suitable of the `deconvlucy` function.

Events were drawn from the Micromegas-MMThGEM data taken with the NI-DAQ readout in Kobe, the experimental setup and analysis of the raw data for these runs was described in Chapter 8. Analysis was confined to y-strip events as the signal to noise ratio of events on those strips was considerably lower. The raw signal events in a given dimension consist of an array of 4000 timebins $\times$ 16 channels with each timebin corresponding to a 0.4 µs sample and each channel corresponding to the 0.5 mm instrumented strip pitch. The stored value at each position in the array is the 12 bit ADC value of the channel and timebin.

The intial importation step occurs in C++/ROOT code and consists of pedestal subtraction and the application of an SG-smooth (previously described in Section 8.3) to the raw waveforms. The raw waveforms were then truncated to a window of 300 timebins (120 µs) centred manually on the event signal. Truncating the events like this eliminates a large number of bins containing only electronic noise from the deconvolution. The resulting signal window is stored in MATLAB readable format by the ROOT code. An example signal event displayed in ROOT and in the imported MATLAB format are shown in Figure 9.4. The 90°rotation between the two figures is due to MATLAB having Column-major ordering as opposed to the C based Row-major ordering. It was decided that preserving the array format was more important than consistent plotting so event plots in MATLAB are all presented with this orientation.

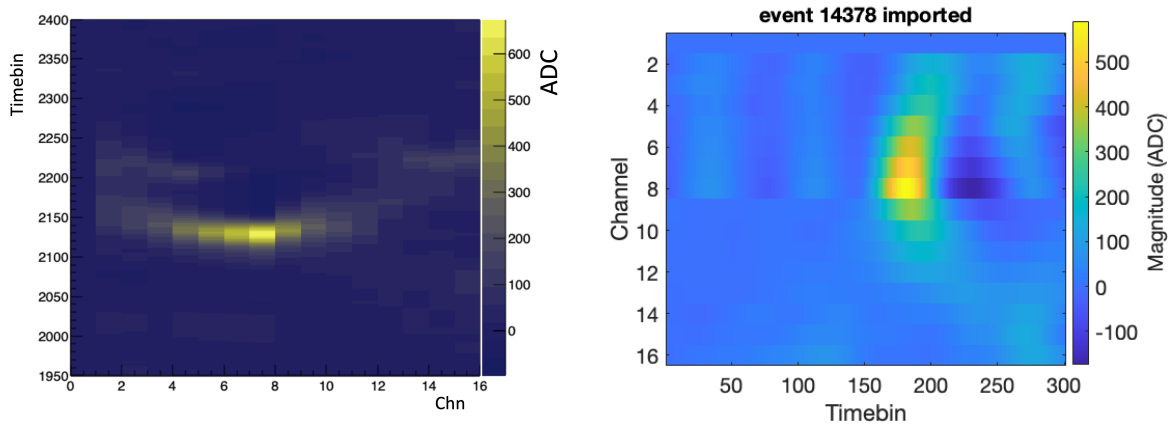

(a) 2d plot in ROOT.

(b) Imported into MATLAB.

Figure 9.4: Event 14378 from run 20200301T131916: ^{60}Co in 40 Torr SF_6 y-strip signal from micromegas-MMThGEM.

Once imported into MATLAB further processing is performed on the array before input to the `deconvlucy` function. One significant issue with the data array at this point is that there are negative values of ADC after pedestal subtraction which cannot be trivially eliminated; baseline undershoot following the main peak is inherent to the charge dissipation in the device (as a result of the net motion of charge being away from the central strips). The Richardson-Lucy algorithm doesn't handle negative numbers so some way of dealing with this is required. Several approaches to compensating for the baseline undershoot were attempted and it was determined that the best results were obtained with a simple offset of the baseline such that all ADC values are positive produced the best reconstruction. The offset in each case is performed such that the lowest ADC value in the event is zero. This offset is likewise applied to the PSF described in the next section.

After this the signal array is padded with 8 additional rows (channels) and 150 additional columns (timebins) on each side filled with zero signal. Padding the array like this is necessary because a significant amount of the event signal diffuses off the edge of the instrumented readout. Limiting the size of the array to the 16 instrumented channels would result in a significant fraction of the PSF of signal bins being located outside the array width and could contribute to artifacts such as ringing.

As a final step, a weight array the same size as the signal array is created, each bin corresponding to a working signal channel is assigned a weight of one, all other bins (corresponding to dead channels and the padding) are assigned a weight of zero. The weight array is one of the inputs of the `deconvlucy` function and the contents define the weight assigned to each bin in the signal array in the deconvolution. A MATLAB display of an example signal and weight array ready for the deconvolution is shown in Figure 9.5.

The padding results in a significant amount of the array being empty, with original bins clearly differentiated due to the offset baseline. The padded bins and the dead channels however do not contribute to the deconvolved signal as a result of the corresponding zero values in the weighting array.

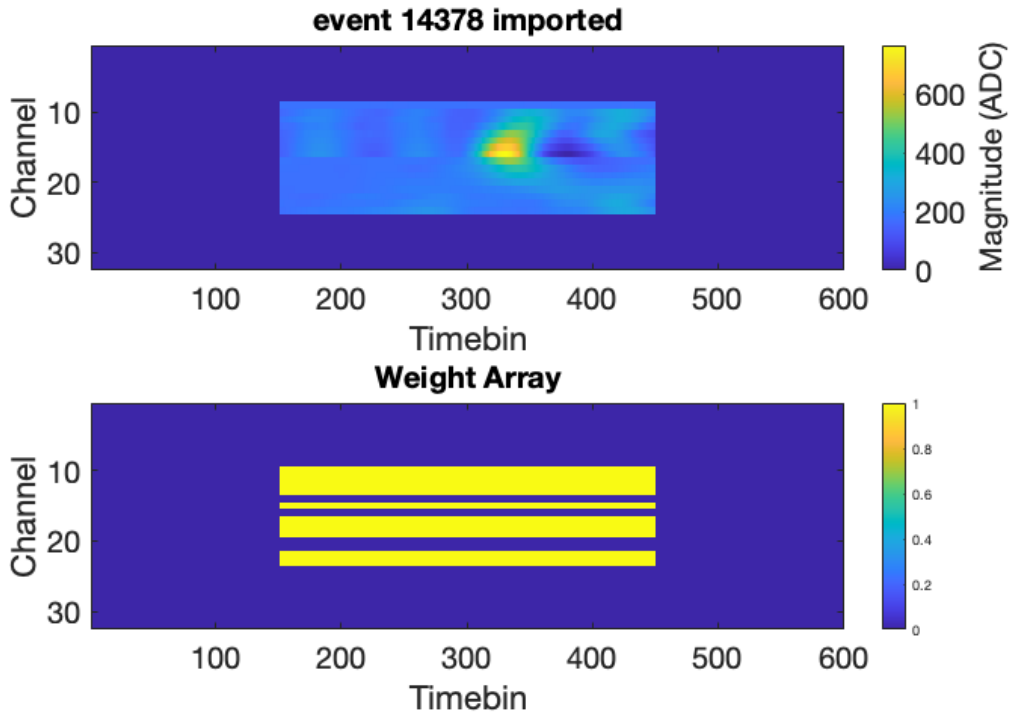

Figure 9.5: Example MATLAB signal (top) and weight (bottom) arrays prior to execution of deconvolution for Event 14378 from run 20200301T131916.

9.3.2 Creating a point spread function

The PSF is the function with which the underlaying data is convolved to produce the observed signal, it is equivalent to the detector response to a single 'pixel' of signal. While we do have an analytic model for the charge dissipation which describes well bulk properties like channel peaking time, it only crudely accounts for the conversion of charge distribution to signal and the resulting approximation of the signal is insufficient to construct a point spread function. Instead the point spread function is constructed from a real event which appears close to the expected effect of charge dissipation from a point source. Event 41003 from run 20200301T143151 is selected as the basis for the point spread function as it is a compact (neutron candidate) event and because of how it is positioned on the readout.

The Kobe data contains a number of signal channels which did not receive signal because of dead electronics or connector issues. The interpolation discussed in Section 8.3 enabled more consistent analysis of events with dead channels but nonetheless likely introduces some distortion to the signal. It was considered important not to rely on the interpolation of dead channels where possible for the construction of the PSF, to recover the dead channels the signal is instead reflected around its centre. Event 41003 is ideal for this as it is effectively symmetric around the line $chn = 3.5$, which enables dead channels 0, 5 and 6 to be recovered by reflection of the channels 7, 2 and 1 respectively. Being orientated to one side of the readout also enables a PSF of width 20 strips to be constructed, important for good deconvolution of poorly centred events.

The steps taken to convert the raw event to into a PSF array are as follows

1. The event is heavily smoothed to remove noise with an SG filter of order 3 and length 50

2. Pedestal subtraction of each waveform is performed

3. A reflection around the centre of the event ($chn = 3.5$) is used to populate the dead channels 5 and 6 rather than interpolation

4. Dead channels 10 and 11 are filled by interpolation

5. The array is resized to 32×600

6. The upper channels are reflected down around former channel 4 to fill former channels 0-3 and the newly added channels from the resize

7. All bins which are not part of the main peak are zeroed

8. A circular rotation of the array to centre the peak is performed

9. The array is normalised to an area of 1

Figure 9.6 shows raw event 41003 from run 20200301T143151 and the PSF generated from it with the above algorithm in MATLAB. The shape present in the final PSF is

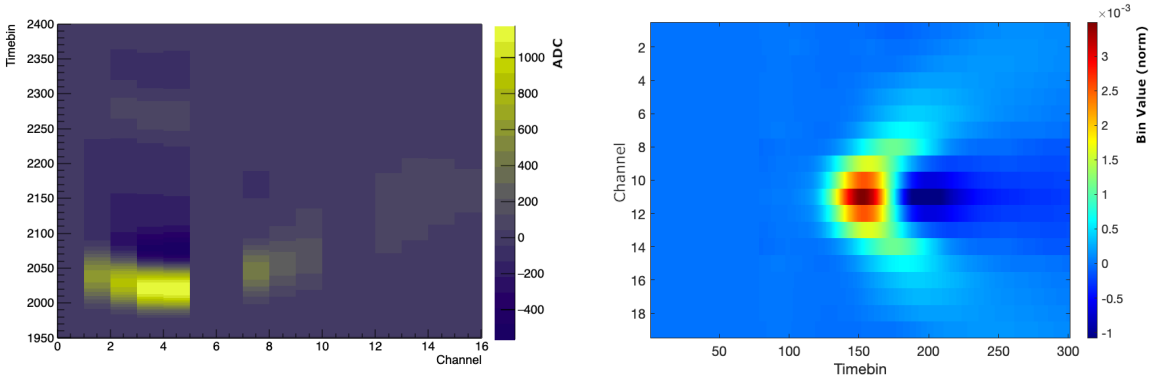

(a) Raw event 41003 from run 20200301T143151.

(b) PSF generated from event 41003 and imported into Matlab.

Figure 9.6: Raw event 41003 and the PSF generated for deconvolution.

entirely dominated by the crescent shaped charge dissipation and is symmetric around it's centre. If this PSF is sufficiently close to the effect of the charge dissipation on the event signal then the Richardson-Lucy deconvolution should be able to recover deconvolved event signal without the charge dissipation.

9.3.3 Selecting the number of iterations

The Richardson-Lucy algorithm is iterative, with increasing iterations converging on a solution to the deconvolution problem. Too few iterations results in an only partial deconvolution while too many iterations wastes processing power and will tend to fit the noise rather than the data. There is no perfect way to determine the number of iterations which produces the 'best' deconvolution due to the diverse nature of deconvolution problems which can be addressed [165]. Consequently visual inspection of the deconvolved image remains the most general and reliable way to arrive at a number of iterations.

Event 14378 from run 20200301T131916 (^{60}Co in 40 Torr SF_6) is used as a test as there are multiple identifiable peaks within a single event and significant noise features. An ideal number of deconvolution iteration would leave the distinct signal peaks visible while eliminating the noise features and the charge dissipation. Figure 9.7 shows the effect of increasing the number of deconvolution iterations on the event signal. The panels show the raw event signal and the signal after 10, 20, 40, 80 and 100 iterations.

The raw event (top left in the figure) has significant sinusoidal noise on the first ASIC board, the main signal peak is centred at (*chn* =16,*timebin* =180) and two smaller ones are centred at (13,260) and (23,260), the charge dissipation is prominent and spans the width of the readout for the main peak. After 10 iterations the sinusoidal noise is invisible

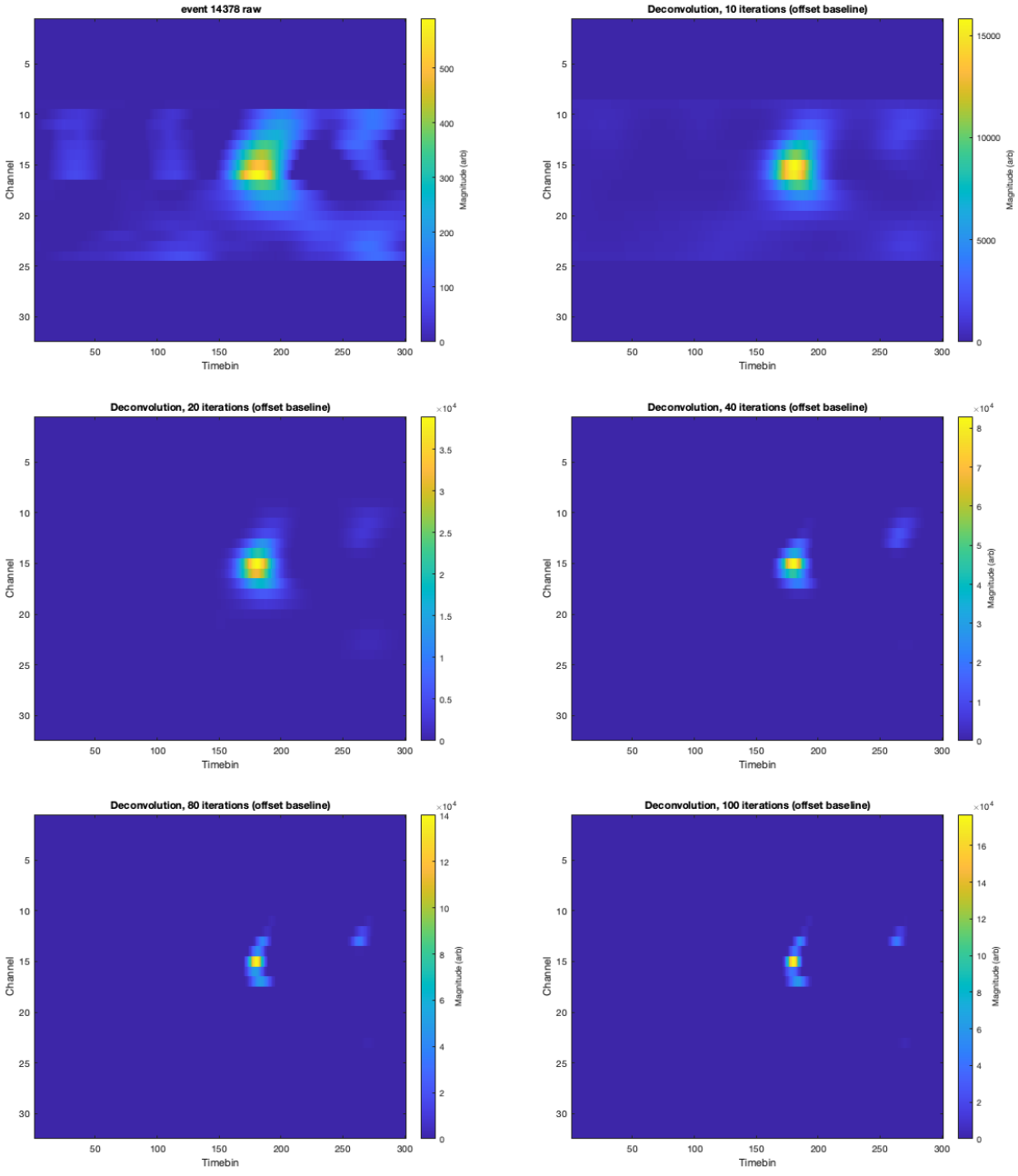

Figure 9.7: Event 14378 from run 20200301T131916, y strips signal (offset). Raw (top left) and after 10, 20, 40, 80 and 100 iterations of the Richardson-Lucy deconvolution.

and the part of the main peak corresponding to the charge dissipation is considerably less wide. After 20 iterations each of the peaks identified in the raw event are fully separated and the peak at (23,260) is almost invisible, the charge dissipation is still visible but only spans about 10 channels. After 40 iterations the peak at (23,260) is completely eliminated, the charge dissipation of the main peak spans only 6 channels. At 80 and 100 iterations the width of the peaks on each channel is on the order of 20 timebins, the distribution of signal across channels still somewhat resembles charge dissipation although the width is only on the order of 5 channels.

Note the integral charge is preserved meaning that the magnitude of the peak is much higher in the deconvolved arrays.

At only a few iterations the charge dissipation still makes up a significant portion of the signal. Applying more than about 50 iterations on the other hand compresses the event down to very few active pixels, applying iterations to the point that the event compresses to this extent is more unstable and gives an impression of more structure than could realistically be resolved.

Around 30-40 iterations appears to well suppress the charge dissipation while preserving the expected gaussian shape of the underlaying recoils. It was decided that 30 iterations was close to the optimal number for the deconvolution of the micromegas data and this number of iterations is adopted going forward.

9.4 Applying deconvolution to micromegas data

To determine the efficacy of the deconvolution, it is applied to a number of different events collected during the micromegas-MMThGEM runs with the NI-DAQ in Kobe. The events were selected from the SF_6 data only and the CF_4:SF_6 data is completely neglected in this analysis. SF_6 events are selected because CF_4:SF_6 is known to have a significantly larger fraction of minority carriers (negative ions which drift at a different rate to the primary charge carrier). The presence of minority carriers results in clusters of charge arriving before or afer the majority of the signal, which might significantly confuse the deconvolution.

The three criteria for the selection of events for deconvolution were that they were well centred, they didn't contain any artifacts and they had a good signal to noise ratio. The centering and artifacts criteria were met using the fiducialisation and noise cuts described in Section 8.3. As the noise was fairly consistent across runs, good signal to noise ratio was enforced by a minimum energy cut equal to the average of the 5.9 keV ^{55}Fe peak.

As was shown in Chapter 4, the 5.9 keV electron recoils produced by ^{55}Fe x-rays are expected to form ionisation tracks from 1 mm to 4 mm long in 40 Torr SF_6. Structure on this scale has been consistently observed in the ^{55}Fe data, although it is considerably obscured by the charge dissipation. Demonstrating that the deconvolution helps resolve electron tracks from the charge dissipation at these low energies would be a positive result for the use of the technique. Figure 9.8 shows the sample deconvolved ^{55}Fe events 76 and 142 from the 40 Torr SF_6 run 20200302T180611.

A large fraction of the signal in the deconvolved events is located coincident with the main signal peak in the raw signal. In addition the deconvolved events show a 'tail' of signal which extends outside the main signal peak. Close inspection of the events shows that the location of the tail is consistent with features visible in the raw signal. The deconvolution however appears to remove the charge dissipation which otherwise partially obscures this structure.

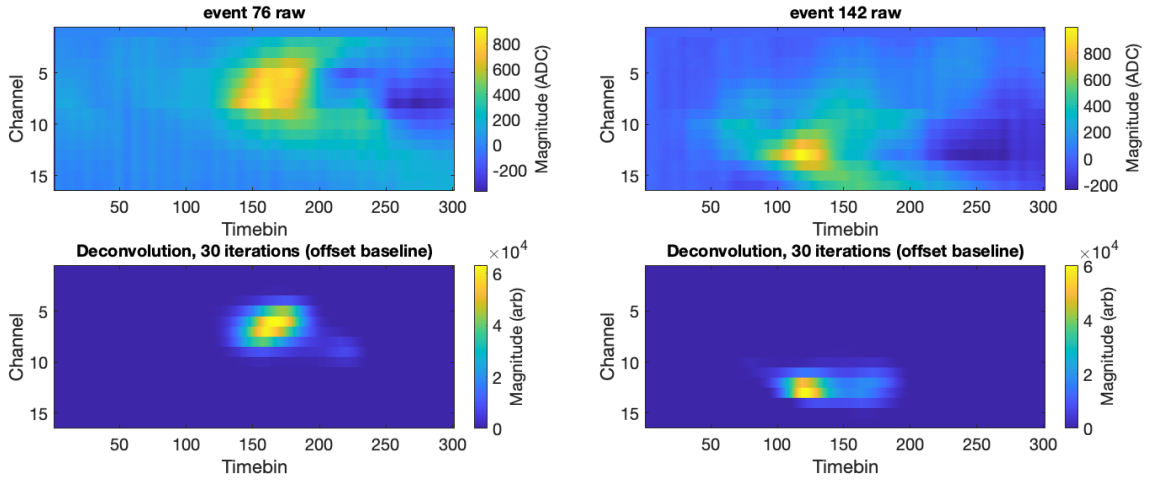

Figure 9.8: Sample raw (top) and deconvolved (bottom) ^{55}Fe events from run 20200302T180611 for the y strip signal on high gain channels.

The spatial length corresponding to the deconvolved recoil signal is estimated to be about 2.8 mm and 1.1 mm for events 76 and 142 respectively. This is consistent with the ranges of electron recoils expected from simulation. The deconvolved signal for event 76 is consistent with an electron recoil traveling in the (-y,-z) direction in detector coordinates and the signal for event 142 is consistent with a recoil traveling in the -z direction. The form of the deconvolved electron recoil events is consistent with what would be expected if there were no charge dissipation occurring.

Nuclear recoil events on the other hand are expected to be much more compact and the amount of structure visible after drift is expected to be fairly small. Low energy nuclear recoil candidate events are selected from the 40 Torr SF_6 run 20200302T155829 based on the NR discrimination parameters described in Section 8.6. Figure 9.9 shows some sample deconvolved ^{241}Cf events from run 20200302T155829.

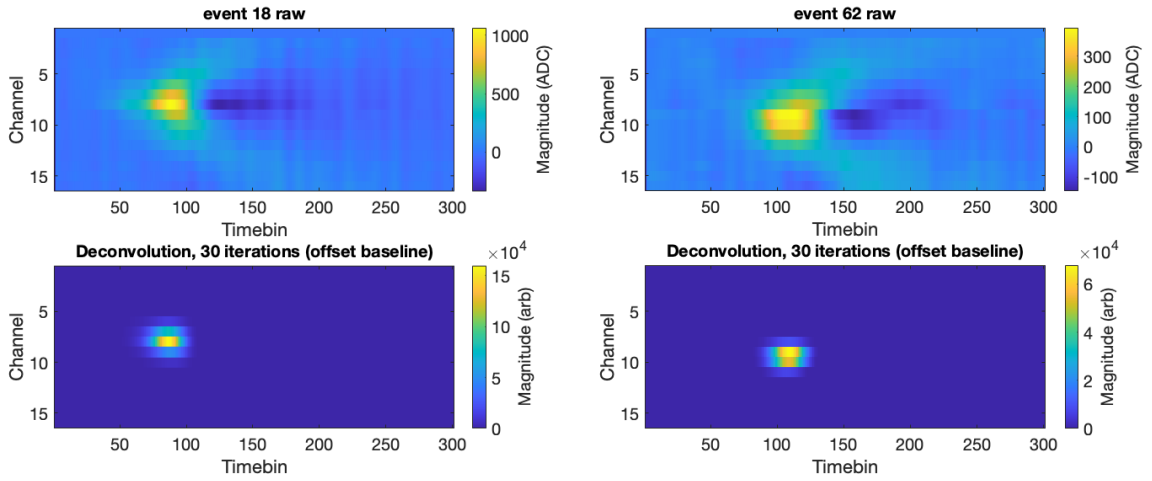

Figure 9.9: Sample raw (top) and deconvolved (bottom) neutron events from run 20200302T155829 for the y strip signal on high gain channels.

The ^{241}Cf events are much more compact and track-like structure is not resolvable, the deconvolved structure is close to gaussian in each case. The neutron source location in

20200302T155829 is below the vessel which means that the neutron tracks are expected to be traveling upward in the figure, although this is not apparent. The deconvolved signal remains consistent with the signal expected from the simulations performed in Chapter 4.

For high energy nuclei, the tracks are considerably longer; to explore the effect of deconvolution on extended track like events, alpha events from the ^{241}Am run 20200302T181705 are examined. Figure 9.10 shows some sample alpha events deconvolved with the Richardson-Lucy deconvolution.

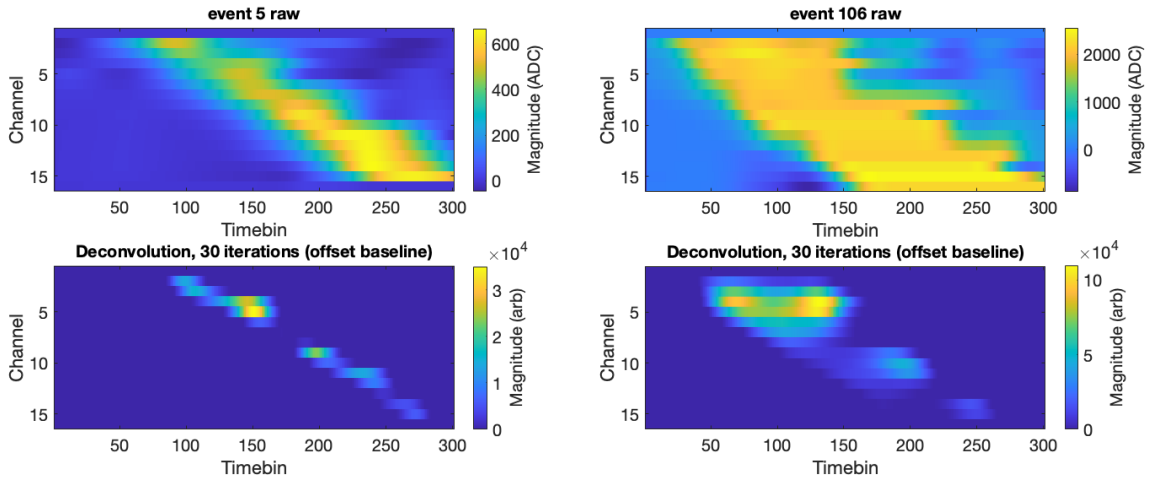

Figure 9.10: Sample raw (top) and deconvolved (bottom) alpha events from run 20200302T181705 for the y strip signal on high gain channels.

In this case the deconvolution significantly narrows the width of the track and assigns a significant amount of charge to the portion of the track around channel 5. The assignment of a large amount of the charge to one side of the track can be attributed to the later portions of a track at this angle being degenerate with charge dissipation from the start of the track. The finite width of the readout in this case contributes to the issue as charge deposited off the edge of the readout can't contribute to the deconvolved signal. In this case the deconvolved signal does not appear to be physical; although the deconvolution follows the path of the track the charge is clearly assigned incorrectly. The alpha tracks underline some of the limitations of deconvolution and the ways in which the results produced might be misleading if the deconvolution is not performed carefully.

9.5 Modification of resistive layer

Deconvolution is a way to mitigate the effect of charge dissipation which is intrinsic to the micromegas device used in previous chapters. Tuning the resistivity of the micromegas or else removing the resisitive layer altogether presents an alternative way to mitigate the effects of the dissipation.

The resistivity of a DLC layer can be tuned to a certain extent when it is deposited by changing the sputtering time or impregnating N_2 or other gasses into the layer [166]. To obtain a qualitative idea of the rate of charge dissipation, the analytical solution for charge dissipation in a resistive layer parallel to a grounded plane described in Section 9.1 is used. Starting with Equation 7.12, which is the charge opposite a strip at a given offset, an approximation of the peaking time can be arrived at by differentiating in time to give

the equation

$$\frac{\partial Q_{strip}}{\partial t} = \frac{Q\sqrt{T}t^{-\frac{3}{2}}}{b\sqrt{8\pi}}\left[\left(y_n - \frac{w}{2}\right)e^{-\left(\frac{y_n-\frac{w}{2}}{b\sqrt{\frac{8t}{T}}}\right)^2} - \left(y_n + \frac{w}{2}\right)e^{-\left(\frac{y_n+\frac{w}{2}}{b\sqrt{\frac{8t}{T}}}\right)^2}\right]. \tag{9.6}$$

This equation provides the rate of arrival of charge above a given strip with width w and centre y_n due to the dissipation of an initially point charge, Q, at the origin. The characteristic time of the dissipation, T, is given by the equation $T = 2b\epsilon_0 R$ where b is the separation between the resistive layer and grounded plane and where R is the resistivity of the resistive layer.

Equation 9.6 is plotted as a function of strip offset from the charge arrival point and time in Figure 9.11 for surface resistivities of 5, 50 and 500 MΩ/□. All of the bins for which $\frac{\partial Q_{strip}}{\partial t} < 0$ are set to zero to make the colour scale readable.

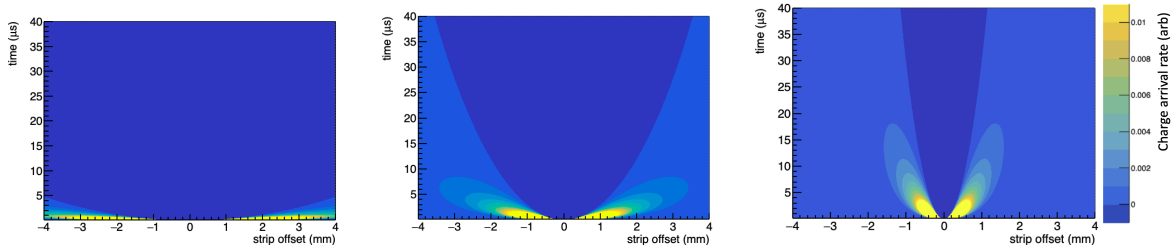

(a) 5 MΩ/□ (b) 50 MΩ/□ (c) 500 MΩ/□

Figure 9.11: Rate of arrival of charge at a 80 µm wide strip at given offset for the analytic model of dissipation in a resistive layer for different resistivities.

These plots of Equation 9.6 can be considered a crude representation of the event shapes expected with the different surface resistivities. The 50 MΩ/□ resistive layer is equivalent to the micromegas device used in the previous chapters. The charge arrival rate shows symmetric 'wings' around the charge arrival point with a similar shape to the signal events such as that in Figure 9.4. The time at which the most charge is present on a given strip (boundary of blue region) is quadratic with the strip offset from the charge arrival point.

For a 5 MΩ/□ resistive layer, the charge dissipates very quickly resulting in a dissipation profile which is closer to flat in time. Charge arriving above a different strip immediately after the initial charge arrival in this case would be on top of the dissipating charge from the initial interaction, making separating such clusters difficult. The fast dissipation however means that a relatively short time needs to elapse before charge has dissipated to an extent that subsequent clusters of charge can be observed without issue. Overall the flatter dissipation profile would improve the resolution of structure offset in time but exacerbate the issues with resolving structure differentiated in x or y. The 500 MΩ/□ resistive layer on the other hand tightens the distribution in space and elongates it in time due to much slower dissipation, which would help resolve structure offset in space but conversely worsen the ability to distinguish charge separated in time. Any moderate modifications the the resistive layer can therefore be seen as a trade-off between resolution in time and space.

In the extreme case of near zero resistivity the charge would dissipate close to instantly on the detector time scale which would result in little to no observable signal as the initial

motion of charge toward a strip is countered by the immediate dissipation evacuating it. Approaching infinite resistivity on the other hand would result in charge dissipation too slow to be observed on the timescale of the charge collection in the detector and would result in nearly undistorted events. The issue with ultra-high resistivity is that slow evacuation of charge can result in charge-up of the resistive layer under irradiation, which will degrade the detector gain and can create non-uniformities in the field. A micromegas for which charge extraction from the resistive layer occurred over many seconds might be suitable for rare event search applications where the event rate is low enough that charge up of the layer isn't a significant issue. This would resolve the charge dissipation issue but would pose issues for characterising and calibrating such a device.

Beyond increasing or decreasing the resistivity of the micromegas another option would be to have no resistive layer at all, this would remove the dissipation issue but would result in a device more prone to damaging itself or its electronics with sparks. Micromegas like this can still be manufactured in bulk although large devices might be written off entirely by sparking in a single location.

9.6 Conclusions

This chapter explored some strategies that might be adopted to mitigate the charge dissipation intrinsic to resistive layer micromegas detectors with a focus on deconvolution. The deconvolution shows potential for the recovery of signal that isn't completely obscured by the charge dissipation in a way that would help to assist analysis. For electron recoils and short nuclear recoils the deconvolved signal was consistent with the expected shape of the recoils. There are limits to the signal that can be recovered by this method however, some solutions of the minimisation problem which the Richardson-Lucy deconvolution solves are degenerate, particularly when significant charge is lost off the readout edge as in alpha events. A full re-analysis of the micromegas data with the deconvolution implemented is outside the scope of the work presented here, although this preliminary qualitative analysis suggests that there is scope for significant improvement using deconvolution.

An alternative solution is to use another micromegas with a resistivity which is either higher or lower than the $50\,\mathrm{M\Omega/\square}$ of the current micromegas. This would not eliminate the dissipation but would modify the diffusion time which could enable better resolution in either time or space while exacerbating the resolution in the other dimension. An extremely high resistivity layer might be worth exploring specifically for low rate applications which would resolve the charge dissipation issue but would be challenging to characterise. A detector without a resistive layer is another alternative although sparking might present a significant reliability problem particularly for large areas.

Further development of the MMThGEM-micromegas combination in negative ion gases should consider the effect of charge dissipation on the signal particularly when it is desirable to resolve structure within an events on the order of millimeter scale. Hardware solutions present various trade-offs which should be considered in the detector design stage while it appears that deconvolution can mitigate the effect of the dissipation within the analysis to a certain extent although further work in this area is required.

Chapter 10

Feasibility of a Gas TPC for Reactor Neutrino Studies

The ability of gas based detectors to produce good ER-discrimination and directionality with a low energy threshold opens the possibility of applications in neutrino physics. Of particular interest is Coherent Elastic Neutrino-Nucleus Scattering (CEνNS), a low energy neutrino scattering process which, like WIMP and fast neutron scatters, produces a nuclear recoil in the scattering medium. The CEνNS process has by far the largest cross-section of any low energy neutrino couplings, making neutrino detection with fairly small fiducial mass viable given a proximate neutrino source.

The CEνNS process was first observed in 2017 by the COHERENT collaboration [67, 167] in a CsI[Na] scintillator exposed to neutrinos produced by an accelerator. More recently the same team has also reported an observation of coherent scattering in Argon at the same facility [168]. At the time of writing the COHERENT experiments have produced the only reported observations of the CEνNS process, the relative lack of data means that there is still significant scope to discover beyond the standard model neutrino interactions. Described here for the first time is an initial study of prospects for applying the gas TPC technology this field which would benefit from the active background rejection and directionality which gas TPCs are capable of.

The two available man made neutrino sources consist of spallation sources and nuclear reactors. Spallation sources produce bunches of neutrinos from the interactions of an accelerator-produced proton beam with a static target, the bunched nature of the neutrinos simplifies background discrimination because triggering can be coincident with the beam 'on'. Nuclear reactors provide an alternative source of neutrinos produced from the fission reactions which power them, they have the advantage of generally higher deliverable neutrino exposure, although the lack of a definite trigger means that strong background rejection is a necessity for a detector using a reactor source.

The powerful background rejection that a gas based detector can achieve would be particularly useful for a reactor based CEνNS detection experiment. A potential location for such an experiment is the Hartlepool nuclear power station in the UK, which operates two reactors and have signaled a willingness to host experiments on their site.

The detection of CEνNS interactions by a gas TPC would provide a strong demonstration of the technology required for a large gas based nuclear recoil detector such as the proposed CYGNUS detector [83]. Although the primary purpose of the CYGNUS detector is the detection of dark matter WIMPs, a secondary physics objective is as a neutrino observatory focusing on Solar neutrinos interacting through the CEνNS and

Electron Scattering (ES) processes. Exploring both CEνNS and electron scattering of neutrinos using a reactor neutrino source would be a strong demonstration of the physics reach of a scalable readout for the CYGNUS experiment. The low-threshold strip-based readout described in the previous chapters of this thesis is a potential candidate for further development towards this end.

This chapter presents a study of the feasibility of a short baseline gas-based reactor neutrino detector focusing on the CEνNS process. First existing detectors focused on CEνNS recoils are discussed in Section 10.1. Section 10.2 describes the calculation of the recoil rate in a potential detector, this includes the determination of the CEνNS cross-section, the reactor anti-neutrino flux and effects of ionisation quenching on recoils. Section 10.3 focuses on a potential deployment at the Hartlepool nuclear power station; describing the locations of a potential detector and the relative advantages and disadvantages of each site including the respective CEνNS recoil rates. The CEνNS recoil spectrum induced by solar neutrinos in each of the detector gasses is described in Section 10.4. Finally Section 10.5 presents the conclusions of the chapter and the overall results of the study.

10.1 Existing CEνNS experiments

The low energy recoils produced by the CEνNS process have meant that it is a fairly understudied process. No gas based detectors have yet been deployed to observe the CEνNS process but a number of other technologies have been deployed. This section provides a brief overview of the existing CEνNS detection efforts and the associated detector technologies.

The first experimental observation of the CEνNS was published in 2017 by the COHERENT collaboration [167]. The detector consisted of a sodium-doped CsI crystal with a total mass of 14.6 kg located at the Spallation Neutron Source (SNS) at Oak Ridge National Laboratory.

The SNS produces neutrons by directing a proton beam at a mercury target, with an isotropic neutrino flux produced as a byproduct. The proton source is pulsed with a frequency of 60 Hz and pulse width of 1 µs, each pulse produces approximately $\sim 4 \times 10^{19}$ neutrinos of each flavour. The pulsed nature of the source enables the CEνNS recoils to be observed as an event excess immediately after the proton delivery on target.

The COHERENT CsI detector was located at a standoff of about 20 m from the SNS target and consisted of a CsI[Na] crystal with scintillation light observed by a single low-background PMT. The detector was shielded with HDPE, lead and water tanks and included an active muon veto, additionally it was insulated from neutrons from the SNS target by about 15 m of concrete and gravel. The analysis of the data was sensitive to nuclear recoils down to 4.25 keV and did not discriminate between electron and nuclear recoils. An event excess of 134 ± 22 was reported for the time window coincident with the proton delivery consistent with standard model expectations from the CEνNS process.

The COHERENT collaboration also operates a number of other detectors for CEνNS recoils including a single-phase liquid argon (LAr) detector, an NaI crystal and a liquid scintillator [167, 169]. At the time of writing the LAr detector has also observed CEνNS recoils while the other detectors have yet to reach sufficant sensitivities to report observations [168]

An alternative source of neutrinos available on earth are civilian nuclear reactors which produce a continuous flux of neutrinos and have significantly higher overall neutrino

luminosities than pulsed sources like the SNS The CONNIE experiment is the only existing detector focusing on the CEνNS process for reactor neutrinos at the time of writing. The experiment is located at the Angra 2 nuclear reactor in Brazil with a standoff of 30 m from one of the 3.8 GW cores [170]. The detector consists of an array of CCD sensors with recoils observed in the extra thick Silicon wafer of the CCD itself [171]. The pitch of the CCD pixels is 15 µm and the detector is sensitive to recoiling Si nuclei down to 1 keV. While the CONNIE experiment has yet to reach the sensitivity needed to observe CEνNS recoils, they have accumulated 3.7 kgday of low threshold detector exposure near a nuclear reactor with a significant number of background events.

10.2 Determination of the electron and nuclear recoil rates

The interaction rate observable in a detector is dependent on the incident particle flux and energy spectrum, on the interaction cross-section, and on the fraction of the produced interactions observable by a detector. This section presents the calculation of the cross-section of the CEνNS and ES processes, the expected reactor anti-neutrino spectrum and the effect of ionisation quenching on the resulting recoil spectrum. These factors are then synthesised into a calculation of the recoil rates in a set of common detector gasses at a nominal stand-off from a reactor core.

10.2.1 The CEνNS process

Neutrinos can interact with nuclei through charged current interactions, mediated by the exchange of a $W^{\pm}$ boson, or through a neutral current interaction which is mediated by a Z^0 boson. The CEνNS process is a type of neutral current interaction which occurs between any flavour of neutrino and an atomic nucleus. Neutral current interactions generally occur between the neutrino and an individual nucleon in the target nucleus, what differentiates CEνNS is that the interaction acts upon the entire nucleus [172]. This occurs when the final states of the possible interactions with the individual nucleons which comprise the nucleus add coherently. The coherence is conditional on the de Broglie wavelength of the exchanged Z boson being sufficiently large to 'probe' the entirety of the target nucleus, this limits the magnitude of the momentum which can be exchanged in a CEνNS interaction.

The differential cross-section of the CEνNS interaction is independent of neutrino flavour and is given by the equation

$$\frac{d\sigma_{NS}}{dE_{rec}}(E_\nu, E_{rec}) = \frac{G_F^2}{8\pi}[Z(4\sin^2\theta_W - 1) + N]^2 M(2 - \frac{E_{rec}M}{E_\nu^2})|f(q)|, \tag{10.1}$$

where M, N and Z are the mass, neutron number and atomic number of the target nucleus, G_F is the Fermi coupling constant, θ_W is the weak mixing angle and E_{rec} and E_ν are the recoil and incident neutrino energy respectively [173]. The nuclear form factor, $f(q)$, starts to impact the cross section for larger neutrino energies, for iron for example $|f(q)|$ is unity up neutrino energies of about$\sim$ 40 MeV. For reactor and solar neutrino energies, with $E_\nu < 20$ MeV, this effect can be safely neglected for all the considered nuclei.

The overall cross section is close to proportional to N^2 due to the higher neutral scattering cross-section of neutrons as opposed to protons. Conversely the momentum transferred by an interaction decreases with increasing nuclear mass. The maximum nuclear recoil energy that a neutrino of energy E_ν can induce is $\frac{2E_\nu^2}{M}$ due to the kinematics of an elastic scatter, for $E_{rec} < \frac{2E_\nu^2}{M}$ the differential cross section is unphysically negative.

10.2.2 The ES process

Another important neutrino interaction is elastic neutrino-Electron Scattering (ES), which might be expected to form a significant part of the neutrino signal and a background to a CEνNS measurement. Electron scattering is a purely leptonic process which is mediated by the exchange of the $W^\pm$ or Z^0 boson. In this case both charged-current and neutral-current interactions produce the same end state so the cross section considered is the sum of the all the tree level processes for which $\nu e^- \rightarrow \nu e^-$. Radiative corrections are neglected for this calculation as the precision of the uncorrected form is sufficient.

The differential cross section of electron scattering to the first order is

$$\frac{d\sigma_{ES}}{dE_e} = \frac{2G_F^2 m_e}{\pi}(g_1^2 + g_2^2(1 - \frac{E_e}{E_\nu})^2 - g_1 g_2 \frac{m_e E_e}{{E_\nu}^2}), \tag{10.2}$$

where E_e is the electron recoil energy and g_1 and g_2 are constants dependent on neutrino flavour [62]. the values of g_1 and g_2 for the various neutrino flavours are

$$g_1^{(\nu_e)} = g_2^{(\bar{\nu}_e)} = \frac{1}{2} + \sin^2\theta_W \simeq 0.73, \tag{10.3}$$

$$g_2^{(\nu_e)} = g_1^{(\bar{\nu}_e)} = \sin^2\theta_W \simeq 0.23, \tag{10.4}$$

$$g_1^{(\nu_{\mu,\tau})} = g_2^{(\bar{\nu}_{\mu,\tau})} = -\frac{1}{2} + \sin^2\theta_W \simeq -0.27, \tag{10.5}$$

$$g_2^{(\nu_{\mu,\tau})} = g_1^{(\bar{\nu}_{\mu,\tau})} = \sin^2\theta_W \simeq 0.23. \tag{10.6}$$

Owing to the low mass of electrons, they will generally have a higher energy than a CEνNS nuclear recoil from the same neutrino. The per-atom interaction rate for the ES interaction is proportional to the number of electrons, Z, in contrast to the CEνNS which is proportional to N^2.

10.2.3 Neutrino capture reactions

In addition to scattering off a nucleus, electron anti-neutrinos can also participate in a process called Inverse Beta Decay (IDB) on hydrogen which consists of the reaction $\bar{\nu_e}(p,n)e^+$. Analogous reactions exist for protons bound in larger nuclei with a large range of possible final states, with common products including neutrons and gamma rays. In the neutrino energy range $E_\nu < 50\,\text{MeV}$ the cross section of these reactions is well described by the shell model [64].

Due to the complexity of the model required to determine the cross section and the wide range of final states, IDB and equivalent processes are not considered in depth in this study. Neutrino captures in the building, vessel and shielding which produce neutrons will likely contribute slightly to the backgrounds of the experiment.

10.2.4 Reactor anti-neutrino flux

The CEνNS and ES cross-sections are both sensitive to neutrino energy and the overall recoil rate will be proportional to the total neutrino flux. Consequently a determination of the neutrino flux produced by a reactor is an important part of the determination of the observed signal. This section focuses on a general model for the neutrino spectrum of a reactor, the specifics for the Hartlepool reactors which are the focus of this study are described in Section 10.3.

The decays of the fission fragments in a nuclear reactor generate a flux of anti-neutrinos which is proportional to the thermal power of the reactor. There are hundreds of potential branches for each of the fission reactions in a reactor; consequently rather than considering individual decays, the average generated energy and neutrinos of the fission fragments and their daughters over a timescale of months are considered for each primary isotope. The primary fissioning isotopes in a power generating nuclear reactor are ^{235}U, ^{238}U, ^{239}Pu and ^{241}Pu. The rate of the various processes varies with the fuel composition which is itself a function of reactor live time. For the calculation of the anti-neutrino spectrum the typical values for the fission ratios of the respective isotopes reported in [174] are used, the relative fission rates are shown in Table 10.1. The two main contributions to the fission rate are ^{235}U, which comprises over half of fissions, and ^{239}Pu, which comprises about a third of fissions.

Table 10.1 also list the effective energy release, Q, for each fission reaction which tends to increase with isotope mass number. The value of is Q determined from the mass difference between the initial isotope and the weighted sum of the beta-stable fission products with some corrections in [175]. Taking the average energy release weighted by the relative fission rates of each isotope, $\langle Q \rangle$, gives an average energy release of 205.8 MeV/fission. The fissions per unit thermal power of the reactor is equal to the inverse of this value, which gives fission rate of 3.03×10^{16} fissions/s/MW. For the 1500 MW Hartlepool reactors of interest here, described in Section 10.3, this yields a total of 5×10^{19} fissions/s.

Table 10.1: Typical values of the relative rates of fissions of different isotopes in a reactor [174] and effective energy release per fission for each isotope [175].

Reaction	**Relative rate (%)**	Q (MeV fission^{-1})
^{235}U	55	202
^{238}U	7	204
^{239}Pu	32	211
^{241}Pu	6	232

There are other contributions to the neutrino flux, which include the decays of the products of the ^{238}U(n,γ)^{239}U reaction, and the fission of ^{239}U and ^{239}Np. These reaction contribute anti-neutrinos with $E_\nu < 1.5$ MeV, these contributions are neglected in the analysis due to the fairly small contribution to the final spectrum.

The $\bar{\nu_e}$ spectrum in the range 2-8 MeV for the fission fragments of each isotope are obtained from literature [59] [176]. The determination of the energy spectrum of the produced anti-neutrinos are based on inversions of the beta decay spectrum of fission fragments from individual elements. A histogram of the total $\bar{\nu_e}$ flux is constructed out of the histograms for the individual reactions using the proportions in Table 10.1. Figure 10.1 shows the determined reactor anti-neutrino energy spectrum per fission, with

contributions from different isotopes also shown. The neutrino flux decreases at a more than exponential rate across the energy range, with the same general shape across all the isotopes.

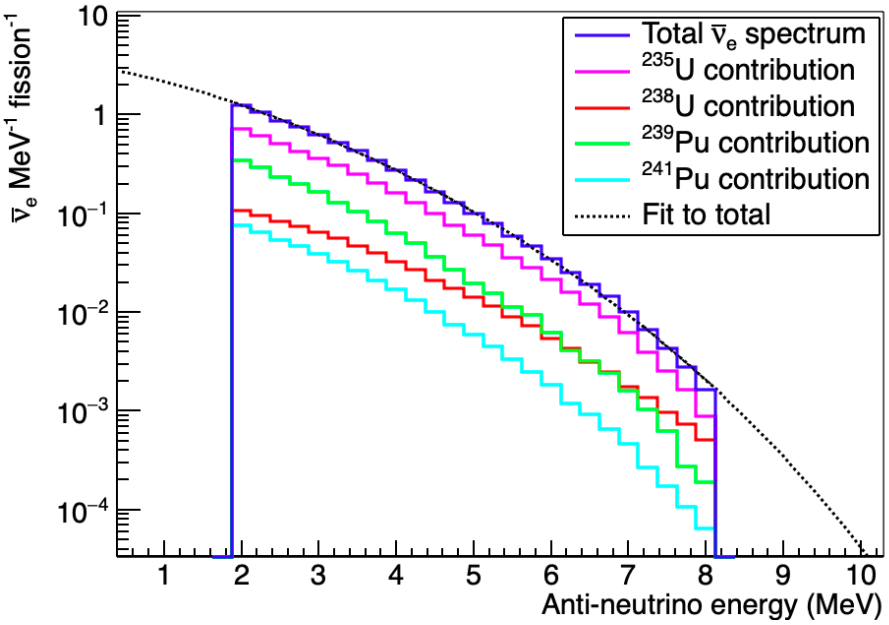

Figure 10.1: Total differential anti-neutrino spectrum for simplified reactor model and the contributions from each individual isotope and fit to total.

The number of anti-neutrinos with energy 8 MeV is almost 100 times lower than the number at 2 MeV, illustrating the sharp drop off in rate with energy. The total determined flux is fitted with an exponential function of the form $y = e^{p_0+p_1x+p_2x^2+p_3x^3+p_4x^4}$ which is used to extrapolate to neutrino energies from 0.25 MeV to 12 MeV. The determined coefficients for the fit are $p_0 = 1.146$, $p_1 = -0.282$, $p_2 = -0.102$, $p_3 = 0.00709$ and $p_4 = -0.00053$. Neutrinos with energy above 12 MeV make a negligible contribution to observable event rates and are neglected.

The differential neutrino flux, $\frac{dN_{\bar{\nu_e}}}{dE_{\bar{\nu_e}}}$, at a given distance, r, from the centre of a reactor core is obtained by multiplying the per-fission neutrino spectrum by the factor $\frac{P_{th}}{\langle Q \rangle}\frac{1}{4\pi r^2}$, where P_{th} is the thermal power of the reactor and $\langle Q \rangle$ is the average energy release per fission. Here the reactor core is approximated as a point source rather than an ≈10 m diameter cylinder more typical of civilian reactors. For the areas which are accessible for detectors, approximating the reactor as a point source is not expected to make a significant difference to the determined recoil rates.

10.2.5 Ionising Quenching Factor of the gasses

After a neutrino scattering interaction in a detector, the resulting recoil has to be detected. For recoiling nuclei only a fraction of the transferred energy is deposited as ionising energy and is therefore visible to the detector. The Ionisation Quenching Factor (IQF) is a measurement of the fraction of the energy of a recoil which is deposited as ionising energy. As was dicussed in Section 4.2.2 the Lindhard model provides a good approximation for the IQF of elemental gasses. It was shown in Section 2.1 that the Lindhard model also provides a good fit to the IQF of SF_6 results from SRIM which provides the most comprehensive model available for the quenching in SF_6 at time of writing.

The IQF from the Lindhard model for many of the gasses used in this study can be seen in Figure 2.2. The IQF decreases with decreasing energy, with the gradient becoming steeper as the energy approaches zero. Heavier elements have a smaller quenching factor at all energies which means the observable energy for recoils in those gasses will be significantly lower. As most of the CEνNS recoils are expected to have energy <10 keV the quenching will have a significant effect on the observed energy spectrum; resulting in a reduction of the observable energy by a factor of 20-90%. When referring to the ionising energy deposited by a nuclear recoil, the unit keV-electron-equivalent (keVee) is used to distinguish from the total recoil energy in keV. For electrons, which are not effected by quenching, the units keVee and keV are equivalent.

10.2.6 Neutrino recoil energy spectrum

To determine the CEνNS recoil rate per nucleus, the product of the neutrino flux and differential cross section are integrated over neutrino energy. The differential recoil rate for a given element in a detector can then be determined by multiplying by N_t, which is the number of nuclei of the given element in the target;

$$\frac{dR_t}{dE_{rec}}(E_{rec}) = N_t \int_{\sqrt{\frac{E_{rec}M}{2}}}^{\infty} \frac{dN_\nu}{dE_\nu} \frac{d\sigma}{dE_{rec}} dE_\nu. \tag{10.7}$$

The lower limit of the integration, $\sqrt{\frac{E_{rec}M}{2}}$, is the lowest neutrino energy that can induce a recoil of energy E_{rec}. The recoil rate is dependent on the detector offset from the reactor core as well as the number and type of nuclei in the fill gas as the CEνNS cross-section is dependent on the target element. For compound gasses, the recoil rates for each of the constituent elements can be determined separately and added together.

Figure 10.2a shows the variation in recoil rate with energy for a set of common detector gases at a stand-off of 10 m from one of the Hartlepool 1500 MW reactor cores approximated as a point source. The integration is performed numerically using the fit to the differential neutrino spectrum presented in Section 10.2.4 and the cross-sections for the CEνNS and ES processes from Sections 10.2.1 and 10.2.2.

The CEνNS recoil rate drops off quickly with energy; at 10 keV the recoil rate for all of the gasses apart from helium is less than 1×10^{-2} recoils (kg-day)$^{-1}$ keV^{-1}. Recoil energies of lighter nuclei skew toward higher energy, this is consistent with the kinematics that would be expected in elastic collisions with a significantly lighter particle. The rate of electron recoils from the ES process is also shown, the plotted line is the ES rate for helium; the other targets have only small variations in the ES rate which is proportional to the electron content of a kilogram of the target gas. The electron recoil spectrum is nearly flat below 100 keV and drops off sharply in the MeV region, extending to far higher energy than the CEνNS recoils.

As discussed in Section 10.2.5, only a fraction of the energy deposited in the detector by a recoil nucleus will be observable as ionising energy. This fraction is described by the quenching factor which is important to include in a calculation when considering detector sensitivities. Figure 10.2b shows the variation in recoil rate with deposited ionising energy (i.e. with the quenching included) for various gasses at 10 m stand off from a 1500 MW reactor. Only gasses for which the Lindhard model is known to be a good approximation are included, which means only noble gases and SF_6. Because the IQF varies with energy, the addition of quenching is not a simple linear shift of the recoil distribution and results

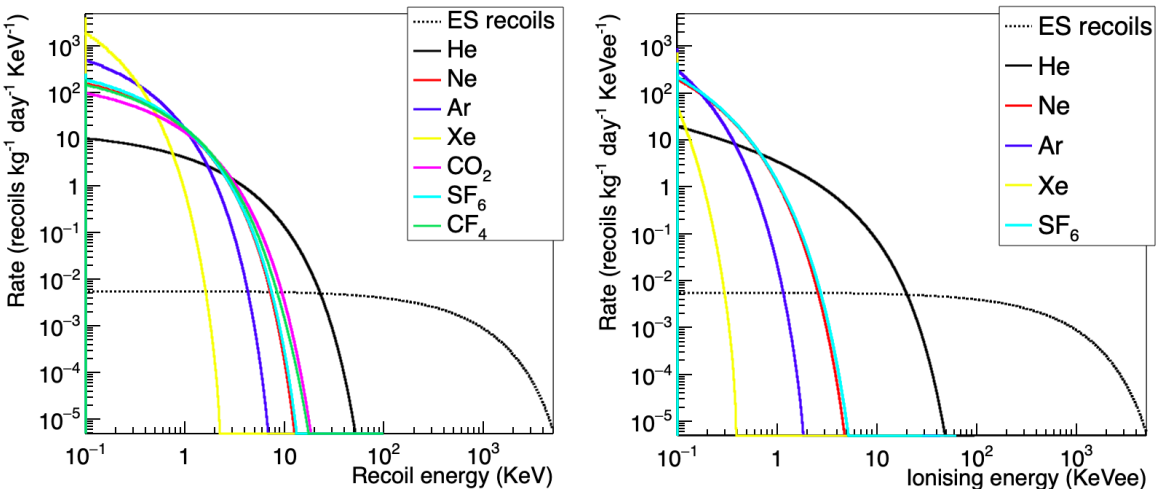

(a) Recoil energy.

(b) Observable energy (Lindhard quenching).

Figure 10.2: Energy spectrum of CEνNS induced nuclear recoils in a set of common detector gasses at 10 m from a 1500 MW nuclear reactor approximated as a point source, also shown rate of ES electron recoils in Helium.

in a change in the shape of the spectrum. The trend of a sharp drop off in the recoil rate with energy is broadly the same, although the addition of quenching makes the drop-off in recoil rate with energy even steeper. More massive elements suffer the most from the shift due to a combination of lower IQFs and the already sharp drop-off in the recoil rate with energy. Helium is affected the least, with the points at which it crosses each axis being similar and the main difference being a 'flattening' of the downward curve. The ES ionising energy spectrum is identical to the raw recoil energy spectrum as quenching does not effect electron recoils in the plotted energy range.

Using the quenched recoil rates, the number of observable recoils in a detector with a given energy threshold can be determined. The number of observable CEνNS recoils above ionising thresholds of 0.5, 1, 2, and 5 keVee in the gases for which the quenching was determined for a kilogram-day of exposure are shown in Table 10.2.

Target Gas	Detectable recoils (kg^{-1} day^{-1})			
	Energy threshold			
	5 keVee	2 keVee	1 keVee	0.5 keVee
He	1.17	3.57	5.91	8.27
Ne	3.82×10^{-7}	1.13×10^{-2}	3.39×10^{-1}	2.56
Ar	0	5.09×10^{-12}	2.54×10^{-3}	2.46×10^{-1}
Xe	0	0	0	0
SF_6	2.78×10^{-6}	1.64×10^{-2}	3.86×10^{-1}	2.68
ES (He)	2.85	2.87	2.87	2.88

Table 10.2: Rate of recoils with ionising energy above a given threshold for detector gasses at 10 m from a 1500 MW Hartlepool reactor core.

There are consistently more recoils observable in Helium than the other gasses for all the plotted thresholds, which can be attributed to the higher energy and ionising energy of helium recoils. Conversely there are zero observable recoils for the heaviest element,

Xenon, at any threshold. The recoil rates for the other noble gasses are ordered in terms of mass number with Neon having the second highest rate after Helium and Argon having the second lowest rate after Xenon. The recoil rates in SF_6 are broadly similar to Neon which is consistent with the fact that the most abundant isotopes of Fluorine and Neon differ only by a single proton. A significant finding is that the CEνNS rate enhancement conferred by the higher neutron number of heavier nuclei is more than offset by the lower recoil energies and IQF of heavy nuclei.

Another significant trend is the exponential dependence of the event rate on the energy threshold for the heavier nuclei. Lowering the energy threshold from 2 keVee to 1 keVee for example results in a twenty-fold increase in the observed event rate for an SF_6 based detector. Energy thresholds this low will certainly present a challenge for gas detector technologies with good discrimination and directionality at this threshold being even more challenging.

The final row of Table 10.2 shows the number of ES induced electron recoils in Helium at each threshold. The fairly flat electron energy spectrum at this energy results in the number of observed electron scatters being close to constant with threshold. Furthermore the fact that the rate of electron scatters are proportional to the electron content of the gas and not affected by quenching means that the ES rate is similar for all the gasses. For gasses other than helium, ES recoils will dominate the neutrino signal at recoil energies >3 keVee. Strong ER discrimination will be required for the ≈2.9 recoils (kg-day)$^{-1}$ ES signal to be disentangled from the CEνNS signal.

10.3 Hartlepool reactor

This work focuses specifically on the feasibility of a detector installed at the Hartlepool nuclear power plant and the signal expected from the reactor cores present there. The Hartlepool power station consists of two Advanced Gas-cooled Reactors (AGRs), these use high pressure CO_2 as coolant which enables them to operate with a higher thermal efficiency than conventional boiling water reactors. The thermal power of each core is about 1500 MW and each is contained in a large pre-stressed concrete vessel which presents an absolute limit on the closest that a detector can be placed. This section will use the rates determined previously to arrive at the recoil rates at a number of potential detector locations within the Hartlepool reactor building. Other considerations such as floor space, accessibility and separation from reactor activities are also considered for each site as well as general considerations for operating at a working commercial reactor facility.

10.3.1 Lab locations

During a visit to the Hartlepool power plant in 2018 three potential locations for a lab/experimental area were identified within the reactor building. We will refer to the lab locations as A, B and C in order of increasing distance from the north reactor core, which is the nearest core in all cases. Following is a short description of each of the sites and the access and space considerations of each.

Site A Located as close to the reactor core as it is possible to be, in a small vacated equipment hut right on the edge of the pressure vessel. The space suffers from small floor space (∼2 m by ∼3 m) and having restricted access, any equipment needing to be manually carried up a narrow stairway with width 40 cm. The size and access

considerations will likely limit the maximum size of a detector deployed here to the decaliter scale.

Site B Located in a room adjacent to the hall containing the reactor vessels, part of the room is a (non-critical) access route and foot traffic through the room by reactor workers should be expected. The available space is significantly larger, around $40\,\mathrm{m}^2$ with two stories of head room and the area is accessible for pallet trucks and trolleys, which would make cubic meter scale detectors feasible. Equipment deployed at this site would need to fit through a single doorway with width 1 m which might make pressure vessels of side lengths larger than this unfeasible.

Site C Located in the former laundry room for the station, this is the furthest away from the reactor of any of the sites, but has the largest working space and best access. The floor space available is in excess of $100\,\mathrm{m}^2$ which should be more than sufficient for a detector vessel, equipment and shielding. The room is accessible by forklift and a pair of double doors can be used for cargo, making pressure vessels with side length up to about 1.5 meters feasible to install.

To determine the neutrino flux that would be observed at each site, the distance from the centre of a potential detector to each reactor core was determined from plans of the building. Potential detector locations are selected assuming half a meter clearance from the lab wall nearest the north reactor, the displacements relative to the reactor cores and neutrino fluxes for each location are shown in Table 10.3.

Table 10.3: The displacements from each reactor core centre of a potential detector at each identified site and the total neutrino flux expected.

lab	**North core (m)**	**South core (m)**	**North core $\bar{\nu}_e$ flux ($10^{12}\mathbf{cm}^{-2}\ \mathbf{s}^{-1}$)**	**South core $\bar{\nu}_e$ flux ($10^{12}\mathbf{cm}^{-2}\mathbf{s}^{-1}$)**
A	13.7	31.8	13.20	2.50
B	18.7	36.8	7.07	1.82
C	36.9	77.4	1.80	0.41

For each of the lab locations the south core is at least twice as far away as the north core which means that the neutrino flux is less than a quarter of that from the north core. The distance from the core correlates with the accessibility and available space of each of the sites meaning there is a distinct trade-off between flux at the detector and the maximum size of detector that might be deployed.

10.3.2 Neutrino signal at proposed detector sites

The event rate at each of the proposed detector sites can be determined by a simple scaling of the recoil rate by the inverse square of the distance. Consequently site A will experience the largest event rate per unit fiducial mass while site C will experience the smallest rate. The sites however have very different levels of access and available space, as a result the size of detector which can be deployed at each site varies. The deployed detector size has a direct effect on the observable event rate and must be considered when comparing the event rates at each site.

An approximation of the maximum deployable detector size at each site is to assume a cubic vessel with a side length equivalent to the minimum width of the access route to the site. There are ways around this limit, such as assembling the vessel from sections on site or a modular detector composed of several vessels but as other factors like floor space also scale with access size for the labs considered the stated approximation is used for comparison . The access sizes are for site A, B and C are 0.4 m, 1 m and 1.5 m respectively, resulting in respective approximate detector volumes of 0.064 m^3, 1 m^3 and 3.4 m^3.

The recoil rate from neutrinos from the north core assuming a 0.5 keVee threshold at each site in a cubic meter of each gas at atmospheric pressure is shown in Table 10.4. Also shown is the recoil rate observed in the maximum deployable detector volume at each site: 0.064 m^3, 1 m^3 and 3.4 m^3 for sites A, B and C respectively. The event rate due to neutrinos from the south core at each site can be determined by scaling to the neutrino fluxes in Table 10.3.

	Recoil rate (atm^{-1} m^{-3} day^{-1})			Rate in deployable detector (day^{-1})		
Target Gas	Site A	Site B	Site C	Site A	Site B	Site C
He	0.79	0.42	0.11	0.05	0.42	0.37
Ne	1.23	0.66	0.17	0.08	0.66	0.58
Ar	0.23	0.13	0.03	0.01	0.13	0.10
SF_6	8.81	4.73	1.21	0.56	4.73	4.11

Table 10.4: Rate of CEνNS recoils for neutrinos from the 1500 MW Hartlepool north reactor core at each site for a detector with threshold of 0.5 keVee. The 'deployable detector' considered consists of gas volumes of 0.064 m^3, 1 m^3 and 3.38 m^3 for sites A, B and C respectively.

The variation in event rate with target gas in Table 10.4 is consistent with that observed in Table 10.2 (Xenon is excluded as the event rate is zero at all sites). The event rate also decreases with site distance from the reactor core as would be expected. Considering gas volume rather than mass confers a rate advantage to the more massive elements due to their generally higher density. This is particularly obvious for SF_6 which achieves a recoil rate per unit volume in excess of ten times that of helium for the 0.5 keVee threshold considered.

As access size and floor space for the sites considered correlates with distance from the reactor core, considering the 'deployable detector' size makes the sites significantly more competitive than simply examining the recoils per unit mass. The small available vessel size offsets the larger event rate available at site A resulting in the by far the smallest event rate of the sites despite the largest neutrino flux. Sites B and C are competitive on event rate, enough so that other considerations might also be taken into account.

10.3.3 Anticipated backgrounds

A significant consideration in the design of a detector is the suppression of potential backgrounds to a manageable level. There is a significant number of factors which have to be determined in more depth than this work explores to accurately determine the ambient backgrounds. This section only consists of a broad qualitative look at the main backgrounds anticipated. A dedicated radiation study/assay of the site focusing on the

kinds of backgrounds of concern should be considered the next step in a potential detector deployment.

Measurements by the health physics department at Hartlepool suggest that the reactor and fueling activities do not contribute significantly to the background radiation at the proposed lab locations. The largest source of radiation in the lower levels of the reactor building is actually natural radon originating from the area's rock. In addition to radon the primary radioactive backgrounds are expected originate from the natural radioactivity of the concrete and steel of the building and reactor vessel and from cosmic rays. The overhead concrete, metal ducting and miscellaneous plant are expected to result in a few meters water equivalent of overburden in the various labs, resulting in a somewhat reduced cosmic rate as compared to surface flux. Overall local radioactive background at each location is expected to be about the same and comparable to that encountered in any surface lab.

The design of the detector shielding will have a significant effect on the background event rate in the detector. The water blocks used by the DRIFT detector might provide a good blueprint for the shielding, although the size and potential for leaks would make deployment of this solution at site A impossible. Polyethylene and lead are more compact and stable solutions which would be significantly easier to deploy in a small space. Shielding could significantly reduce the background from steel and concrete, at the energy range of interest the main irreducible background is expected to originate from secondary products of cosmic rays.

The CONNIE experiment [170] might be considered a good guide for the expected backgrounds at a reactor. The shielding of the CONNIE experiment consists of polyethylene and lead layers and is comparable to the shielding that might be deployed around a potential gas based detector. The background rate observed in the CONNIE experiment was around 5×10^3 events/day/kg/keV in the energy range 1 keVee to 14 keVee and primarily consists of electrons.

The ER-rejection factor for simulated 5 keVee helium recoils in a 755:5 Torr He:SF_6 mixture was determined to be 1×10^3 in [83] for a simple one parameter analysis. This would need to be increased by a factor of about 16 to produce a recoil sample which is 50% electrons and 50% recoils in a helium based detector at site A. Promising work is underway to explore methods of increasing the efficiency of electron rejection in gas detectors which might make ER-discrimination of this magnitude feasible. Furthermore the directional capabilities of a gas TPC could also assist significantly in discrimination against the isotropic background.

10.3.4 Other considerations for operation at a reactor

Working in the reactor building of a nuclear reactor presents a number of challenges which need to be considered in addition to the raw event rates and detector sizes. This section describes some of the additional considerations for a potential detector and how they effect each of the individual sites.

One issue is access for the physicists on the project, without proper clearance visitors must be escorted at all times which is inconvenient and also might prevent work entirely during busy times such as reactor shutdowns. This is uniform to all of the sites considered as they are all in the same controlled area of the Hartlepool site.

Another issue is electrical; the building hosts a lot of heavy machinery and industrial activity, large amounts of ground noise and poor power quality should be expected

and accounted for. The VIDARR experiment for example encountered significant power supply noise issues during operation near a reactor despite the significant shielding of an ISO shipping container [177]. An Uninterruptible Power Supply (UPS) unit designed for power supply related noise issues or a similar solution would likely be necessary for the operation of a gas detector under these circumstances.

Significantly all microwave-band communication is also prohibited due to those bands being occupied by vital equipment. This means that data transfer and detector control must at the very least be wired, and digitisation and storage might well have to occur on-site. This consideration makes the larger lab spaces more attractive as they could also accommodate supporting server racks and hard-drives.

Finally any activities undertaken in the reactor building will be expected to meet stringent safety standards, with reactor operations always taking precedence over any experiment. Flammable or toxic target gasses would very likely be entirely prohibited and activities like soldering or welding might also be impossible to perform on site. The standards at sites A and B are anticipated to be particularly strict considering their direct access to the vessel hall. Site C is much more isolated from the work undertaken in the rest of the reactor building which would make accommodations for detector activities easier from a safety standpoint.

10.3.5 Site recommendations

There are a number of factors which effect the potential of each of the proposed sites. Proximity to the reactor core is an important factor as it directly effects the recoil rates in a given target. For the sites considered however the most reactor proximate location, site A, also has the worst access and available space. Site C is the furthest away but also provides the most separation from reactor activities and has the most available space and best access. Site B is between the two in terms of distance and accessibility, although it is the least separated from other reactor workers with necessary foot traffic in the room. The better access and space available to sites B and C would enable the deployment of a larger detector which can more than offset the longer stand-off of the two sites compared to site A.

Overall site C is considered the best location for a prospective detector; although the neutrino flux is the lowest, preliminary calculations suggest this is offset by the ability to deploy a larger detector. Practical considerations further tip the balance in favour of site C as it has the most floor space and is well separated from the reactor operations which is anticipated to simplify the deployment and make working conditions more comfortable. If a detector is deployed other considerations such as cost and the selected gas mixture and pressure will play a role in the ultimate volume and target mass of a detector which might change the relative desirability of each of the sites.

10.4 CEνNS from Solar neutrinos

For detectors which are not in proximity to a man-made neutrino source, the largest source of neutrinos on Earth is the Sun. CEνNS recoils from solar neutrinos are expected to form an irreducible background for (non-directional) WIMP detectors. This limit to the sensitivity of most detectors to WIMPs is referred to as the 'neutrino floor'.

While a reactor near detector would not feasibly have the mass required to observe the CEνNS scattering of solar neutrinos, one of the development goals of such a detector

would likely be to inform the development of a larger detector which would be capable of observing these recoils such as CYGNUS [83]. The solar neutrino recoil spectrum is therefore of interest for a potential reactor CEνNS detector as a forward looking consideration.

Solar neutrinos are produced primarily by the pp-chain and CNO cycle fusion reactions which power the Sun. In order to calculate the recoil rate at Earth from solar neutrinos, the solar neutrino flux spectra are taken from literature and the conversion to recoil rate proceeds as described in previous sections. The solar neutrino spectrum used for the calculations is shown in Figure 10.3. The pp,pep,^{7}Be, ^{15}O, ^{13}N and ^{17}F spectra are taken from [66], the spectrum for ^{8}B is from [178], and the relative fluxes at earth are from [179]. Excluded is the *hep* reaction as it contributes very little to the total flux and makes a negligible contribution to CEνNS recoils.

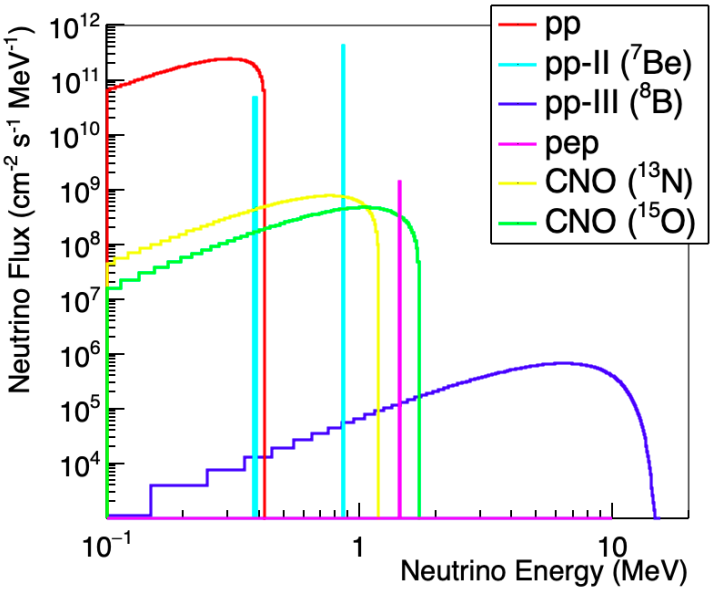

Figure 10.3: Solar neutrino spectra at Earth used in calculation of recoil rate.

The determined CEνNS recoil spectrum in a number of detector gasses due to solar neutrinos is shown in Figure 10.4. The rate is determined as is described in Section 10.2.1, because the CEνNS rate is independent of flavour, neutrino oscillation does not need to be accounted for in the calculation.

The rate of solar neutrino CEνNS recoils is a factor of at least 1×10^3 lower than the rate of reactor recoils, illustrating the necessity of a significantly larger detector than would be deployed at a reactor. A detector on the order of 1000 m^3 would be required to observe these solar neutrinos at a significant rate, not coincidentally this is the proposed size of the CYGNUS detector. Another significant feature of the solar neutrino recoil spectrum is the presence of significant structure owing the discrete contributions to the flux from different reactions. The majority of the recoils from above 1 keV are due to the high energy neutrinos from the decay of $^{8}_{5}$B in the pp-III chain. The contributions from other reactions are particularly visible in the spectrum of He recoils due to the higher momentum transfer for the light nuclei.

As observed with the reactor recoils, the inclusion of quenching results in a significant downward shift in the observable recoil energies, particularly for heavy nuclei. Similar to a reactor neutrino detector, a helium fill will produce the highest energy recoils per unit

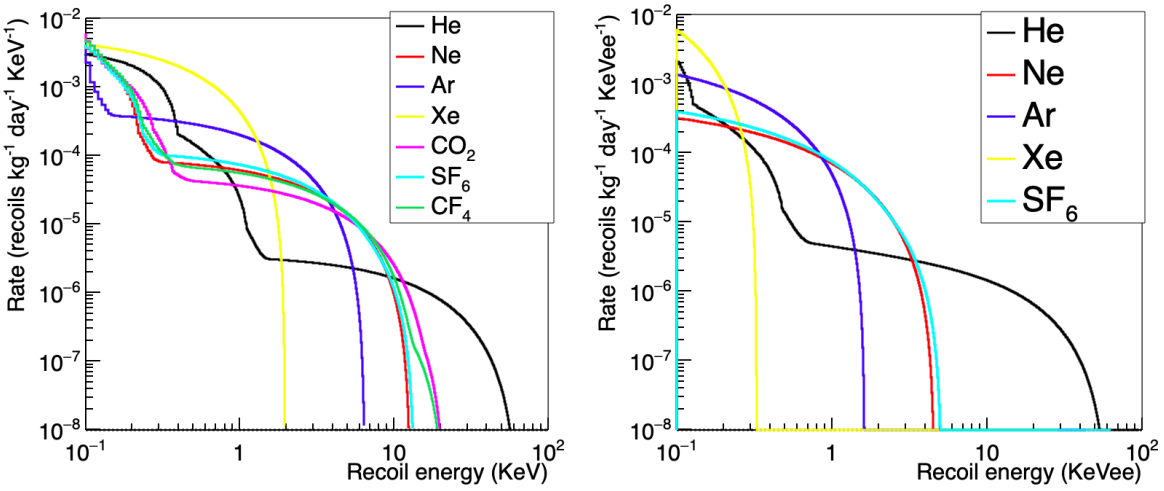

(a) Recoil energy.

(b) Observable energy (Lindhard quenching).

Figure 10.4: Energy spectrum of CEνNS induced nuclear recoils in a set of common detector gasses from solar neutrinos.

target mass. For a threshold on the order of 1 keVee, a Helium, Neon, Argon or SF_6 fill would be feasible.

10.5 Conclusions

The neutrino-nucleus scattering cross section enhancement provided by low energy coherent scattering means that a fairly low mass detector with a sufficient energy threshold proximate to a nuclear reactor could potentially observe reactor neutrinos. The CEνNS process has yet to be observed at a reactor, although experiments to do so are ongoing, and a measurement of the process would provide an interesting neutrino physics result.

The low mass requirement for a potential CEνNS detector makes a gas based detector competitive in this field. This chapter presented a determination of an anticipated reactor neutrino spectrum and the resulting CEνNS recoil energy spectrum in a number of detector gasses. The effect of ionisation quenching on the recoil spectrum was addressed in order to determine the effect of detector energy threshold on the observable recoil rate. The recoil rates at a set of potential detector sites at the Hartlepool nuclear power station were assessed along with other practical considerations. It was determined that the furthest site was actually the most feasible given it's relative accessibility, space and isolation.

Overall the primary considerations for any gas detector looking for CEνNS recoils at a reactor will be energy threshold, background discrimination, and deployable target mass. The feasibility of a gas based CEνNS detector will be very dependent on the capabilities of the deployed technology with an energy threshold on the order of 1 keVee required for neutrinos to induce observable recoils in kilogram-day exposures. This is challenging but possible, although further work is likely needed to optimise energy thresholds and background discrimination to acceptable levels.

Chapter 11

Conclusions

Low energy nuclear recoils are among the few signatures of the passage of WIMPs, fast neutrons and neutrinos though matter. The entirety of the information about the respective primary particles available to a detector is contained in the created recoils. Most nuclear recoil detectors are unable to measure the recoil direction and are only sensitive to recoil energy. There are numerous benefits to the measurement of a nuclear recoil's direction across a variety of applications.

For WIMP detection, directionality enables discrimination against the otherwise irreducible solar neutrino background and provides an unambiguous signal of dark matter WIMPs. For fast neutrons directionality enables the identification of a neutron source in a cluttered environment and can provide positive source identification with fewer events. For neutrinos the identification of the recoil direction is necessary for a CEνNS recoil observatory to disentangle the different neutrino sources which contribute to the detector signal.

Gas TPCs are one of the few detector technologies which are capable of extracting directional information from keV scale nuclear recoils. The feasibility of a gas detector for WIMP detection, fast neutron assay and CEνNS neutrino detection is heavily dependent on the volume cost. Developing scalable technologies for gas TPC detectors is therefore of paramount importance for the practical implementation of a directional detector for any of these applications. Negative ion drift gases present a method of extending the drift length of a TPC without degrading the signal, coupling a negative ion drift gas with a readout which can be manufactured in bulk was the primary goal of this work.

The ThGEM presented an attractive amplification device for a scalable readout due to it's ability to self-support and obtain high gains in low pressure gas. While it was found that the ThGEM was capable of sufficient gains to observe keV events in low pressure gas, the sparks present at operating voltages presented issues for the long term, stable operation of a device incorporating the technology.

Simulations were used to explore the properties of keV recoils in low pressure gas, particularly exploring particle ranges and the expected ionisation created by each particle and the systematics associated with the ThGEM experiments. A model of SF_6 drift and diffusion was used to determine the 1d parameters which would be most suited to ER discrimination and directionality and confirmed that observed features of the detector signal were consistent with physics occurring on the particle level.

The MM-ThGEM was tested as an alternative to the ThGEM which used layers of mesh to create the amplification fields reduce the role of the dielectric in field shaping. This work reported the first operation of a MM-ThGEM device in a negative ion gas.

The MM-ThGEM was found to escape a number of the problems encountered with the ThGEM, being far more robust against sparking and achieving significant gains across a number of pressures.

While the MM-ThGEM provided good electron amplification and reconstruction of the 1-d projected charge distribution, a lot of information is gained from readouts which are segmented to enable event reconstruction in multiple dimensions. Specifically strip readouts were known to provide the best trade off between cost and resolution. A bulk resistive layer micromegas was selected the readout technology which best met the requirements of scalability, stability and resolution. The micromegas was shown to be able to obtain significant gas gain in SF_6 although not enough to observe the keV scale recoils of interest.

Combining the novel MM-ThGEM with the resistive layer micromegas resulted in a significant enhancement of the threshold and resolution obtained on the strips. The micromegas-MMThGEM enabled the first observation of KeV scale events in SF_6 with a micromegas strip readout. The combination showed significant gain and achieved three-dimensional reconstruction of alpha tracks and ^{55}Fe electron recoils. The micromegas-MMThGEM also demonstrated compatibility with the new Kobe NI-DAQ amplification and digitisation electronics. The scalability of the electronics being also a significant contribution to the ability of a technology to obtain a large volume. The micromegas-MMThGEM was shown to operate well with the NI-DAQ system under exposure from alpha particles, x-rays, neutrons and gamma rays from the ^{241}Am, ^{55}Fe, ^{252}Cf and ^{50}Co sources. Rejection of all observed electron recoils down to low energy was demonstrated against neutron data and statistical differences were observed in under different neutron exposure directions consistent with directional information encoded in recoils. Charge dissipation in the resistive layer was shown to obscure recoil detail to an extent, deconvolution was shown to enable significant mitigation of the effect.

Overall the micromegas-MMThGEM technology presents significant promise as a scalable readout for a negative ion drift gas TPC. The MM-ThGEM overcomes the most significant issues encountered with the ThGEM in SF_6 and it's combination with the micromegas enable the extraction of directional information in 3d.

The application of gas TPC technology to the detection of the CEνNS process in reactor neutrinos with the conclusion that it is feasible. A low energy threshold on the order of 1 keV and good ER-discrimination would be required to make a measurement of that process.

Bibliography

[1] K. N. Abazajian, J. K. Adelman-McCarthy, M. A. Agüeros, *et al.*, "The seventh data release of the Sloan digital sky survey," *The Astrophysical Journal Supplement Series*, vol. 182, pp. 543–558, May 2009.

[2] Y. Akrami *et al.*, "Planck 2018 results. I. Overview and the cosmological legacy of Planck," July 2018.

[3] F. Zwicky, "Die rotverschiebung von extragalaktischen nebeln," *Helvetica Physica Acta*, vol. 6, pp. 110–127, 1933.

[4] V. C. Rubin and J. F. W. Kent, "Rotation of the Andromeda nebula from a spectroscopic survey of emission regions," *The Astrophysical Journal*, vol. 159, p. 379, feb 1970.

[5] V. C. Rubin, N. Thonnard, and J. F. W. K., "Rotational properties of 21 SC galaxies with a large range of luminosities and radii, from NGC 4605 (R = 4kpc) to UGC 2885 (R = 122 kpc)," *The Astrophysical Journal*, vol. 238, p. 471, June 1980.

[6] D. Huterer, "Weak lensing, dark matter and dark energy," *General Relativity and Gravitation*, vol. 42, pp. 2177–2195, July 2010.

[7] D. Clowe, M. Bradač, A. H. Gonzalez, *et al.*, "A direct empirical proof of the existence of dark matter," *The Astrophysical Journal*, vol. 648, pp. L109–L113, Aug. 2006.

[8] K. Heitmann, N. Frontiere, E. Rangel, *et al.*, "The Last Journey. I. an extreme-scale simulation on the Mira supercomputer," *The Astrophysical Journal Supplement Series*, vol. 252, p. 19, Jan. 2021.

[9] S.-H. Oh, C. Brook, F. Governato, *et al.*, "The central slope of dark matter cores in dwarf galaxies: Simulations versus things," *The Astronomical Journal*, vol. 142, p. 24, June 2011.

[10] P.A. Zyla *et al. (Particle Data Group)*, "2020 review of particle physics.," *Prog. Theor. Exp. Phys.*, vol. 083C01, 2020.

[11] K. Krane, *Modern Physics*, ch. Cosmology: The Origin and Fate of the Universe, pp. 530–535. Wiley, 1996.

[12] M. Battaglieri, A. Belloni, A. Chou, *et al.*, "US Cosmic Visions: New Ideas in Dark Matter 2017: Community Report," 2017.

[13] E. G. M. Ferreira, "Ultra-light dark matter," *ArXiv e-print 2005.03254*, 2021.

[14] L. Barack, V. Cardoso, S. Nissanke, *et al.*, "Black holes, gravitational waves and fundamental physics: a roadmap," *Classical and Quantum Gravity*, vol. 36, p. 143001, June 2019.

[15] L. D. Duffy and K. van Bibber, "Axions as dark matter particles," *New Journal of Physics*, vol. 11, p. 105008, Oct. 2009.

[16] K. Nakamura *et al. (Particle Data Group)*, "Axions and other similar particles," *J. Phys. G*, vol. 37, p. 075021, 2010.

[17] L. Zhong, S. A. Kenany, K. Backes, *et al.*, "Results from phase 1 of the HAYSTAC microwave cavity axion experiment," *Physical Review D*, vol. 97, May 2018.

[18] Z. Ahmed, D. S. Akerib, S. Arrenberg, *et al.*, "Search for axions with the CDMS experiment," *Physical Review Letters*, vol. 103, Oct. 2009.

[19] CAST Collaboration, "New CAST limit on the axion–photon interaction," *Nature Physics*, vol. 13, pp. 584–590, May 2017.

[20] ADMX Collaboration , "Axion Dark Matter eXperiment: Run 1b analysis details," *Phys. Rev. D*, vol. 103, p. 032002, Feb. 2021.

[21] K. Abe, K. Hiraide, K. Ichimura, *et al.*, "Search for dark matter in the form of hidden photons and axion-like particles in the X-MASS detector," *Physics Letters B*, vol. 787, pp. 153 – 158, 2018.

[22] E. Armengaud, C. Augier, A. Benoît, *et al.*, "Searches for electron interactions induced by new physics in the EDELWEISS-III germanium bolometers," *Physical Review D*, vol. 98, Oct. 2018.

[23] E. Aprile, J. Aalbers, F. Agostini, *et al.*, "Excess electronic recoil events in XENON1t," *Physical Review D*, vol. 102, Oct. 2020.

[24] T. Asaka, M. Shaposhnikov, and M. Laine, "Lightest sterile neutrino abundance within the νMSM," *Journal of High Energy Physics*, vol. 2007, pp. 091–091, Jan. 2007.

[25] E. Bulbul, M. Markevitch, A. Foster, *et al.*, "Detection of an unidentified emission line in the stacked X-ray spectrum of galaxy clusters," *The Astrophysical Journal*, vol. 789, p. 13, June 2014.

[26] F. A. Aharonian, H. Akamatsu, F. Akimoto, *et al.*, "Hitomi constraints on the 3.5 keV line in the perseus galaxy cluster," *The Astrophysical Journal*, vol. 837, p. L15, Mar. 2017.

[27] C. Benso, V. Brdar, M. Lindner, and W. Rodejohann, "Prospects for finding sterile neutrino dark matter at KATRIN," *Physical Review D*, vol. 100, Dec. 2019.

[28] Z. G. Berezhiani, "Astrophysical implications of the mirror world with broken mirror parity," *Acta Phys. Polon. B*, vol. 27, pp. 1503–1516, 1996.

[29] R. Foot and S. Vagnozzi, "Dissipative hidden sector dark matter," *Physical Review D*, vol. 91, Jan. 2015.

[30] J. L. Feng, M. Kaplinghat, H. Tu, and H.-B. Yu, "Hidden charged dark matter," *Journal of Cosmology and Astroparticle Physics*, vol. 2009, pp. 004–004, July 2009.

[31] J. L. Feng, "Dark matter candidates from particle physics and methods of detection," *Annual Review of Astronomy and Astrophysics*, vol. 48, pp. 495–545, Aug. 2010.

[32] F. Mayet, A. Green, J. Battat, *et al.*, "A review of the discovery reach of directional dark matter detection," *Physics Reports*, vol. 627, pp. 1–49, Apr. 2016.

[33] N. W. Evans, C. A. O'Hare, and C. McCabe, "SHM^{++} refinement of the standard halo model for dark matter searches in light of the gaia sausage," *Physical Review D*, vol. 99, Jan. 2019.

[34] F. Ruppin, J. Billard, E. Figueroa-Feliciano, and L. Strigari, "Complementarity of dark matter detectors in light of the neutrino background," *Phys. Rev. D*, vol. 90, p. 083510, Oct. 2014.

[35] E. Aprile, J. Aalbers, F. Agostini, *et al.*, "Light dark matter search with ionization signals in XENON1T," *Physical Review Letters*, vol. 123, p. 251801, Dec. 2019.

[36] A. Abdelhameed, G. Angloher, P. Bauer, *et al.*, "First results from the CRESST-III low-mass dark matter program," *Physical Review D*, vol. 100, Nov. 2019.

[37] E. Armengaud, C. Augier, A. Benoît, *et al.*, "Searching for low-mass dark matter particles with a massive Ge bolometer operated above ground," *Physical Review D*, vol. 99, Apr. 2019.

[38] E. Behnke, M. Besnier, P. Bhattacharjee, *et al.*, "Final results of the PICASSO dark matter search experiment," *Astropart. Phys.*, vol. 90, pp. 85–92, Apr. 2017.

[39] C. Amole, M. Ardid, I. Arnquist, *et al.*, "Dark matter search results from the PICO-60 C_3F_8 bubble chamber," *Physical Review Letters*, vol. 118, June 2017.

[40] D. Akimov, H. Araújo, E. Barnes, *et al.*, "WIMP-nucleon cross-section results from the second science run of ZEPLIN-III," *Physics Letters B*, vol. 709, no. 12, pp. 14 – 20, 2012.

[41] A. Aguilar-Arevalo, D. Amidei, D. Baxter, *et al.*, "Results on low-mass weakly interacting massive particles from a 11 kg-day target exposure of DAMIC at SNOLAB," 2020.

[42] G. Adhikari, P. Adhikari, E. B. de Souza, *et al.*, "An experiment to search for dark-matter interactions using sodium iodide detectors," *Nature*, vol. 564, pp. 83–86, Dec. 2018.

[43] C. Fu, X. Cui, X. Zhou, *et al.*, "Spin-dependent weakly-interacting-massive-particle–nucleon cross section limits from first data of PandaX-II experiment," *Phys. Rev. Lett.*, vol. 118, p. 071301, Feb. 2017.

[44] J. Billard, E. Figueroa-Feliciano, and L. Strigari, "Implication of neutrino backgrounds on the reach of next generation dark matter direct detection experiments," *Physical Review D*, vol. 89, Jan. 2014.

[45] D. Dubbers and M. G. Schmidt, "The neutron and its role in cosmology and particle physics," *Reviews of Modern Physics*, vol. 83, pp. 1111–1171, Oct. 2011.

[46] and P A Zyla, R. M. Barnett, J. Beringer, *et al.*, "Review of particle physics," *Progress of Theoretical and Experimental Physics*, vol. 2020, Aug. 2020.

[47] A. Collins, S. Fletcher, and R. Davies, "ISIS neutron and muon source annual review 2019," Tech. Rep. RAL-TR-2020-001, Rutherford Appleton Laboratory, 2019.

[48] V. Valkovic, *14 MeV Neutrons*. Taylor & Francis Ltd., 2015.

[49] R. E. F. J. Kenneth Shultis, *Fundamentals of Nuclear Science and Engineering*. CRC PR INC, 2007.

[50] R. T. Kouzes, E. R. Siciliano, J. H. Ely, P. E. Keller, and R. J. McConn, "Passive neutron detection for interdiction of nuclear material at borders," *Nuclear Instruments and Methods in Physics Research Section A: Accelerators, Spectrometers, Detectors and Associated Equipment*, vol. 584, pp. 383–400, Jan. 2008.

[51] G. F. Knoll, *Radiation Detection and Measurement*. PAPERBACKSHOP UK IMPORT, 2010.

[52] S. Mughabghab, *Neutron Cross Sections: Neutron Resonance Parameters and Thermal Cross Sections, Part A: Z=1-60 (Neutron cross sections series)*. Academic Press, 2012.

[53] S. F. Mughabghab, *Neutron Cross Sections, Volume 1B: Neutron Resonance Parameters and Thermal Cross Sections Part B: Z=61-100 (Neutron Cross Sections, Vol 1)*. Academic Press, 1984.

[54] ICRP, "The 2007 recommendatations of the international commission on radiological protection," *Annuals of the ICRP*, vol. 103, no. 37, pp. 2–4, 2007.

[55] T. Goričanec, D. Kotnik, Ž. Štancar, L. Snoj, and M. Kromar, "Predicting ex-core detector response in a PWR with monte carlo neutron transport methods," *EPJ Web of Conferences*, vol. 225, p. 03007, 2020.

[56] B. Woringer, "UK EPR: Pre-construction safety report. sub-chapter 7.6 – instrumentation." UKEPR-0002-075, 2012.

[57] R. A. Tinguely, A. Rosenthal, R. Simpson, *et al.*, "Neutron diagnostics for the physics of a high-field, compact, $q \geq 1$ tokamak," *Fusion Engineering and Design*, vol. 143, pp. 212–225, June 2019.

[58] Borexino Collaboration, "Neutrinos from the primary proton–proton fusion process in the sun," *Nature*, vol. 512, pp. 383–386, Aug. 2014.

[59] P. Huber, "Determination of antineutrino spectra from nuclear reactors," *Physical Review C*, vol. 84, p. 024617, Aug. 2011.

[60] P. Mészáros, "Astrophysical sources of high-energy neutrinos in the IceCube era," *Annual Review of Nuclear and Particle Science*, vol. 67, pp. 45–67, Oct. 2017.

[61] J. A. Formaggio and G. P. Zeller, "From eV to EeV: Neutrino cross sections across energy scales," *Reviews of Modern Physics*, vol. 84, pp. 1307–1341, Sept. 2012.

[62] C. W. K. Carlo Giunti, *Fundamentals of Neutrino Physics and Astrophysics*. Oxford University Press, 2007.

[63] K. Zuber, *Neutrino Physics*. Oxford: IoP, 2004.

[64] E. Kolbe, K. Langanke, G. Martínez-Pinedo, and P. Vogel, "Neutrino–nucleus reactions and nuclear structure," *Journal of Physics G: Nuclear and Particle Physics*, vol. 29, pp. 2569–2596, Oct. 2003.

[65] K. M. Tsui, K. Okumura, Y. Nakajima, R. Akutsu, and S.-K. Collaboration, "Super-K Gd project: Neutron-tagging algorithm," *Summary of Lectures by the Physical Society of Japan*, vol. 72.2, pp. 337–337, 2017.

[66] J. N. Bahcall, "Gallium solar neutrino experiments: Absorption cross sections, neutrino spectra, and predicted event rates," *Physical Review C*, vol. 56, pp. 3391–3409, Dec. 1997.

[67] D. Akimov, J. B. Albert, P. An, *et al.*, "Observation of coherent elastic neutrino-nucleus scattering," *Science*, vol. 357, pp. 1123–1126, Aug. 2017.

[68] F. N. Flakus, "Detecting and measuring ionizing radiation - a short history," *IAEA Bulletin*, vol. 23, no. 4, pp. 31–36, 1981.

[69] J. F. Ziegler, J. P. Biersack, and M. D. Ziegler, *SRIM - The Stopping and Range of Ions in Matter*. Lulu Press, 2007.

[70] L. G. Christophorou, J. K. Olthoff, and M. V. V. S. Rao, "Electron interactions with CF4," *Journal of Physical and Chemical Reference Data*, vol. 25, pp. 1341–1388, Sept. 1996.

[71] D. Rodrigues, K. Andersson, M. Cababie, *et al.*, "Absolute measurement of the fano factor using a skipper-ccd," *FERMILAB-PUB-20-283-E*, 2020.

[72] U. Fano, "Ionization yield of radiations. II. the fluctuations of the number of ions," *Physical Review*, vol. 72, pp. 26–29, July 1947.

[73] J. Lindhard, V. Nielsen, M. Scharff, and P. Thomsen, "Integral equations governing radiation effects," *Matematisk-fysiske Meddelelser Det Kongelige Danske Videnskabernes Selskab*, vol. 33, no. 10, 1963.

[74] P. Sorensen, "Atomic limits in the search for galactic dark matter," *Physical Review D*, vol. 91, Apr. 2015.

[75] D. R. Nygren, "Origin and development of the TPC idea," *Nuclear Instruments and Methods in Physics Research Section A: Accelerators, Spectrometers, Detectors and Associated Equipment*, vol. 907, pp. 22–30, Nov. 2018.

[76] S. Ramo, "Currents induced by electron motion," *Proceedings of the IRE*, vol. 27, pp. 584–585, Sept. 1939.

[77] F. J. Iguaz, E. Ferrer-Ribas, A. Giganon, and I. Giomataris, "Characterization of microbulk detectors in argon- and neon-based mixtures," *Journal of Instrumentation*, vol. 7, pp. P04007–P04007, Apr. 2012.

[78] M. E. Rose and S. A. Korff, "An investigation of the properties of proportional counters. i," *Phys. Rev.*, vol. 59, pp. 850–859, June 1941.

[79] S. D. Pinto, "Micropattern gas detector technologies and applications the work of the RD51 collaboration," in *IEEE Nuclear Science Symposuim Medical Imaging Conference*, pp. 802–807, 2010.

[80] D. P. Snowden-Ifft, "Discovery of multiple, ionization-created CS2 anions and a new mode of operation for drift chambers," *Review of Scientific Instruments*, vol. 85, p. 013303, jan 2014.

[81] N. Phan, R. Lafler, R. Lauer, *et al.*, "The novel properties of SF6 for directional dark matter experiments," *Journal of Instrumentation*, vol. 12, pp. P02012–P02012, Feb. 2017.

[82] W. Blum, W. Riegler, and L. Rolandi, *Particle Detection with Drift Chambers*. Springer-Verlag GmbH, 2008.

[83] S. E. Vahsen, C. A. J. O'Hare, W. A. Lynch, *et al.*, "Cygnus: Feasibility of a nuclear recoil observatory with directional sensitivity to dark matter and neutrinos," *ArXiv e-print 2008.12587*, 2020.

[84] I. A. Costa, "i2DBSCAN: an iterative density-based clustering algorithm for CYGNO experiment," in *The CYGNUS 2019 workshop on directional dark matter detection*, 2019.

[85] Q. Riffard, D. Santos, O. Guillaudin, *et al.*, "MIMAC low energy electron-recoil discrimination measured with fast neutrons," *Journal of Instrumentation*, vol. 11, pp. P08011–P08011, Aug. 2016.

[86] S. Wu, Q. Yue, W. Lai, *et al.*, "Near threshold pulse shape discrimination techniques in scintillating CsI(tl) crystals," *Nuclear Instruments and Methods in Physics Research Section A: Accelerators, Spectrometers, Detectors and Associated Equipment*, vol. 523, pp. 116–125, May 2004.

[87] J. Battat, E. Daw, A. Ezeribe, *et al.*, "First measurement of nuclear recoil head-tail sense in a fiducialised WIMP dark matter detector," *Journal of Instrumentation*, vol. 11, pp. P10019–P10019, Oct. 2016.

[88] D. Maire, G. Bosson, O. Guillaudin, *et al.*, "Neutron energy reconstruction and fluence determination at 27 keV with the LNE-IRSN-MIMAC MicroTPC recoil detector," *IEEE Transactions on Nuclear Science*, vol. 63, pp. 1934–1941, June 2016.

[89] S. E. Vahsen, M. T. Hedges, I. Jaegle, *et al.*, "3-D tracking in a miniature time projection chamber," *Nuclear Instruments and Methods in Physics Research Section A: Accelerators, Spectrometers, Detectors and Associated Equipment*, vol. 788, pp. 95–105, 2015.

[90] K. Nakamura, K. Miuchi, S. Iwaki, *et al.*, "NEWAGE," *Journal of Physics: Conference Series*, vol. 375, p. 012013, July 2012.

[91] J. B. R. Battat, S. Ahlen, T. Caldwell, *et al.*, "DMTPC: Dark matter detection with directional sensitivity," *ArXiv e-print 1012.3912*, Dec. 2010.

[92] E. Baracchini, R. Bedogni, F. Bellini, *et al.*, "Directional dark matter searches with the CYGNO project," *Journal of Physics: Conference Series*, vol. 1468, p. 012039, Feb. 2020.

[93] R. Cerulli, "Low background techniques toward a ZnWO4 directionality experiment," *International Journal of Modern Physics A*, vol. 32, p. 1743009, Oct. 2017.

[94] K. Hirota, T. Ariga, M. Hino, *et al.*, "Neutron imaging using a fine-grained nuclear emulsion," *Journal of Imaging*, vol. 7, p. 4, Jan. 2021.

[95] N. Polukhina and N. Starkov, "New experiment for WIMP direct search (NEWSdm)," *EPJ Web of Conferences*, vol. 191, p. 02023, 2018.

[96] A. Weltz, B. Torres, L. McElwain, *et al.*, "Development of a modular directional and spectral neutron detection system using solid-state detectors," *Nuclear Instruments and Methods in Physics Research Section A: Accelerators, Spectrometers, Detectors and Associated Equipment*, vol. 792, pp. 28–37, 2015.

[97] A. Peurrung, D. Stromswold, R. Hansenand, P. Reeder, and D. Barnett, "Long-range neutron detection," Tech. Rep. PNNL-13044, PNNL, 1999.

[98] R. T. Klann, G. Perret, and J. Sanders, "Coated gallium arsenide neutron detectors: Results of characterization measurements," Report ANL-06/42, Argonne National Laboratories, 2006.

[99] G. A. Wurden, R. E. Chrien, C. W. Barnes, *et al.*, "Scintillating-fiber 14 MeV neutron detector on TFTR during DT operation," *Review of Scientific Instruments*, vol. 66, pp. 901–903, 1995.

[100] N. Mascarenhas, W. Mengesha, J. Peel, and D. Sunnarborg, "Directional neutron detectors for use with 14 MeV neutrons," Report SAND2005-6255, Sandia National Laboratories, 2005.

[101] A. Roccaro, H. Tomita, S. Ahlen, *et al.*, "A background-free direction-sensitive neutron detector," *Nuclear Instruments and Methods in Physics Research Section A: Accelerators, Spectrometers, Detectors and Associated Equipment*, vol. 608, no. 2, pp. 305 – 309, 2009.

[102] I. Jaegle, P. Lewis, M. Garcia-Sciveres, *et al.*, "Compact, directional neutron detectors capable of high-resolution nuclear recoil imaging," *Nuclear Instruments and Methods in Physics Research Section A: Accelerators, Spectrometers, Detectors and Associated Equipment*, vol. 945, p. 162296, Nov. 2019.

[103] S. Fukuda, Y. Fukuda, T. Hayakawa, *et al.*, "The super-kamiokande detector," *Nuclear Instruments and Methods in Physics Research Section A: Accelerators, Spectrometers, Detectors and Associated Equipment*, vol. 501, pp. 418–462, Apr. 2003.

[104] I. Collaboration, "Evidence for high-energy extraterrestrial neutrinos at the IceCube detector," *Science*, vol. 342, pp. 1242856–1242856, Nov. 2013.

[105] N. Jelley, A. B. McDonald, and R. H. Robertson, "The sudbury neutrino observatory," *Annual Review of Nuclear and Particle Science*, vol. 59, pp. 431–465, Nov. 2009.

[106] J. H. Seo, Z. Atif, C. D. Shin, and K. K. Joo, "Search for reactor neutrino directionality using a LAB-based gd-loaded liquid scintillation detector," *Nuclear Instruments and Methods in Physics Research Section A: Accelerators, Spectrometers, Detectors and Associated Equipment*, vol. 969, p. 164001, July 2020.

[107] R. Chechik, M. Cortesi, A. Breskin, *et al.*, "Thick GEM-like (THGEM) detectors and their possible applications," *ArXiv e-print physics/0606162v1*, 2006.

[108] C. Shalem, R. Chechik, A. Breskin, and K. Michaeli, "Advances in thick GEM-like gaseous electron multipliers—part i: atmospheric pressure operation," *Nuclear Instruments and Methods in Physics Research Section A: Accelerators, Spectrometers, Detectors and Associated Equipment*, vol. 558, pp. 475–489, Mar. 2006.

[109] C. Shalem, R. Chechik, A. Breskin, K. Michaeli, and N. Ben-Haim, "Advances in thick GEM-like gaseous electron multipliers part II: Low-pressure operation," *Nuclear Instruments and Methods in Physics Research Section A: Accelerators, Spectrometers, Detectors and Associated Equipment*, vol. 558, pp. 468–474, Mar. 2006.

[110] R. Chechik, A. Breskin, and C. Shalem, "Thick GEM-like multipliers—a simple solution for large area UV-RICH detectors," *Nuclear Instruments and Methods in Physics Research Section A: Accelerators, Spectrometers, Detectors and Associated Equipment*, vol. 553, pp. 35–40, Nov. 2005.

[111] M. Cortesi, R. Alon, R. Chechik, *et al.*, "Investigations of a THGEM-based imaging detector," *Journal of Instrumentation*, vol. 2, pp. P09002–P09002, Sept. 2007.

[112] M. Pitt, P. Correia, S. Bressler, *et al.*, "Measurements of charging-up processes in THGEM-based particle detectors," *Journal of Instrumentation*, vol. 13, pp. P03009–P03009, Mar. 2018.

[113] C. Inc, *CR-150-R5 evaluation board: application guide.* https://www.cremat.com/CR-150-R5.pdf.

[114] Fast ComTec, *CR-111 charge sensitive preamplifier: application guide*, 2006.

[115] Fast ComTec, *CR-200 Gaussian shaping amplifier (Rev. 2): application guide*, 2006.

[116] H. Junde, "Nuclear Data Sheets for A = 55," *Nuclear Data Sheets*, vol. 109, pp. 787–942, Apr. 2008.

[117] V. Bakhshi-Zade, I. Garzanov, V. Labushkin, V. Nedovesov, and E. E. V.P. Chechev, "Tables of Evaluated Standard Data on Decay and Radiation Characteristics of Radionuclides Used for Calibration of Semiconductor Spectrometers in -Ray Energy Range of 5-140 keV," *Program and Theses, Proc. 38th Ann. Conf. Nucl. Spectrosc. Struct. At. Nuclei, Baku*, p. 539, 1988.

[118] S. R. Hunter, J. G. Carter, and L. G. Christophorou, "Electron attachment and ionization processes in CF4, c2f6, c3f8, and n-c4f10," *The Journal of Chemical Physics*, vol. 86, pp. 693–703, Jan. 1987.

[119] Z.-Y. He, J.-R. Zhou, Z.-J. Sun, *et al.*, "Experimental studies of THGEM in different ar/CO2 mixtures," *Chinese Physics C*, vol. 38, p. 056003, May 2014.

[120] J. Burns, T. Crane, A. Ezeribe, *et al.*, "Characterisation of large area THGEMs and experimental measurement of the townsend coefficients for CF4," *Journal of Instrumentation*, vol. 12, pp. T10006–T10006, Oct. 2017.

[121] R. Morrow, "A survey of the electron and ion transport properties of SF6," *IEEE Transactions on Plasma Science*, vol. 14, no. 3, pp. 234–239, 1986.

[122] G. Alner, H. Araujo, A. Bewick, *et al.*, "The DRIFT-II dark matter detector: Design and commissioning," *Nuclear Instruments and Methods in Physics Research Section A: Accelerators, Spectrometers, Detectors and Associated Equipment*, vol. 555, pp. 173–183, Dec. 2005.

[123] S. Burgos, E. Daw, J. Forbes, *et al.*, "First measurement of the head–tail directional nuclear recoil signature at energies relevant to WIMP dark matter searches," *Astroparticle Physics*, vol. 31, pp. 261–266, May 2009.

[124] J. Battat, A. Ezeribe, J.-L. Gauvreau, *et al.*, "Low threshold results and limits from the DRIFT directional dark matter detector," *Astroparticle Physics*, vol. 91, pp. 65–74, May 2017.

[125] A. Scarff, *Developments Towards a Scaled-Up One-Dimensional Directional Dark Matter Detector*. PhD thesis, University of Sheffield, 2017.

[126] M. Alexeev, R. Birsa, F. Bradamante, *et al.*, "Status of COMPASS RICH-1 upgrade with MPGD-based photon detectors," *EPJ Web of Conferences*, vol. 174, p. 01004, 2018.

[127] S. Biagi, "DEGRAD - transport of electrons in gas mixtures." URL: http://degrad.web.cern.ch/degrad/, Last updated: 2019. Accessed: 17/07/2020.

[128] S. Biagi, "DEGRAD 1.0 - auger cascade model for electron thermalisation in gas mixtures produced by photons or particles in electric and magnetic fields." URL: https://indico.cern.ch/event/245535/contributions/531797/attachments/420757/584265/cern.rd51.2013.pdf, Last updated: 2013. Accessed: 16/07/2020.

[129] D. Pfeiffer, L. D. Keukeleere, C. Azevedo, *et al.*, "Interfacing geant4, garfield++ and degrad for the simulation of gaseous detectors," *Nuclear Instruments and Methods in Physics Research Section A: Accelerators, Spectrometers, Detectors and Associated Equipment*, vol. 935, pp. 121–134, Aug. 2019.

[130] I. Lopes, H. Hilmert, and W. F. Schmidt, "Ionisation of gaseous and liquid sulphur hexafluoride by60co γ-radiation," *Journal of Physics D: Applied Physics*, vol. 19, pp. L107–L110, June 1986.

[131] O. Guillaudin, J. Billard, G. Bosson, *et al.*, "Quenching factor measurement in low pressure gas detector for directional dark matter search," *EAS Publications Series*, vol. 53, pp. 119–127, 2012.

[132] S. Agostinelli, J. Allison, K. Amako, *et al.*, "Geant4—a simulation toolkit," *Nuclear Instruments and Methods in Physics Research Section A: Accelerators, Spectrometers, Detectors and Associated Equipment*, vol. 506, pp. 250–303, July 2003.

[133] G. Collaboration, "Geant 4 user guide." http://geant4-userdoc.web.cern.ch/geant4-userdoc/UsersGuides/IntroductionToGeant4/html/index.html, Published: 2018. Accessed: June 2020.

[134] T. G. Collaboration, *The Geant 4 Physics referance Manual*.

[135] "Geant4 Cross Reference: Geant4/examples/extended/electromagnetic/TestEm7."

[136] L. Urban, "A model for multiple scattering in geant4," *Monte Carlo 2005 Topical Meeting*, Jan. 2005.

[137] L. Pandola, C. Andenna, and B. Caccia, "Validation of the geant4 simulation of bremsstrahlung from thick targets below 3 MeV," *Nuclear Instruments and Methods in Physics Research Section B: Beam Interactions with Materials and Atoms*, vol. 350, pp. 41–48, May 2015.

[138] M. Tanabashi *et al. (Particle Data Group) Physical Review D*, vol. 98, p. 030001, 2018.

[139] E. A. Lorch, "Neutron spectra of ^{241}Am/B, ^{241}Am/Be, ^{241}Am/F, ^{242}Cm/Be, ^{238}Pu/^{13}C and ^{252}Cf isotopic neutron sources," *The International Journal of Applied Radiation and Isotopes*, vol. 24, pp. 585–591, Oct. 1973.

[140] M. S. Naidu and A. N. Prasad, "Mobility and diffusion of negative ions in sulphur hexafluoride," *Journal of Physics D: Applied Physics*, vol. 3, pp. 951–956, June 1970.

[141] R. de Olivera and M. Cortesi, "First performance evaluation of a multi-layer thick gaseous electron multiplier with in-built electrode meshes—MM-THGEM," *Journal of Instrumentation*, vol. 13, pp. P06019–P06019, jun 2018.

[142] M. Cortesi, S. Rost, W. Mittig, *et al.*, "Multi-layer thick gas electron multiplier (m-THGEM): A new MPGD structure for high-gain operation at low-pressure," *Review of Scientific Instruments*, vol. 88, p. 013303, Jan. 2017.

[143] H. Schindler, "Garfield++ user guide." https://garfieldpp.web.cern.ch/garfieldpp/documentation/UserGuide.pdf, Feb. 2017.

[144] P. Lightfoot, N. Spooner, T. Lawson, S. Aune, and I. Giomataris, "First operation of bulk micromegas in low pressure negative ion drift gas mixtures for dark matter searches," *Astroparticle Physics*, vol. 27, pp. 490–499, July 2007.

[145] P. Linstrom, "Nist chemistry webbook, nist standard reference database 69," 1997.

[146] K. Nikolopoulos, P. Bhattacharya, V. Chernyatin, and R. Veenhof, "Electron transparency of a micromegas mesh," *Journal of Instrumentation*, vol. 6, pp. P06011–P06011, June 2011.

[147] P. Campion, "Spurious pulses in proportional counters," *Nuclear Instruments and Methods*, vol. 112, pp. 75–81, Sept. 1973.

[148] G. W. Penney, S. F. Nygren, and R. E. Voshall, "Photoionization as the secondary mechanism in a townsend breakdown," *IEEE Transactions on Communication and Electronics*, vol. 83, pp. 203–208, Mar. 1964.

[149] H. Genz, D. Harmer, and R. Fink, "Measurement by two-dimensional pulse analysis of the time and energy distributions of afterpulses in proportional counters," *Nuclear Instruments and Methods*, vol. 60, pp. 195–200, Mar. 1968.

[150] R. J. Lafler, *Studying The Properties Of SF6 Gas Mixtures For Directional Dark Matter Detection.* PhD thesis, UNM, 2019.

[151] Y. Giomataris, P. Rebourgeard, J. Robert, and G. Charpak, "MICROMEGAS: a high-granularity position-sensitive gaseous detector for high particle-flux environments," *Nuclear Instruments and Methods in Physics Research Section A: Accelerators, Spectrometers, Detectors and Associated Equipment*, vol. 376, pp. 29–35, June 1996.

[152] I. Giomataris, R. D. Oliveira, S. Andriamonje, *et al.*, "Micromegas in a bulk," *Nuclear Instruments and Methods in Physics Research Section A: Accelerators, Spectrometers, Detectors and Associated Equipment*, vol. 560, pp. 405–408, May 2006.

[153] M. Nakazawa, T. Kishishita, M. Shoji, *et al.*, "Prototype analog front-end for negative-ion gas and dual-phase liquid-ar TPCs," *Journal of Instrumentation*, vol. 14, pp. T01008–T01008, Jan. 2019.

[154] T.-H. Lin, A. Düdder, M. Schott, *et al.*, "Signal characteristics of a resistive-strip micromegas detector with an integrated two-dimensional readout," *Nuclear Instruments and Methods in Physics Research Section A: Accelerators, Spectrometers, Detectors and Associated Equipment*, vol. 767, pp. 281–288, Dec. 2014.

[155] M. Byszewski and J. Wotschack, "Resistive-strips micromegas detectors with two-dimensional readout," *Journal of Instrumentation*, vol. 7, pp. C02060–C02060, Feb. 2012.

[156] W. Riegler, "Electric fields, weighting fields, signals and charge diffusion in detectors including resistive materials," *Journal of Instrumentation*, vol. 11, pp. P11002–P11002, Nov. 2016.

[157] H. Maeda, Y. Nagasaka, H. Sendai, *et al.*, "Control functionality of DAQ-middleware," *Journal of Physics: Conference Series*, vol. 513, p. 012020, June 2014.

[158] Y. Nagasaka, H. Maeda, H. Sendai, *et al.*, "Communication architecture of DAQ-middleware," in *2012 18th IEEE-NPSS Real Time Conference*, IEEE, June 2012.

[159] B. Kirby, "Stt readout electronics using the vmm3 asic," in *DUNE-IT simulations 63rd meeting*, 2019.

[160] R. Schafer, "What is a savitzky-golay filter? [lecture notes]," *IEEE Signal Processing Magazine*, vol. 28, pp. 111–117, July 2011.

[161] S. B. Damelin and W. J. Miller, *The Mathematics of Signal Processing*. Cambridge University Press, 2009.

[162] L. B. Lucy, "An iterative technique for the rectification of observed distributions," *The Astronomical Journal*, vol. 79, p. 745, June 1974.

[163] W. H. Richardson, "Bayesian-based iterative method of image restoration," *Journal of the Optical Society of America*, vol. 62, p. 55, Jan. 1972.

[164] MathWorks, "deconvlucy - Deblur image using Lucy-Richardson method." URL: https://uk.mathworks.com/help/images/ref/deconvlucy.html. Accessed: 09/02/2021.

[165] G. L. Almeida, M. I. Silvani, E. S. Souza, and R. T. Lopes, "A stopping criterion to halt iterations at the richardson-lucy deconvolution of radiographic images," *Journal of Physics: Conference Series*, vol. 630, p. 012003, July 2015.

[166] J. Lee, B. H. Choi, J.-H. Yun, and Y. S. Park, "Characteristics of nitrogen doped diamond-like carbon films prepared by unbalanced magnetron sputtering for electronic devices," *Journal of Nanoscience and Nanotechnology*, vol. 16, pp. 4893–4896, May 2016.

[167] M. Cadeddu, F. Dordei, C. Giunti, *et al.*, "Physics results from the first COHERENT observation of coherent elastic neutrino-nucleus scattering in argon and their combination with cesium-iodide data," *Physical Review D*, vol. 102, July 2020.

[168] D. Akimov, J. Albert, P. An, *et al.*, "First measurement of coherent elastic neutrino-nucleus scattering on argon," *Physical Review Letters*, vol. 126, Jan. 2021.

[169] D. Akimov, J. Albert, P. An, *et al.*, "First constraint on coherent elastic neutrino-nucleus scattering in argon," *Physical Review D*, vol. 100, Dec. 2019.

[170] A. Aguilar-Arevalo, X. Bertou, C. Bonifazi, *et al.*, "Exploring low-energy neutrino physics with the coherent neutrino nucleus interaction experiment," *Physical Review D*, vol. 100, Nov. 2019.

[171] A. Aguilar-Arevalo, X. Bertou, C. Bonifazi, *et al.*, "Results of the engineering run of the coherent neutrino nucleus interaction experiment (CONNIE)," *Journal of Instrumentation*, vol. 11, pp. P07024–P07024, July 2016.

[172] D. Z. Freedman, D. N. Schramm, and D. L. Tubbs, "The weak neutral current and its effects in stellar collapse," *Annual Review of Nuclear Science*, vol. 27, pp. 167–207, Dec. 1977.

[173] A. Drukier and L. Stodolsky, "Principles and applications of a neutral-current detector for neutrino physics and astronomy," *Physical Review D*, vol. 30, pp. 2295–2309, Dec. 1984.

[174] H. T. Wong, H. B. Li, S. T. Lin, *et al.*, "Search of neutrino magnetic moments with a high-purity germanium detector at the Kuo-Sheng nuclear power station," *Physical Review D*, vol. 75, p. 012001, Jan. 2007.

[175] X. B. Ma, W. L. Zhong, L. Z. Wang, Y. X. Chen, and J. Cao, "Improved calculation of the energy release in neutron-induced fission," *Physical Review C*, vol. 88, July 2013.

[176] F. T. Avignone and Z. D. Greenwood, "Calculated spectra of antineutrinos from the fission products of ^{235}U, ^{238}U, and ^{239}Pu, and antineutrino-induced reactions," *Phys. Rev. C*, vol. 22, pp. 594–605, Aug. 1980.

[177] J. Coleman, C. Metelko, M. Murdoch, *et al.*, "VIDARR: Aboveground reactor monitoring," *Journal of Physics: Conference Series*, vol. 1216, p. 012007, Apr. 2019.

[178] W. T. Winter, S. J. Freedman, K. E. Rehm, and J. P. Schiffer, "The ^{8}B neutrino spectrum," *Physical Review C*, vol. 73, Feb. 2006.

[179] J. N. Bahcall, M. H. Pinsonneault, and S. Basu, "Solar models: Current epoch and time dependences, neutrinos, and helioseismological properties," *The Astrophysical Journal*, vol. 555, pp. 990–1012, July 2001.